ISTITUTO NAZIONALE DI FISICA NUCLEARE
Laboratori Nazionali di Frascati

FRASCATI PHYSICS SERIES

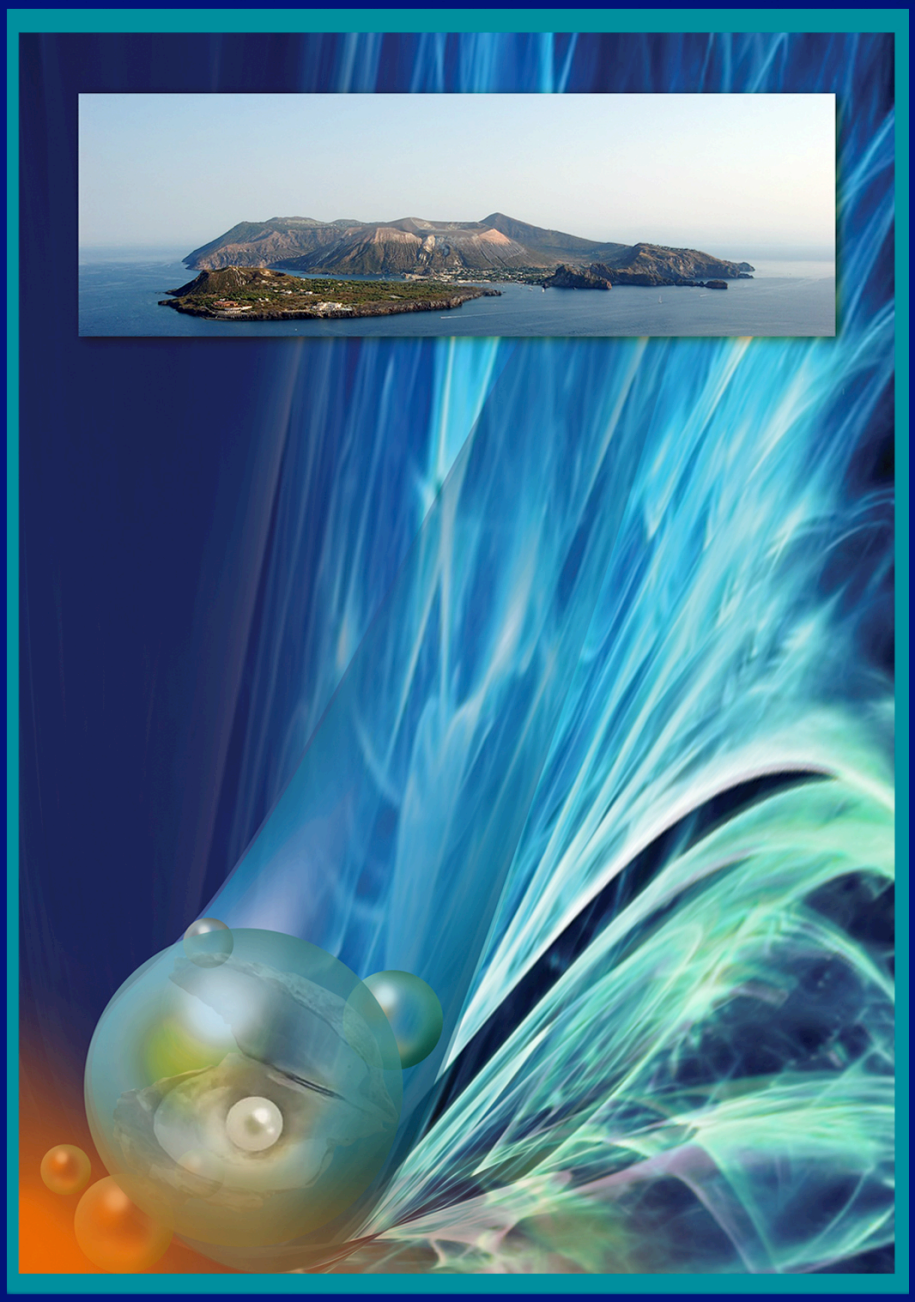

Vulcano 2014

Frontier Objects in Astrophysics and Particle Physics

Editors:
R. Fusco Femiano, G. Mannocchi, A. Morselli, G. Trinchero

FRASCATI PHYSICS SERIES

Series Editor
Rossana Centioni

Technical Editor
Debora Bifaretti

Cover by Claudio Federici

Volume LVIII

Istituto Nazionale di Fisica Nucleare – Laboratori Nazionali di Frascati
Divisione Ricerca
SIDS – Servizio Informazione e Documentazione Scientifica
Ufficio Biblioteca e Pubblicazioni
P.O. Box 13, I-00044 Frascati Roma Italy
email: sis.publications@lnf.infn.it

ISBN 978-88-86409-63-6

VULCANO Workshop
Frontier Objects in Astrophysics and Particle Physics
2014

Vulcano Workshop 2014

Frontier Objects in AstroPhysics and Particle Physics

Dark Matter

Cosmology and Astroparticle

Astrophysics and Cosmology

Particle Physics and Interactions

Cosmic Ray origin, Gamma and Neutrino Astronomy

Neutrinos

Cosmic Rays

* Slides are available at https://agenda.infn.it/conferenceOtherViews.py?view=nicecompact&confId=7266

FOREWORD

The fifteenth edition of the Vulcano workshop: *Frontier objects in Astrophysics and Particle Physics* was organized jointly by the National Institute for Nuclear Physics (INFN) and the National Institute for Astrophysics (INAF). The workshop was held in the Conference Room of the Therasia Resort (Vulcano Island, Sicily, Italy) from May 18th to May 24th and was attended by more than 100 scientists world wide.

This workshop is certainly one of the first that since 1986 has the aim to gather people from High Energy Astrophysics and Particle Physics to discuss the most recent highlights in these fields. It is well known that at the beginning of the 80's the Universe was considered the greatest particle accelerator of the world to test the Grand Unified Theories ideas. Of course a machine hard to use because all the experiments happened only once, a long time ago. The connection between particle physics and cosmology was nicely illustrated by the cosmic serpent published by Sheldon Glashow in 1982, the serpent swallowing its tail. Today, gigantic underground accelerators and space crafts probe everyday this connection. In particular Cosmology provides three fundamental questions for the Universe as confirmed by the latest Planck results, namely: what is Dark Energy ? What is Dark Matter ? And why in the Universe we have matter and not antimatter, and therefore one of the goals of this workshop was to discuss if these questions may be resolved, at least partially, by particle physics.

The final scientific program was selected by the Scientific Organizing Committe chaired by Roberto Fusco-Femiano (INAF) and Giampaolo Mannocchi (INFN) and composed by: Simone dell'Agnello (INFN), Pino Di Sciascio (INFN), Aurelio Grillo (INFN), Aldo Morselli (INFN), Luigi Piro (INAF), Marco Ricci (INFN) and Gian Carlo Trinchero (INAF).

The Local Organizing Committee was composed by Maria Cristina D'Amato (INFN), Roberto Fusco-Femiano, Giampaolo Mannocchi, and Lia Sabatini (INFN) with the precious help of Alessio Gorgi (INAF). A special thank to Maria Cristina D'Amato and Lia Sabatini for their fundamental work not only in the preparatory phase but also during and after the conclusion of the workshop, allowing us to receive numerous compliments on the level of the Conference.

Roberto Fusco-Femiano and Giampaolo Mannocchi

Frascati Physics Series Vol. 58 (2014)
Frontier Objects in Astrophysics and Particle Physics
May 18-24, 2014

Cosmology and astrophysics with the thermal component of the Clusters of Galaxies

S. Ettori
INAF, Osservatorio Astronomico di Bologna, via Ranzani 1, Bologna, Italy
INFN, Sezione di Bologna, viale Berti Pichat 6/2, Bologna, Italy

Abstract

The key tool to use galaxy clusters as astrophysical laboratories and cosmological probes is the knowledge of the distribution of the their gravitating and baryonic mass. I'll illustrate how the estimates of the gas mass fraction and of the mass concentration can be used as robust cosmological tests. I'll show how the use of generalized X-ray scaling relations can help to reduce the scatter in reconstructing the total mass.

1 Introduction to the Clusters of Galaxies

The distribution of the gravitating mass in galaxy cluster is the key ingredient to use them as astrophysical laboratories and cosmological probes. In the presently favourite hierarchical scenario of cosmic structure formation, direct relations hold between observables in the electromagnetic spectrum and the

depth of the cluster potential produced from a matter component expected to be dynamically cold and electromagnetically dark (see e.g. reviews in Allen, Evrard & Mantz 2011; Kravtsov & Borgani 2012).

It was in the early thirties that the role of a *missing mass* to explain the gravitational effect observed in rich clusters of galaxies was highlighted from Zwicky (1937), opening the still-debated issue on how to relate their bounding mass to their observables. Since 1950s, galaxy clusters have been characterized from galaxies overdensities in the optical bands. Therefore, the *Richness* in number of galaxies, the total luminosity of cluster galaxies $L_{\rm opt}$, the velocity dispersion of member galaxies, and the shear and strong lensing features induced from the mass distribution of intervening galaxy clusters on background galaxies have been the tools to measure the mass and the distribution of galaxy clusters in systems at relatively low redshift ($z < 0.3$; see, e.g., the MaxBCG catalog from the Sloan Digital Sky Survey and the constraints it provided on the cosmological parameters in Rozo et al. 2010).

Another efficient technique to discover and characterize galaxy clusters is by mapping the distortion of the Cosmic Microwave Background spectrum due to the inverse Compton scattering induced from the high-energy electrons present in the hot intra-cluster medium (ICM). Clear detections of these features (named Sunyaev-Zeldovich -1972, SZ- effect; see review by Carlstrom et al. 2002) occurred in the late 90s. Many surveys over wide areas of the sky have started to produce results (e.g., the South Pole Telescope reported the first SZ-discovered clusters in Staniszewski et al. 2009; the Atacama Cosmology Telescope has reported their initial catalog of SZ-discovered clusters in Marriage et al. 2011; the *Planck* collaboration has presented the first cosmological constraints with a sample of 189 high signal-to-noise clusters in Planck Collaboration 2013). The integrated SZ signal, being proportional to the ICM pressure along the line-of-sight, can be used as proxy of the total cluster mass.

In the X-ray band, the gas luminosity, gas temperature and gas mass are the direct proxies of the cluster gravitational potential. X-ray observations occurred to be particularly successful because galaxy clusters appear as well resolved extended emission with a total luminosity that is proportional to the square of the gas density. As summarized in the following section, and widely discussed in the review by Ettori et al. (2013a), the new generation of X-ray observatories have enhanced other view on the use of galaxy clusters as

astrophysical laboratories and cosmological probes.

1.1 Galaxy clusters in the X-ray band

Galaxy clusters form through the hierarchical accretion of cosmic matter. The end products of this process are virialized structures with about 15% of their mass in the form of thermalized plasma detectable in X-ray and through the SZ effect. This gas is almost primordial in its chemical composition, and when it collapses into the dark matter (DM) halos typical of galaxy clusters ($> 10^{14} M_{\odot}$), it undergoes shocks and adiabatic compression, reaching densities of about 10^{-3} particles cm^{-3} and temperatures of the order of 10^8 K. Hence, under these physical conditions, the plasma is optically thin and in ionization equilibrium.

In recent years, measurements of the spatially-resolved X-ray properties of galaxy clusters have definitely improved thanks to the arcsec resolution and large collecting area of the present X-ray satellites, like *Chandra* and *XMM-Newton*. For instance, central luminous regions have shown *fronts*, i.e. sharp contact discontinuities between regions of gas with different densities. The classic *bow shocks* are driven by infalling subclusters. The *cold fronts* are found in mergers as well as around the central density peaks in relaxed clusters and are caused by motion of cool, dense gas clouds in the ambient higher-entropy gas. These clouds are either remnants of the infalling subclusters, or the displaced gas from the cluster's own cool cores (see, e.g., review in Markevitch & Vikhlinin 2007).

Present observations provide routinely reasonable estimates of the gas density, $n_{\rm gas}$, and temperature, $T_{\rm gas}$, up to about R_{500} ($\approx 0.7 R_{200}$[1]). Radial profiles of these quantities allow to evaluate both the interagted gas mass and the total gravitating mass through the assumption of a spherically symmetric ICM in hydrostatic equilibrium with the DM potential. On the other hand, more than two-thirds of the typical cluster volume, just where primordial gas is accreting and DM halo is forming, is still unknown for what concerns both its mass distribution and its thermodynamical properties (see e.g. review by Reiprich et al. 2013). Noticeable progress in characterizing these regions, where

[1] R_{Δ} is defined as the radius of the sphere that encloses a mean mass density of Δ times the critical density at the cluster's redshift; R_{200} defines approximately the virialized region in galaxy clusters

the X-ray surface brightness is comparable to the level of the fore/background, has occurred recently thanks to *Suzaku* exposures (e.g. Urban et al. 2014), and to the combined analyses of *ROSAT* PSPC observations and data of the SZ signal provided from *Planck* (e.g. Eckert et al. 2013).

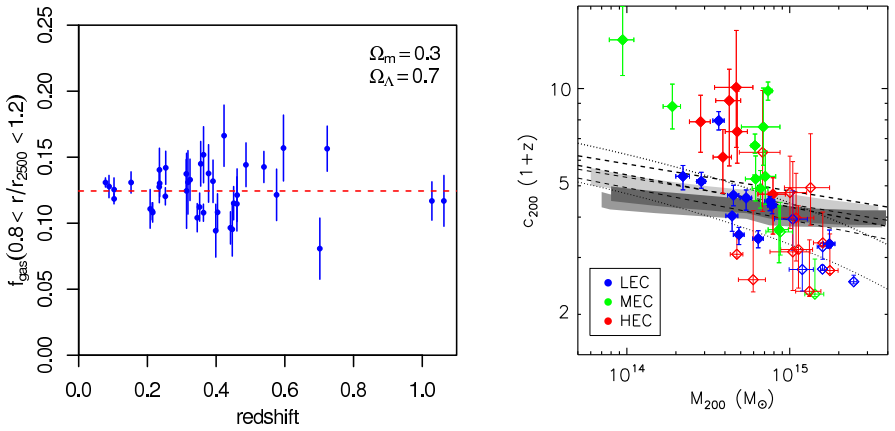

Figure 1: **(Left)** Distribution of the X-ray gas mass fraction measured in a shell around R_{2500} as a function of redshift in a ΛCDM model (from Mantz et al. 2014). **(Right)** Data in the plane (c_{200}, M_{200}) used to constrain the cosmological parameters (Ω_m, σ_8). The colour-code refers to the dynamical state of the clusters accordingly to the level of entropy measured in their cores (*Low/Medium/High Entropy Core*, from more relaxed to more disturbed objects). See Ettori et al. (2010) for details.

2 Mass profiles as cosmological proxies

In this section, we present how the distribution of the total and baryonic mass in galaxy clusters can be used to validate the scenario of structure formation in a CDM Universe. We discuss here the two cases that provide the most stringent limits nowadays (along with the cluster mass function discussed in e.g. Allen , Evrard & Mantz 2011) (i) the gas mass fraction, and (ii) the concentration-mass relation.

2.1 The gas mass fraction as a cosmological probe

The gas mass fraction, $f_{\rm gas} = M_{\rm gas}/M_{\rm tot}$, as inferred from X-ray observations of clusters of galaxies uses and combines two independent methods to constrain the cosmological parameters (see, e.g., Mantz et al. 2014 and references therein): (i) the relative amount of baryons with respect to the total mass observed in galaxy clusters is compared to the cosmic baryon fraction to provide a direct constraint on $\Omega_{\rm m}$, (ii) the parameters that describe the geometry of the Universe (specifically Ω_Λ or w) are limited by assuming that the gas fraction is constant in time.

No selection effect is expected to occur in the application of the gas mass fraction method once the clusters are selected to ensure (i) the use of the hydrostatic equilibrium equation to recover the total mass, and (ii) a negligible contribution from non-gravitational energy in the region of interest to allow the use of cross–calibration with numerical simulations, such as the estimate of the depletion parameter (see below). The selection of X-ray morphologically round, relaxed, hot, massive systems dominated energetically by gravitational collapse satisfies both these conditions. Using *Chandra* observations of 40 such objects, Mantz et al. (2014; see Fig. 1) obtain values of $\Omega_{\rm m} = 0.27 \pm 0.04$, $\Omega_\Lambda = 0.65 \pm 0.2$, and, on the equation of state of the dark energy w, -0.98 ± 0.26.

2.2 The concentration-mass relation

Within a cold DM model of the Universe, the $N-$body simulations of structure formation indicate that halos aggregate with a typical mass density profile characterized by only 2 parameters, the concentration c and the scale radius $r_{\rm s}$ (e.g. Navarro, Frenk & White 1997 –NFW). The product of these two quantities fixes the radius within which the mean cluster density is 200 times the critical value at the cluster's redshift[2]. With this prescription, the structural properties of DM halos from galaxies to galaxy clusters are dependent on the halo mass, with systems at higher masses less concentrated. Moreover, the concentration depends upon the properties of the cosmological background at the assembly redshift, which happens to be later in cosmologies with lower matter density, $\Omega_{\rm m}$, and lower normalization of the linear power spectrum on

[2] $R_{200} = c_{200} \times r_{\rm s}$ and the cluster's volume $V = 4/3\pi R_{200}^3$ is equal to $M_{200}/(200\rho_{c,z})$, where M_{200} is the cluster gravitating mass within R_{200}

scale of $8h^{-1}$ Mpc, σ_8. Under these conditions of formation, less concentrated DM halos at given mass are expected. The concentration – mass relation, and its evolution in redshift, is therefore a strong prediction obtained from CDM simulations of structure formation and is quite sensitive to the assumed cosmological parameters (e.g. NFW; Bullock et al. 2001). To constrain the cosmological parameters of interest, σ_8 and $\Omega_{\rm m}$, Ettori et al. (2010; see Fig. 1) calculate the set of values for these parameters that minimizes the sum of the error-weighted differences between the predicted and observed concentration parameters. Using the 11 most relaxed systems in our sample, we measure $sigma_8\,\Omega_{\rm m}^{0.56\pm0.04} = 0.39 \pm 0.02$ (error bars at 2σ level). By using the gas mass fraction method described in the previous section, this degeneracy can be further broken to measure $\sigma_8 = 0.83 \pm 0.1$ and $\Omega_{\rm m} = 0.26 \pm 0.02$.

However, because a calibration, for a given mass, is needed to map the observed distribution of the concentrations with the expected one as a function of σ_8, $\Omega_{\rm m}$ and redshift, we also note how the cosmological constraints depend upon the models adopted to relate the properties of a DM halo to the background cosmology. In particular, to make this technique more reliable and robust, $N-$body simulations produced with different input cosmological parameters over cosmological volumes large enough to sample massive ($> 10^{14} M_\odot$) DM halos are required.

3 The generalized scaling relations in X-ray galaxy clusters

In the context of the self-similar model for X-ray galaxy clusters, simple relations hold between observables and hydrostatic mass $M_{\rm tot}$ (see e.g. review in Giodini et al. 2013). In Ettori (2013), I show that these relations can be extended to a general form in which multiple observables, like gas luminosity, mass and temperature, can be combined: $M_{\rm tot} \propto L^\alpha M_g^\beta T^\gamma$, where the values of the slopes satisfy the relation $4\alpha + 3\beta + 2\gamma = 3$. Some projections of this plane (see Fig. 2) are particularly useful in looking for a minimum scatter between X-ray observables and hydrostatic mass: $M_{\rm tot} \propto A^a B^b$, where A is either M_g or L, $B = T$ and $b = 1.5\ -(1\ +0.5d)\ a$, with $d = 1(2)$ for M_g (L). Using published data set, I show that some projections of these generalized scaling relations (gSR) are the most efficient relations, holding among observed physical quantities in the X-ray band, to recover the cluster gravitating mass. This conclusion is based on the evidence that they provide the lowest χ^2, the lowest

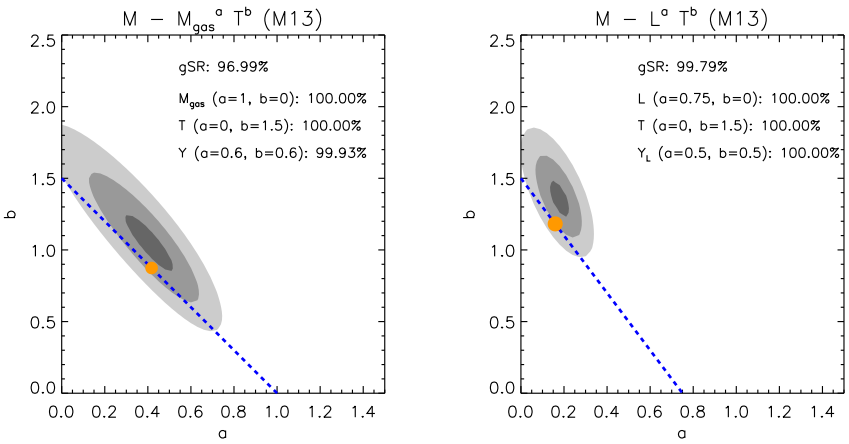

Figure 2: 1–3–5 σ likelihood contours for two interesting parameters ($\Delta\chi^2 = 2.3, 11.8, 28.76$, respectively). By construction, the best-fitting results from the "gSR" (orange dot) are in correspondence of the intersection between the predicted behaviour for the self-similar prediction (blue dashed line) and the contours. Labels in the plot indicate the level of confidence (in percentage) by which the quoted solutions deviate from the minimum χ^2 in the $\{a, b\}$ plane. M13 refers to the sample of galaxy clusters described in Mahdavi et al. (2013).

total scatter and the lowest intrinsic scatter among the studied scaling laws on both galaxy group and cluster mass scales. By the application of the gSR, the intrinsic scatter is reduced in all the cases down to a relative error on the reconstructed mass below 16 per cent.

4 Conclusions

An understanding of the physical processes involved in galaxy cluster assembly is an essential requirement for realistic models of cosmic structure formation. However, current X-ray data are unable to constrain the bulk motions of the ICM, cannot detect easily the hot gas much beyond R_{500} (or only 10% of the cluster volume) even in bright local systems, and lack spatial resolution, throughput, and spectral resolution to map the distribution of the heavy elements within the cluster atmosphere beyond the bright central regions of the nearest objects. Overall, our vision of the thermodynamics and enrichment

of the ICM should draw a consistent picture of the history of circulation of baryons through cosmic time. A major advance in X-ray sensitivity and spectral resolution, in combination with high spatial resolution, is needed to be able to make breakthroughs in these aspects of cluster physics. A large collecting area X-ray telescope such as the one that will be available with the next ESA L2 mission Athena (e.g. Nandra et al. 2013, Ettori et al. 2013b) will allow such progress to be made. It will also provide valuable insights into to the understanding of complementary datasets from ongoing and future radio observations (e.g. SKA), high angular resolution SZ millimetric data (e.g. GBT, IRAM, SRT, CCAT), observations of the cold baryons in galaxies (e.g. from JWST, ALMA, and E-ELT), and of the dark matter via lensing data (LSST, Pan-STARRS, Euclid).

5 Acknowledgements

I would like to warmly thank Roberto Fusco Femiano and Giampaolo Mannocchi, the SOC and the LOC to have well organized such interesting workshop on the crossroad between astro- and particle- physics. I also acknowledge all my collaborators and the co-authors of my publications for continuous, prolific discussion and interaction.

6 References

Allen S.W. et al., 2011, ARAA, 49, 409; Bullock J. S. et al., 2001, MNRAS, 321, 559; Carlstrom J.E. et al., 2002, ARAA, 40, 643; Eckert D. et al., 2013, A&A, 551, A22; Ettori S. et al., 2010, A&A, 524, 68; Ettori S. et al., 2013a, SSRv, 177, 119; Ettori S. et al., 2013b, arXiv1306.2322; Ettori S., 2013, MNRAS, 435, 1265; Giodini S. et al., 2013, SSRv, 177, 247; Kravtsov A.V., Borgani S., 2012, ARAA, 50, 353; Mahdavi A. et al., 2013, ApJ, 767, 116; Mantz A.B. et al., 2014, MNRAS, 440, 2077; Markevtich M., Vikhlinin A., 2007, Phys. Rev., 443, 1; Marriage T.A. et al., 2011, ApJ, 737, 61; Nandra K. et al., 2013, arXiv1306.2307; Navarro J.F. et al., 1997, ApJ, 490, 493; Planck 2013 results. XX, A&A in press; Rozo E. et al., 2010, ApJ, 708, 645; Reiprich T.H. et al., 2013, SSRv, 177, 195; Staniszewski Z. et al., 2009, ApJ, 701, 32; Sunyaev R. A., Zel'dovich Y. B., 1972, Comm.Astr.Sp.Phys., 4, 173; Urban O. et al., 2014, MNRAS, 437, 3939; Zwicky F., 1937, ApJ, 86, 217.

Frascati Physics Series Vol. 58 (2014)
Frontier Objects in Astrophysics and Particle Physics
May 18-24, 2014

BBN, NEUTRINOS AND NUCLEAR ASTROPHYSICS

Carlo Gustavino
INFN Sezione di Roma, I-00185 Roma, Italy

Abstract

The big bang nucleosynthesis (BBN) theory describes the formation of light isotopes in the first minutes of cosmic time, as a result of the competition between the universal expansion rate and the yields of relevant nuclear reactions. Since the expansion rate is proportional to the density of relativistic particles, the abundances of light isotopes allows to constrain the number of neutrinos species. In particular the primordial abundance of deuterium $(D/H)_{obs}$ is presently measured with high accuracy, providing a constraint on the number of neutrino families consistent only broadly with the three neutrino species foreseen by the standard model. The most important obstacle to improve the constraints on the existence of dark radiation is the uncertainty of the $^2H(p,\gamma)^3He$ cross section at BBN energies. This reaction will be studied at the underground Gran Sasso Laboratory (LNGS) with by the LUNA accelerator. The goal is to measure the cross section of the $^2H(p,\gamma)^3He$ reaction at BBN energies with high accuracy. The forthcoming LUNA measurement and its impact in cosmology, as well as in particle and nuclear physics is discussed.

Table 1: *List of the leading reactions and corresponding rate symbols controlling the deuterium abundance after BBN. The last column shows the error on the ratio D/H coming from experimental (or theoretical) uncertainties in the cross section of each reaction, for a fixed baryon density $\Omega_b h^2 = 0.02207$.*

Reaction	Rate Symbol	$\sigma_{D/H} \cdot 10^5$
$p(n,\gamma)^2H$	R_1	± 0.002
$d(p,\gamma)^3He$	R_2	± 0.062
$d(d,n)^3He$	R_3	± 0.020
$d(d,p)^3H$	R_4	± 0.0013

1 Introduction

In the standard cosmology the expansion rate of the universe is governed by the Freidmann equation:

$$H^2 = \frac{8\pi}{3} G\rho \tag{1}$$

Were H is the Hubble parameter, G is the Newton's gravitational constant and ρ is the energy density which, in the early Universe, is dominated by the "radiation", i.e. the contributions from massless or extremely relativistic particles. The only known relativistic particle at the Big Bang Nucleosynthesis (BBN) epoch are the photons and the three neutrino families. Indeed, the primordial abundance of isotopes depends on the radiation density, on the baryon density Ω_b and on the nuclear cross sections of BBN chain. The measured abundance of deuterium D/H_{obs} in Damped Lyman-Alpha (DLA) systems at high redshifts has been recently measured with high precision [1)], providing $(D/H)_{obs} = (2.53 \pm 0.04) \times 10^{-5}$. The theoretical value obtained assuming standard ΛCDM model, the baryon density measured by the PLANCK experiment [2)]and using the public BBN code PArthENoPE [3)] is $(D/H)_{BBN} = (2.65 \pm 0.07) \times 10^{-5}$. Interestingly, the theoretical value of D/H is less accurate with respect to the measured one, mainly because of the uncertainties of the BBN nuclear processes responsible for the initial deuterium production and its subsequent processing into $A = 3$ nuclei. The four leading reactions responsible of the deuterium abundance are listed in Table 1 [4)]. This table shows that the main source of uncertainty is presently due to the radiative capture process $D(p,\gamma)^3He$ converting deuterium into ^3He.

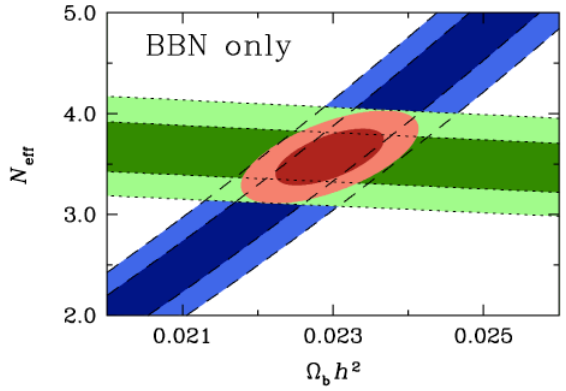

Figure 1: *The 1 σ and 2 σ confidence contours (dark and light shades respectively) for N_{eff} and $\Omega_{b,0}$ derived from the primordial deuterium abundance (blue), the primordial He mass fraction (green), and the combined confidence contours (red)* [1].

2 Baryon density.

The most recent CMB-derived baryon density is provided by the PLANCK collaboration [2]. Assuming standard ΛCDM model:

$$\Omega_{b,0}(CMB) = (2.205 \pm 0.028)/h^2 \tag{2}$$

In this equation, $\Omega_{b,0}$ is the present day baryon density of the universe and h is the Hubble constant in units of 100 $km\ s^{-1}\mathrm{Mpc}^{-1}$.
The baryon density can be independently inferred by means of standard BBN theory, by comparing the observed deuterium abundance with the abundance obtained with BBN prediction [1]:

$$\Omega_{b,0}(BBN) = (2.202 \pm 0.019 \pm 0.041)/h^2 \tag{3}$$

The error terms in eq. 3 reflect the uncertainties in observed deuterium abundance and BBN calculation [1]. The latter is due to the 3% uncertainty of computed $(D/H)_{BBN}$, that is mainly due to the experimental error of $^2H(p,\gamma)^3He$ cross section at BBN energies [5, 1]. Therefore, to improve the $\Omega_{b,0}(BBN)$ accuracy, is necessary a renewed measurement of the $^2H(p,\gamma)^3He$ cross section

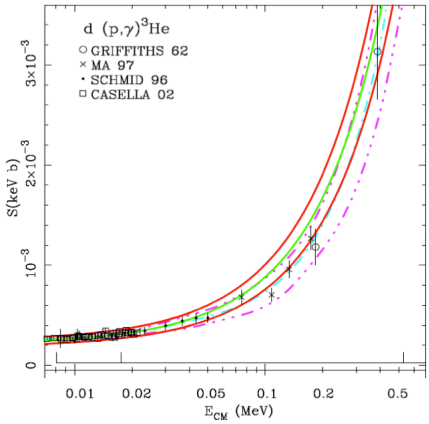

Figure 2: *S-factor data for the reaction* $^2H(p,\gamma)^3He$. *The best-fit curve (dash-dot curves) and theoretical calculation (solid) are shown. All errors are shown as* 2 σs.

in the BBN energy range.

3 Neutrinos

In cosmology, the definition of "neutrino" is any relativistic particle contributing to the radiation density with respect to photons. For standard cosmology the number of effective neutrino families is $N_{eff} = 3.046$ [1)]. The CMB-only bound obtained by the PLANCK experiment is [2)]:

$$N_{eff}(CMB) = 3.36 \pm 0.34 \tag{4}$$

It is possible to bound the density of relativistic species by comparing the predicted and the observed abundances of ^4He and D/H [1, 5)]. the BBN-only bound reported in [1)] is:

$$N_{eff}(BBN) = 3.57 \pm 0.18 \tag{5}$$

It is worth to point out that CMB and BBN constraints are in good agreement and provide a suggestive, but still inconclusive, hint of the presence of dark radiation. The BBN bound on N_{eff} is graphically shown in Figure 1. The

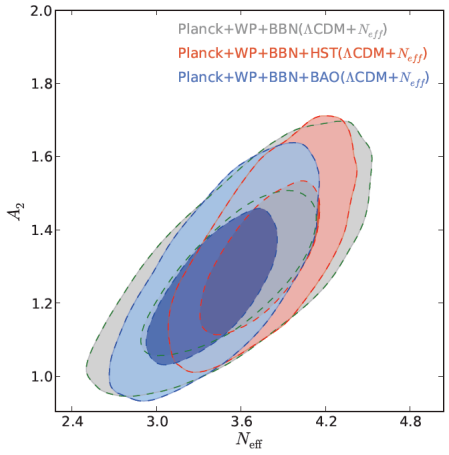

Figure 3: *2-D contour plots in the N_{eff} vs A_2 plane, showing preferred parameter regions at the 68% and 95% confidence levels in the case of the extended ΛCDM model with extra relativistic degrees of freedom.* [4].

confidence contours related to the ^4He abundance (green bands) are due to systematics errors of observations. Instead, the uncertainty due to the deuterium abundance (blue bands) is mainly due to the paucity of $^2H(p,\gamma)^3He$ data at BBN energies, making the study of the $D(p,\gamma)^3He$ reaction at low energy also important for the neutrino physics.

4 The deuterium abundance and $D(p,\gamma)^3He$ reaction.

In nuclear astrophysics the nuclear cross section $\sigma(E)$ is often factorized as follows:

$$\sigma(E) = \frac{S(E)e^{-2\pi\eta^*}}{E} \tag{6}$$

In this formula, the exponential term takes into account the Coulomb barrier, while the astrophysical factor $S(E)$ contains all the nuclear effects. The Sommerfeld parameter η^* is given by $2\pi\eta^* = 31.29Z_1Z_2(\mu/E)^{1/2}$. Z_1 and Z_2 are the nuclear charges of the interacting nuclei. μ is their reduced mass (in units of a.m.u.), and E is the center of mass energy (in units of keV).
Figure 2 shows the data of the $D(p,\gamma)^3He$ reaction in literature. The precise

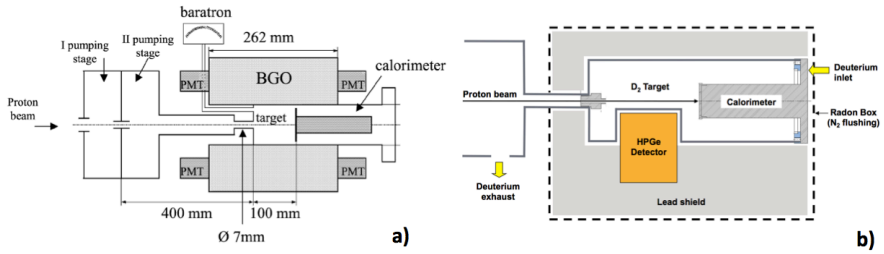

Figure 4: *a): Scheme of gas target setup and BGO detector. b): Scheme of gas target setup and HPGe detector.*

low-energy data come from the LUNA measurement performed with the 50 kV accelerator [6]. Only a single dataset of S_{12} is currently available in the relevant BBN energy range, in which the authors state systematic uncertainty of 9% [7]. Figure 2 also shows the behavior of S_{12} obtained by the theoretical "ab initio" calculation [5, 8]. It is worthwhile to note that the theoretical result is systematically larger than the best fit value derived from the experimental data in the BBN energy range. The existing difference between theory and data let some author to adopt the theoretical curve [5] or the S_{12} value obtained from measurements [2]. Figure 3 shows the 2-D contour plots in the N_{eff} vs A_2 plane, where A_2 is the $D(p,\gamma)^3He$ reaction rate normalized to the value obtained with data fit [4]. Interestingly, the figure 3 favor a $S_{12}(E)$ trend close to the one obtained with *ab initio* calculation, and a N_{eff} value higher than 3 [4]. Therefore, the measurement of $S_{12}(E)$ at BBN energies is of primary importance in theoretical nuclear physics and to understand the origin of the $\sim$ 20% difference between data and *ab initio* calculation for the ^3He isotope [5, 8].

5 The $D(p,\gamma)^3$He reaction at LUNA

The feasibility of studying the ^2H(p,γ)^{3}He reaction ($Q = 5.5\ MeV$) at low energy and with good accuracy has been demonstrated with the previous LUNA 50 kV accelerator (see figure 2), in the $2.5 < E_{cm}(keV) < 22$ energy range [6]. The present LUNA 400 kV facility [9] make possible to extend the measurements up to $E_{cm} = 266\ keV$, i.e. well inside the BBN energy range. Figure

4 a) shows the scheme of the setup used in [6], where a barrel BGO detector is implemented. The high efficiency ($\sim 70\%$) of the BGO detector reduces the dependence of the detector response on the angular distribution of the emitted γ rays and thus is a prerequisite to achieve a low systematic uncertainty. The detection efficiency can be determined by precise Monte Carlo simulations, as well as performing dedicated measurements and calibrations, e.g. by measuring the absolute efficiency exploiting the 340 keV resonance in the $^{19}F(p,\alpha\gamma)^{16}O$ reaction ($E_\gamma = 6.13\ MeV$). With the proposed setup the expected counting rate (full detection γ-peak) is of the order of $10^4 - 10^5$ $events/hour$ in the $40 < E_{cm}(keV) < 266$ energy range, making the measurements with BGO detector relatively fast for what concern statistics and allowing to precisely determine the beam heating effect by varying target pressure and beam intensity, in order to unfold the target density in asymptotical conditions. Finally, the beam intensity error can be minimized by a proper calibration of the calorimeter (1.5% uncertainty in ref. [11]). Although the large angular coverage of BGO detector makes the counting yield nearly independent of the angular distribution of emitted photons, an exhaustive study of the $^2H(p,\gamma)^3He$ reaction includes the study of angular distribution of emitted γ-rays, in order to precisely evaluate the response of BGO detector. This study can be accomplished by using the HPGe detector facing the gas target in a close geometry, as it is shown in figure 4b). The angular distribution can be inferred by exploiting the high energy resolution of the detector and the doppler effect affecting the energy of γ's produced along the beam line by the $^2H(p,\gamma)^3He$ reaction. This study is also important for theoretical nuclear physics, because in *ab initio* calculation the interaction details are considered. Therefore, it predict the angular distribution of photons produced in the $^2H(p,\gamma)^3He$ reaction.

6 Conclusions

The improvements of direct observations of deuterium abundance [1] and the accuracy of CMB data [2] make the lack of ^{2}H(p,γ)^{3}He reaction data at BBN energies the main obstacle to improve the constraints on $\Omega_{b,0}(BBN)$, N_{eff} and lepton degeneracy ξ [1, 5]. The study of the $^2H(p,\gamma)^3He$ reaction in the BBN energy range will be performed with the LUNA facility at the underground Gran Sasso laboratory, where the very low environmental background allows

accurate measurements at energies below the coulomb barrier [12]. With the present 400 kV LUNA accelerator it is possible to measure the $^2H(p,\gamma)^3He$ cross section in the $40 < E_{cm}(keV) < 266$ energy range with an accuracy better than 3%, i.e. considerably better than the 9% systematic uncertainty estimated in [7]. This goal can be achieved by using the BGO detector already used in [6]. The accurate measurement of the $^2H(p,\gamma)^3He$ absolute cross section will be accomplished with the study of the angular distribution of emitted γ-rays by means of a large Ge(Li) detector, in order to compare the data with *ab initio* predictions.

References

1. R. Cooke *et al*,, arXiv:1308.3240 [astro-ph.CO].
2. PLANCK collaboration: arXiv:1303.5076v1 [astro-ph.CO] 20 Mar 2013.
3. O. Pisanti *et al*, Comput. Phys. Commun. 178, 956 (2008).
4. E. Di Valentino *et al*, arXiv:1404.7848v1 [astro-ph.CO] 30 Apr 2014.
5. K.M. Nollett and G.P. Holder: arXiv:1112.2683v1 [astro-ph.CO] 12 Dec 2011.
6. C. Casella *et al*, Nuclear Physics A **706** 203216. (2002).
7. L. Ma *et al*, Phys. Rev. C **55**, 588 (1997).
8. L. E. Marcucci *et al*, Phys. Rev. C **72**, 014001 (2005).
9. A. Formicola *et al*, Nucl. Instr. and Meth. A **507** 609 (2003).
10. M. Anders *et al*, Eur. Phys. J. A **49** 28 (2013).
11. H. Costantini *et al*, Nuclear Physics A **814** 144158 (2008).
12. A. Caciolli *et al*, Eur. Phys. J. A 39, 179 (2009).

Frascati Physics Series Vol. 58 (2014)
Frontier Objects in Astrophysics and Particle Physics
May 18-24, 2014

OPEN PROBLEMS IN GRAVITATIONAL PHYSICS

S. Capozziello
Dipartimento di Fisica, Universitá di Napoli "Federico II", and INFN Sez. di Napoli, Via Cinthia, I-80126 - Napoli, Italy,
Gran Sasso Science Institute (INFN), Viale F. Crispi, 7, I-67100, L' Aquila, Italy.

G. Lambiase
Dipartimento di Fisica "E.R. Caianiello", Universitá di Salerno, and INFN Sez. di Napoli I-84084 Fisciano (Sa), Italy.

Abstract

We discuss some fundamental issues underlying gravitational physics and point out some of the main shortcomings of Einstein's General Relativity. In particular, after taking into account the role of the two main objects of relativistic theories of gravity, i.e. the metric and the connection fields, we consider the possibility that they are not trivially related so that the geodesic structure and the causal structure of the spacetime could be disentangled, as supposed in the Palatini formulation of gravity. In this perspective, the Equivalence Principle, in its weak and strong formulations, can play a fundamental role in discriminating among competing theories. The possibility of its violation at quantum level could open new perspectives in gravitational physics and in unification with other interactions. We shortly debate the possibility of equivalence principle measurements by ground-based and space experiments.

1 Introduction

As it is well known, General Relativity (GR) is based on the fundamental assumption that space and time are entangled into a single spacetime structure assigned on a Riemannian manifold. Being a dynamical structure, it has to reproduce, in the absence of gravitational field, the Minkowski spacetime.

Like any relativistic theory of gravity, GR has to match some minimal requirements to be considered a self-consistent physical theory. First of all, it has to reproduce the Newtonian dynamics in the weak-energy limit, hence it must be able to explain the astronomical dynamics related to the orbits of planets and the self-gravitating structures. Moreover, it passes some observational tests in the Solar System that constitute its experimental foundation [1)].

However, GR should be able to explain the Galactic dynamics, taking into account the observed baryonic constituents (*e.g.* luminous components as stars, sub-luminous components as planets, dust and gas), radiation and Newtonian potential which is, by assumption, extrapolated to Galactic scales. Besides, it should address the problem of large scale structure as the clustering of galaxies. On cosmological scales, it should address the dynamics of the universe, which means to reproduce the cosmological parameters as the expansion rate, the density parameter, and so on, in a sef-consistent way. Observations and experiments, essentially, probe the standard baryonic matter, the radiation and an attractive overall interaction, acting at all scales and depending on distance: this interaction is gravity.

In particular, Einstein's GR is based on four main assumptions. They are

> The "*Relativity Principle*" - there is no preferred inertial frames, i.e. all frames are good frames for Physics.
>
> The "*Equivalence Principle*" - inertial effects are locally indistinguishable from gravitational effects (which means the equivalence between the inertial and the gravitational masses). In other words, any gravitational field can be locally cancelled.
>
> The "*General Covariance Principle*" - field equations must be " covariant" in form, i.e. they must be invariant in form under the action of spacetime diffeomorphisms.

The "*Causality Principle*" - each point of space-time has to admit a universally valid notion of past, present and future.

On these bases, Einstein postulated that, in a four-dimensional spacetime manifold, the gravitational field is described in terms of the metric tensor field $ds^2 = g_{\mu\nu}dx^\mu dx^\nu$, with the same signature of Minkowski metric. The metric coefficients have the physical meaning of gravitational potentials. Moreover, he postulated that spacetime is curved by the distribution of the energy-matter sources.

The above principles require that the spacetime structure has to be determined by either one or both of the two following fields: a Lorentzian metric g and a linear connection Γ, assumed by Einstein to be torsionless. The metric g fixes the causal structure of spacetime (the light cones) as well as its metric relations (clocks and rods); the connection Γ fixes the free-fall, *i.e.* the locally inertial observers. They have, of course, to satisfy a number of compatibility relations which amount to require that photons follow null geodesics of Γ, so that Γ and g can be independent, *a priori*, but constrained, *a posteriori*, by some physical restrictions. These, however, do not impose that Γ has necessarily to be the Levi-Civita connection of g [2)].

It should be mentioned, however, that there are many shortcomings of GR, both from a theoretical point of view (non-rinormalizability, the presence of singularities, and so on), and from an observational point of view. The latter indeed clearly shows that GR is no longer capable of addressing Galactic, extragalactic and cosmic dynamics, unless the source side of field equations contains some exotic form of matter-energy. These new elusive ingredients are usually addressed as *dark matter"* and *dark energy* and constitute up to the 95% of the total cosmological amount of matter-energy [3)].

On the other hand, instead of changing the source side of the Einstein field equations, one can ask for a "geometrical view" to fit the missing matter-energy of the observed Universe. In such a case, the dark side could be addressed by extending GR including more geometric invariants into the standard Hilbert - Einstein Action. Such effective Lagrangians can be easily justified at fundamental level by any quantization scheme on curved spacetimes [4)]. However, at present stage of the research, this is nothing else but a matter of taste, since no final probe discriminating between dark matter and extended gravity has been found up to now. Finally, the bulk of observations that should be considered

is so high that an effective Lagrangian or a single particle will be difficult to account for the whole phenomenology at all astrophysical and cosmic scales.

2 Metric or connections?

In the GR formulation, Einstein assumed that the metric g of the space-time is the fundamental object to describe gravity. The connection $\Gamma^{\alpha}_{\mu\nu} = \left\{ \begin{array}{c} \alpha \\ \mu\nu \end{array} \right\}_g$ is constituted by coefficients with no dynamics. Only g has dynamics. This means that the single object g determines, at the same time, the causal structure (light cones), the measurements (rods and clocks) and the free fall of test particles (geodesics). Spacetime is therefore a couple $\{\mathcal{M}, g\}$ constituted by a Riemannian manifold and a metric. Even if it was clear to Einstein that gravity induces freely falling observers and that the Equivalence Principle selects an object that cannot be a tensor (the connection Γ) - since it can be switched off and set to zero at least in a point - he was obliged to choose it (the Levi - Civita connection) as being determined by the metric structure itself.

In the Palatini formalism a (symmetric) connection Γ and a metric g are given and varied independently. Spacetime is a triple $\{\mathcal{M}, g, \Gamma\}$ where the metric determines rods and clocks (i.e., it sets the fundamental measurements of spacetime) while Γ determines the free fall. In the Palatini formalism, $\Gamma^{\alpha}_{\mu\nu} = \left\{ \begin{array}{c} \alpha \\ \mu\nu \end{array} \right\}_g$ are differential equations. The fact that Γ is the Levi-Civita connection of g is no longer an assumption but becomes an outcome of the field equations.

The connection is the gravitational field and, as such, it is the fundamental field in the Lagrangian. The metric g enters the Lagrangian with an "ancillary" role. It reflects the fundamental need to define lengths and distances, as well as areas and volumes. It defines rods and clocks that we use to make experiments. It defines also the causal structure of spacetime. However, it has no dynamical role. There is no whatsoever reason to assume g to be the potential for Γ, nor that it has to be a true field just because it appears in the action.

3 The role of Equivalence Principle

The Equivalence Principle (EP) is strictly related to the above considerations and could play a very relevant role in order to discriminate among theories.

In particular, it could specify the role of g and Γ selecting between the metric and Palatini formulation of gravity. In particular, precise measurements of EP could say us if Γ is only Levi - Civita or a more general connection disentangled, in principle, from g.

Let us discuss some topics related to the EP. Summarizing, the relevance of this principle comes from the following points:

- Competing theories of gravity can be discriminated according to the validity of EP;
- EP holds at classical level but it could be violated at quantum level;
- EP allows to investigate independently geodesic and causal structure of spacetime.

From a theoretical point of view, EP lies at the physical foundation of metric theories of gravity. The first formulation of EP comes out from the theory of gravitation formulates by Galileo and Newton, i.e. the Weak Equivalence Principle (WEP) which asserts the inertial mass m_i and the gravitational mass m_g of any physical object are equivalent. The WEP statement implies that it is impossible to distinguish, locally, between the effects of a gravitational field from those experienced in uniformly accelerated frames using the simple observation of the free falling particles behavior.

A generalization of WEP claims that Special Relativity is locally valid. Einstein realized, after the formulation of Special Relativity, that the mass can be reduced to a manifestation of energy and momentum. As a consequence, it is impossible to distinguish between an uniform acceleration and an external gravitational field, not only for free-falling particles, but whatever is the experiment. According to this observation, Einstein EP states:

- The WEP is valid.
- The outcome of any local non-gravitational test experiment is independent of the velocity of free-falling apparatus.
- The outcome of any local non-gravitational test experiment is independent of where and when it is performed in the universe.

One defines as "local non-gravitational experiment" an experiment performed in a small-size of a free-falling laboratory. Immediately, it is possible to realize that the gravitational interaction depends on the curvature of spacetime, i.e. the postulates of any metric theory of gravity have to be satisfied. Hence the following statements hold:

- Spacetime is endowed with a metric $g_{\mu\nu}$.
- The world lines of test bodies are geodesics of the metric.
- In local freely falling frames, called local Lorentz frames, the non-gravitational laws of physics are those of Special Relativity.

One of the predictions of this principle is the gravitational red-shift, experimentally verified by Pound and Rebka in 1960 [1)]. Notice that gravitational interactions are excluded from WEP and Einstein EP.

In order to classify alternative theories of gravity, the gravitational WEP and the Strong Equivalence Principle (SEP) has to be introduced. On the other hands, the SEP extends the Einstein EP by including all the laws of physics in its terms. That is:

- WEP is valid for self-gravitating bodies as well as for test bodies (gravitational WEP).
- The outcome of any local test experiment is independent of the velocity of the free-falling apparatus.
- The outcome of any local test experiment is independent of where and when in the universe it is performed.

Alternatively, the Einstein EP is recovered from SEP as soon as the gravitational forces are neglected. Many authors claim that the only theory coherent with SEP is GR.

A very important issue is the consistency of EP with respect to the Quantum Mechanics. GR is not the only theory of gravitation and, several alternative theories of gravity have been investigated from the 60's [4)]. Considering the spacetime to be special relativistic at a background level, gravitation can be treated as a Lorentz-invariant field on the background. Assuming the possibility of GR extensions, two different classes of experiments can be conceived:

- Tests for the foundations of gravitational theories considering the various formulations of EP.
- Tests of metric theories where spacetime is a priori endowed with a metric tensor and where the Einstein EP is assumed always valid.

The subtle difference between the two classes of experiments lies on the fact that EP can be postulated a priori or, in a certain sense, "recovered" from the self-consistency of the theory. What is today clear is that, for several fundamental reasons, extra fields are necessary to describe gravity with respect to the other interactions. Such fields can be scalar fields or higher-order corrections of curvature invariants [4]. For these reasons, two sets of field equations can be considered: The first set couples the gravitational field to the non-gravitational contents of the Universe, i.e. the matter distribution, the electromagnetic fields, etc. The second set of equations gives the evolution of non-gravitational fields. Within the framework of metric theories, these laws depend only on the metric and this is a consequence of the Einstein EP. In the case where Einstein field equations are modified and matter field are minimally coupled with gravity, we are dealing with the so-called *Jordan frame*. In the case where Einstein field equations are preserved and matter field are non-minimally coupled, we are dealing with the so-called *Einstein frame*. Both frames are conformally related but the very final issue is to understand if passing from one frame to the other (and vice versa) is physically significant. Clearly, EP plays a fundamental role in this discussion. In particular, the question is if it is always valid or can be violated at quantum level.

4 Conclusions

Two of the main challenges of gravitational physics is to test EP in order to discriminate among competing theories of gravity and establish its validity at quantum level. Different ground-based and space experiments are devoted to this target that is strictly related to the connection of gravity with other interactions. In some sense, considering gravity under the same standard of the other interactions is become a compelling issue after the discovery of Higgs boson at CERN. For example, very recently a new mission, denoted STE-QUEST (Space-Time Explorer and QUantum Equivalence Principle Space Test) has

been proposed. This mission is designed to answer a range of questions in fundamental physics by performing precision measurements with high accuracy atomic sensors. In particular, STE-QUEST would like to test the Einstein EP, to explore the boundaries with the quantum world, and to search for new fundamental constituents [5, 6]. This will provide a great opportunity for testing fundamental theories of gravity, and, in particular, those theories that extend GR.

Acknowledgements

S.C. acknowledges the support of INFN (*iniziativa specifica* QGSKY). G. L. thanks the ASI (Agenzia Spaziale Italiana) for partial support (contract ASI I/034/12/0).

References

1. C.M. Will, Theory and Experiment in Gravitational Physics, 2nd ed. Cambridge University Press, Cambridge, UK (1993).
2. M. Ferraris, M. Francaviglia, C. Reina, Gen. Rel. Grav. **14** (1982) 243.
3. S. Capozziello and G. Lambiase, New Adv. in Physics , **7** (2013) 13.
4. S. Capozziello and M. De Laurentis, Phys.Rept. **509** (2011) 167.
5. B. Altschul et al., to appear in Advances in Space Research (2014), arXiv:1404.4307 [gr-qc].
6. http://sci.esa.int/ste-quest/

Frascati Physics Series Vol. 58 (2014)
Frontier Objects in Astrophysics and Particle Physics
May 18-24, 2014

OBSERVATIONAL PROSPECTS IN THE ELECTROMAGNETIC DOMAIN OF GRAVITATIONAL WAVE SOURCES

Marica Branchesi on behalf of
the LIGO Scientific Collaboration and the Virgo Collaboration
INFN, Sezione di Firenze, I-50019 Sesto Fiorentino;
Università degli Studi di Urbino Carlo Bo, I-61029 Urbino, Italy

Abstract

A new exciting frontier of observational astronomy will soon start to be explored: the current upgrade of gravitational wave ground-based detectors, LIGO and Virgo, should make possible to observe gravitational wave signals for the first time. Expected sources of gravitational waves include the most energetic astrophysical events such as the merger of neutron stars and/or black holes and the core collapse of massive stars. These events are believed to produce electromagnetic transients, like gamma-ray bursts and supernovae. The simultaneous use of electromagnetic facilities and gravitational-wave detectors will give the unique opportunity to catch the electromagnetic signatures of gravitational wave sources and to observe the same source with different messengers (GW and photons). The paper outlines the challenges, opportunities and strategies to develop and carry on multi-messenger searches.

1 Introduction

In the next decade the new generation of ground-based gravitational wave detectors, the advanced LIGO [1)] and advanced Virgo interferometers [2), 3)], will come on-line and will observe the sky as a network with the aim to directly detect for the first time gravitational wave (GW) signals. Detectable astrophysical sources can be divided into two classes on the basis of their emitted signals: transient and continuous sources. The former emit signals with a duration in the detection band significantly shorter than the observation time and which cannot be re-observed, the latter emit quasi-periodic waves whose frequency changes slowly. Transient GW signals are expected to be emitted from the coalescence of binary systems of compact objects (COs), neutron stars (NS) and/or stellar mass BHs [4), 5)] and core-collapse of massive stars [6)]. Continuous GW signals are expected from spinning NSs if they are not perfectly symmetric around their rotation axis.

The initial LIGO and Virgo observations have not detected gravitational-wave signals, but they have estimated upper limits on the source rate and on GW emission amplitude. The search for GWs from compact binary coalescence with total mass between 2 and 25 solar masses, for example, have given cumulative rate upper limits of the binary coalescence of binary neutron star, neutron star- black hole and binary black hole systems of 1.3×10^{-4}, 3.1×10^{-5} and $6.4 \times 10^{-6}\mathrm{Mpc}^{-3}\mathrm{yr}^{-1}$, respectively [7)]. These rates are two to three orders of magnitude above the astrophysically predicted ones. The detection probability will dramatically improve with the advanced detectors which will provide a factor of ten increase in sensitivity over the initial detectors, corresponding to a factor of thousand increase in the number of detectable sources. Tens of binary coalescence per year are expected to be observable [8)].

GW searches for 195 known targeted pulsars [9)] with initial LIGO and Virgo made it possible to place upper limits on the rotational energy loss due to the emission of GWs, and thus on the NS ellipticity . For the Crab and Vela pulsars, the results constrain the fraction of rotational energy loss to less than about 1% and 10%, respectively, of their spin-down luminosities.

The advanced GW detectors are expected to come on-line in 2015 [10)]. Their sensitivity should make it possible to observe GW signals by opening a new window in the (astro)physical study of gravitational collapse, explosion mechanisms, and ultra-dense matter stellar structure. The simultaneous availability of sensitive GW detectors and ground-based and space electromagnetic

(EM) observatories will allow scientists to use powerful multi-messengers, GWs and photons, to probe the most energetic events in the Universe.

2 Electromagnetic Emission from Gravitational Wave Sources

The discovery of the EM counterpart of a GW signal will be a key ingredient to characterize the astrophysical source and maximize the science return of GW observations. It would increase the confidence in the astrophysical origin of the GW signal. It would give a precise localization and potentially lead to the identification of the host galaxy. GW and EM radiations will provide complementary insight into the progenitor (mass, spin, distance, etc.) and the environment physics (temperature, density, redshift), giving a complete picture to understand the engines that power the double-messenger emission, e.g [12, 11]. The GW/EM observations compared with theoretical models will shed light on a plethora of open questions including the birth and evolution of CO and the Equation of State of matter at extreme densities in the stellar crust and interiors of NS.

The merger of NS-NS or NS-BH, and the core collapse of massive stars are expected to produce the gamma ray bursts (GRBs) and supernovae (SN). GRBs release a huge amount of energy (up to 10^{53} erg isotropic-equivalent energy [13]) within a few seconds that results in a hot, highly relativistic fireball, which undergoes internal dissipation and leads to gamma-ray prompt beamed emission. The fireball evolves later into a blast wave as it decelerates against the external medium, producing an afterglow emission [14] visible in X-rays, optical, radio, and in some cases gamma rays. The afterglow emission can last minutes, hours, months after the prompt emission and it can be observed over a wider viewing angle. According to the traditional classification schemes GRBs are divided into long GRBs and short GRBs on the basis of the prompt emission duration. While for the long GRBs, SN emission in the same location of the GRB strongly support the core-collpase of massive star as progenitor [15], for the short GRBs there are some observational evidences that indicate the NS-NS and NS-BH merger as possible progenitor. Their association with older stellar populations and the larger distance to the host galaxy centers compared to long-GRBs are in good agreement with predictions for the binary NS system distribution, see [16].

The merger of COs is also expected to emit [17], an isotropic optical/infrared thermal short-lived emission, called "kilonova", powered by the

radioactive decay of heavy elements synthesized through rapid neutron capture in the sub-relativistic merger ejecta [18, 19, 20]. The Hubble Space Telescope follow-up of the short GRB130603B showed the first observational tentative evidence of kilonova emission [21] by observing, 9 days after the prompt emission, an excess in the near-infrared consistent with kilonova predictions.

The NS-NS (NS-BH) mergers are expected to be detectable by the advanced detector network up to the range (location- and system orientation-averaged distance) of 200 Mpc (400 Mpc) with corresponding likely rate of $40\mathrm{yr}^{-1}$ ($10\ \mathrm{yr}^{-1}$) [8]. The core-collapse of massive stars, due to the small energy emitted in GWs, are expected to be detectable within our Galaxy [6], and out to larger distances of 1 Mpc to tens of Mpc in more optimistic scenarios e.g. [22, 23].

The most promising EM counterpart emission is expected to be associated with NS-NS and NS-BH merger. Figure 1 shows the optical emissions expected for a source at a distance of 200 Mpc. The solid lines represent the brightest and faintest on-axis (whose narrow relativistic jet points towards the observer) short GRB observed afterglows [24]. The afterglow brightness decays rapidly as a power law $t^{-}\alpha$ with α in the range 1 to 1.5 [13]. The small-dashed lines represent the synthetic off-axis afterglows of GRBs [25] with energy jet of 10^{50}erg, jet angle of 0.2, observer angle of 0.4, and a uniform interstellar medium density of $10^{-3}\mathrm{cm}^{-3}$ (bottom line) and $1\mathrm{cm}^{-}3$ (top line). The dashed lines represent three different models of kilonova emission. The Piran et al. (2013) kilonova is a bolometric light curve obtained for a BH-NS merger with NS mass of $1.4\,\mathrm{M}_{\odot}$, BH mass of $10\,\mathrm{M}_{\odot}$, and iron opacity. The curve represents an upper-limit to the true R-band luminosity since it assumes that all of the bolometric luminosity is emitted in the R-band. The Metzger et al. (2010) kilonova is a blackbody emission for an ejecta mass of 10^{-2} solar mass, and iron opacity. The Barnes & Kasen (2013) assumes an ejecta with low velocity (0.1 c) and mass (10^{-3} solar mass), and lanthanides opacities.

The above emissions can be detectable with sensitive instruments. Each of them require an adequate plan of observational epochs to detect and follow the light curves (flux vs time). A GW event, which is observable independently of the system orientation, is more likely to be associated with an isotropic kilonova and off-axis GRB signals than an on-axis GRB afterglow. The rate of on-axis GRBs with respect to off-axis depend on the jet beaming angle, whose value is poorly constrained so far [18, 26].

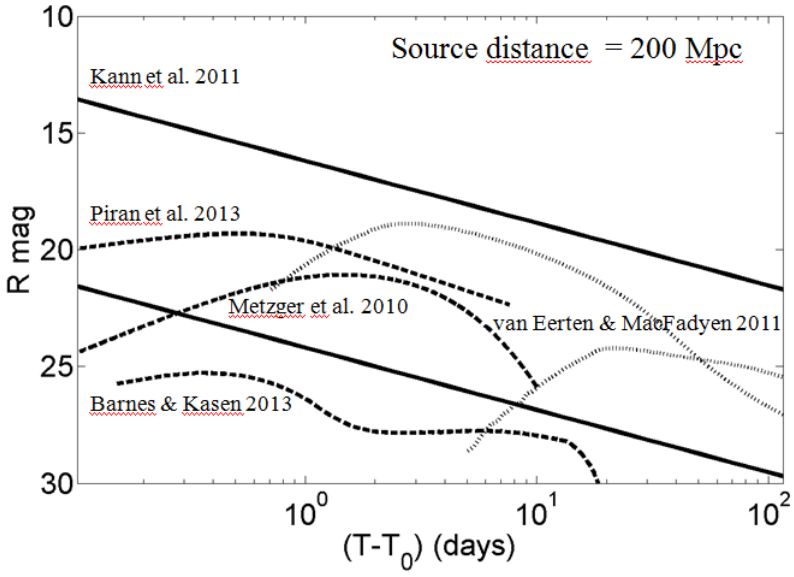

Figure 1: *Optical R-band emission expected from a NS-NS and NS-BH merger at a distance of 200 Mpc. The coalescence of NS-NS and NS-BH is the most promising source of GW transient signals*

3 Multi-messenger searches

On the basis of the emission timescales, two types of searches have been developed to detect the GW and EM signals associated with the same astrophysical source: the *"electromagnetically triggered search"* and the *"electromagnetic follow-up of GW events"*. The former search uses the EM detections to perform the GW analysis, the latter uses the GW candidate events to trigger EM observations.

The most promising analysis able to associate the GW event with the prompt emission of a GRB is the *"electromagnetically triggered search"*, which searches for GW signals in temporal and spatial coincidence with the observed GRBs [27, 28]. This search can be used to investigate the nature of a single gamma-ray event, e.g. [29], and also for statistical studies over the GRB population [27, 28].

Vice versa, a prompt identification of GW candidates will allow astronomers

to organize EM-follow up observations able to detect GRB afterglow, kilonova and supernova emissions. The Virgo and LIGO collaborations (LVC) have developed low-latency GW pipelines to detect compact binary coalescence [30] and unmodeled GW bursts. The pipelines generate alerts for significant GW-candidate events and send alerts in low latency. The first EM follow-up program (Dec 17 2009 to Jan 8 2010 and Sep 4 to Oct 20 2010) was performed during the last LIGO/Virgo science run [31]. The off-line analysis [32, 33] of the GW data alone showed no evidence of an astrophysical origin for the GW candidates identified by the low-latency pipelines. All the detected EM transients were consistent with the EM background [34, 35]. The 2009-2010 EM follow-up program was a great exercise to point out all the challenges to search for an EM counterpart.

The main challenge is the sky location uncertainty associated with a GW signals. The sky position is mainly evaluated by "triangulation" using the arrival time delay between detector sites and it is of order of several tens to hundreds of square degrees. These sky areas are larger than the field of view of the majority of the EM telescopes. Thus, adequate observational strategies, which use tiling of many telescopes and/or galaxy targeting, need to be developed. Furthermore, in large sky area there are many contaminating transients not associated with the GW event, which need to be removed to detect the EM counterpart.

4 Electromagnetic Follow-up of Gravitational Wave Candidate Events in The Advanced Detector Era

Since the advanced LIGO and Virgo network will continue to consist of three sites (until additional detectors come on-line in Japan and possibly in India, 2022+) the GW events will continue to be typically localized into regions of tens to hundreds of square degrees [10]. The detection of relatively faint rapid transients in large sky areas and the identification of a unique counterpart will require hierarchical searches: 1) sensitive wide-FOV (about 10 sq. degrees) telescopes able to cover the entire GW sky localization area, 2) "Fast and smart" software to rapidly detect and classify transient events, and select a sample of candidate counterparts, 3) larger telescopes and spectroscopic follow-up to characterize the candidates, see e.g. [34, 36].

In 2012 LVC agreed on the policy to share significant GW candidates. "Until the first four GW events have been published, triggers will be shared

promptly only with groups of astronomers who have signed a Memorandum of Understanding (MoU) with LVC". At the end of 2013 a call for proposals to sign MoUs was opened and it received high participation. Currently about sixty astronomer groups, agencies and astrophysical institutions are involved in the LVC EM follow-up program with about 150 instruments, which will cover the entire accessible EM spectrum and which are distributed worldwide. The call for MoU will be renewed every year. The field of multi-messenger astronomy is ready to enter a new and exciting era.

5 Acknowledgments

M. Branchesi acknowledges financial support from the Italian Ministry of Education, University and Research (MIUR) through grant FIRB 2012 RBFR12PM1F.

6 References

References

1. G.M. Harry for the LIGO Scientific Collaboration, Classical and Quantum Gravity **27**, 084006 (2010).
2. F. Acernese *et al.*, Virgo Technical Report VIR-0027A-09, https://tds.egogw.it/ql/?c=6589 (2009)
3. T. Accadia *et al.*, Virgo Document VIR-0128A-12, https://tds.egogw.it/ql/?c=8940 (2012)
4. A. Abramovici, Science **256**, 325 (1992)
5. C. Cutler & K.S. Thorne, General Relativity and Gravitation **72** (2002)
6. C.D. Ott *et al.*, ApJ **768**, 115 (2013)
7. J. Abadie *et al.*, Phyiscal Review D **85**, 082002 (2012)
8. J. Abadie *et al.*, Classical and Quantum Gravity **27**, 173001 (2010)
9. J. Aasi *et al.*, ApJ **785**, 119 (2014)
10. J. Aasi *et al.*, arXiv:1304.0670
11. B.S. Sathyaprakash & B.F. Schutz, Living Reviews in Relativity **12**, 2 (2009)

12. I. Bartos *et al.*, Classical and Quantum Gravity **30**, 123001 (2013)
13. E. Nakar, Physics Reports **442**, 166 (2007)
14. P. Meszaros, RPPhys **69**, 2259 (2006)
15. J. Hjorth & J.S. Bloom, Cambridge Astrophysics Series **51**, 169 (2012)
16. E. Berger, NewAR **55**, 1 (2011)
17. L.-X. Li, B. Paczyński, ApJ **507**, L59 (1998)
18. B.D. Metzger *et al.*, MNRAS **406**, 2650 (2010)
19. T. Piran, E. Nakar & S. Rosswog, MNRAS **430**, 2121 (2013)
20. J. Barnes, & D. Kasen, ApJ **775**, 18 (2013)
21. N.R. Tanvir *et al.*, Nature **500**, 547, 2013
22. C.L. Fryer & M.S. Warren, ApJ **574**, 65 (2002)
23. A.L. Piro & E. Pfahl, ApJ **658**, 1173 (2007)
24. D.A. Kann *et al.*, ApJ **734**, 96 (2011)
25. van Eerten & MacFadyen, ApJ **733**, L37 (2011)
26. Coward *et al.*, MNRAS **425**, 2668 (2012)
27. J. Abadie *et al.*, ApJ **760**, 12 (2012)
28. J. Aasi *et al.*, Physical Review Letters **113**, 011102 (2014)
29. J. Abadie *et al.*, ApJ **755**, 2 (2012)
30. J. Abadie *et al.*, A&A **541**, A155 (2012)
31. J. Abadie *et al.*, A&A **539**, A124 (2012)
32. J. Abadie *et al.*, PhysRevD **85**, 122007 (2012)
33. J. Abadie *et al.*, PhyRevD **85**, 082002 (2012)
34. J. Aasi *et al.*, ApJS **211**, 7 (2014)
35. P.A. Evans *et al.*, ApJS **203**, 28 (2012)
36. L.P Singer *et al.*, ApJ **776**, L34 (2013)

Frascati Physics Series Vol. 58 (2014)
Frontier Objects in Astrophysics and Particle Physics
May 18-24, 2014

Cosmological Dynamics of Nonminimal Coupled Theories

Jorge Páramos
Departamento de Física e Astronomia and Centro de Física do Porto,
Faculdade de Ciências da Universidade do Porto,
Rua do Campo Alegre 687, 4169-007 Porto, Portugal

Rafael Ribeiro
Departamento de Física,
Instituto Superior Técnico, Universidade de Lisboa,
Av. Rovisco Pais 1, 1049-001 Lisboa, Portugal

Abstract

In this work a dynamical system approach to nonminimal coupled $f(R)$ theories is developed; its usefulness in determining cosmological solutions is illustrated by applying it to distinct models and obtaining the ensuing fixed points. Stability and physical interpretation are discussed, including their viability as candidates for dark energy. A more detailed analysis can be found in Ref. [1].

1 Introduction

General Relativity (GR) enjoys outstanding success at solar system and local scales [2, 3], elegantly presenting an account of gravitation based upon first principles. However, the enduring quest for the nature of dark matter and dark energy, as well as the need for inflation and other issues, has prompted some researchers to expand GR by considering a non-linear functional of the scalar

curvature — the so called $f(R)$ theories [4]; this approach is naturally extended by coupling matter and curvature in a nonminimal way [5] (for early proposals see Ref. [6, 7, 8, 9]). This nonminimal coupling (NMC) leads to several implications, from Solar System [10] and stellar dynamics [11, 12, 13, 14] to close like-time curves [15], wormholes [16] and modifications to the well-known energy conditions [17] (see Ref. [18] for a thorough review). It is also able to mimic dark matter [19, 20], dark energy [21, 22, 23] and explain post-inflationary preheating [24, 25] and cosmological structure formation [26].

From a fundamental standpoint, a NMC can arise from Quantum Electrodynamics in curved spacetime one-loop vacuum-polarization effects [27], as well as in the context of matter scalar fields [28, 29] or Riemann-Cartan geometry [30].

2 The Model

A generalization of the Einstein-Hilbert action can be made with a NMC included in the action [5],

$$S = \int d^4x\sqrt{-g}\,[\kappa f_1(R) + f_2(R)\mathcal{L}] \quad , \quad \kappa = \frac{c^4}{16\pi G}, \tag{1}$$

where $f_i(R)$ are arbitrary functions of the scalar curvature R, g is the metric determinant and $\mathcal{L}$ the matter Lagrangian density. The standard Einstein-Hilbert action is recovered when $f_1(R) = R - 2\Lambda$ and $f_2(R) = 1$. By varying the action with respect to the metric, the field equations are obtained,

$$FG_{\mu\nu} = \frac{1}{2}f_2T_{\mu\nu} + \triangle_{\mu\nu}F + \frac{1}{2}g_{\mu\nu}\kappa f_1 - \frac{1}{2}g_{\mu\nu}RF, \tag{2}$$

where $F = \kappa f_1' + f_2'\mathcal{L}$, the prime denotes derivation with respect to the scalar curvature, $\triangle_{\mu\nu} \equiv \bigtriangledown_\mu \bigtriangledown_\nu - g_{\mu\nu}\Box$, and $T_{\mu\nu}$ is the matter energy-momentum tensor. The generalized Bianchi identities lead to the non-conservation law

$$\bigtriangledown^\mu T_{\mu\nu} = \frac{f_2'}{f_2}\left(g_{\mu\nu}\mathcal{L} - T_{\mu\nu}\right)\bigtriangledown^\mu R. \tag{3}$$

Aiming at the study of the recent accelerated expansion of our universe, a flat spacetime is considered with the line element $ds^2 = -dt^2 + a^2(t)dV^2$, where $a(t)$ is the scale factor and dV is the volume element; matter is assumed to behave as a perfect fluid, with an energy-momentum tensor $T^{\mu\nu} = (\rho + P)\,u^\mu u^\nu + Pg^{\mu\nu}$

derived from the Lagrangean density $\mathcal{L} = -\rho$ [31], where ρ and P are the energy density and pressure of the perfect fluid, respectively, and u^μ its four-velocity.

Just like in GR or $f(R)$ theories, the energy-momentum tensor is conserved in a cosmological setting, since Eq. (3) yields the continuity equation $\dot{\rho} + 3H(1+w)\rho = 0$, where $H = \dot{a}/a$ is the Hubble parameter and $w = P/\rho$ is the equation of state (EOS) parameter. The modified Friedmann equation is obtained by inserting the metric in the tt component of the field equations (2),

$$H^2 = \frac{1}{3F}\Big[\frac{1}{2}f_2\rho - 3HF'\dot{R} - 9H^2(1+w)f_2'\rho - \frac{1}{2}\kappa f_1 + \frac{RF}{2}\Big]. \tag{4}$$

3 Dynamical System Approach

The solutions of the field equations can be attained by studying its equivalent dynamical system of dimensionless variables

$$x = -\frac{F'\dot{R}}{FH},\ y = \frac{R}{6H^2},\ z = -\frac{\kappa f_1}{6FH^2},\ \Omega_1 = \frac{f_2\rho}{6FH^2},\ \Omega_2 = -\frac{3(1+w)f_2'\rho}{F}\ , \tag{5}$$

with $F' \equiv \kappa f_1'' - f_2''\rho$. The number of variables of the problem was increased by the introduction of this coupling — for $f(R)$ theories, only four variables were required [32]; the modified Friedmann equation (4) reads $1 = x+y+z+\Omega_1+\Omega_2$, acting as a restriction to the phase space. For a constant F (studied in Ref. [23]), the condition $x = -\Omega_2$ is verified.

The following autonomous system is determined by varying the variables with respect to the number of *e-folds* $N = \ln a$,

$$\begin{cases} \frac{dx}{dN} = x\left[x - y + \Omega_2\left(1 + \frac{\alpha_2}{\alpha}\right)\right] - 1 - y - 3z + 3w\Omega_1 + \Omega_2\left[3\left(1+w\right) - y\right] \\ \frac{dy}{dN} = y\left[-x/\alpha + 2\left(2-y\right)\right] \\ \frac{dz}{dN} = z\left[x\left(1 - \alpha_1/\alpha\right) + \Omega_2 + 2\left(2-y\right)\right] \\ \frac{d\Omega_1}{dN} = \frac{\Omega_2 xy}{3\alpha(1+w)} + \Omega_1\left[1 - 3w + x + \Omega_2 - 2y\right] \\ \frac{d\Omega_2}{dN} = \Omega_2\left[x\left(1 - \frac{\alpha_2}{\alpha}\right) - 3\left(1+w\right) + \Omega_2\right] \end{cases} \tag{6}$$

with the dimensionless parameters $\alpha = F'R/F$, $\alpha_1 = f_1'R/f_1$ and $\alpha_2 = f_2''R/f_2'$. These express the chosen functions $f_1(R)$ and $f_2(R)$ and must be computed as a function of the variables for each particular model (analogously to the Υ parameter defined in Ref. [32]). It is possible to show that

$$\alpha_1 = \frac{y}{z}\left[\frac{\Omega_2}{3(1+w)} - 1\right] \quad , \quad \alpha = \frac{f_1''R}{f_1'}\left[1 - \frac{\Omega_2}{3(1+w)}\right] + \frac{\alpha_2\Omega_2}{3(1+w)}. \tag{7}$$

With the adopted metric, the Ricci scalar reads $R = 6(2H^2 + \dot{H}) = 6H^2(1 - q)$, where $q = -\ddot{a}a/(\dot{a})^2$ is the deceleration parameter. Since our universe appears to be expanding at an accelerated rate, a stable solution with $q < 0 \rightarrow y > 1$ is needed. In GR an exotic fluid (dark energy) with negative pressure, $w < -1/3$ is required, since $q = (1 + 3w)/2$.

The definition of the scalar curvature yields $\dot{H} = (y - 2)H^2$, implying

$$a(t) = (t/t_0)^{\frac{1}{2-y}}, \quad y = 2 \quad \vee \quad a(t) = e^{H_0 t}, \quad y \neq 2 \tag{8}$$

The general solution for the energy density can be determined from the continuity equation, $\rho(t) = \rho_0 a(t)^{-3(1+w)}$ and from the definition of Ω_2

$$\rho = \frac{\kappa f_1' \Omega_2}{f_2' \left[\Omega_2 - 3(1 + w)\right]}. \tag{9}$$

For $\Omega_2 = 3(1+w)$ there appears to be a divergence in the density: physically, a fixed point with this value of Ω_2 will correspond to a regime where $f_2'\rho \gg \kappa f_1'$.

3.1 $f(R)$ Theories

In order to confirm the results obtained in Ref. [32], the case $f(R)$ is considered by choosing $f_1(R) = f(R), \quad f_2(R) = 1$, so that $\alpha_1 = -y/z$, the variable Ω_2 vanishes trivially, α only depends on the derivatives of our arbitrary function $f(R)$ and α_2 does not appear in the equations. The obtained dynamical system is indeed equivalent to the one reported in Ref. [32], as expected (for an extensive discussion see also Ref. [33]).

3.2 Power Law Nonminimal Coupling

To study the influence of a NMC in cosmology, a simple case $f_1(R) = R$ and $f_2(R) = 1 + \left[R/(12M^2)\right]^n$ is considered (studied in Refs. [21, 23]), where M is a characteristic curvature scale. This enables a constant parameter $\alpha_2 = n - 1$, and allows for the determination of the fixed points of the dynamical system (6), shown in Table 1 together with the evolution of the scale factor $a(t)$.

The first fixed point is in the $f_2'\rho \gg \kappa$ regime and yields a De Sitter phase with constant Hubble parameter

$$H_0 = M \left[n \left(2 + \frac{3w}{2} \right) - 1 \right]^{-1/(2n)}. \tag{10}$$

	$(x,\, y,\, z,\, \Omega_1, \Omega_2)$	$a(t)$
1	$(0, 2, 0, -4-3w, 3(1+w))$	$e^{H_0 t}$
2	$\left(\frac{4-2n(4+3w)}{2n-1}, \frac{n(-2+4n+3w)}{1-3n+2n^2}, 0, \frac{2-4n-3w}{1-3n+2n^2}, 3(1+w)\right)$	$\left(\frac{t}{t_0}\right)^{\frac{1-3n+2n^2}{2-n(4+3w)}}$
3	$\left(\frac{6n(1+w)}{1-4n-3w}, -\frac{1-4n-3w}{2(n-1)}, \frac{1-2n-3w}{2(n-1)}, \frac{1}{1-n}, -\frac{6n(1+w)}{1-4n-3w}\right)$	$\left(\frac{t}{t_0}\right)^{\frac{2(1-n)}{3(1+w)}}$

Table 1: Fixed points and respective solutions for a power law NMC.

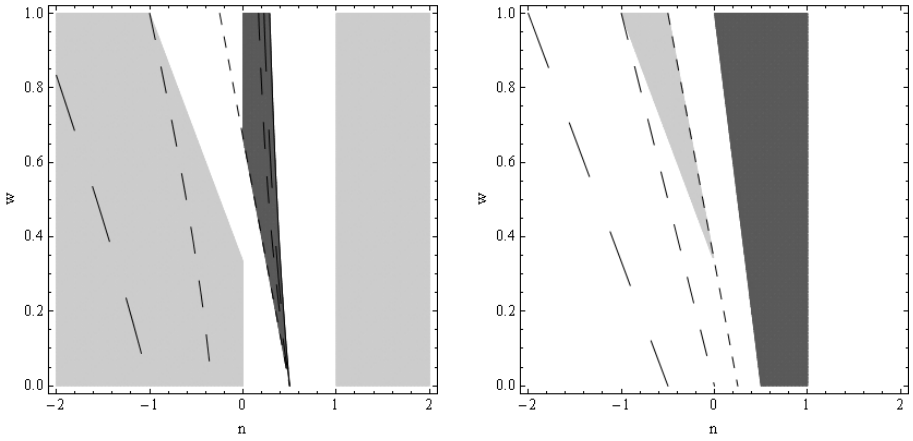

(a) Second fixed point. (b) Third fixed point

Figure 1: The light grey region corresponds to the a stable fixed point, the dark grey region to an unstable fixed point and the remaining to a saddle point. Large, medium and short dash indicate $q = 0$, $q = 1/2$ and $q = 1$, respectively. The continuous line corresponds to $q = -1$.

It is unstable for $2/(4+3w) < n < 1$ and a saddle otherwise.

From Ref. [21], one sees that the second fixed point (with $w = 0$) also fulfils condition $f_2'\rho \gg \kappa$: for $n = 2/(4+3w)$, it is indeed equal to the first. As expected, the NMC contribution is dominant, since $\Omega_2 = 3(1+w)$. The stability of the second and third points is shown in Fig. 1.

The third point has constant F, since $x = -\Omega_2$ and the energy density is

$$\rho(t) = \frac{24\kappa M^2}{1-2n-3w}\left[\frac{3^2(1+w)^2M^2}{(1-n)(1-4n-3w)}t^2\right]^{n-1}. \qquad (11)$$

This result is different from the one attained in the $f_2'\rho \ll \rho$ regime studied in Ref. [21]: in the latter, $f_2'\rho = 0$ was effectively assumed, and thus $F = \kappa \neq \kappa(1-4n)/(1-2n)$. This point is only consistent if the power law dominates and corresponds to the generalization of the matter solution of GR.

3.3 Power law NMC and curvature term

Although not shown here, for brevity, one may expand upon the previous results by considering two power-law terms, $f_1(R) = R + R_1 \left(R/R_1\right)^{n_1}$ and $f_2(R) = 1 + \left(R/R_2\right)^{n_2}$, where R_i are characteristic curvature scales. Ten distinct fixed points are obtained: of these, six have a vanishing $\Omega_2 = 0$, so that the contribution from f_1' dominates; three additional depend on the NMC and match those presented in section 3.2, while one fixed point depends on both functions (see Ref. [1]) for a thorough discussion).

4 Conclusion

In this work, a dynamical system approach was made on NMC theories, and the ensuing dynamical system for the most general case with two arbitrary functions presented; as expected, the NMC dynamical system can be specified to a pure $f(R)$ theory when $f_2(R) = 1$, yielding the results obtained in Ref. [32].

An application to a power law NMC model was presented, for illustration: amongst other considerations, it was shown that the solutions obtained are in general agreement with Ref. [21]. Other possible uses of this method (pursued in Ref. [1]) include an exponential NMC and power law dependencies for both $f_1(R)$ and $f_2(R)$; the latter shows that the assumption $f_2'(R)\rho =$const. adopted in Ref. [23] indeed corresponds to fixed points arising from a dynamical system analysis. A plethora of fixed points arises, some of which are attractors that could be candidates for inflation or dark energy — depending on whether they dominate dynamics at early or late times, respectively.

It should be highlighted that this method depends on the adopted variables, with other choices leading to different results; furthermore, the existence of desirable fixed points is, by itself, insufficient, as one is left to show that a history of the Universe connecting these exists and is compatible with known cosmographic constraints [34]. Notwithstanding, the method here presented serves to motivate further studies of the revealed scenarios.

5 Acknowledgements

This work was partly developed during the context of the *2014 Vulcano Workshop*, in Vulcano, Italy. J.P. thank the organization for the hospitality displayed, and O. Bertolami for fruitful discussions.

References

1. R. Ribeiro and J. Páramos, arXiv:1409.3046 [gr-qc].
2. C. M. Will, Living Rev. Rel. **9**, 3 (2006).
3. O. Bertolami and J. Páramos, "The experimental status of Special and General Relativity", *Handbook of Spacetime*, Springer, Berlin (2014).
4. A. De Felice and S. Tsujikawa, Living Rev. Rel. **13**, 3 (2010).
5. O. Bertolami, C. G. Böhmer, T. Harko and F. S. N. Lobo, Phys. Rev. D **75**, 104016 (2007).
6. L. Amendola and D. Tocchini-Valentini, Phys. Rev. D **64**, 043509 (2001).
7. S. 'i. Nojiri and S. D. Odintsov, PoS WC **2004**, 024 (2004).
8. G. Allemandi, A. Borowiec, M. Francaviglia and S. D. Odintsov, Phys. Rev. D **72**, 063505 (2005).
9. T. Koivisto, Class. Quant. Grav. **23**, 4289 (2006).
10. O. Bertolami, R. March and J. Páramos, Phys. Rev. D **88**, 064019 (2013).
11. O. Bertolami and J. Páramos, Phys. Rev. D **77**, 084018 (2008).
12. O. Bertolami and A. Martins, Phys. Rev. D **85**, 024012 (2012).
13. J. Páramos and C. Bastos, Phys. Rev. D **86**, 103007 (2012).
14. O. Bertolami and J. Páramos, arXiv:1306.1177 [gr-qc].
15. O. Bertolami and R. Z. Ferreira, Phys. Rev. D **85**, 104050 (2012).
16. N. Montelongo Garcia and F. S. N. Lobo, Class. Quant. Grav. **28**, 085018 (2011).

17. O. Bertolami and M. C. Sequeira, Phys. Rev. D **79**, 104010 (2009).

18. O. Bertolami and J. Páramos, Int. J. Geom. Meth. Mod. Phys. **11**, 1460003 (2014)

19. O. Bertolami and J. Páramos, JCAP **03**, 009 (2010).

20. O. Bertolami, P. Frazão and J. Páramos, Phys. Rev. D **86**, 044034 (2012).

21. O. Bertolami, P. Frazão and J. Páramos, Phys. Rev. D **81**, 104046 (2010).

22. O. Bertolami and J. Páramos, Phys. Rev. D **84**, 064022 (2011).

23. O. Bertolami and J. Páramos, Phys. Rev. D **89**, 044012 (2014).

24. O. Bertolami, P. Frazão and J. Páramos, Phys. Rev. D **83**, 044010 (2011).

25. A. A. Starobinsky, Phys. Lett. B **91**, 99 (1980).

26. O. Bertolami, P. Frazão and J. Páramos, JCAP **1305**, 029 (2013).

27. I. T. Drummond and S. J. Hathrell, Phys. Rev. D **22**, 343 (1980).

28. T. Damour and G. Esposito-Farese, Class. Quant. Grav. **9**, 2093 (1992).

29. O. Bertolami and J. Páramos, Class. Quant. Grav. **25**, 245017 (2008).

30. H. F. M. Goenner, Found. Phys. **14**, 9 (1984).

31. O. Bertolami, F. S. N. Lobo and J. Páramos, Phys. Rev. D **78**, 064036 (2008).

32. S. Carloni, A. Troisi and P. K. S. Dunsby, Gen. Rel. Grav. **41**, 1757 (2009).

33. S. Carloni, P. K. S. Dunsby, S. Capozziello and A. Troisi, Class. Quant. Grav. **22**, 4839 (2005).

34. Y. G. Gong and A. Wang, Phys. Rev. D **75**, 043520 (2007).

Frascati Physics Series Vol. 58 (2014)
Frontier Objects in Astrophysics and Particle Physics
May 18-24, 2014

NEW RESULTS FROM DAMA/LIBRA: FINAL MODEL-INDEPENDENT RESULTS OF DAMA/LIBRA-PHASE1 AND PERSPECTIVES OF PHASE2

R. Bernabei, P. Belli, S. d'Angelo, A. Di Marco, F. Montecchia
Dip. di Fisica, Università di Roma "Tor Vergata" and INFN, I-00133 Rome, Italy
F. Cappella, A. d'Angelo, A. Incicchitti
Dip. di Fisica, Università di Roma "La Sapienza" and INFN, I-00185 Rome, Italy
V. Caracciolo, R. Cerulli
Laboratori Nazionali del Gran Sasso, I.N.F.N., Assergi, Italy
C.J. Dai, H.L. He, X.H. Ma, X.D. Sheng, R.G. Wang, Z.P. Ye
IHEP, Chinese Academy, P.O. Box 918/3, Beijing 100039, China

Abstract

The DAMA/LIBRA–phase1 and the former DAMA/NaI data (cumulative exposure 1.33 ton × yr, corresponding to 14 annual cycles) give evidence at 9.3 σ C.L. for the presence of Dark Matter (DM) particles in the galactic halo, on the basis of the exploited model independent DM annual modulation signature by using highly radio-pure NaI(Tl) target. Few arguments on results and comparisons will be summarized.

1 Introduction

About 80 years of experimental observations and theoretical arguments have pointed out – both at Galaxy and larger scales – that a large fraction of the Universe is composed by Dark Matter particles [1].

[1]For completeness, we recall that some efforts to find alternative explanations to Dark Matter have been proposed such as *MOdified Gravity Theory*

The presently running DAMA/LIBRA ($\simeq$ 250 kg of full sensitive target-mass) [1, 2, 3, 4, 5, 6, 7, 8] experiment, as well as the former DAMA/NaI ($\simeq$ 100 kg of full sensitive target-mass) [9, 10, 11, 12, 13], has the main aim to investigate the presence of DM particles in the galactic halo by exploiting the model independent DM annual modulation signature (originally suggested in Ref. [14]). Moreover, the developed highly radio-pure NaI(Tl) target-detectors [1] and the adopted procedures assure as well sensitivity to a wide range of DM candidates (both inducing nuclear recoils and/or electromagnetic radiation), interaction types and astrophysical scenarios.

As a consequence of the Earth's revolution around the Sun, which is moving in the Galaxy with respect to the Local Standard of Rest towards the star Vega near the constellation of Hercules, the Earth should be crossed by a larger flux of DM particles around $\simeq$ 2 June and by a smaller one around $\simeq$ 2 December[2]. In the former case the Earth orbital velocity is summed to the one of the solar system with respect to the Galaxy, while in the latter the two velocities are subtracted. This DM annual modulation signature is very distinctive since the effect induced by DM particles must simultaneously satisfy all the following requirements: the rate must contain a component modulated according to a cosine function (1) with one year period (2) and a phase that peaks roughly $\simeq$ 2 June (3); this modulation must only be found in a well-defined low energy range, where DM particle induced events can be present (4); it must apply only to those events in which just one detector of many (9 in DAMA/NaI and 25 in DAMA/LIBRA) actually "fires" (*single-hit* events),

(MOG) and *MOdified Newtonian Dynamics* (MOND); they hypothesize that the theory of gravity is incomplete and that a new gravitational theory might explain the experimental observations. MOND modifies the law of motion for very small accelerations, while MOG modifies the Einstein's theory of gravitation to account for an hypothetical fifth fundamental force in addition to the gravitational, electromagnetic, strong and weak ones. But: i) there is no general underlying principle; ii) they are generally unable to account for all small and large scale observations; iii) they fail to reproduce accurately the Bullet Cluster; iv) generally they require some amount of DM particles as seeds for the structure formation.

[2]Thus, the DM annual modulation signature has a different origin and peculiarities than the seasons on the Earth and than effects correlated with seasons (consider the expected value of the phase as well as the other requirements listed below).

since the DM particle multi-interaction probability is negligible (5) and this offers in DAMA experiments an unique further way of signal identification and background rejection; the modulation amplitude in the region of maximal sensitivity must be $\simeq 7\%$ for usually adopted halo distributions (6), but it can be larger (even up to $\simeq 30\%$) in case of some possible scenarios such as e.g. those in Ref. [15, 16]. Thus, this signature is model independent, very effective and, in addition, it allows the test of a large range of DM candidates, of cross sections and of halo densities.

In particular, the experimental observable in DAMA experiments is the modulated component of the signal in NaI(Tl) target and not the constant part of it as in other approaches as those by CDMS, Xenon, etc., where in addition e.g. detectors and/or many (by the fact largely uncertain) data selections/subtractions, etc. are applied.

The DM annual modulation signature might be mimicked only by systematic effects or side reactions able to account for the whole observed modulation amplitude and to simultaneously satisfy all the requirements given above. No one is available or suggested by anyone over more than a decade [1, 2, 5, 6, 8, 11].

The signature itself acts as a strong background reduction as pointed out since the early paper by Freese et al., and especially when all the above peculiarities can be experimentally verified in suitable dedicated set-ups as it is the case of the DAMA experiments.

2 The results of DAMA/LIBRA–phase1 and DAMA/NaI

The total exposure of DAMA/LIBRA–phase1 is: 1.04 ton $\times$ yr in seven annual cycles; when including also that of the first generation DAMA/NaI experiment it is 1.33 ton $\times$ yr, corresponding to 14 annual cycles. The variance of the cosine during the DAMA/LIBRA–phase1 data taking is 0.518, showing that the set-up has been operational evenly throughout the years [2, 6].

Many independent data analyses have been carried out [2, 6] and all of them confirm the presence of a peculiar annual modulation in the *single-hit* scintillation events in the 2-6 keV energy interval, which – in agreement with the requirements of the signature – is absent in other part of the energy spectrum and in the *multiple-hit* scintillation events in the same 2-6 keV energy interval (this latter correspond to have "switched off the beam" of DM particles). All

the analyses and details can be found in the literature given above.

Here due to the pages restriction, we just show in Fig. 1 the time behaviour of the experimental residual rates of the *single-hit* scintillation events for DAMA/NaI [11] and DAMA/LIBRA–phase1 [2, 6] cumulatively in the (2–6) keV energy interval; the data points present the experimental errors as vertical bars and the associated time bin width as horizontal bars. The superimposed curve is the cosinusoidal function behaviour $A\cos\omega(t-t_0)$ with a period $T=\frac{2\pi}{\omega}=1$ yr, a phase $t_0=152.5$ day (June 2^{nd}) and modulation amplitudes, A, equal to the central values obtained by best fit on the data points. The dashed vertical lines correspond to the maximum expected for the DM signal (June 2^{nd}), while the dotted vertical lines correspond to the minimum. The major upgrades are also pointed out.

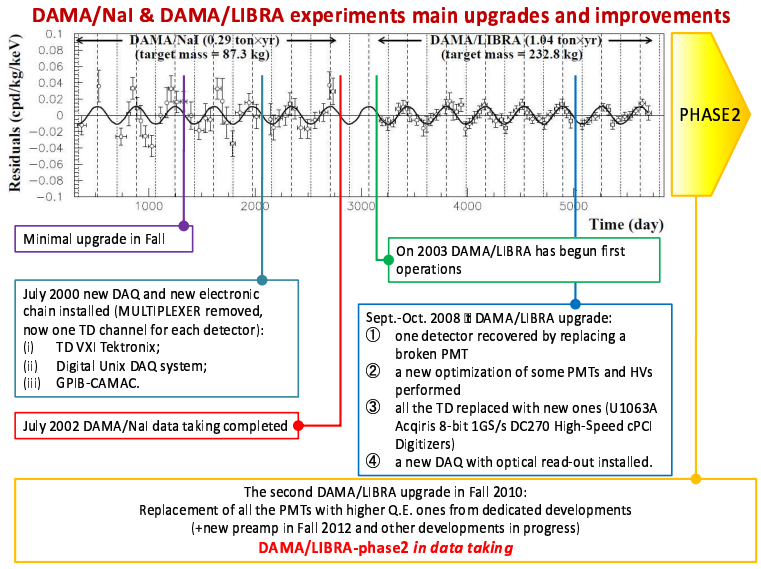

Figure 1: *Experimental residual rate of the single-hit scintillation events measured by DAMA/NaI and DAMA/LIBRA–phase1 in the (2–6) keV energy interval as a function of the time. See text. The major upgrades are also pointed out.*

In order to continuously monitor the running conditions, several pieces

of information are acquired with the production data and quantitatively analysed. In particular, all the time behaviours of the running parameters, acquired with the production data, have been investigated: the modulation amplitudes obtained for each annual cycle when fitting the time behaviours of the parameters including a cosine modulation with the same phase and period as for DM particles are well compatible with zero. In particular, no modulation has been found in any possible source of systematics or side reactions; thus, cautious upper limits (90% C.L.) on possible contributions to the DAMA/LIBRA measured modulation amplitude have been derived (see e.g. [2]). It is worth noting that they do not quantitatively account for the measured modulation amplitudes, and also are not able to simultaneously satisfy all the many requirements of the signature. Similar analyses have also been done for the DAMA/NaI data [11].

For completeness we mention that sometimes naive statements are put forwards as the fact that in nature several phenomena may show some kind of periodicity. The point is whether they might mimic the annual modulation signature in DAMA/LIBRA (and former DAMA/NaI), i.e. whether they might be not only quantitatively able to account for the whole observed modulation amplitude but also able to simultaneously satisfy all the requirements of the DM annual modulation signature. The same is also for side reactions. This has already been quantitatively investigated in our literature [1, 2, 5, 6, 8, 17, 18]. In particular, any relevant contribution to the DAMA modulation effect from the μ and from neutrons induced by μ can be excluded for the many scientific arguments discussed in details in Ref. [5] and recalled in Ref. [6]. Moreover, we also recall that the neutrons of whatever origin, surviving the shield against them, can be and have been quantitatively studied in various ways in DAMA experiments (see literature quoted above). For example, even when cautiously assuming a 10% modulation (of whatever origin) of the fast neutrons flux, and even assuming the same phase and period as for the DM case, the corresponding modulation amplitude is 2-3 orders of magnitude lower than the DAMA observed modulation amplitude. Finally, in no case neutrons (of whatever origin) can mimic the DM annual modulation signature since some of the peculiar requirements of the signature would fail, such as the neutrons would induce e.g. variations in all the energy spectrum, variation in the multiple hit events, etc. which were not observed.

In conclusion, the model-independent DAMA results give evidence – at

9.3σ C.L. in 14 annual cycles independent measurements - for the presence of DM particles in the galactic halo satisfying all the many requirements of the exploited signature.

2.1 On comparisons

No direct model independent comparison is possible in the field when different target materials and/or approaches are used; the same is for the indirect searches.

In order to perform corollary investigations on the nature of the DM particles, model-dependent analyses are necessary[3]; thus, many theoretical and experimental parameters and models are possible and many hypotheses must also be exploited.

Many candidates, interactions, halo models, etc. are possible, while specific experimental and theoretical assumptions are generally adopted in a single arbitrary scenario without accounting neither for existing uncertainties nor for alternative possible scenarios, interaction types, etc.

The obtained DAMA model independent evidence is compatible with a wide set of scenarios regarding the nature of the DM candidate and related astrophysical, nuclear and particle Physics. For examples some given scenarios and parameters are discussed e.g. in Ref. [9, 11, 2, 6]. Further large literature is available on the topics (see for example in the bibliography of Ref. [6]). Moreover, both the negative results and all the possible positive hints are largely compatible with the DAMA model-independent DM annual modulation results in various scenarios considering also the existing experimental and theoretical uncertainties; the same holds for indirect approaches; see e.g. arguments in Ref. [6] and references therein.

As regards the recent plot from Snowmass and that in Ref. [19], widely used in this conference about the "status of the Dark Matter search", it should be noted that it does not point out at all the real status of Dark Matter searches since: i) Dark Matter has wider possibilities than WIMPs inducing just nuclear recoil with spin-independent interaction under single (largely arbitrary) set of

[3]For completeness, we recall that it does not exist any approach to investigate the nature of the candidate in the direct and indirect DM searches, which can offer that information independently on assumed astrophysical, nuclear and particle Physics scenarios

assumptions; ii) neither the uncertainties for existing experimental and theoretical aspects nor alternative assumptions (which at present stage of knowledge are possible as well) are accounted for; iii) they do not include possible systematic errors affecting the data from which the exclusion plots are derived (such as e.g. "extrapolations" of energy threshold, of energy resolution and of efficiencies, quenching factors values, convolution with poor energy resolution, correction for non-uniformity of the detector, multiple subtractions/selection of detectors and/or data, assumptions on quantities related to halo model, form factors, scaling laws, etc.); iv) the DAMA implications – even adopting the many arbitrary assumptions considered there – appear incorrect[4]. On the other hand, for a similar picture one should quote in details the adopted "cooking" for each case otherwise it is even more meaningless. It also should be noted – in addition – that in those plots the allowed regions from the DAMA 9.3 σ C.L. model-independent evidence (1.33 ton $\times$ yr total exposure; confirmed over 14 independent experiment of 1 year each one) and from some recent possible published hints (only some kg $\times$ day exposure) are presented at level of 90% C.L. from the minimum found for each one by the author(s) of those plots under their own (often arbitrary) adopted "assumptions". Considering the well different C.L. of the experimentally observed effects, a more correct procedure would be to refer the allowed regions to the absence of signal (which is a common reference level).

It is also worth to remind that DAMA experiments are not only sensitive to DM particles with Spin-independent coupling inducing just nuclear recoils, but also to other couplings and to other DM candidates as those giving rise to

[4]We take this occasion to recall that in the DAMA/LIBRA experiment the measured counting rate in the cumulative energy spectrum is about 1 cpd/kg/keV in the lowest energy bins; this latter is the sum of the constant background contribution and of the constant part of the signal S_0. As discussed e.g. in TAUP2011 [18], the constant background in the cumulative spectrum in the 2-4 keV energy region is estimated to be not lower than about 0.75 cpd/kg/keV; this gives an upper limit on S_0 of about 0.25 cpd/kg/keV. Thus, the S_m/S_0 ratio is equal or larger than about 0.01/0.25. To not account for this experimental fact is one of the reasons (together with other erroneous assumptions also on some other experimental quantities) of the incorrect allowed regions put forward as "DAMA" by most authors and in the plots mentioned above for the very particular (arbitrary) scenario they adopt.

part or all the signal in electromagnetic form. Finally, scenarios exist in which other kind of targets/approaches are disfavoured or even blind.

3 DAMA/LIBRA–phase2 and perspectives

An important upgrade has started at end of 2010 replacing all the PMTs with new ones having higher Quantum Efficiency; details on the developments and on the reached performances in the operative conditions are reported in Ref. [4]. They have allowed to lower the software energy threshold of the experiment to 1 keV and improve also other features as e.g. the energy resolution [4].

Since the fulfillment of this upgrade, DAMA/LIBRA–phase2 – after optimization periods – is continuously running in order: (1) to increase the experimental sensitivity thanks to the lower software energy threshold; (2) to improve the corollary investigation on the nature of the DM particle and related astrophysical, nuclear and particle physics arguments; (3) to investigate other signal features and second order effects. This requires long and dedicated work for reliable collection and analysis of very large exposures.

In the future DAMA/LIBRA will also continue its study on several other rare processes as also the former DAMA/NaI apparatus did.

Finally, further future improvements of the DAMA/LIBRA set-up to increase the sensitivity (possible DAMA/LIBRA-phase3) and the developments towards the possible DAMA/1ton, we proposed in 1996, are considered.

4 Conclusions

The data of DAMA/LIBRA–phase1 have further confirmed the presence of a peculiar annual modulation of the *single-hit* events in the (2–6) keV energy region satisfying all the many requirements of the DM annual modulation signature; the cumulative exposure by the former DAMA/NaI and DAMA/LIBRA–phase1 is 1.33 ton $\times$ yr.

As required by the DM annual modulation signature: 1) the *single-hit* events show a clear cosine-like modulation as expected for the DM signal; 2) the measured period is equal to (0.998 ± 0.002) yr well compatible with the 1 yr period as expected for the DM signal; 3) the measured phase (144 ± 7) days is compatible with $\simeq 152.5$ days as expected for the DM signal; 4) the modulation is present only in the low energy (2–6) keV interval and not in other

higher energy regions, consistently with expectation for the DM signal; 5) the modulation is present only in the *single-hit* events, while it is absent in the *multiple-hit* ones as expected for the DM signal; 6) the measured modulation amplitude in NaI(Tl) of the *single-hit* events in the (2–6) keV energy interval is: (0.0112 ± 0.0012) cpd/kg/keV (9.3 σ C.L.). No systematic or side processes able to simultaneously satisfy all the many peculiarities of the signature and to account for the whole measured modulation amplitude is available.

DAMA/LIBRA–phase2 is continuously running in its new configuration with a lower software energy threshold aiming to improve the knowledge on corollary aspects regarding the signal and on second order effects as discussed e.g. in Ref. [6, 8].

Few comments on model–dependent comparisons have also been addressed here.

References

1. R. Bernabei *et al.*, Nucl. Instr. and Meth. A 592 (2008) 297.
2. R. Bernabei *et al.*, Eur. Phys. J. C 56 (2008) 333; Eur. Phys. J. C 67 (2010) 39; Eur. Phys. J. C 73 (2013) 2648.
3. P. Belli *et al.*, Phys. Rev. D 84 (2011) 055014.
4. R. Bernabei *et al.*, J. of Instr. 7 (2012) P03009.
5. R. Bernabei *et al.*, Eur. Phys. J. C 72 (2012) 2064.
6. R. Bernabei *et al.*, Int. J. of Mod. Phys. A 28 (2013) 1330022.
7. R. Bernabei *et al.*, Eur. Phys. J. C 62 (2009) 327; Eur. Phys. J. C 72 (2012) 1920; Eur. Phys. J. A 49 (2013) 64.
8. R. Bernabei *et al.*, Eur. Phys. J. C 74 (2014) 2827.
9. R. Bernabei *et al.*, Phys. Lett. B 389 (1996) 757; Phys. Lett. B 424 (1998) 195; Phys. Lett. B 450 (1999) 448; Phys. Rev. D 61 (2000) 023512; Phys. Lett. B 480 (2000) 23; Phys. Lett. B 509 (2001) 197; Eur. Phys. J. C 23 (2002) 61; P. Belli *et al.*, Phys. Rev. D 66 (2002) 043503.
10. R. Bernabei *et al.*, Il Nuovo Cim. A 112 (1999) 545;

11. R. Bernabei *et al.*, La Rivista del Nuovo Cimento 26 n.1 (2003) 1-73; Int. J. Mod. Phys. D 13 (2004) 2127.

12. R. Bernabei *et al.*, Int. J. Mod. Phys. A 21 (2006) 1445; Eur. Phys. J. C 47 (2006) 263; Int. J. Mod. Phys. A 22 (2007) 3155; Eur. Phys. J. C 53 (2008) 205; Phys. Rev. D 77 (2008) 023506; Mod. Phys. Lett. A 23 (2008) 2125.

13. R. Bernabei *et al.*, Phys. Lett. B408 (1997) 439; P. Belli *et al.*, Phys. Lett. B460 (1999) 236; Phys. Rev. C60 (1999) 065501; R. Bernabei *et al.*, Phys. Rev. Lett. 83 (1999) 4918; Il Nuovo Cimento A112 (1999) 1541; Phys. Lett. B 515 (2001) 6; F. Cappella *et al.*, Eur. Phys. J.-direct C14 (2002) 1; R. Bernabei *et al.*, Eur. Phys. J. A 23 (2005) 7; Eur. Phys. J. A 24 (2005) 51; Astrop. Phys. 4 (1995) 45; R. Bernabei, in the volume *The Identification of Dark Matter*, World Sc. Pub. (1997) 574.

14. K.A. Drukier *et al.*, Phys. Rev. D 33 (1986) 3495; K. Freese *et al.*, Phys. Rev. D 37 (1988) 3388.

15. D. Smith and N. Weiner, Phys. Rev. D 64 (2001) 043502; D. Tucker-Smith and N. Weiner, Phys. Rev. D 72 (2005) 063509; D. P. Finkbeiner *et al*, Phys. Rev. D 80 (2009) 115008.

16. K. Freese *et al.*, Phys. Rev. D 71 (2005) 043516; K. Freese *et al.*, Phys. Rev. Lett. 92 (2004) 11301.

17. R. Bernabei *et al.*, AIP Conf. Proceed. 1223 (2010) 50; in the volume *Frontier Objects in Astrophysics and Particle Physics*, ed. S.I.F. (Vulcano, 2010), p. 157 [*arXiv:1007.0595*]; Can. J. Phys. 89 (2011) 11; Physics Procedia 37 (2012) 1095; *arXiv:1210.6199*; *arXiv:1211.6346*.

18. R. Bernabei et al., J. Phys.: Conf. Ser. 203, 012040 (2010), *arXiv:0912.4200* [http://taup2009.lngs.infn.it/slides/jul3/nozzoli.pdf, talk given by F. Nozzoli].

19. Review of Particle Properties: http://pdg.lbl.gov/2013/reviews/rpp2013-rev-dark-matter.pdf

Frascati Physics Series Vol. 58 (2014)
Frontier Objects in Astrophysics and Particle Physics
May 18-24, 2014

DIRECT SEARCH FOR DARK MATTER WITH TWO-PHASE XENON DETECTORS: CURRENT STATUS OF LUX AND PLANS FOR LZ

The LUX Collaboration*

Abstract

*D.S. Akerib, H.M. Araújo, X. Bai, A.J. Bailey, J. Balajthy, E. Bernard, A. Bernstein, A. Bradley, D. Byram, S.B. Cahn, M.C. Carmona-Benitez, C. Chan, J.J. Chapman, A.A. Chiller, C. Chiller, T. Coffey, A. Currie, , L. de Viveiros, A. Dobi, J. Dobson, E. Druszkiewicz, B. Edwards, C.H. Faham, S. Fiorucci, C. Flores, R.J. Gaitskell, V.M. Gehman (*corresponding author*), C. Ghag, K.R. Gibson, M.G.D. Gilchriese, C. Hall, S.A. Hertel, M. Horn, D.Q. Huang, M. Ihm, R.G. Jacobsen, K. Kazkaz, R. Knoche, N.A. Larsen, C. Lee, B. Lenardo, K.T. Lesko, A. Lindote, M.I. Lopes, D.C. Malling, R. Mannino, D.N. McKinsey, D.-M. Mei, J. Mock, M. Moongweluwan, J. Morad, A.St.J. Murphy, C. Nehrkorn, H. Nelson, F. Neves, R.A. Ott, M. Pangilinan, P.D. Parker, E.K. Pease, K. Pech, P. Phelps, L. Reichhart, T. Shutt, C. Silva, V.N. Solovov, P. Sorensen, K. O'Sullivan, T.J. Sumner, M. Szydagis, D. Taylor, B. Tennyson, D.R. Tiedt, M. Tripathi, S. Uvarov, J.R. Verbus, N. Walsh, R. Webb, J.T. White, M.S. Witherell, F.L.H. Wolfs, M. Woods, C. Zhang

The search for dark matter reaches back generations and remains one of the most compelling endeavors in the hunt for physics beyond the Standard Model. Experiments attempting to directly detect WIMP dark matter have made remarkable progress in increasing sensitivity to elastic scattering of WIMPs on nuclei. The LUX experiment is a 370-kg, two-phase, xenon TPC currently running at SURF, 4850 feet below Lead, SD. LUX recently completed its first science run and was sensitive to spin independent WIMP scattering at cross sections below 10^{-45} cm^2 for WIMP masses of approximately 20 to 80 GeV. Preparations for the final science run of LUX are currently underway, with final results expected in 2015. We will present results from and current status of the LUX experiment, as well as plans for a follow-on, multi-ton-scale xenon experiment at SURF.

1 Introduction to WIMP Dark Matter

Astronomical evidence for the existence of non-luminous, heavy "dark matter" has been accumulating since Fritz Zwicky's observations of the Coma Cluster [1, 2], and subsequent observations of spiral galaxy rotation curves [3]. The advent of ever higher resolution and sensitivity telescopes has allowed for numerous gravitational lensing surveys, which quantified the structure of the dark matter surrounding galaxies and clusters [4, 5]. High-precision measurements of the cosmic microwave background by WMAP [6] and then Planck [7] also strongly favor the existence of dark matter. Observations of cosmic isotope abundances strongly constrain the baryon mass of the Universe to be much less than the total mass fraction [8], leaving the balance to be comprised of some heavy, non-luminous, non-baryonic component. We assume that this part of the cosmic mass fraction is a gas of primordial relic particles, and give them the general name, "Weakly Interacting Massive Particle" (WIMP). WIMPs must be electrically neutral and only interact with baryons very rarely. As a result, most experiments endeavoring to detect WIMP dark matter look for recoiling nuclei, uncorrelated in time with any other event in the data stream. Such dark matter search experiments maximize their sensitivity with very low backgrounds (to remove events that might obscure rare signals) and very low energy thresholds (to remain sensitive to the smallest possible signatures in any individual event).

2 Design of the LUX Detector

The drive for lower backgrounds and lower thresholds has strongly informed the design of the LUX dark matter detector. Xenon was chosen as the target material for several reasons. Xenon has no long-lived radioactive isotopes, meaning that there are no background events intrinsic to the detector medium. Xenon's boiling temperature is fairly high (165 K), making the cryogenic engineering problem a more tractable one. Liquid xenon has a rather high density ($\sim$ 3 g/cm^3), meaning that with position reconstruction we can focus our search on the cleanest, quietest, most central volume of the detector. The high atomic mass of xenon means that the sensitivity for coherent WIMP scattering on nuclei (which scales roughly as A^2) is favorable for xenon compared to other targets. Xenon also has good material properties related to its dielectric breakdown (allowing for a high bias field) and chemical inactivity (which allows for the efficient removal of any electronegative impurities that will attenuate the ionization signal). Xenon has an extremely high scintillation yield, allowing for a much lower energy threshold than most detectors (the only complication is that the scintillation light from xenon is emitted at 175 nm, well into the vacuum ultraviolet).

The LUX detector itself (shown in Figure 1), is a two-phase time projection chamber (TPC) filled with 370 kg of liquid xenon, installed at the 4850-foot level of the Sanford Underground Research Facility (SURF). The TPC is read out by an array of 122 photomultiplier tubes (PMT). The windows of the LUX PMTs are made from synthetic quartz, making them directly sensitive to xenon scintillation light. The inside of the detector volume is lined with high-purity teflon (PTFE), which is an almost perfect diffuse reflector at 175 nm, allowing for even better light collection and therefore lower energy threshold.

There are two types of signals in the LUX detector. Primary scintillation (or "S1") comes from ionizing radiation depositing energy in the xenon. Such energy depositions can also ionize xenon atoms. Ionization electrons loosed from their parent atoms are drifted upward through the bulk of the detector in an external electric field. This field is created in the drift volume by a total of five wire grids. The top and bottom grids shield the PMTs from the drift field. The cathode and gate grids define the drift field in the liquid. The anode grid defines the extraction field (with the gate grid) for pulling ionization electrons out of the liquid, because the liquid-gas boundary is halfway between them.

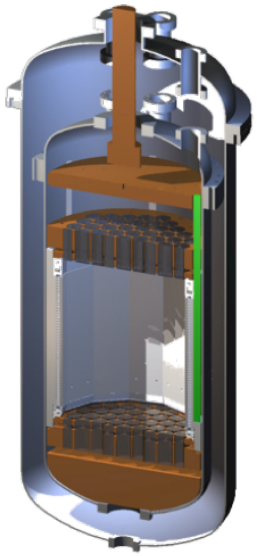

Figure 1: *A cross section rendering of the LUX detector.*

The ionization signal ("S2") is read out with electroluminescent light in the gas region with the top PMT array.

Three-dimensional position of each energy deposition in the LUX detector is reconstructed event-by-event in a two step process. Position perpendicular to the drift field is defined by the pattern of hits in the top PMT array, and position along the drift field is defined by the time between the S1 and S2 light. Position reconstruction in LUX allows for a fiducialization cut and subsequent self shielding of the quietest inner region from the PMT arrays and construction materials, which are much more naturally radioactive than the xenon itself. LUX was designed to have a fiducial mass of 100 kg of xenon, and the first physics result was produced with a fiducial mass of 118 kg. The proportion of each signal in S1 and S2 allow for the discrimination between electron recoil events (which should all be backgrounds) and nuclear recoils (which is how WIMP scatters should be observed). In addition to the shielding against cosmic rays provided by the rock overburden underground, the LUX detector collects data from inside a water shield tank instrumented with twenty

eight-inch Hamamatsu PMTs to serve as an active veto.

3 Previous LUX Science Output

There have been three separate runs in the LUX science program, and preparations are underway for a fourth. LUX runs 1 and 2 were engineering and commissioning runs on the surface [9]. Between the second and third LUX run, the detector was moved underground. LUX run 3 was the first WIMP search run for the LUX experiment, running from April to August of 2013. In October 2013, LUX published its first WIMP search limit based on run 3 data [10]. The LUX run 3 limit (see Figure 2) is the first one to place a spin independent WIMP nucleon scattering limit below a cross section level of 10^{-45} cm^2. This

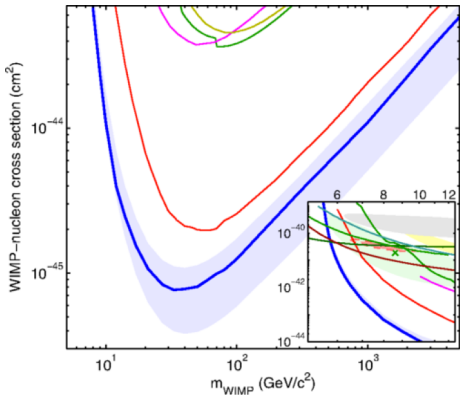

Figure 2: *90% Confidence limits on WIMP nucleon scattering from LUX Run 3 data, Blue (line and band) LUX 2013 result [10]. For comparison, we include limits from: XENON100 (red), ZEPLINIII (magenta), CDMSII (green) and EDELWEISSII (dark yellow). The inset shows limits and results for WIMP nucleon scattering at low mass. The low mass region also includes results (closed regions) from: CoGeNT (orange), CDMSII-Si (green), CRESSTII (yellow), and DAMA-LIBRA (grey).*

limit also excluded (at the 90% confidence level) nearly all of the anomalous results at low WIMP mass from several previous experiments. Much of this success was due to the extensive calibration program for the LUX experiment. For run 3, this included: external sources, internal ^{83m}Kr injections uniformly

distributed throughout the xenon volume, and a tritiated methane injection.

4 Status of the LUX Experiment

At the conclusion of LUX run 3, LUX underwent a series of upgrades and maintenance in preparation for its fourth and final science run. Principally, this involved a wire grid conditioning campaign aimed at increasing the drift and extraction fields in the LUX detector to further enhance performance for run 4. Additionally, bias supplies for the veto PMTs and the process control for xenon circulation and recovery were upgraded. Finally, we included data from a D-D generator to calibrate the low-energy nuclear recoil response of LUX using double scatter events from this nearly monochromatic source of neutrons. The WIMP scattering sensitivity for LUX run 4 will surpass that of run 3 by almost an order of magnitude (to approximately 10^{-46} cm^2), and will conclude the LUX experiment.

5 Plans for the LZ Experiment

Design of a next-generation experiment based on the LUX design has been underway for some time. The collaboration began as a fusion of the LUX and ZEPLIN collaborations (making the new experiment's name "LZ"). A rendering of the LZ detector design is shown in Figure 3. The heart of the detector is a much larger version of the LUX detector, installed in the same water tank. The total mass will be approximately seven tons ($\sim 20\times$ LUX) and the fiducial mass will be five tons ($\sim 50\times$ LUX). In addition to building a larger TPC, several upgrades to the veto system will also be made. The xenon space outside of the TPC will be instrumented to collect scintillation light. There will also be a liquid scintillator veto (gadolinium loaded linear alkyl benzene) outside the xenon cryostat but inside the outer water shield. The larger xenon volume and mode sophisticated veto will increase any potential WIMP signal and lower the background, making LZ's WIMP-nucleon cross section sensitivity approach 10^{-48} cm^2. LZ was recently approved as one of the "Generation 2" dark matter searches by the Department of Energy.

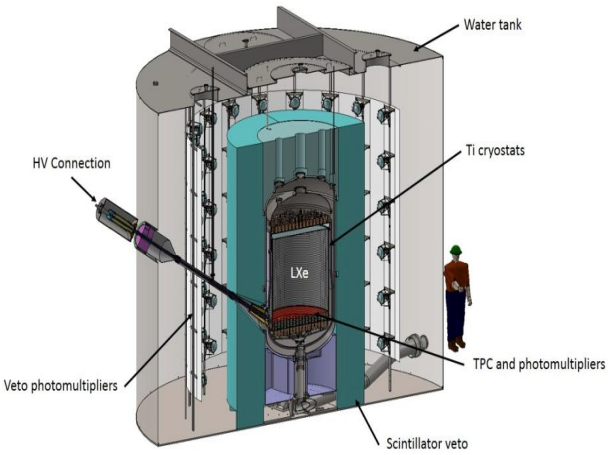

Figure 3: *A cross section rendering of the LZ detector including the TPC, veto, and grid bias feedthroughs.*

6 Conclusions and Discussion

Evidence for the existence of dark matter represents one of the currently most promising avenues for the discovery of physics beyond the Standard Model. While this evidence has been seen in astronomical observations for nearly a century, laboratory evidence continues to elude the scientific community. Two-phase xenon TPC detectors represent one of the most scientifically promising experimental techniques for filling this gap in our understanding of the Universe, and the LUX and LZ collaborations are well positioned to move forward in this endeavor over the next several years.

7 Acknowledgements

This work was partially supported by the U.S. Department of Energy (DOE) under award numbers DE-FG02-08ER41549, DE-FG02-91ER40688, DE-FG02-95ER40917, DE-FG02-91ER40674, DE-NA0000979, DE-FG02-11ER41738, DE-SC0006605, DE-AC02-05CH11231, DE-AC52-07NA27344, and DE-FG01-91ER40618; the U.S. National Science Foundation under award numbers PHYS-0750671, PHY-0801536, PHY-1004661, PHY-1102470, PHY-1003660, PHY-1312561, PHY-

1347449; the Research Corporation grant RA0350; the Center for Ultra-low Background Experiments in the Dakotas (CUBED); and the South Dakota School of Mines and Technology (SDSMT). LIP-Coimbra acknowledges funding from Fundao para a Cincia e Tecnologia (FCT) through the project-grant CERN/FP/123610/2011. Imperial College and Brown University thank the UK Royal Society for travel funds under the International Exchange Scheme (IE120804). The UK groups acknowledge institutional support from Imperial College London, University College London and Edinburgh University, and from the Science and Technology Facilities Council for PhD studentship ST/K502042/1 (AB). The University of Edinburgh is a charitable body, registered in Scotland, with registration number SC005336.

References

1. F. Zwicky. *Helv. Phys. Ac.* **6** (1933) 110.
2. F. Zwicky. *Astr. J.* **86** (1937) 217. doi:10.1086/143864
3. K.G. Begeman, *et al. Mon. Not. Roy. Astr. Soc.*, **249** (1991) 523.
4. Douglas Clowe, *et al. The Astr. J. Lett.* **648** (2006) L109. doi:10.1086/508162. arXiv:astro-ph/0608407
5. Dietrich, *et al. Nature*, **487** (2012) 202
6. G.F. Hinshaw *et al. The Astr. J. Supp.* **208** (2013) 19H. arXiv:1212.5226 [astro-ph.CO]
7. (P.A.R. Ade, *et al.*) *Astr. and Astrophys.* **566** (2014) A54. doi:10.1051/0004-6361/201323003. arXiv:1303.5076 [astro-ph.CO]
8. D. Tytler, J.M. O'Meara, N. Suzuki, and D. Lubin. *Phys. Scr.* **2000** (2000) T85. doi:10.1238/Physica.Topical.085a00012. arXiv:astro-ph/0001318
9. D.S. Akerib *et al.* (LUX Collaboration). *Astr. Part. Phys.* **45** (2013) 34. arXiv:1210.4569 [astro-ph.IM]. doi:10.1016/j.astropartphys.2013.02.001
10. D.S. Akerib *et al.* (LUX Collaboration). *Phys. Rev. Lett.* **112** (2014) 091303. arXiv:1310.8214 [astro-ph.CO]. doi:10.1103/PhysRevLett.112.091303

Frascati Physics Series Vol. 58 (2014)
Frontier Objects in Astrophysics and Particle Physics
May 18-24, 2014

Recent results from the XENON100 experiment and future goals of the XENON project

Marcello Messina,
Columbia University, Physics Department, 530 West 120th Street New York, NY 10027
on behalf of the
XENON collaboration

Abstract

The XENON experiment is dedicated to searching for evidence of dark matter particles interacting directly with ordinary matter, with particular focus on the Weakly Interacting Massive Particle (WIMP). The past XENON experimental program consisted of two detectors, with similar design but increasing mass, at the Gran Sasso underground laboratory in Italy. XENON100, the most recently operated detecor, led the field until 2013, putting a limit on the WIMP-nucleon cross section of $2 \times 10^{-45}\,\mathrm{cm}^2$ (90% C.L.) at a WIMP mass of 55 GeV. The last phase of the project foresees the construction of XENON1T, a detector with a total Xe mass of three tonnes. Construction of XENON1T started in 2013, and commissioning is expected by the Summer of 2015.

1 Introduction

The XENON dark matter program is devoted to the search for Weakly Interacting Massive Particles (WIMPs) by detecting particles created by the scattering of a WIMP off a of xenon nucleus [1]. So far two detectors have been built: XENON10 [3] operated at the Laboratori Nazionali del Gran Sasso (LNGS) from 2006 - 2007, and XENON100 [2] which is still taking data after continuous operation at LNGS since 2008. XENON100 was designed to fit inside the improved passive shield built at LNGS for XENON10. Beyond an increase in mass, the success of XENON100 is based on careful selection of only low radioactivity detector components [4], the distillation of the Xe with a dedicated column [2] to reduce the contamination of radioactive ^{85}Kr to a level of few parts per trillion (ppt) for Ru12, while it was 19 ppt for Run10, and the placement of only the lowest radioactive components near the target volume.

The next generation detector, XENON1T, will have an instrumented mass of roughy two tonnes, and will have an expected sensitivity to the spin-independent WIMP-nucleon cross section of $2 \times 10^{-47}\,\mathrm{cm}^2$.

The construction of XENON1T started in 2013, and it is expected to enter its first commissioning phase by Summer 2015.

2 The principle of a dual-phase TPC

Fig. 1 shows a schematic of the XENON two-phase (liquid-gas) time projection chamber (TPC), and a sketch of the signals produced by the electronic and nuclear recoils. Any particle interaction in the liquid Xe (LXe) produces direct scintillation photons, labelled as S1, and ionization electrons. An electric field applied across the LXe volume drifts the ionization electrons from the interaction point towards the liquid-gas interface. Subsequently, the electrons are extracted into the gas phase, where they undergo proportional scintillation (referred to as the S2 signal) [7]. Both the S1 and S2 signals are detected by means of photomultiplier tubes (PMTs) located below the cathode (bottom array), and in the gas phase (top array). The TPC can resolve the full, three-dimensional position of the interaction vertex using the time difference between the S1 and S2 signals (which, with knowledge of the electron drift velocity in LXe, gives the z-coordinate) and the localized S2 signal measured in the top PMT array (which gives the x- and y-coordinates). This feature is used

to define a fiducial volume inside which the expected signal-to-background is significantly enhanced , due to the excellent stopping power of the outer layers of LXe. Further, the ratio of the size of the S2 and S1 signals is significantly different for electronic recoils (from γ and β scatters) and nuclear recoils (from scatters with a neutron or WIMP candidate), providing powerful rejection of background interactions from electromagnetically interacting particles [8]. The irreducible background from neutrons can be estimated *a priori* and reduced with passive shielding, an active muon veto counter to reduce muon-spallation neutrons, and by selecting components with the lowest possible amount of radioactive contaminants.

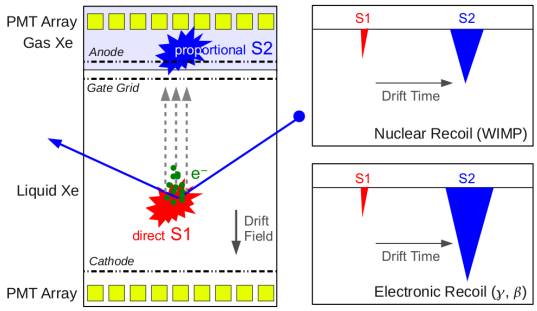

Figure 1: Schematic drawing of a generic xenon TPC and the two signals measured by it. (Left) Sketch of the TPC and the definition of the S1 and S2 signals. (Right) Sketch of the signal amplitudes for nuclear recoils originating from WIMPs and neutrons or by electronic recoils from γ and β background.

3 The XENON detectors

In the following sections, some details will be given about the XENON100 detector and its on-going analyses, and about XENON1T, currently under construction.

3.1 The XENON100 detector

The XENON100 TPC is defined by a cylindrical field cage with a height of 30.5 cm and a radius of 15.3 cm. The TPC is designed to contain 62 kg of LXe in its instrumented target A total mass of 99 kg of LXe instrumented with

PMTs surround the field cage and acts as a veto detector. The instrumented target volume is optically separated from the veto by means of 24 interlocking PTFE panels that have very high reflectivity (> 0.98) at the LXe scintillation wavelength. The field cage is closed at the bottom by the cathode, and on top by the gate grid.

A layer of xenon gas above the liquid is obtained using system akin to a diving bell, which allows precise control of the liquid-gas interface level. Two arrays of Hamamatsu R8520-06-Al 1" square PMTs, specially selected for low radioactivity [9], detect light in the TPC. 80 PMTs are located below the cathode, and are devoted mainly to measuring the S1 signal. Similarly, 98 PMTs are located in the gas phase, primarily to detect the S2 signal. A layer of LXe about 4 cm thick surrounds the TPC on all sides and is observed by 64 additional PMTs of the same type. The TPC is mounted in a double-walled 316-T-stainless-steel cryostat made of components that were screened to low level of radioactivity.

Due to the inherent radioactive contamination of the cryogenics system, ceramic feedthroughs, and other components, the detector is cooled remotely, and all parts with a known high radioactive contamination are installed far from the TPC itself, outside of the passive shield. The XENON100 experiment is installed underground at LNGS, with a rock overburden of 3600 m water-equivalent that reduces the surface muon flux by a factor of 10^6. To further reduce the environmental background an additional shield of copper, polyethylene, and lead was designed [3]. The entire shield rests on a 25 cm thick slab of polyethylene. An additional outer layer of 20 cm of water was added on top and on three sides of the shield to further reduce the neutron background.

3.2 Latest results of XENON100

Prior to any physics analysis, the response of the detector to nuclear recoils is studied in detail and the scale of the energy released to the nucleus is defined. In practice, the correspondence between the number of photoelectrons (PE) measured and the actual energy of the recoil is established. Separate measurements are performed to set the energy scale for nuclear and electronic recoils, the difference being in the amount of quenching of the signal in the two processes [15].

After the response of the detector was sufficiently well known, through

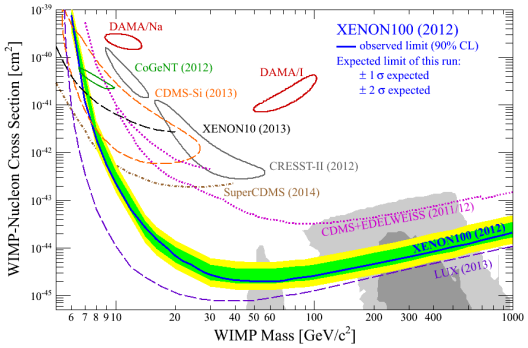

Figure 2: The best limit published by the XENON100 experiment on the spin-independent WIMP-nucleon interaction cross section is reported together with other exclusion or allowed regions, based on other experimental measurements. The gray areas in the lower right corner of the plot indicate regions of the parameter space favored by various theoretical models. The plot is adapted from [2].

dedicated calibration runs, an analysis on 225 days of blinded physics data was performed, and the results published in [2]. Two candidate events were observed in the dark matter signal region. Those events were consistent with an upward background fluctuation at 26% probability, given the expected background of (1.0 ± 0.2) events. By interpreting the observation as a null result, a limit of 2×10^{-45} cm^2 at 55 GeV and 90% C.L. was obtained for a spin-indendent WIMP-nucleon interaction (see Fig. 2) [2]. That limit has only recently been superseded by a measurement from the LUX collaboration [6], as also shown in Fig. 2. The XENON100 and LUX exclusion limits are in tension with claimed observations coming from DAMA [10], CRESST [11], CDMS [12] and CoGeNT [13].

In parallel, with on-going data taking at XENON100, additional analyses have been performed on the already unblinded data. As one example, an analysis of the data assuming a spin-dependent WIMP-nucleon interaction was pursued in [14]. In this model, WIMPs couple to an unpaired nucleon in the nucleus, and only nuclei with an odd number of nucleons are expected to yield observable signals. Xenon is a good target for such a measurement, as there are two naturally occurring isotopes with an odd number of nucleons: ^{129} Xe (spin-1/2) and ^{131}Xe (spin-3/2). They comprise 26.2% and 21.8%,

respectively, of the xenon in XENON100. Limits extracted from this analysis are very competitive with others, especially in the WIMP-neutron cross section where the most stringent published limit was set.

Beyond standard WIMP analyses, the low background of XENON100 allows for the study of axion-like dark matter by exploiting the axio-electric effect, as suggested in [17]. Two types of axion signals were analyzed using the observed S1 signal spectrum: solar axions, with an meV-scale mass, and Axion Like Particles (ALPs), with a keV-scale mass. In one case, a continuum energy spectrum of the electron is expected, while in the other case, the electron is expected to have kinetic energy equal to the mass of the axion minus the binding energy of the electron. In both cases, a competitive limit was set on the coupling constant between the electron and the axion (g_{Ae}) [18]. This result represents the first axion search using a dual-phase TPC.

3.3 The XENON1T detector

XENON1T will be the next step in the search for dark matter. The increase in total mass (to 3 tonnes), coupled with the reduction in background levels to 6×10^{-5} events/kg/day/keV$_{\rm ee}$, allow for two order of magnitude imporvement in sensitivity with respect to XENON100. The sensitivity curve expected is shown in Fig. 3. To stop neutrons from reaching the fiducial volume, and to tag cosmic muons (and associated neutrons), the TPC and its cryostat are immersed in 700 t of water contained in a stainless steel tank. The tank is equipped with an active muon veto with 84 PMTs, allowing a 99% efficiency in tagging crossing muons and 74% efficiency for showering events. The expected total background inside the fiducial volume is less than 0.5 event per year.

It is worth noticing that XENON1T has been designed to allow for the rapid deployment of a new detector with a total xenon mass of up to seven tonnes (termed XENON1T upgrade). This new detector can be realized using the same cyogenic and purification infrastructure and will be housed in the existing XENON1T water tank - only modifications to the inner vessel of the cryostat and the TPC itself will be needed.

The construction of XENON1T is progressing rapidly. Fig. 4-left shows the water tank and the service building, which will house the main experimental subsystems. Fig. 4-right shows the cryostat support structure which will hold the cryostat at the center of the water volume.

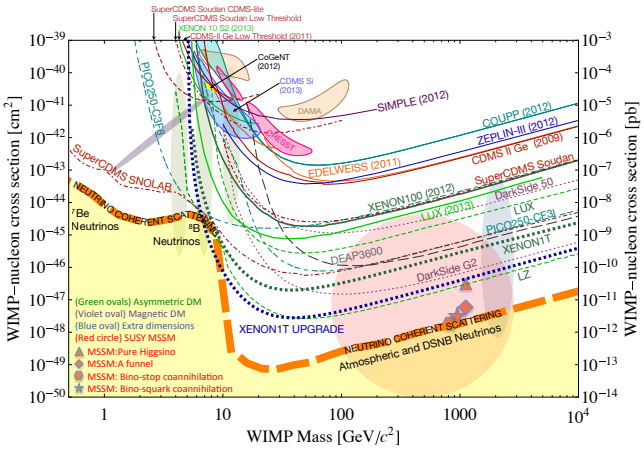

Figure 3: The sensitivity reach of XENON1T and its upgrade is shown along with current experimental results.

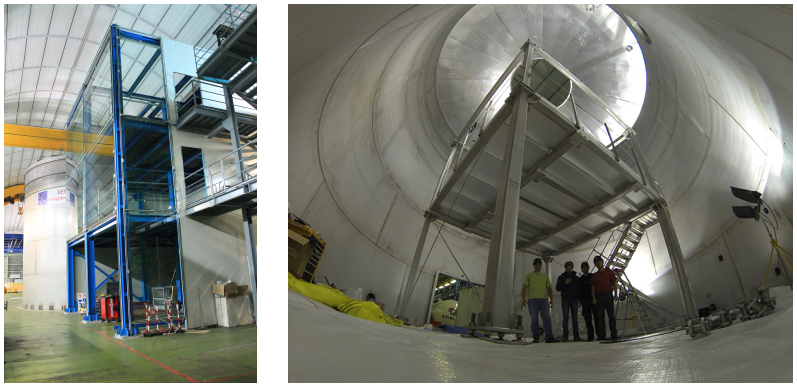

Figure 4: The two pictures of the on-going construction of XENON1T. (Left) The muon veto water tank (completed in the fall of 2013) and the accompanying service building (under construction). (Right) The cryostat support structure installed in the water tank.

4 Conclusion

We have presented the status of the XENON dark matter program, highlighting both recent analysis results from XENON100 and prospects for the next

generation detector, XENON1T, and its envisioned upgrade. The XENON collaboration has been a leader in the field of dark matter direct detection for many years, and thanks to the XENON1T project, the collaboration will look to stay at the forefront of this exciting and challenging field.

References

1. M.W. Goodman, E. Witten, Phys. Rev. D **31** 3059, (1985).
2. E. Aprile *et al*, Phys. Rev. Lett. **109**, 181301, (2012).
3. E. Aprile *et al.*, Astropart. Phys. **34**, 679, (2011).
4. E. Aprile *et al.*, Astropart. Phys. **35** 43, (2011).
5. E. Aprile *et al.*, Phys. Rev. Lett. **97**, 081302, (2006).
6. Phys. Rev. Lett. **112**, 091303, (2014)
7. B.A. Dolgoshein, V.N. Lebedenko, B.U. Rodionov,JETP Lett. **11**, 513, (1970).
8. E. Aprile *et al.*, Phys. Rev. Lett. **97**, 081302 (2006).
9. E. Aprile *et al.*, Astropart. Phys. **35** 43, (2011).
10. R. Bernabei *et al.*, Eur. Phys. J. C **56**, 333-355 (2008).
11. G.Angloher *et al.*, Eur. Phys. J. C 72, 1971 (2012).
12. R. Agnese *et al.*, Phys. Rev. Lett. 111, 251301 (2013).
13. C.E. Aalseth *et al.*, Phys. Rev. D**88** 012002 (2013).
14. E. Aprile *et al.*, Phys. Rev. Lett. 111 (2013) 021301
15. E. Aprile *et al.*, Phys. Rev. D **88**, 012006 (2013).
16. E. Aprile *et al.*, Phys. Rev. C **84**, 045805 (2011).
17. K. Arisaka *et al.*, Astropart. Phys. **44** ,59 (2013).
18. E. Aprile *et al*, submitted to Phys. Rev. D (2014).

Frascati Physics Series Vol. 58 (2014)
Frontier Objects in Astrophysics and Particle Physics
May 18-24, 2014

SEARCH FOR GAMMA-RAY SPECTRAL LINES WITH THE FERMI LARGE AREA TELESCOPE AND STATUS OF THE 135 GEV FEATURE

Andrea Albert
On Behalf of the *Fermi*-LAT Collaboration
W. W. Hansen Experimental Physics Laboratory,
Kavli Institute for Particle Astrophysics and Cosmology,
Department of Physics and SLAC National Accelerator Laboratory,
Stanford University, Stanford, CA 94305, USA

Abstract

An overwhelming amount of evidence suggests that non-baryonic dark matter (DM) constitutes $\sim 27\%$ of the energy density of the Universe. Particle DM candidates like Weakly Interacting Massive Particles (WIMPs) and gravitinos are promising since they may produce monochromatic gamma rays via annihilation or decay detectable by the *Fermi* Large Area Telescope (*Fermi* LAT). The detection of a gamma-ray spectral line is often considered a "smoking gun" signature of DM interactions, which would also indicate the existence of physics beyond the Standard Model. I will present results from recent searches for monochromatic lines from 100 MeV to 300 GeV by the *Fermi*- LAT Collaboration, and discuss the systematic uncertainties involved.

1 INTRODUCTION

Astrophysical observations imply that $\sim 27\%$ of the energy density of the Universe is non-baryonic cold dark matter (DM) [1)]. While substantial astro-

physical evidence exists for DM through its gravitational interaction, little is known about the composition of the DM or its properties, and many theoretical candidates have been proposed. A popular class of models [2, 3, 4] predict the DM is a weakly interacting massive particle (WIMP), which we denote by χ. Another particle DM candidate is the gravitino (denoted by $\Psi_{3/2}$) [5]. If we assume WIMPs explain all of the DM in the Universe and are a thermal relic (i.e. were in thermal equilibrium in the early Universe), then we expect them to have a mass in the GeV to TeV range and an s-wave annihilation cross section of $\sim 3 \times 10^{-26}\,\mathrm{cm}^3\,\mathrm{s}^{-1}$ (see Ref. [6] for a recent, precise calculation of $\langle\sigma v\rangle$). Alternatively, the relic density of gravitinos from thermal production in the early Universe can account for all the observed DM today for gravitino masses above $\mathcal{O}(1)\,\mathrm{keV}$ [7]. In these searches, one typically assumes a single-particle DM hypothesis, though in reality multiple DM species may exist.

If such a DM particle exists and annihilates into standard model particles with the thermal relic cross section, then we should be able to detect signatures of such interactions in regions of high DM density. One such signature would be the creation of γ rays with a continuum of energies via annihilations into intermediate states (e.g. $\chi\chi \to b\bar{b}$). As the original annihilation (and subsequent daughter) particles propagate, γ rays will be produced. This smooth continuum signature is difficult to distinguish from the γ-ray emission from other astrophysical processes. Therefore, it is challenging to search for potential DM γ-ray signals in astrophysically complex regions of the sky like the Galactic Center (GC).

A relatively "clean" (i.e. containing negligible background) γ-ray DM signature would be the production of γ-ray spectral lines. DM annihilation directly into γ rays ($\chi\chi \to \gamma\gamma$) will produce monochromatic γ rays with $E_\gamma = m_\chi$. Note that DM annihilation (or decay) into a γ ray and a neutral particle (e.g. $\Psi_{3/2} \to \gamma\nu$) will also produce a monochromatic signal at a shifted energy. No other astrophysical processes are expected to produce such a narrow γ-ray spectral feature. However, these processes are "loop-suppressed" and therefore expected to have a low branching fraction.

There are systematic uncertainties that may induce a line-like feature that could either fake or mask a signal. When searching for spectral lines below ~ 10 GeV with *Fermi*-LAT data, the statistical uncertainties become so small that the systematic uncertainties dominate.

Here we present results from two recent searches for γ-ray spectral lines by the *Fermi*-LAT Collaboration. The first searched for lines from 5 GeV to 300 GeV in 5 regions on interest (ROIs) of the sky and included a detailed study of the reported line-like feature at $\sim$ 135 GeV in the GC [8]. The second searched for lines from 100 MeV to 10 GeV in 2 ROIs and incorporated systematic uncertainties consistently in the fitting procedure [9]. We refer the

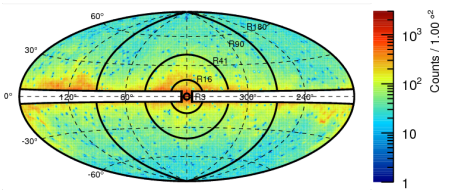

Figure 1: Counts map for the high-energy line search dataset binned in $1^\circ \times 1^\circ$ spatial bins in the R180 ROI, and plotted in Galactic coordinates using the Hammer-Aitoff projection. Also shown are the outlines of the other ROIs (R3, R16, R41, and R90) used in this search. Same as Fig. 2 in Ref. [8]

reader to those works for details regarding the results summarized here.

2 FERMI-LAT INSTRUMENT AND DATA SELECTION

Both searches use data collected by the Large Area Telescope on board the *Fermi* γ-ray space telescope (*Fermi* LAT). The *Fermi* LAT is a pair-conversion telescope that observes the entire γ-ray sky from 20 MeV to >300 GeV every 3 hours (while operating in normal survey mode). Details regarding the *Fermi* LAT and its performance can be found in Refs. [10, 11]. Additionally, a brief summary of the *Fermi*-LAT instrument and event selections can be found in Sec. 2 of Ref [8]. Both searches obtained their datasets using the `P7REP_CLEAN` event selection. Additionally, events with a zenith angle >100° were removed from both datasets to remove excess emission from the bright limb of the Earth.

The high-energy line search dataset contained events taken in the first 3.7 years of operation (2008-08-04 to 2012-04-12) in the energy range 2.6 to 541 GeV. Bright γ-ray point sources from the 2 year *Fermi* point-source catalog [12] were masked. Four different ROIs were obtained from optimizing the signal-to-noise ($(S)/\sqrt{B}$) for DM annihilation assuming 4 different Galactic DM density profiles: contracted NFW ($\gamma = 1.3$), Einasto [13], NFW [14], and isothermal [15] (see Sec.III of Ref. [8] for details). Additionally, a large full-sky (minus the background-dominated off-center Galactic plane) ROI was used to search for a monochromatic signal from DM decay. We call the ROIs R3, R16, R41, R90, and R180 respectively. Figure 1 shows all 5 ROIs used in the high-energy line search.

The low-energy line search dataset contained events taken in the first 5.2 years of operation (2008-08-04 to 2013-10-15) in the energy range 56.5 MeV to 11.5 GeV. Known point sources were not masked in this search since below ~ 1 GeV the point spread function is $> 1^\circ$, which would cause us to mask most

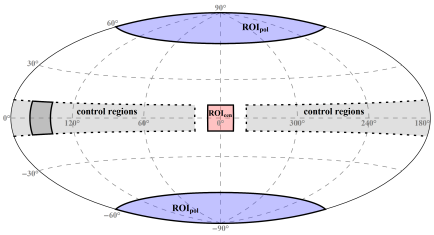

Figure 2: Skymap of ROIs used in the low-energy line search; plotted in Galactic coordinates using the Hammer–Aitoff projection. The region $\mathrm{ROI_{pol}}$ (blue) is optimized for the signal-to-background ratio in the case of DM decay, while the region $\mathrm{ROI_{cen}}$ (red) is optimized for the signal-to-background ratio in the case of DM annihilation. The dashed line encloses the area for the control regions along the Galactic plane (light grey), while the grey region is an example of one of the 31 control regions used in the low-energy line search. Same as Fig. 2 in Ref. [9].

of our search region (especially in the GC). The corresponding uncertainty from this choice is incorporated consistently into the fitting procedure along with systematic uncertainties from background modelling, energy-dependent variations in the *Fermi*-LAT effective area, and residual cosmic-ray contamination in the γ-ray dataset. The expected level of these systematic uncertainties was estimated by fits for line-like features in control regions. Two ROIs were optimized for DM annihilation assuming an Einasto profile [13] and DM decay. We call them $\mathrm{ROI_{cen}}$ and $\mathrm{ROI_{pol}}$ respectively. The optimization criteria differed slightly from that used in the high-energy line search since this search was limited by systematic uncertainties as opposed to statistical uncertainties. Figure 2 shows the 2 ROIs used in the low-energy line search as well as the control regions along the Galactic Ridge.

3 SPECTRAL LINE ANALYSIS

3.1 HIGH-ENERGY LINE SEARCH RESULTS

We performed a maximum likelihood analysis to search for spectral lines from 5 to 300 GeV in 5 ROIs. We fit in sliding energy windows of $\pm 6\sigma_E(E_\gamma)$, where $\pm\sigma_E(E_\gamma)$ is the energy resolution (68%) at the fit energy. Since we fit in narrow energy windows, we approximate the background spectrum to be a power law and allow the index to float in the fit. We use an energy dispersion model that incorporates the quality of the energy reconstruction on an event-by-event basis (see Sec.IV of Ref. [8] for more details). We find no significant

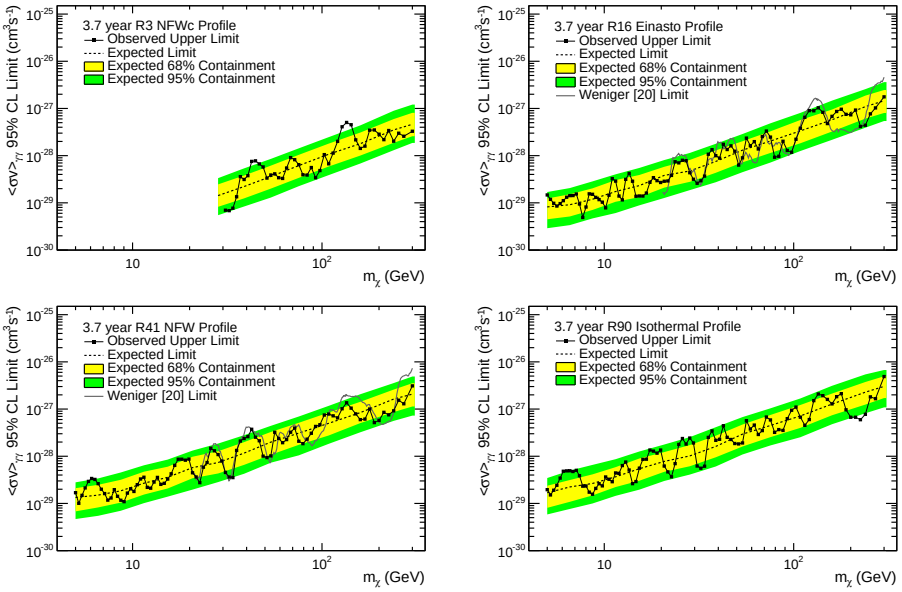

Figure 3: 95% CL $\langle \sigma v \rangle_{\gamma\gamma}$ upper limits for each DM profile considered in the corresponding optimized ROI. Yellow (green) bands show the 68% (95%) expected containment derived from 1000 single-power law (no DM) MC simulations. The dashed lines show the median expected limits from those simulations. The solid gray line shows the limits derived by [16] (an independent search for spectral lines from 20−300 GeV) when comparable ROIs and identical DM density profiles were used. Same as Fig. 10 from Ref. [8]

detections an therefore set limits on the DM cross section for annihilation to γ rays (see Fig. 3). Note that the green and yellow bands show the 68% and 95% containment of the expected sensitivity based on statistical fluctuations only. We also compare our limits to those obtained by an independent analysis [16] and note that similar results were obtained in both analyses.

Our most significant fit occurred in our smallest ROI (R3, a 3° GC ROI) at 135 GeV. This is the same feature reported in earlier works at 130 GeV [17, 16], but the energy has shifted due to the use of a dataset reprocessed with updated calorimeter calibration constants. The significance of the 135 GeV feature is less than other works (1.5σ global) and the feature in the data is significantly narrower than the expected *Fermi*-LAT energy dispersion. When allowing a scale factor (between 0 and 1) on the width of the energy dispersion model to

float in the fit, a value $s_\sigma = 0.32^{+0.22}_{-0.07}$ was preferred where the quote errors are at the 95% confidence level. This points to a non-physical explanation of the feature like a statistical fluctuation. Additionally, we did a cross check using data from the bright Earth's limb. These are γ rays produced by cosmic-ray interactions in the upper atmosphere of the Earth. Above 3 GeV, we expected the energy spectrum to follow a simple power law and contain no line-like features. Therefore this is a very useful control region for our line search. We detect a small line-like feature in the Earth Limb at 135 GeV, which seems to be caused by energy-dependent variations in the *Fermi*-LAT effective area. While this feature in the Limb cannot account for all of what is seen in the GC, it does suggest that a systematically induced line-like feature may be partially responsible for the GC feature. We also show that with increased exposure (4.4 years vs. 3.7 years), the significance of the 135 GeV feature in the GC is shrinking rather than growing. The local significance of the 135 GeV feature in R3 was 3.2σ in the 3.7 year dataset and 2.9σ in the 4.4 year dataset. This supports the hypothesis that the feature is predominantly a statistical fluctuation.

3.2 LOW-ENERGY LINE SEARCH RESULTS

We perform a maximum likelihood analysis to search for spectral lines from 100 MeV to 10 GeV in 2 ROIs. This search differs from the one summarized above because the statistical uncertainty on the number of signal counts is much less than the systematic uncertainty (the search is dominated by systematic uncertainties). This is because the number of events in each fit window is very large. Consequently, any small deviation from a power-law in the background spectra can result in a largely statistically significant, but false, line-like feature. We fit in sliding energy windows of $\pm 2\sigma_E(E_\gamma)$, which is narrower than in the high-energy line search. As the window gets wider, the systematic uncertainty from modelling the background as a power law increases, which the statistical uncertainty decreases. This narrower window is optimal at $\sim$ 1 GeV in the case where the fit is dominated by systematic uncertainties.

In both the high-energy and the low-energy line search, we chose to quantify the most relavant systematic uncertainties in terms of a "fractional signal" ($\delta f = \frac{\delta n_{sig}}{\mathrm{b_{eff}}}$). $\mathrm{b_{eff}}$ is given by

$$b_{\mathrm{eff}} = \int_{E_i^-}^{E_i^+} dE \, \frac{\mathcal{D}_{\mathrm{eff}}(E|E_\gamma)\alpha E^{-\Gamma}\mathcal{E}(E)}{\alpha E^{-\Gamma}\mathcal{E}(E) + \mathcal{D}_{\mathrm{eff}}(E|E_\gamma)} \,, \tag{1}$$

where α and γ are determined from a power-law only fit to the data (with $n'_{\mathrm{sig}} = 0$ fixed). The most relevant systematic uncertainties are those that would mask or induce a line-like feature. In the fitting procedure for the low-energy line search, we include δf in our likelihood definition as a nuisance parameter.

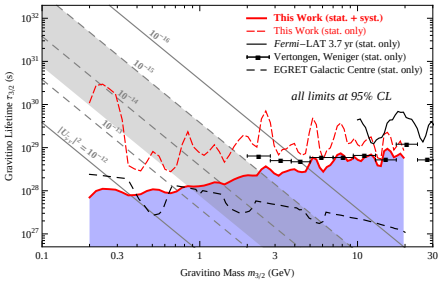

Figure 4: Parameter space of decaying gravitino DM given in terms of the gravitino lifetime and the gravitino mass. The diagonal band shows the allowed parameter space for gravitino DM in the $\mu\nu$SSM. The numbers on the solid and dashed lines show the corresponding value of the photino–neutrino mixing parameter, as discussed in [9]. The theoretically most favored region is colored in grey. We also show several 95% CL lower limits on the gravitino lifetime coming from γ-ray observations. The blue shaded region is excluded by the limits derived in this work. Same as Fig. 6 in [9]

.

We limit the size of the nuisance parameter with a Gaussian constraint where the width is determined from fits in control regions ($\sigma_{sys} = \frac{\delta f}{\mathrm{b_{eff}}}$).

To estimate δf, we perform fits in $20^\circ \times 20^\circ$ ROIs along the Galactic Plane, excluding the 5 center-most squares. This is a region of the sky where the non-DM diffuse γ-ray emission is expected to dominate over any potential DM line signal. Therefore, any lines observed in this region would be due to systematic uncertainties like modelling the background as a power law, energy-dependent variations in the effective area, point-source contamination, and residual cosmic-ray contamination.

No spectral lines were observed and 95% confidence level upper limits on the particle DM annihilation cross section and lower limits on the particle DM decay lifetime were derived. We present the lifetime limits in the context of the DM being a gravitino in the supersymmetric extension of the Standard Model called $\mu\nu$SSM [18] in Fig. 4.

4 SUMMARY

The *Fermi*-LAT Collaboration has searched for γ-ray spectral lines from DM annihilation to decay from 100 MeV to 300 GeV. No spectral lines have been detected and bounds on both the DM annihilation cross section and decay lifetime have been determined. In the case of the low-energy line search, these

limits incorporate systematic uncertainties consistently in the limits for the first time.

All *Fermi*-LAT analyses, including these specific searches, are expected to improve with increased exposure and understanding of the instrument.

5 ACKNOWLEDGMENTS

The *Fermi*-LAT Collaboration acknowledges support from a number of agencies and institutes for both development and the operation of the *Fermi* LAT as well as scientific data analysis. These include NASA and DOE in the United States, CEA/Irfu and IN2P3/CNRS in France, ASI and INFN in Italy, MEXT, KEK, and JAXA in Japan, and the K. A. Wallenberg Foundation, the Swedish Research Council and the National Space Board in Sweden. Additional support from INAF in Italy and CNES in France for science analysis during the operations phase is also gratefully acknowledged.

References

1. **Planck Collaboration** Collaboration, P. Ade et al., *Planck 2013 results. XVI. Cosmological parameters*, arXiv:1303.5076.

2. S. P. Martin, *A Supersymmetry primer*, hep-ph/9709356.

3. D. Chung et al., *The Soft supersymmetry breaking Lagrangian: Theory and applications*, *Phys.Rept.* **407** (2005) 1–203, [hep-ph/0312378].

4. L. Pape and D. Treille, *Supersymmetry facing experiment: Much ado (already) about nothing (yet)*, *Rept.Prog.Phys.* **69** (2006) 2843–3067.

5. K.-Y. Choi, D. E. López-Fogliani, C. Muñoz, and R. R. de Austri, *Gamma-ray detection from gravitino dark matter decay in the $\mu\nu$SSM*, *JCAP* **1003** (2010) 028, [arXiv:0906.3681].

6. G. Steigman, B. Dasgupta, and J. F. Beacom, *Precise Relic WIMP Abundance and its Impact on Searches for Dark Matter Annihilation*, *Phys.Rev.* **D86** (2012) 023506, [arXiv:1204.3622].

7. H. Pagels and J. R. Primack, *Supersymmetry, Cosmology and New TeV Physics*, *Phys.Rev.Lett.* **48** (1982) 223.

8. **Fermi-LAT Collaboration** Collaboration, M. Ackermann et al., *Search for Gamma-ray Spectral Lines with the Fermi Large Area Telescope and Dark Matter Implications*, *Phys.Rev.* **D88** (2013) 082002, [arXiv:1305.5597].

9. A. Albert, G. A. Gomez-Vargas, M. Grefe, C. Munoz, C. Weniger, et al., *Search for 100 MeV to 10 GeV gamma-ray lines in the Fermi-LAT data and implications for gravitino dark matter in the $\mu\nu$SSM*, *Submitted to JCAP* (2014) [arXiv:1406.3430].

10. ***Fermi*-LAT Collaboration** Collaboration, W. B. Atwood et al., *The Large Area Telescope on the Fermi Gamma-Ray Space Telescope Mission*, ApJ **697** (June, 2009) 1071–1102, [arXiv:0902.1089].

11. ***Fermi*-LAT Collaboration** Collaboration, M. Ackermann et al., *The Fermi Large Area Telescope on Orbit: Event Classification, Instrument Response Functions, and Calibration*, ApJS **203** (Nov., 2012) 4, [arXiv:1206.1896].

12. ***Fermi*-LAT Collaboration** Collaboration, P. L. Nolan et al., *Fermi Large Area Telescope Second Source Catalog*, *Astrophys.J.Suppl.* **199** (2012) 31, [arXiv:1108.1435].

13. J. F. Navarro et al., *The diversity and similarity of simulated cold dark matter haloes*, MNRAS **402** (Feb., 2010) 21–34, [arXiv:0810.1522].

14. J. F. Navarro, C. S. Frenk, and S. D. M. White, *The Structure of Cold Dark Matter Halos*, ApJ **462** (May, 1996) 563, [astro-ph/].

15. J. N. Bahcall and R. M. Soneira, *The universe at faint magnitudes. I - Models for the galaxy and the predicted star counts*, ApJS **44** (Sept., 1980) 73–110.

16. C. Weniger, *A Tentative Gamma-Ray Line from Dark Matter Annihilation at the Fermi Large Area Telescope*, *JCAP* **1208** (2012) 007, [arXiv:1204.2797].

17. L. Bergstrom, G. Bertone, J. Conrad, C. Farnier, and C. Weniger, *Investigating Gamma-Ray Lines from Dark Matter with Future Observatories*, *JCAP* **1211** (2012) 025, [arXiv:1207.6773].

18. D. López-Fogliani and C. Muñoz, *Proposal for a supersymmetric standard model*, *Phys.Rev.Lett.* **97** (2006) 041801, [hep-ph/0508297].

Frascati Physics Series Vol. 58 (2014)
Frontier Objects in Astrophysics and Particle Physics
May 18-24, 2014

ARE WE REALLY SEEING DARK MATTER SIGNALS FROM THE MILKY WAY CENTER?

Germán A. Gómez-Vargas
Instituto de Fisíca, Pontificia Universidad Católica de Chile
INFN, Sezione di Roma "Tor Vergata"

Abstract

The center of the Milky Way is one of the most interesting regions of the γ-ray sky because of the potential for indirect dark matter (DM) detection. It is also complicated due to the many sources and uncertainties associated with the diffuse γ-ray emission. Many independent groups have claimed a DM detection in the data collected by the Large Area Telescope on board the Fermi γ-ray Satellite from the inner Galaxy region at energies below 10 GeV. However, an exotic signal needs to be disentangled from the data using a model of known γ-ray emitters, i.e. a background model. We point out that deep understanding of background ingredients and their main uncertainties is of capital importance to disentangle a dark matter signal from the Galaxy center.

1 Introduction

The Fermi Large Area Telescope (*Fermi*-LAT), the main instrument of the Fermi satellite, which has been in orbit since June 11, 2008 [1)], performs γ-ray measurements covering an energy range from $\sim$ 20 MeV to $>$ 300 GeV over the whole celestial sphere. The *Fermi*-LAT has detected point and small extended sources, e.g. blazars, supernova remnants (SNRs) and pulsars [2)], and a strong diffuse component in the whole sky first observed by the OSO-3 satellite in the inner Galaxy region [3)]. See images of the region around the Galaxy center at different energies as seen by *Fermi*-LAT in figure 1. The main contribution of the emission detected in the direction of the inner Galaxy is made of: outer Galaxy, true inner Galaxy, foreground emission, unresolved sources, point or small extended sources, extragalactic emission, possible dark matter (DM) contribution, and cosmic ray (CR) instrumental background; see lower right panel of figure 1.

The possible DM contribution to γ-ray data in the inner Galaxy direction can be calculated convolving some fundamental characteristics of DM candidates with the distribution of DM, ρ, as predicted by cosmological N-body simulations. The basic characteristics of DM candidates relevant for γ-ray calculations are: DM mass m_{DM}, thermal average of DM-Standard Model (SM) cross section times DM relative velocity $\langle\sigma_{ann}v\rangle$ and the number of γ rays produced per annihilation N_γ[1]. In this way we can calculate the flux of DM-induced γ rays:

$$\frac{d\Phi_\gamma}{dE}(E) = \frac{\langle\sigma_{ann}v\rangle}{8\pi m_\chi^2}\sum Br^i\frac{dN_\gamma^i}{dE}(E)\int_{\Delta\Omega}d\Omega\int d\lambda\rho^2(\lambda,\Psi). \quad (1)$$

The DM density ρ integrated over the line of sight λ and the angular region of the sky $\Delta\Omega$ is the so called *J-factor*. Assuming that DM is made of weakly interacting massive particles (WIMPs) produced thermally in the early universe, the value of $\langle\sigma_{ann}v\rangle$ must be $\approx 3\times10^{-26}$ cm^3/s to produce observed DM relic abundance. The largest value of the J-factor is in the Galactic Center, where due to the large uncertainty in ρ, DM can either, overshoot data or only contribute modestly to the observed emission. Using the former possibility the thermal cross section was excluded for a large range of m_{DM} [4)]. In the latter

[1]assuming that DM particle is stable

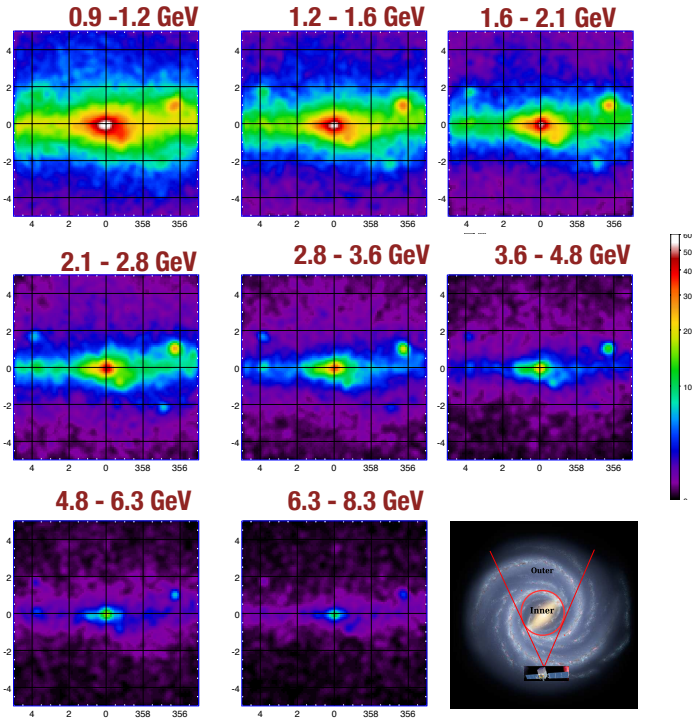

Figure 1: *Fermi-LAT view of the Milky Way center in different energy bands (color scale is the same in all maps). In the lower right panel a schematic of the GC view by the Fermi-LAT.*

case, DM-induced γ rays would appear as an exotic contribution in *Fermi*-LAT data of the region around the GC. We need to understand the non-exotic contributions, i.e. the background, in order to disentangle a possible DM signal.

Many independent groups have claimed a DM detection in the data collected by the Fermi-LAT from the GC region [5, 6, 7, 8, 9, 10, 10, 11, 12, 13]. This source may be due to DM particles annihilating, but other plausible phenomena may be responsible for this. All these analyses are based on the subtraction of background models: diffuse interstellar emission and point sources [2], from the data. To build these diffuse models there are two ap-

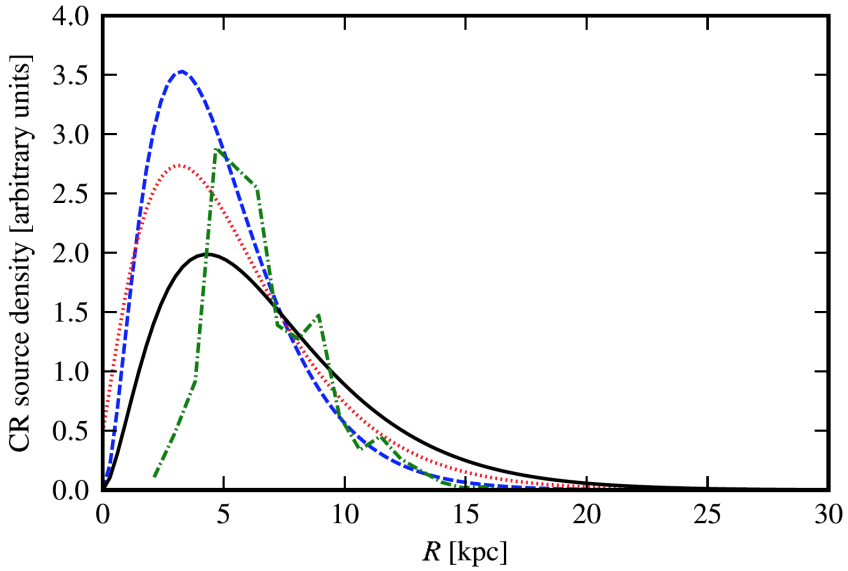

Figure 2: Primary CR nuclei and electron source distribution for the large-scale diffuse Galactic models used in [15]. Solid black, SNR (Lorimer). Dashed blue, pulsars (Lorimer). Dotted red, pulsar (Yusifov). Dash-dotted green, OB-stars

proaches, to use CR propagation codes such as GALPROP[2], or the template fitting method. The ingredients needed for both approaches and their uncertainties are presented in section 2. The main idea of the methods and their issues are discussed in section 3. Section 4 we address the question: are we seeing DM signals from the Galaxy center?

2 Ingredients for building diffuse models and their uncertainties

The γ-ray diffuse emission in the inner Galaxy is created by interaction of CR with interestellar gas (pion decay and bremsstrahlung), radiation fields (ICS), and magnetic fields (synchrotron). So, to build diffuse emission models of this

[2]For a detailed description of the GALPROP code and the most recent release that we use in this work (version 54), we refer the reader to the dedicated website `http://galprop.stanford.edu`

region some basic ingredients are needed, they are listed here:

- **Molecular Hydrogen H2:** Concentrated mostly in the plane. The main tracer is CO. Distance information from velocity and a rotation curve is used to assign the gas to galactocentric rings. The standard method of assigning velocity to distance, in order to create the rings, breaks down toward the GC. The so call Xco factor to convert CO to H2 column density is believed to vary as a function of the galactocentric radius. However, the exact form of the variation is not well know.

- **Atomic Hydrogen HI:** The 21 cm line HI map used is from [14]. As for H2, distance information from velocity and a rotation curve is used to assign the gas to galactocentric rings. The main uncertainty comes from the spin temperature T_s. The code uses a single T_s value among many possibilities. Indeed, HI is a mixture of various phases, observations of T_s show it to vary from tens of K up to thousands of K, so that the adoption of a single T_s[3] is in any case an approximation.

- **Galactocentric rings toward the GC:** The kinematic resolution of the method used to relate velocity and distance vanishes for directions near the GC. We linearly interpolate each annulus independently across the range $|l| < 10^\circ$ to get an estimate of the radial profile of the gas. Nevertheless, the innermost annulus is entirely enclosed within the interpolated region, necessitating a different method to estimate its column density. For HI the innermost annulus contains ∼60% more gas than its neighbouring annulus. This is a conservative number. For CO, we assign all high velocity emission in the innermost annulus. See Appendix 2 of [15] for more details.

- **Interstellar Radiation Field (ISRF):** Emission from stars, and the scattering, absorption, and re-emission of absorbed starlight by dust in the ISM. The `FRaNKIE` code [16] is used to model the distribution of optical and infrared (IR) photons throughout the Galaxy. Further details about the ISRF model and recent developments about modelling this component, can be found in Appendix 3 of [15]. The main uncertainty

[3] In [15] only 2 T_s extreme values were used, 150

is the overall input stellar luminosity and how it is distributed amongst the components of the model (bulge, thin and thick disk, and halo)

- **CR injection and propagation:** SNRs are widely accepted as the main sources of CRs. However, their distribution is not well determined. Pulsars are SN explosion end states and their distribution is better determined than SNRs, but still, it suffers from observational biases. CR propagation is not well understood and its uncertainties involve spectra injection, transport parameters, halo size, etc. In figure 2 we present the distribution of CR widely used, as e.g. in [15].

- **Inverse-Compton Scattering (ICS):** Optical photons are the principal target for high energy electrons to produce ICS emission in the energy range $\sim$ 50 MeV -100 GeV. The ICS template is brightest in the direction of the inner Galaxy, and while it should be smooth because of the physics of radiation in the Galaxy, there are most likely fluctuations in that component that are not modelled with GALPROP. A dedicated study of the ISRF and the CR source distribution in the direction of the inner Galaxy to be able to estimate this contribution is needed.

There are some extended sources not included here such as the Fermi Bubbles [17, 18, 19] and Loop I [20] . Templates that model these sources must be included in order to have an accurate description of the γ-ray sky observed by the *Fermi*-LAT.

3 Recipes

- **CR propagation codes:** GALPROP code calculates the propagation of CR, and computes diffuse γ-ray emission in the same framework. Each run using specific realistic astrophysical inputs together with theoretical models corresponds to a potentially different background model for DM searches. By varying these inputs within their limits, many diffuse emission models can be created. GALPROP accounts for effects such as diffusion, reacceleration, and energy loss via mechanisms such as synchrotron radiation. In [15] different GALPROP models were compared with data, finding that all of them are in good (20%) agreement with all sky data

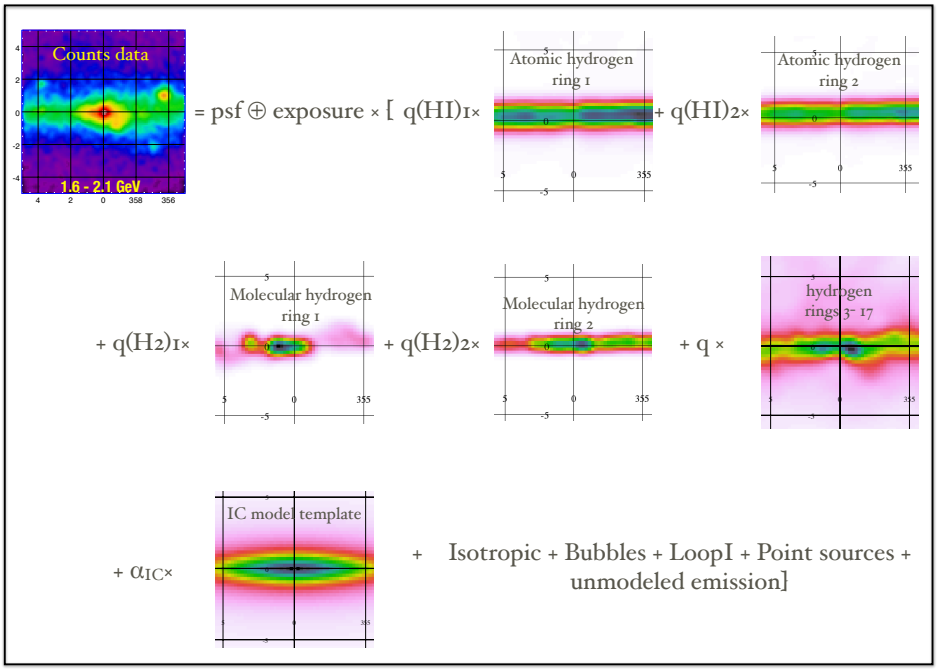

Figure 3: *Template fitting method. At different energy bins, templates correlated with gas, IC and some extended sources are directly fitted to the data.*

- **Template fitting method:** At some particular energy, the γ-ray intensity is modelled as a linear combination of gas column-density map template, a predicted IC intensity map and a residual intensity of unmodeled emission. Figure 3 presents the idea of this method. The diffuse models provided by the *Fermi*-LAT collaboration[4] to study point or small extended sources are created using this method.

All the template-based models provided by the *Fermi*-LAT collaboration are fitted to the whole-sky with the purpose of serving as background models for analysis of pointlike or small sources, and as such tried to pick up as much

[4]http://fermi.gsfc.nasa.gov/ssc/data/access/lat/BackgroundModels.html

extended emission as possible. The double fit (original one plus GC fit) introduces complications in the interpretation of the results which are not trivial to understand.

Any model based on the gas maps created for full sky analysis will not be very good in the inner Galaxy by design. The linear interpolation used for the distance estimator is a very basic approximation and can not be used to estimate the diffuse emission in that inner Galaxy region. A very dedicated study on the gas templates is needed to understand that region.

The most important message is that if one wants to study extended emission in the direction of inner Galaxy region there is no ready-made solution in terms of a diffuse background model to use. None of the models up to now are adequately describing γ-ray emission from that region.

4 Are we really seeing DM signals from the Milky Way center?

Maybe yes, it is clear from maps in figure 1 that there is an extended γ-ray source in the very GC, whatever its nature is. But, we can not be sure it is a DM signal as far as we do not understand the background at the level needed to characterise its spectrum and morphology. Beside this, there is an implicit assumption in the modelling discussed above: steady state. It is a strong assumption since it is very likely that the GC has a violent history, two recent papers [21, 22] present cases where past activity in the GC may yield γ-ray emission with similar properties to DM sources.

We need new molecular and atomic gas, CR and γ-ray data to shed light on the nature of the GC region at high energies. We already have new gas data waiting to be studied in the context of γ-ray astronomy [23, 24, 25]. Regarding new γ-ray data, from space there are some proposals to build new satellites [26, 27, 28, 29]. From Earth, the Cherenkov Array Telescope (CTA) will provide insight on the mysterious phenomena at the Milky Way center [30].

5 Acknowledgements

Thanks to Guðlaugur Jóhannesson and Luigi Tibaldo. Also thanks to Luis Labarga and Carlos Muñoz for comments on the manuscript. The work of GAGV was supported by Conicyt Anillo grant ACT1102. GAGV thank for the support of the Spanish MINECO's Consolider-Ingenio 2010 Programme

under grant MultiDark CSD2009-00064. This work was also supported in part by MINECO under grant FPA2012-34694.

References

1. Fermi-LAT Collaboration, W. Atwood *et al.*, Astrophys. J. **697** (2009) 1071–1102 [arXiv:1206.1896 [astro-ph.IM]].

2. Nolan, P. L., Abdo, Fermi-LAT Collaboration, P. L. Nolan *et al.*, Astrophys. J. S. **199** (2012) 31

3. W. L. Kraushaar, *et al.*, Astrophys. J. **177** (1972) 341

4. G. A. Gmez-Vargas, M. Fornasa, F. Zandanel, A. J. Cuesta, C. Munoz, F. Prada and G. Yepes, JCAP **1202** (2012) 001 [arXiv:1110.3305 [astro-ph.HE]].

5. Vitale, V., Morselli, A., & for the Fermi/LAT Collaboration 2009, Proceedings of the 2009 Fermi Symposium, eConf Proceedings C091122 [arXiv:0912.3828]

6. D. Hooper and L. Goodenough, Phys. Lett. B **697** (2011) 412 [arXiv:1010.2752 [hep-ph]].

7. Morselli, A., Canadas, B., & V. Vitale on behalf of the Fermi LAT collaboration 2010, Il Nuovo Cimento C - Colloquia on physics [arXiv:1012.2292]

8. D. Hooper and T. Linden, Phys. Rev. D **84** (2011) 123005 [arXiv:1110.0006 [astro-ph.HE]].

9. K. N. Abazajian and M. Kaplinghat, Phys. Rev. D **86** (2012) 083511 [arXiv:1207.6047 [astro-ph.HE]].

10. O. Macias and C. Gordon, Phys. Rev. D **89** (2014) 063515 [arXiv:1312.6671 [astro-ph.HE]].

11. K. N. Abazajian, N. Canac, S. Horiuchi and M. Kaplinghat, Phys. Rev. D **90** (2014) 023526 [arXiv:1402.4090 [astro-ph.HE]].

12. T. Daylan, D. P. Finkbeiner, D. Hooper, T. Linden, S. K. N. Portillo, N. L. Rodd and T. R. Slatyer, arXiv:1402.6703 [astro-ph.HE].

13. F. Calore, I. Cholis and C. Weniger, arXiv:1409.0042 [astro-ph.CO].

14. P. M. W. Kalberla, W. B. Burton, D. Hartmann, E. M. Arnal, E. Bajaja, R. Morras and W. G. L. Poppel, Astron. Astrophys. **440**, 775 (2005) [astro-ph/0504140].

15. Fermi-LAT Collaboration, M. Ackermann *et al.*, Astrophys. J. **750** (2012) 3.bibl [arXiv:1202.4039 [astro-ph.HE]].

16. T. A. Porter, I. V. Moskalenko, A. W. Strong, E. Orlando and L. Bouchet, Astrophys. J. **682** (2008) 400.

17. G. Dobler, D. P. Finkbeiner, I. Cholis, T. R. Slatyer and N. Weiner, Astrophys. J. **717** (2010) 825 [arXiv:0910.4583 [astro-ph.HE]].

18. M. Su, T. R. Slatyer and D. P. Finkbeiner, Astrophys. J. **724** (2010) 1044 [arXiv:1005.5480 [astro-ph.HE]].

19. M. Ackermann *et al.* [Fermi-LAT Collaboration], Astrophys. J. [arXiv:1407.7905 [astro-ph.HE]].

20. J.-M. Casandjian, I. Grenier, for the Fermi Large Area Telescope Collaboration 2009, arXiv:0912.3478

21. A. X. Gonzalez-Morales, S. Profumo and F. S. Queiroz, arXiv:1406.2424 [astro-ph.HE].

22. J. Petrovic, P. D. Serpico and G. Zaharijas, arXiv:1405.7928 [astro-ph.HE].

23. N. M. McClure-Griffiths, J. M. Dickey, B. M. Gaensler, *et al.* 2012, apjs, 199, 12

24. M. Schultheis, B. Q. Chen, B. W. Jiang, *et al.* 2014, aap, 566, A120

25. Planck Collaboration, A. Abergel, *et al.* 2011, aap, 536, A24

26. A. Morselli, *et al.* Nuclear Physics B 239?240 (2013) 193-198 [arXiv:1406.1071]

27. S. Torii, *et al.* , Nucl. Phys. Proc. Suppl. **150** (2006) 345.

28. A. Moiseev, A. M. Galper, Adriani, *et al.* 2013, arXiv:1307.2345

29. http://astromev.in2p3.fr

30. M. Doro, J. Conrad, D. Emmanoulopoulos, *et al.* 2013, Astroparticle Physics, 43, 189

Frascati Physics Series Vol. 58 (2014)
Frontier Objects in Astrophysics and Particle Physics
May 18-24, 2014

Searches for dark matter with the Cherenkov Telescope Array

Farnier Christian
Oskar Klein Centre for Cosmoparticle Physics, Stockholm University
for the CTA Consortium

Abstract

The current paradigm of the Universe states that more than 80% of its mass content consists of dark matter of unknown origin. Since the first hints more than eighty years ago, the quest for dark matter identification is one of the most important questions in Physics. Well motivated candidates in form of weakly interactive massive particles as well as axion-like particles could give rise to detectable signatures in gamma rays. The Cherenkov Telescope Array, the next generation of imaging atmospheric Cherenkov telescopes, will possess incomparable sensitivity to gamma-ray signals from few tens of GeV to few hundreds of TeV allowing to test a wide range a dark matter scenarios.

1 Observation of very high energy photons with the Cherenkov Telescope Array

Over the last decade, observations of very high energy (VHE; E>30 GeV) photons have permitted to realise tremendous advance in the understanding of the most energetics phenomena and revealed a new window on our Universe. At those energies, fluxes are too low to be studied in detail from space and the atmosphere being opaque to gamma rays, ground-based experiments rely on the observations of extended showers of secondary particles initiated in the upper atmosphere. Imaging atmospheric Cherenkov telescope (IACT) experiments such as H.E.S.S., MAGIC or VERITAS recording the very brief flashes of Cherenkov radiation, are able to reconstruct the energy, direction and nature of the primary particle.

The Cherenkov Telescope Array (CTA) will be the next generation of IACT instrument, consisting of two arrays of telescopes located in both hemispheres for a complete sky coverage. With several dozens of telescopes of different sizes spread over one to three square kilometres, CTA will probe an energy range spanning from few tens of GeV to hundred TeV. The large number of telescopes will drastically enhance the angular resolution, and with enlarged field of view cameras, CTA will be able to study the morphology of wide sources as well as search for extended emissions. Compared to the current generation of IACTs, CTA will provide a gain of more than one order of magnitude in sensitivity [7)], increasing the number of expected sources to more than 1000 and will be the first facility of this type to operate as an observatory [2)].

2 Dark matter

Over the past 80 years, a significant amount of evidences have accumulated, suggesting that our Universe is primarily dominated by Dark Energy and Dark Matter (DM). In the ΛCDM concordance model, non standard particles composing the DM would have been non-relativistic at the epoch of reionization creating the seeds of gravitational well from which large scale structures are believed to arise from the infall of smaller dark matter halos. Although the presence of DM is now established at all scales, from dwarf spheroidal galaxies up to galaxy clusters, its nature remains one of most challenging and exciting mystery of modern Physics.

In several theories beyond the Standard Model, new particles often arise in the energy mass scale between few GeV to several TeV. In this mass range, particles interacting through the exchange of weak bosons are often referred to as weakly interacting massive particles (WIMPs). Encompassing a broad class of particle physics candidates (SUSY relics, Kaluza-Klein states, massive Dirac neutrinos, etc), their abundance would *naturally* match current observations (see [8] for a review).

Another exciting possibility would be the presence of axion-like particles (ALPs). Similar to axions introduced to solve the strong CP problem [15], ALPs couple to photon in presence of a magnetic field. While ALPs are much lighter ($\sim$ neV) than WIMPs and are produced by a different mechanism, they have similar effects to galaxy formation and the origin of the large scale structures. Furthermore, ALPs have been evoked to explain the potential anomalous opacity of the universe [12].

3 WIMP searches

The expected gamma-ray flux from WIMP annihilations for a direction Ψ and averaged over the opening angle of the detector $\Delta\Psi$, is given by

$$\frac{d\Phi_\gamma}{dE_\gamma}(E_\gamma, \Psi) = \frac{1}{8\pi} \int_{\Delta\Psi} \frac{d\Omega}{d\Psi} \int_{l.o.s} dl(\Psi) {\rho_\chi}^2 \frac{\langle \sigma_{\rm ann} v \rangle}{{m_\chi}^2} \sum_f B_f \frac{dN_\gamma^f}{dE_\gamma}, \qquad (1)$$

where the integration is performed along the line of sight (l.o.s.), $\langle \sigma_{\rm ann} v \rangle$ is the average velocity-weighted annihilation cross section, m_χ the mass of the DM particle, ρ_χ the DM density, B_f the branching ratio into channel f and N_γ^f the number of photons per annihilation.

Accurate measurements of WIMP-induced gamma ray signals can therefore lead to the discovery of several characteristics of the exotic components, e.g its mass, annihilation cross-section, or distribution. CTA will have the capabilities to search for a WIMP signal in very different targets (see [10] for an extended discussion). The following sections discuss the search for a gamma-ray continuum towards two of the most promising targets: dwarf spheroidal galaxies (dSphs) and the galactic centre region; as well as the prospects to discover a gamma-ray line signature of WIMPs.

3.1 *Dwarf spheroidal galaxies*

Dwarf spheroidal galaxies (dSphs), satellites of the Milky Way, are largely dominated by DM and devoid of standard astrophysical emitters [5]. The detection of one or several dSphs would clearly establish the presence of WIMPs. Although their DM distribution profile remains under debate, studies of the kinematics of their stellar content provide estimates of their amount of DM and associated uncertainty, which is used to establish robust limits on the WIMP annihilation cross-section.

Prospects for the search of a WIMP induced continuum of gamma rays towards Segue 1, one of the most DM dominated and most promising dSph, are reported in fig.1. Although the detection of a DM signal from known targets seems challenging, the situation could soon evolve as surveys by forthcoming experiments, e.g. DES or LSST, are likely to discover new targets.

3.2 *Galactic centre region*

The galactic centre region is indubitably the brightest source of gamma rays from WIMP annihilations. Its detection however faces two important challenges: the DM density in the inner few parsec is rather uncertain due to the presence of the super-massive black hole, Sgr A*; the presence of a strong point-like source coincident with Sgr A* [4], as well as an extended emission along the galactic plane [3], both likely due to standard astrophysical processes, make it difficult to disentangle an additional DM component.

Using a region in the direct vicinity of the peak of the DM distribution but outside of the galactic plane, e.g. almost devoid on standard astrophysical contamination but still holding large amount of DM, led to the most stringent limits on the WIMP annihilation cross-section for masses above 400 GeV [1], although still one order of magnitude away from cosmological models compatible with the cosmic microwave background. Thanks to its improved sensitivity, and a larger field of view, CTA will have the possibility to probe a large fraction of the WIMP parameter space, see fig.1, complementing collider and direct detection experiments.

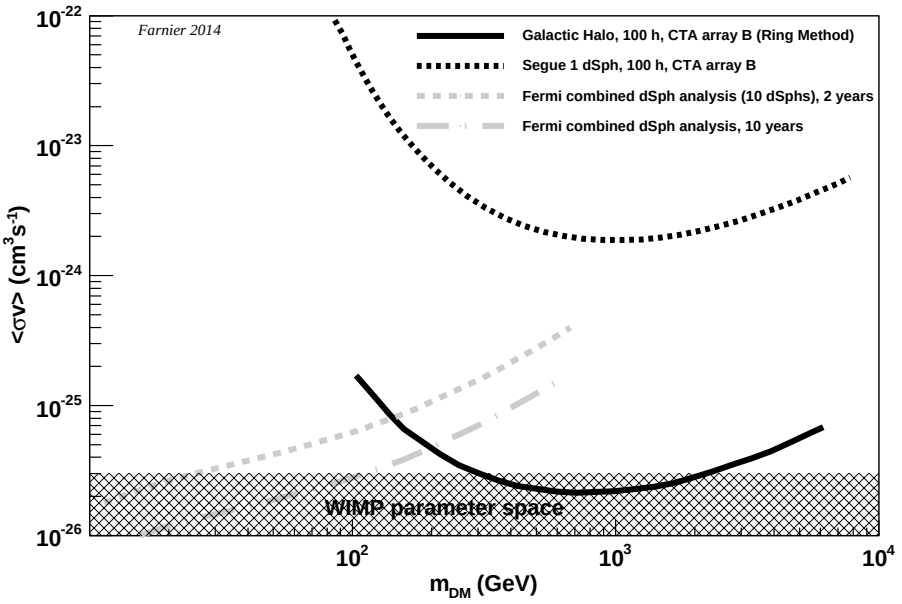

Figure 1: *CTA prospects for WIMP searches for 100 h of observations of the galactic centre halo (plain black curve) and Segue 1 dSph (back dashed curve). For comparison, Fermi 10 dSphs 2 years combined limit and 10 years prospects are also displayed (resp. dashed and dot-dashed grey curves). [Figure adapted from* [10]*].*

3.3 *Line and line-like signals*

While previous sections focused on the search of smooth continuum of gamma rays, mainly arising from the decay of neutral pions, this section presents the search of sharper features, e.g. line or line-like signals. Although loop suppressed, several scenarios with large monochromatic gamma-ray lines from WIMP annihilations occurring at energy $E_\gamma = m_\chi \times [1 - {m_X}^2/4{m_\chi}^2]$ ($X = \gamma, Z, H$ or some new neutral state) have been presented [11]. In addition, sharp features resembling a line signal given the finite energy resolution of the detector, can arise from hard photons radiated by virtual charged particles created in the annihilation process [9]. In both cases, the detection of such sharp features would be a smoking gun for the presence of annihilating WIMPs, as no

astrophysical signal is expected to mimic it, and provide important information on the DM, e.g its mass.

The good energy resolution and large collection area of CTA will provide excellent sensitivities to line-like signals even for limited observation time [6]. Additional exposure will likely allow to probe more complex scenarios, e.g the presence of a second emission line, allowing important insights on the characteristics of the WIMPs.

4 Search for axion-like particles (ALPs)

ALPs are expected to convert to photons (and *vice versa*) in the presence of magnetic fields. In the TeV range, this effect could distort the spectra of gamma-ray sources, and in particular of active galactic nuclei (AGN) located at large distances, which photon beam potentially crosses several magnetic fields (in the jet, host galaxy, galaxy cluster, inter-galactic magnetic field (IGMF) or within our Galaxy). As a main consequence, ALP would induce a drop of the AGN photon flux. However, gamma ray fluxes from distant sources are also expected to be suppressed due to $e^{\pm}$ pair production over the extragalactic background light (EBL), translating into a spectral softening of the source at very high energies. On the contrary, photons converted into ALPs will travel unaffected by the EBL and, in case of back conversion in the galactic magnetic field (GMF), diminishing the apparent opacity of the Universe and boosting the AGN photon flux. It has been shown that, for long lasting AGN flares, CTA will have the capability to test the photon-ALP conversion into the IGMF [10].

More recently, a binned likelihood analysis was introduced to test the presence of ALPs by comparing expected spectra in the optically thick region with and without photon-ALP conversion [14]. An array like CTA will be able to probe a significant fraction of the ALP parameter space invoked to explain the anomalous opacity of the universe [12].

Finally, although the strength and morphology of the GMF remain uncertain, the presence of ALPs could be tested by means of a spectral variation auto-correlation function. Prospects for CTA have been presented in [17]: over the lifetime of the experiment, CTA will detect a large number of AGNs. Assuming a GMF morphology and strength according to [13], CTA will probe photon-ALP coupling down to $g_{\gamma a} = 5 \times 10^{-11}\,\mathrm{GeV}^{-1}$, comparable to direct detection experiments such as CAST or ALPS II.

5 Conclusions

During the past 10 years, IACTs have provided tremendous wealth of information on particle accelerations and extreme phenomena. In the future, CTA will have the capabilities to uncover the mystery of dark matter, probing the existence of WIMPs and axion-like particles.

6 Acknowledgements

We gratefully acknowledge support from the agencies and organisations listed under Funding Agencies at this website: `http://www.cta-observatory.org/`.

7 References

References

1. Abramowski, A., et al., Phys. Rev. Lett., **106**, 161301 (2011)
2. Acharya, B. S., et al., Astroparticle Physics, **43**, 3 (2013)
3. Aharonian, F., et al., Nature, **439**, 695 (2006)
4. Aharonian, F., et al., Phys. Rev. Lett., **97**, 221102 (2006)
5. Battaglia, G., Helmi, A., & Breddels, M., New Astronomy Review, **57**, 52 (2013)
6. Bergström, L., Bertone, G., Conrad, J., Farnier, C., & Weniger, C., JCAP, **11**, 25 (2012)
7. Bernlöhr, K., et al., Astroparticle Physics, **43**, 171 (2013)
8. Bertone, G., Hooper, D., & Silk, J. 2005, Phys. Rep., **405**, 279 (2005)
9. Bringmann, T., Bergström, L., & Edsjö, J., Journal of High Energy Physics, **1**, 49 (2008)
10. Doro, M., et al., Astroparticle Physics, **43**, 189 (2013)
11. Gustafsson, M. et al, Phys. Rev. Lett. **99** (2007) 041301; Dudas, E. et al, JHEP **0908** (2009) 014; Mambrini, Y., JCAP **0912** (2009) 005; Jackson, C. et al, JCAP **1004** (2010) 004; Arina, C. et al, JCAP **1003** (2010) 024.

12. Horns, D., & Meyer, M., JCAP, **2**, 33 (2012)

13. Jansson, R. and Farrar, G.R., Astrophys. J., **757** 14 (2012)

14. Meyer, M., Montanino, D., & Conrad, J. (2014) arXiv:1406.5972

15. Peccei, R. D., Quinn, H. R., Phys. Rev. Lett. **38**, 1440 (1977).

16. Planck Collaboration, Ade, P. A. R., et al. (2013) arXiv:1303.5076

17. Wouters, D., & Brun, P., Phys. Rev. D, **86**, 043005 (2012)

DARK MATTER: A NEW DETECTOR, THE GEYSER

Antonino Pullia
University and INFN Milano Bicocca

January 14, 2015

Abstract

The MOSCAB experiment (Materia OSCura A Bolle) uses a new technique for Dark Matter search. The Geyser technique is applied to the construction of a prototype detector with a mass of 0.5 kg and the encouraging results are reported here; an accent is placed on a big detector of 40 kg in construction at the Milano-Bicocca University and INFN.

1 INTRODUCTION

WIMPs (Weak Interacting Massive Particles) are one of the more suited hypothesis for the non-baryonic candidate of dark matter ; they indeed satisfy the required density compatible with the cosmological constraints; they form galactic halos with a Maxwellian velocity distribution around a mean value of about 230 km/s and with a matter density of about 0.3 GeV/cm^3 at the location of the solar system.
In this talk I will present a new experimental device to search for WIMPs: the Geyser.

Figure 1: Sketch of a Vertical section of the Geyser

2 DESCRIPTION OF A GEYSER

The "old" glorious Bubble Chambers(B.C.) worked following the phenomena described by Glaser [**?**] and Seitz [**?**]; these bubble chambers worked on beams from a accelerators and were ready to reach the right superheated condition when the beam passed through; the seen bubbles were destroyed by a succesive compression of the liquid.
Furtheremore the bubble chambers were used at very high superheated degree to see also the minimum ionizing particle (gamma and electrons).
This behaviour is not useful to search WIMPs; indeed it impossible to foreseen the passage of a Dark Matter Particle! Furtheremore gammas and electrons constitute an important background for WIMPS.
Two improvements were done now:
1)By using ONLY weak superheated states it is possible to keep a bubble chamber sensitive for long periods of time.
2)In such conditions the gammas and electrons are not seen by the bubble chamber(so eliminating an important background for Dark Matter).
The Geyser has these advantages and furthermore does not need a recompression for eliminate the residual bubbles; this is indeed automatic.

In Fig. 1 the sketch of the vertical section of our prototype Geyser is shown:
The Geyser is divided in two parts kept at different temperature:
1)The higher parts contains the vapour (f.i. in our case freon C3F8 at 18 C)
2)The lower part contains liquid freon superheated (f.i. at temperature of 25 C); between these 2 phases a "buffer" liquid (in our case Glycol) is inserted to take the temperatures different.
3)The vapour pressure is practically transmitted to the liquid freon.
The liquid is contained in a quartz vessel; everything is immersed in a plexiglass cilinder containing water; the water is kept by two

thermostats at the choosen temperatures(f.i. 18 C and 25 C) by cupper coils indicated in the figure by small circles; in the high region a pressure equalizer(an elastic rubber membrane) is also visible to take the pressure of the water similar to that of the vapour).
When a bubble is nucleated in the liquid the inner vapour corresponds to the temperature of the liquid (higher) and increases its volume; for the Archimede's law the bubble goes up, cross the Glycol and reach the freon vapour (where the temperature is lower); here the bubble recondenses and goes down for gravity reaching its original condition. Every thing happens without an external operation. It is AUTOMATIC!

The degree of superheat applied must exclude the detection of minimum ionizing particles (electrons and γ rays) and on the contrary it must allow the detection with high efficency of the recoiling ions.

The principal advantages of the Geyser (and of the Bubble techniques) are the following:

1)The strong rejection of the particles of minimum ionization (electrons and γ).

2)The simplicity of the mechanical construction, important for large size detectors and therefore low cost.

3)The very interesting possibility to count multiple neutron interactions and hence subtract the neutron background (the interaction length of a neutron is of the order of (6-9) cm in our liquid). The double or triple interaction in the same frame can be used statistically to evaluate the number of events with a single interaction due to neutrons.

4)The possibility to distinguish the spin dependent interaction of WIMP from spin independent by changing the liquid used.

5)For the Geyser (ONLY) the reset of the detector is automatic and has a very short time (few seconds).
A prototype of Geyser has been constructed with a mass of 0.5 kg in Milano-Bicocca [**?**].

Figure 2: Evolution of a bubble (starting from Lower-Right picture)

With reference to the Fig.1 the quartz vessel of 0.33 liters is immersed in a water bath and it is surrounded by Cu coils with an internal circulating water at the two fixed temperatures.
It contains freon C_3F_8 around 25^0C at a pressure of about 6 bar. The hot freon is separated from the cold freon vapour by the neck of the vessel filled by a buffer liquid (Glycol) with an high thermal capacity.

After an interaction with a neutral particle like a neutron or a WIMP the scattered ion deposits its energy in very small regions (size of the order 0.05-0.1 micron).
In these conditions a bubble can grow and reach a few mm of radius (well visible, see Fig. 2).

Two professional digital cameras monitor in a continuous way at 50 frames per second (fps) the volume in the freon vessel.
Some pixels undergo a change of luminosity when a bubble is generated.
At this point a trigger is launched and a stream of pictures is registered (between -50 and + 50 frames starting from the trigger). After that, the stream of data is stored and visually scanned to see the evolution of the bubbles.

3 RESULTS FROM THE PROTOTYPE

We are working in Milano-Bicocca at the IV floor in a Laboratory provided by the University and INFN.

Bubble formation is well understood [**?**] and depends on the critical radius $R_c = 2\sigma/\Delta p$, where σ is the surface tension of the

Figure 3: dE/dx for ions and electrons

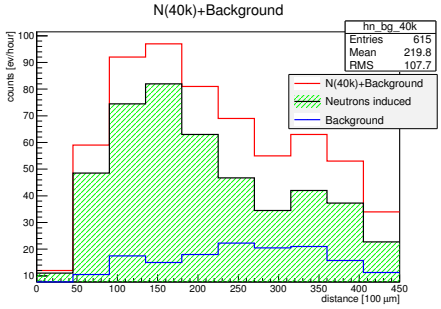

Figure 4: Background and a neutron source

liquid andΔ p the pressure difference between the vapour inside the bubble and the liquid.
Another important quantity is the critical energy E_c necessary for visible bubble formation.
E_c is a function of R_c, σ, Δp and the latent heat of evaporation of the liquid.
In Fig.3 is shown the energy loss dE/dx for C and F ions and also electrons.

Therefore if the energy of recoil is greater than E_c(the critical energy) and stopping power satisfises the relation $(dE/dx)2R_c > E_c$, then a bubble will form. In Fig.3 we show also several sensitivity zones for various vapour temperatures and liquid-vapour temperature differences DT; the experimental regions in which we must work are indicated by the boxes.

I said that the characteristic of a Geyser must be a high rejection

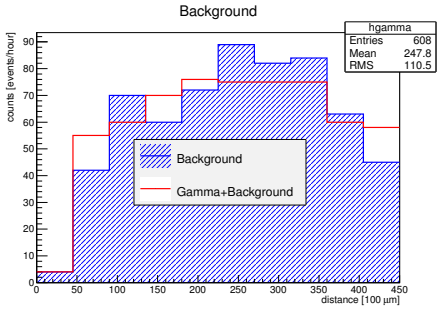

Figure 5: Background and a gamma source

Figure 6: Comparison with the events-Integrated Distribution and (green line) MC + Background

of electrons and γ accompanied by an easy detection of nuclear recoils(similar to the recoiling ions due to an interaction of a WIMP).
To test this point, we placed outside the detector (at a minimal distance from the freon) a neutron source ($Am-Be$ -40 kBq).The results are shown in Fig.4 and we can see that we are very sensitive to the detection of neutrons.
After that we put a gamma rays source (20 kBq ^{22}Na) near the detector and in Fig.5 are shown the background distributions and that obtained with a Gamma source (Na^{22}).
We can remark that in the latter case we obtained compatible results: no excess in events in presence of the radiative source!

In order to compare our data to what is expected from the neutron source we have performed Monte-Carlo calculations using the MCNP package coming from Los Alamos [**?**].

In Fig.6 we compare the distribution (M.C. results + the meaured background) with the corresponding experimental distribution and

we can see a very good general agreement with a threshold of 5 keV; the reported errors are the statistical errors only.

We remark that in the SD case, our sensitivity could be much better (by 4 order of magnitude)than that obtained for the results pubblished by PICASSO,COUPP and Xenon100.

4 Conclusions

A new technique for the direct investigation of Dark Matter has been developed. The good results obtained with a Geyser prototype (with a low threshold= few keV) motivate the construction of larger detector of this type and the 40 kg detector will be ready as soon as possible to obtain very good physics results at the LNGS.
We also would like to claim that this kind of detector would be useful in a neutrino beam to investigate the interaction $\nu + C = \nu + C$.

References

[1] D. Glaser Some effect of Ionizing Radiation on the formation of Bubbles in Liquid. P.R. 87(4):665 (1952)

[2] F. Seitz On the theory of the Bubble Chamber Phys. Fluids 1,2 (1958)

[3] L. Baudis (Direct Dark Matter Searches-Rapporteur Talks) 'New Opportunities in the Physics Landscape at CERN', CERN May 11-13-2009 CERN.

[4] D.V. Bugg 'Progress in Nuclear Physics' Pergamon Press -London,1959 Vol.7,Pag.1.

[5] Manual (mcp) A general Monte Carlo N-Particle trasport Code, Version-5,2008.

Frascati Physics Series Vol. 58 (2014)
Frontier Objects in Astrophysics and Particle Physics
May 18-24, 2014

THE HIGGS AND THE EXCESSIVE SUCCESS OF THE STANDARD MODEL

Guido Altarelli
Dipartimento di Matematica e Fisica, Università di Roma Tre;
INFN, Sezione di Roma Tre,
Via della Vasca Navale 84, I-00146 Rome, Italy
and
CERN, Department of Physics, Theory Unit,
CH-1211 Geneva 23, Switzerland

Abstract

The LHC runs at 7 and 8 TeV have led to the discovery of the Higgs boson at 125 GeV which will remain as one of the major physics discoveries of our time. Another very important result was the surprising absence of any signals of new physics that, if confirmed in the continuation of the LHC experiments, is going to drastically change our vision of the field. Indeed the theoretical criterium of naturalness required the presence of new physics at the TeV scale. At present the indication is that Nature does not too much care about our notion of naturalness. Still the argument for naturalness is a solid one and one is facing a puzzling situation. We review the different ideas and proposals that are being considered in the theory community to cope with the naturalness problem.

1 Introduction

With the discovery at the LHC [1, 2] of a particle that, in all its properties, appears just as the Higgs boson of the Standard Model (SM), the main missing block for the experimental validation of the theory is now in place. The Higgs discovery is the last milestone in the long history (some 130 years) of the development of a field theory of fundamental interactions (apart from quantum gravity), starting with the Maxwell equations of classical electrodynamics, going through the great revolutions of Relativity and Quantum Mechanics, then the formulation of Quantum Electro Dynamics (QED) and the gradual build up of the gauge part of the Standard Model and finally completed with the tentative description of the Electro-Weak (EW) symmetry breaking sector of the SM in terms of a simple formulation of the Englert- Brout- Higgs mechanism [3].

An additional LHC result of great importance is that a large new territory has been explored and no new physics was found. If one considers that there has been a big step in going from the Tevatron at 2 TeV up to the LHC at 8 TeV (a factor of 4) and that only another factor of 1.75 remains to go up to 14 TeV, the negative result of all searches for new physics is particularly depressing but certainly brings a very important input to our field with a big change in perspective. In particular, while New Physics (NP) can still appear at any moment, clearly it is now less unconceivable that no new physics will show up at the LHC.

As is well known, in addition to the negative searches for new particles, the constraints on new physics from flavour phenomenology are extremely demanding: when adding higher dimension effective operators to the SM, the flavour constraints generically lead to powers of very large suppression scales Λ in the denominators of the corresponding coefficients. In fact in the SM there are powerful protections against flavour changing neutral currents and CP violation effects, in particular through the smallness of quark mixing angles. Powerful constraints also arise from the leptonic sector. In particular, we refer to the recent improved MEG result [5] on the $\mu \to e\gamma$ branching ratio, $Br(\mu \to e\gamma) \leq 5.7 \times 10^{-13}$ at 90% C.L. and to other similar processes like $\tau \to (e \text{ or } \mu)\gamma$ and to the bound on the electron dipole moment $|d_e| \lesssim 8.7\ 10^{-29}$ e cm by the ACME Collaboration [6]. In this respect the SM is very special and, as a consequence, if there is new physics, it must be highly non generic in

order to satisfy the present constraints.

There is no evidence of new physics from accelerator experiments (except, perhaps, for the 3-3.5 σ discrepancy of the muon (g-2) [7, 8]). Most of the experimental evidence for NP comes from the sky like for Dark Energy, Dark Matter, baryogenesis and also neutrino oscillations (that were first observed in solar and atmospheric neutrinos). One expected new physics at the EW scale based on a "natural" solution of the hierarchy problem [4]. The absence so far of new physics signals casts doubts on the relevance of our concept of naturalness. In the following we will elaborate on this naturalness crisis.

2 The impact of the Higgs discovery

A particle that, within the present accuracy, perfectly fits with the profile of the minimal SM Higgs has been observed at the LHC. Thus, what was considered just as a toy model, a temporary addendum to the gauge part of the SM, presumably to be replaced by a more complex reality and likely to be accompanied by new physics, has now been experimentally established as the actual realization of the EW symmetry breaking (at least to a very good approximation). It appears to be the only known example in physics of a fundamental, weakly coupled, scalar particle with vacuum expectation value (VEV). We know many composite types of Higgs-like particles, like the Cooper pairs of superconductivity or the quark condensates that break the chiral symmetry of massless QCD, but the LHC Higgs is the only possibly elementary one. This is a death blow not only to Higgsless models, to straightforward technicolor models and other unsophisticated strongly interacting Higgs sector models but actually a threat to all models without fast enough decoupling (in that if new physics comes in a model with decoupling the absence of new particles at the LHC helps in explaining why large corrections to the H couplings are not observed). The mass of the Higgs is in good agreement with the predictions from the EW precision tests analyzed in the SM [9]. The possibility of a "conspiracy" (the Higgs is heavy but it falsely appears as light because of confusing new physics effects) has been discarded: the EW precision tests of the SM tell the truth and in fact, consistently, no "conspirators", namely no new particles, have been seen around.

3 Our concept of naturalness is challenged

The simplicity of the Higgs is surprising but even more so is the absence of accompanying new physics: this brings the issue of the relevance of our concept of naturalness at the forefront. As is well known, in the SM the Higgs provides a solution to the occurrence of unitarity violations that, in the absence of a suitable remedy, occur in some amplitudes involving longitudinal gauge bosons as in $V_L V_L$ scattering, with $V = W, Z$ [10]. To avoid these violations one needed either one or more Higgs particles or some new states (e.g. new vector bosons). Something had to happen at the few TeV scale!

While this prediction is based on a theorem, once there is a Higgs particle, the threat of unitarity violations is tamed and the necessity of new physics on the basis of naturalness has not the same status, in the sense that it is not a theorem. The naturalness principle has been and still remains the main argument for new physics at the weak scale. But at present our confidence on naturalness as a guiding principle is being more and more challenged. Manifestly, after the LHC 7-8 results, a substantial amount of fine tuning is imposed on us by the data. So the questions are: does Nature really care about our concept of naturalness? Apparently not much! Should one give up naturalness? Which form of naturalness is natural?

The naturalness argument for new physics at the EW scale is often expressed in terms of the quadratic cut-off dependence in the scalar sector, before renormalization. If we see the cut-off as the scale where new physics occurs that solves the fine tuning problem, then this new physics must be nearby because the observed scalar mass m and the cut-off should a priori be of the same order (modulo coupling factors). Actually the argument can be formulated in terms of renormalized quantities, with no reference to a cut-off, but rather in terms of a quadratic sensitivity to thresholds at high energy. In the renormalized theory the running Higgs mass m slowly evolves logarithmically according to the relevant beta functions [11]. But in the presence of a threshold at M for a heavy particle with coupling λ_H to the Higgs, the quadratic sensitivity produces a jump in the running mass of order $\Delta m^2 \sim (\lambda_H M)^2/16\pi^2$ (see, for example, [12]). In the presence of a threshold at M one needs a fine tuning of order m^2/M^2 in order to reproduce the observed value of the running mass m at low energy.

The argument for naturalness, although very solid in principle, certainly

has failed so far as a guiding principle. As a consequence: we can no more be sure that within 3 or 10 or 100 TeV..... the solution of the hierarchy problem must be found, which, of course, has negative implications for the design of future Colliders. Moreover, it is true that the SM theory is renormalizable and completely finite and predictive. If you forget the required miraculous fine tuning you are not punished, you find no catastrophe! The possibility that the SM holds well beyond the EW scale must now be seriously considered. The absence of new physics appears as a paradox to us. Still the picture repeatedly suggested by the data in the last 20 years is simple and clear: take the SM, extended to include Majorana neutrinos and some form of Dark Matter, as valid up to some very high energy.

There is actually no strict argument that prevents to extend the validity of the SM at large energies. It turns out that the observed value of the Higgs mass m is a bit too low for the SM to be valid up to the Planck mass with an absolutely stable vacuum. The pure SM evolution of couplings, given the measured values of the top and Higgs masses and of the strong coupling α_s, appears to lead to a metastable Universe with a lifetime longer than the age of the Universe, so that the SM can well be valid up to the Planck mass (if one is ready to accept the immense fine tuning that this option implies). Also, it is puzzling to find that the evolution of the Higgs quartic coupling ends up into a narrow metastability wedge at very large energies. This result is obtained from a recent state-of-the-art evaluation of the relevant boundaries [11]. This criticality looks intriguing and perhaps it should tell us something. Note however that these results are obtained in the assumption of no new physics while possibly the solution of the Dark Matter problem or the presence of whatever new intermediate threshold could change the results. Actually also a peculiar behaviour of the Higgs potential near the Planck mass could alter the evaluation of the Universe lifetime [13]. Thus one cannot guarantee that the simplest picture is actually realized in detail but it is important that this possibility exists.

Thus, ignoring the implied huge fine tuning minimal extensions of the SM are being considered. Neutrino masses can be accommodated by introducing Right-Handed (RH) neutrinos and the See-Saw mechanism. Baryogenesis, which represents a problem in the minimal SM, can be elegantly obtained through leptogenesis. The solution of the crucial Dark Matter (DM) problem

could be in terms of some simple Weakly Interacting Massive Particle (WIMP), or by Axions, or by some keV sterile νs..... Coupling Unification without Supersymmetry (SUSY) could be restored by some large scale threshold, e.g. non-SUSY SO(10) with an intermediate scale (see, for example, Ref. [14]), and so on. We now briefly discuss some of these possibilities.

4 Neutrino masses

It is often stated that neutrino masses are the first observed form of NP. This is true but, in this case, a simple, elegant and conceptually far reaching extension of the SM directly leeds to an attractive framework for ν mass and mixing (for reviews, see Refs. [15]). It is sufficient to introduce 3 RH gauge singlets ν_R, each completing a 16 of $SO(10)$ for one generation, and not artificially impose that the lepton number L is conserved. We consider that the existence of RH neutrinos ν_R is quite plausible also because most GUT groups larger than SU(5) require them. In particular the fact that ν_R completes the representation 16 of SO(10): 16=$\bar{5}$+10+1, so that all fermions of each family are contained in a single representation of the unifying group, is too impressive not to be significant. At least as a classification group SO(10) must be of some relevance in a more fundamental layer of the theory! In the SM, in the absence of ν_R, B and L are accidental symmetries, i.e. no renormalizable gauge invariant B and/or L non-conserving vertices can be built from the fields of the theory. But we know that, even in the absence of ν_R, non perturbative terms (instantons) break B and L (not $B-L$) and so do also non renormalizable operators like the Weinberg dim-5 operator $O_5 = (Hl)_i^T \lambda_{ij} (Hl)_j / \Lambda$. With ν_R the Majorana mass term $M \nu_R^T \nu_R$ is allowed by $SU(2) \otimes U(1)$ (ν_R is a gauge singlet!) and breaks L (and $B-L$). A very natural and appealing description of neutrino masses can be formulated in terms of the see-saw mechanism [16]: the light neutrino masses are quadratic in the Dirac masses and inversely proportional to the large Majorana mass. Note that for $m_\nu \approx \sqrt{\Delta m^2_{atm}} \approx 0.05$ eV and $m_\nu \approx m_D^2 / M$ with $m_D \approx v \approx 200\ GeV$ we find $M \approx 10^{15}\ GeV$ which indeed is an impressive indication for M_{GUT}.

We have seen that in the presence of a threshold at M one needs a fine tuning of order m^2/M^2 in order to reproduce the observed value of the running Higgs mass at low energy. Note that heavy RH neutrinos, which are coupled to the Higgs through the Dirac Yukawa coupling, would contribute in the loop

and it turns out that, in the absence of SUSY, become unnatural at $M \gtrsim 10^7 - 10^8$ GeV [17]. Also, in the pure Standard Model heavy ν_R tend to further destabilize the vacuum and make it unstable for $M \gtrsim 10^{14}$ GeV [18].

The detection of neutrino-less double beta decay [19] would provide direct evidence of L non conservation and of the Majorana nature of neutrinos. It would also offer a way to possibly disentangle the 3 cases of degenerate, normal or inverse hierarchy neutrino spectrum. At present the best limits from the searches with Ge lead to $|m_{ee}| \sim (0.25 - 0.98)$ eV (GERDA +HM +IGEX) and with Xe to $|m_{ee}| \sim (0.12 - 0.25)$ eV (EXO +Kamland Zen), where ambiguities on the nuclear matrix elements lead to the ranges shown. In the next few years, experiments (CUORE, GERDA II, SNO+....) will reach a larger sensitivity on $0\nu\beta\beta$ by about an order of magnitude. Assuming the standard mechanism through mediation of a light massive Majorana neutrino, if these experiments will observe a signal this would indicate that the inverse hierarchy is realized, if not, then the normal hierarchy case still would remain a possibility.

4.1 Baryogenesis via leptogenesis from heavy ν_R decay

In the Universe we observe an apparent excess of baryons over antibaryons. It is appealing that one can explain the observed baryon asymmetry by dynamical evolution (baryogenesis) starting from an initial state of the Universe with zero baryon number. For baryogenesis one needs the three famous Sakharov conditions: B violation, CP violation and no thermal equilibrium. In the history of the Universe these necessary requirements have probably occurred together several times at different epochs. Note however that the asymmetry generated during one such epoch could be erased in following epochs if not protected by some dynamical reason. In principle these conditions could be fulfilled in the SM at the electroweak phase transition. In fact, when kT is of the order of a few TeV, B conservation is violated by instantons (but B-L is conserved), CP symmetry is violated by the Cabibbo-Kobayashi-Maskawa phase and sufficiently marked out-of- equilibrium conditions could be realized during the electroweak phase transition. So the conditions for baryogenesis at the weak scale in the SM superficially appear to be fulfilled. However, a more quantitative analysis [20, 21] shows that baryogenesis is not possible in the SM because there is not enough CP violation and the phase transition is not sufficiently strong first

order, because the Higgs mass is too heavy. In SUSY extensions of the SM, in particular in the minimal SUSY model (MSSM), there are additional sources of CP violation but also this possibility has by now become at best marginal after the results from LEP2 and the LHC.

If baryogenesis at the weak scale is excluded by the data still it can occur at or just below the GUT scale, after inflation. But only that part with $|B - L| > 0$ would survive and not be erased at the weak scale by instanton effects. Thus baryogenesis at $kT \sim 10^{10} - 10^{15}$ GeV needs B-L violation and this is also needed to allow m_ν if neutrinos are Majorana particles. The two effects could be related if baryogenesis arises from leptogenesis then converted into baryogenesis by instantons [22, 23]. The decays of heavy Majorana neutrinos (the heavy eigenstates of the see-saw mechanism) happen with non conservation of lepton number L, hence also of B-L and can well involve a sufficient amount of CP violation. Recent results on neutrino masses are compatible with this elegant possibility. Thus the case of baryogenesis through leptogenesis has been boosted by the recent results on neutrinos.

5 Dark Matter

At present Dark Matter (DM) is the crucial problem. There is by now a robust evidence for DM in the Universe from a variety of astrophysical and cosmological sources. While for neutrino masses and baryogenesis, as we have seen, there are definite ideas on how these problems could be solved, DM remains largely mysterious and is a very compelling argument for New Physics and the most pressing challenge for particle physics.

The 3 active νs cannot make the whole of DM. Nearby sterile νs with $m_\nu \sim$ eV are also inadequate. Bounds from dwarf galaxies require that $m_\nu \gtrsim$ few hundreds eV (Tremaine-Gunn), from galaxies $m_\nu \gtrsim$ few tens eV. Hot DM (like neutrinos) is also excluded by structure formation.

WIMPS with masses in the range $10^{-1} - 10^3$ GeV and electroweak cross-sections remain optimal candidates. For WIMPs in thermal equilibrium after inflation the relic density can reproduce the observed value for typical EW cross-sections. This coincidence is taken as a good indication in favour of a WIMP explanation of DM. In SUSY models with R-parity conservation the neutralino is a very attractive candidate for a WIMP (in SUSY also other candidates are possible like the gravitino). At the LHC there is a great potential

for discovery of most kinds of WIMPs. So far no WIMPs have been observed at the LHC. But the LHC limits on neutralinos are not stringent: in large regions of parameter space $m_\chi \lesssim 350$ GeV is allowed. A strict bound is very low: $m_\chi \gtrsim 25$ GeV (with light s-taus and higgsinos) [24].

The WIMP non-accelerator search continues and is very powerful (LUX, XENON, CDMS.....). The limits are generally given in a plane of mass versus cross-section (either spin dependent or spin independent) for processes like (for example, for fermionic DM χ) $\chi + N \to \chi + N$ or $\chi + \chi \to N + \bar{N}$ with N a nucleon. These processes could go via Z exchange (among SM particles) and the present limits exclude a large range of $Z\chi\chi$ couplings for typical WIMP masses [25]. The axial couplings are the least constrained. Another possible SM mediator is the Higgs boson. Here the limits are less stringent, in particular for a pseudoscalar coupling [25]. At present we can state that there is still plenty of room for WIMPs especially at low masses ($\sim$ 10 -100 GeV), or at large masses $\sim$ 1 - 10 TeV).

A rather minimal explanation for DM could be provided by axions, introduced originally to solve the strong CP problem [26]. For a viable axion model some new particles that carry the $U(1)_{PQ}$ charge must exist at a scale f, for example some fermions Ψ and a scalar A [27, 28, 29]. A part from the chiral anomaly, the $U(1)_{PQ}$ symmetry is broken by the A VEV of order f, which also gives a mass to Ψ of the same order of magnitude modulo some Yukawa-like coupling. The phase of A is the axion field a which is the Goldstone boson associated with the breaking of $U(1)_{PQ}$. It would be massless and only derivatively coupled if not for the chiral anomaly that gives a mass to the axion, inversely proportional to f, hence very small. The typical window for an axion that could explain the observed relic density is $f \sim 10^{10} - 10^{11}$ GeV and $m_a \sim 10^{-4} - 10^{-5}$ eV. The chiral anomaly also induces the decay $a \to \gamma\gamma$, through which the axion can be observed. Clearly experimental axion searches are very important. So far the experiments were not sensitive enough to probe the relevant ranges of f and m_a. Now the Axion Dark Matter Experiment (ADMX) plans to reach the required sensitivity in the next few years.

6 Theory confronts the naturalness riddle

To cope with the naturalness riddle different lines of thought have emerged. Here is a partial list:

1) Insist on minimizing the fine tuning (FT) within the present experimental constraints. In practice this amounts to imagine suitable forms of new physics at an energy scale as close as possible (with new particles that could hopefully be observable at the LHC14).

2) Accept FT only up to a large intermediate scale (i.e. still far below M_{GUT}): e.g. split SUSY.

3) Make the extreme choice of a total acceptance of FT : the most typical approach being the anthropic philosophy.

4) Argue that possibly there is no FT : make the conjecture that there is no new threshold up to M_{Pl} and invoke some miracle within the theory of quantum gravity to solve the naturalness of the EW versus the Planck scale.

We now briefly comment on these different options.

The first possibility is the most conservative and consists of continuing all efforts to minimize the FT. The goal is to implement some form of "Stealth Naturalness": build models where naturalness is restored not too far from the weak scale but the related NP is arranged to be not visible so far. Those are clearly the best scenarios for the next LHC runs! The risk is to end up with baroque models where one is fine-tuning the fine-tuning-suppression mechanism. The two main directions along these lines are SUSY and Composite models. On the SUSY side, which, except for its most minimal versions, still remains the best NP framework, the simplest new ingredients for an orderly retreat [30] are compressed spectra, heavy first two generations and the next-to-minimal NMSSM [31] (with an additional Higgs singlet). These attempts represent the last trench of natural SUSY. In composite Higgs models [32, 33, 34] naturalness is improved by the pseudo-Goldstone nature of the Higgs. However, minimal fine tuning demands the scale of compositeness f to be as close as possible, or the $\xi = v^2/f^2$ parameter to be as large as possible (v being the HIggs VEV). But this is limited by EW precision tests that demand $\xi < 0.05 - 0.2$. Also the measured Higgs couplings interpreted within composite models lead to upper bounds on ξ. While in SUSY models the quadratic sensitivity of the top loop correction to the Higgs mass is quenched by a scalar particle, the s-top, in composite Higgs models the cancelation occurs with a fermion, either with the same charge as the top quark or even with a different charge. For example the current limit from a search of a $T_{5/3}$ fermion of charge 5/3 is $M_{T5/3} \geq 750$ GeV [35] (an exotic charge quark cannot mix with ordinary

quarks: such mixing would tend to push its mass up).

Given that our concept of naturalness has so far failed, there has been a revival of models that ignore the fine tuning problem while trying to accommodate the known facts. For example, several fine tuned SUSY extensions of the SM have been studied like Split SUSY [36] or High Scale SUSY [37, 38]. There have also been reappraisals of non SUSY Grand Unified Theories (GUT) where again one completely disregards fine tuning [39, 40, 14]. In Split SUSY only those s-partners are light that are needed for Dark Matter and coupling unification, i.e. light gluinos, charginos and neutralinos (also A-terms are small) while all scalars are heavy (a hierarchy explained in terms of a chiral symmetry or a discrete parity). As a result also flavour problems are very much eased down. The measured Higgs mass imposes an upper limit to the large scale of heavy s-partners [38] which, for Split SUSY, is at $10^4 - 10^7$ GeV, depending on $\tan\beta$, while in High-Scale SUSY, where all supersymmetric partners have roughly equal masses of order M_{SUSY}, the latter must fall in the range $10^3 - 10^{10}$ GeV, again depending on $\tan\beta$. It is interesting that in both cases the value of M_{SUSY} must be much smaller than M_{GUT}. In both Split SUSY and High-Scale SUSY the relation with the Higgs mass occurs through the quartic Higgs coupling, which in a SUSY theory is related to the gauge couplings. In turn the quartic coupling is connected to the Higgs mass via the minimum condition for the Higgs potential. In Split SUSY it is not granted but still possible that the light gluinos, charginos and neutralinos can be observed at the LHC.

An extreme point of view (but not excluded) is the anthropic evasion of the problem, motivated by the fact that the observed value of the cosmological constant Λ_{cosmo} also poses a tremendous, unsolved naturalness problem [41]. Yet the value of Λ_{cosmo} is close to the Weinberg upper bound for galaxy formation [42]. Possibly our Universe is just one of infinitely many bubbles (Multiverse) continuously created from the vacuum by quantum fluctuations (based on the idea of chaotic inflation). Different physics takes place in different Universes according to the multitude of string theory solutions ($\sim 10^{500}$ [43, 44]). Perhaps we live in a very unlikely Universe but the only one that allows our existence [45], [46]. Given the stubborn refusal of the SM to show some failure and the terrible unexplained naturalness problem of the cosmological constant, many people have turned to the anthropic philosophy also for the SM. Actually applying the anthropic principle to the SM hierarchy problem is

not so convincing. After all, we can find plenty of models that reduce the fine tuning from 10^{14} down to 10^2. And the added ingredients apparently would not make our existence less possible. So why make our Universe so terribly unlikely? Indeed one can argue that the case of the cosmological constant is a lot different: the context is not as fully specified as the for the SM. Also so far there is no natural theory of the cosmological constant. On the other hand there is some similarity: Λ_{cosmo} corresponds to a vacuum energy density in all points of space just like the Higgs VEV v (which actually makes a contribution to Λ_{cosmo} that must be mysteriously canceled). With larger Λ_{cosmo} there is no galaxy formation, with larger v no nuclear physics. The anthropic way is now being kept in mind as a possibility.

We have seen that the hierarchy problem is manifested by the quadratic sensitivity of the scalar sector mass scale m to the physics at large energy scales. In the presence of a threshold at M one needs a fine tuning of order m^2/M^2 in order to reproduce the observed value of the running Higgs mass m at low energy. A possible point of view is that there are no new thresholds up to M_{Planck} (at the price of giving up GUTs, among other things) but, miraculously, there is a hidden mechanism in quantum gravity that solves the fine tuning problem related to the Planck mass [47, 48]. For this one would need to solve all phenomenological problems, like DM, baryogenesis and so on, with physics below the EW scale. This point of view is extreme but allegedly not yet ruled out. In this context the sensational announcement by the BICEP2 Collaboration [49] of the observation of a rather large value of the ratio r of tensor to scalar polarization modes in the Cosmic Microwave Background, $r \sim 0.2 \pm^{0.07}_{0.05}$. This result would imply an energy scale of inflation given by $V_{infl}^{1/4} \sim 2.2\ 10^{16}\ (r/0.2)^{1/4}$ (note the fourth root that makes this energy scale rather insensitive to the precise value of r). The coincidence of this energy scale with M_{GUT} is really amazing. For the implications of the BICEP2 results on axion masses and couplings, see Refs. [50, 51]. It must be stressed that the BICEP2 claim needs to be confirmed by new data, also in view of widespread doubts on the procedure of subtraction of the dust foreground [52].

Possible ways to realize the no threshold program are discussed in Ref. [47]: one has to introduce three RH neutrinos, N_1, N_2 and N_3 which are now light: for N_1 we need m_1 few keV, while $m_{2,3}$ few GeV but with a few eV splitting. With this rather ad hoc spectrum N_1 can explain DM and $N_{2,3}$

baryogenesis. The active neutrino masses are obtained from the see-saw mechanism, but with very small Dirac Yukawa couplings. Then the data on neutrino oscillations can be reproduced. The RH N_i can give rise to observable consequences (and in fact only a limited domain of the parameter space is still allowed). In fact N_1 could decay as $N_1 \to \nu + \gamma$ producing a line in X-ray spectra at $E_\gamma \sim m_1/2$. It is interesting that a candidate line with $E_\gamma \sim 3.5$ keV has been identified in the data of the XMM-Newton X-ray observatory on the spectra from galaxies or galaxy clusters [53]. As for $N_{2,3}$ they could be looked for in charm meson decays if sufficiently light. A Letter of Intent for a dedicated experiment at the CERN SpS has been presented to search for these particles [54].

In this class of theories one can also mention a more restrictive dynamical possibility: scale invariant theories possibly including gravity (see [55] and Refs. therein) where only a-dimensional couplings exist and there is a spontaneous breaking of scale invariance. The problem, not surprisingly, is to explain the two very different scales of symmetry breaking at the EW and the Planck scale.

7 Summary and conclusion

Among the main results at the LHC7-8 have been the discovery of a Higgs boson that, within the limits of the present, not too precise, accuracy, very much looks as minimal, elementary and standard and the absence of any direct or indirect signal of accompanying NP, which was expected on the basis of naturalness. Apparently our naive notion of naturalness has failed as a heuristic principle. We can say that we expected complexity and instead we have found a maximum of simplicity. Of course there are strong empirical evidences for NP beyond the SM that mostly arise not from accelerators but, one could say, from the sky, like Dark Energy, DM, baryogenesis and neutrino masses. But the picture repeatedly suggested by the data in the last 20 years is simple and clear: take the SM, extended to include Majorana neutrinos, which can explain the smallness of active neutrino masses by the see-saw mechanism and baryogenesis through leptogenesis, plus some form of DM, as valid up to some very high energy. Indeed at present in particle physics the most crucial experimental problem is the nature of DM. In this case a vast variety of possible solutions exist from WIMPS to axions or to keV sterile neutrinos or.... Clearly which of the many possible solutions or which combination of them will even-

tually be established will impose a well definite path for going beyond the SM. We have discussed a number of approaches to confront the naturalness riddle, including insisting on minimizing the fine tuning (FT) within the present experimental constraints or accepting FT only up to a large intermediate scale but still far below M_{GUT}), like for split SUSY or making the extreme choice of a total acceptance of FT: as in the anthropic point of view or arguing that possibly there is no FT with no new threshold up to M_{Pl} and invoking some miracle within the theory of quantum gravity (at the price of giving up Grand Unification and heavy RH neutrinos below the Planck scale). Clearly we are experiencing a very puzzling situation but, to some extent, this is good because big steps forward in fundamental physics have often originated from paradoxes. We highly hope that the continuation of the LHC experiments will bring new light on these problems.

8 Acknowledgements

I am very grateful to the Organizers (in particular to Profs. Gianpaolo Mannocchi and Roberto Fusco-Femiano) for their invitation and hospitality. This work has been partly supported by the Italian Ministero dell'Università e della Ricerca Scientifica, under the COFIN program (PRIN 2008), by the European Commission, under the networks "LHCPHENONET" and "Invisibles".

References

1. ATLAS Collaboration, G. Aad *et al.*, Phys.Lett. **B716** 1 (2012), ArXiv:1207.7214.

2. CMS Collaboration, S. Chatrchyan *et al.*, Phys.Lett. **B 716**30 (2012) , ArXiv:1207.7235.

3. F. Englert and R. Brout,Phys. Rev. Lett. **13** 321 (1964) ; P. W. Higgs, Phys. Lett. **12** 132 (1964) ; Phys. Rev. Lett. **13**508 (1964) ; Phys. Rev. **145** 1156 (1966) ; G.S.Guralnik, C.R.Hagen and T.W.B.Kibble, Phys. Rev. Lett. **13**, 585 (1964).

4. E. Gildener, Phys. Rev. **D 14**, 1667 (1976); L. Maiani, in Proc. of the Summer School on Particle Physics, Gif-sur-Yvette, 3-7 Sep 1979, Ed. by M. Davier et al., IN2P3, Paris, France (1979); M. Veltman, Acta Phys.

Polon. **B12** 437 (1981); E. Witten, Nucl. Phys. **B 188**, 513 (1981) and Phys. Lett. **B 105** 267 (1981).

5. MEG Collab., J. Adam *et al*, ArXiv:1303.0754.

6. ACME Collaboration, J. Baron *et al*, Science **343**, 269 (2014), ArXiv:1310.7534.

7. G.W. Bennett et al., Phys. Rev. **D73**, 072003 (2006) ; B. L. Roberts, Chin. Phys. **C34**, 741 (2010).

8. M. Davier, A. Hoecker, B. Malaescu and Z. Zhang, Eur. Phys. J. **C 71**, 1515 (2011); K. Hagiwara *et al.*, J. Phys. **G 38**, 085003 (2011); M.Benayoun *et al.*, ArXiv:1210.7184; M. Davier and B. Malaescu, ArXiv:1306.6374; A. Hoecker and W. Marciano, The Muon Anomalous Magnetic Moment, in Particle Data Group, J. Beringer et al, Phys. Rev. **D86**, 010001(2012).

9. M. Baak *et al.*, (Gfitter), Eur. Phys. J. **C 72**, 2205 (2012), ArXiv:1209.2716; ArXiv:1407.3792; M. Ciuchini*et al.*, JHEP **1308** 106 (2013), ArXiv:1306.4644.

10. B. W. Lee, C. Quigg and H.B. Thacker, Phys.Rev. **D16**1519 (1977).

11. G. Degrassi *et al.*, JHEP **1208** 098 (2012), ArXiv:1205.6497; D. Buttazzo *et al.*, JHEP **1312**089 (2013), ArXiv:1307.3536.

12. See, for example: R. Barbieri, ArXiv:1309.3473.

13. V. Branchina and E. Messina, Phys. Rev. Lett. **111**, 241801 (2013), ArXiv:1307.5193; V. Branchina, ArXiv:1405.7864.

14. G. Altarelli and D. Meloni, JHEP **1308** 021 (2013), ArXiv:1305.1001.

15. G. Altarelli and F. Feruglio, New J. Phys. **6**,106 (2004) , ArXiv:hep-ph/0405048; R. N. Mohapatra and A. Y. Smirnov, Ann. Rev. Nucl. Part. Sci. **56**,569 (2006) , ArXiv:hep-ph/0603118; W. Grimus, PoS P2GC 001 (2006) , ArXiv:hep-ph/0612311; M. C. Gonzalez-Garcia and M. Maltoni, Phys. Rept. **460**,1 (2008) , ArXiv:0704.1800.

16. P. Minkowski, Phys. Letters **B67**,421 (1977); T. Yanagida, in *Proc. of the Workshop on Unified Theory and Baryon Number in the Universe*, KEK,

March 1979; S. L. Glashow, in "Quarks and Leptons", Cargèse, ed. M. Lévy et al., Plenum, 1980 New York, p. 707; M. Gell-Mann, P. Ramond and R. Slansky, in *Supergravity*, Stony Brook, Sept 1979; R. N. Mohapatra and G. Senjanovic, Phys. Rev. Lett. **44**,912 (1980).

17. F. Vissani, ArXiv: hep-ph/9709409.

18. J. Elias-Miro *et al.*, ArXiv:1112.3022; I. Masina, ArXiv:1209.0393.

19. K. Zuber, Acta Phys. Polon. **B37**,1905 (2006), ArXiv:nucl-ex/0610007.

20. K. Kajantie, M. Laine, K. Rummukainen, and M. E. Shaposhnikov, Phys.Rev.Lett. **77** 2887 (1996), arXiv:hep-ph/9605288; M. Dine and A. Kusenko, Rev.Mod.Phys. **76** 1 (2003), arXiv:hep-ph/0303065.

21. For a review see, for example: M. Trodden, Rev. Mod. Phys. **71**, 1463 (1999), ArXiv:hep-ph/9805252.

22. M. Fukugita and T. Yanagida, Phys. Lett. **B 174**, 45 (1986).

23. For reviews see, for example: W. Buchmuller, R.D. Peccei and T. Yanagida, Ann.Rev.Nucl.Part.Sci. **55**, 311 (2005), ArXiv:hep-ph/0502169; S. Blanchet and P. Di Bari, New J. Phys. **14**,125012 (2012) ; T. Hambye, New J. Phys. **14**, 125014 (2012).

24. L. Calibbi, J. M. Lindert, T. Ota, Y. Takanishi, ArXiv:1405.3884.

25. A. De Simone, G. F. Giudice, A. Strumia, ArXiv:1402.6287

26. R. D. Peccei, in CP Violation, ed. C. Jarlskog; Adv. Ser. Direct. High Energy Phys. (Worldscientific Pub. Co., Singapore, 1989) 503.

27. R.D. Peccei, H. R. Quinn, Phys. Rev. Lett. **38** (1977) 1440; Phys. Rev. **D16** (1977) 1791; S. Weinberg, Phys. Rev. Lett. **40** 223 (1978) ; F. Wilczek, Phys. Rev. Lett. **40** 279 (1978).

28. J. E. Kim, AIP Conf.Proc. **1200** 83 (2010) , ArXiv:0909.3908.

29. J.E. Kim and G. Carosi, Rev. Mod. Phys. **82** 557 (2010), ArXiv:0807.3125.

30. G. D. Kribs, A. Martin and A. Menon, ArXiv:1305.1313; K. Krizka, A. Kumar and D. E. Morrissey, ArXiv:1212.4856; R. Auzzi, A. Giveon, S. B. Gudnason and T. Shacham, JHEP **1301** 169 (2013), ArXiv:1208.6263; J. R. Espinosa, C. Grojean, V. Sanz and M. Trott, JHEP **1212** 077 (2012), ArXiv:1207.7355], Z. Han, A. Katz, D. Krohn and M. Reece, JHEP **1208** 083 (2012), ArXiv:1205.5808, H. M. Lee, V. Sanzand M. Trott, JHEP **1205** 139 (2012), ArXiv:1204.0802; Y. Bai, H.-C. Cheng, J. Gallicchio and J. Gu, JHEP **1207** 110 (2012), ArXiv:1203.4813; B. Allanach and B. Gripaios, JHEP **1205** 062 (2012), ArXiv:1202.6616; G. Larsen, Y. Nomura and H. L. Roberts, JHEP **1206** 032 (2012), ArXiv:1202.6339; X.-J. Bi, Q.-S. Yan and P.-F. Yin, Phys.Rev. **D85** 035005 (2012), ArXiv:1111.2250; M. Papucci, J. T. Ruderman and A. Weiler, ArXiv:1110.6926; C. Brust, A. Katz, S. Lawrence and R. Sundrum, JHEP **1203**103 (2012), ArXiv:1110.6670; E. Arganda, J. L. Diaz-Cruz and A. Szynkman, Eur.Phys.J. **C73**2384 (2013) , ArXiv:1211.0163; Phys.Lett. **B722**100 (2013) , ArXiv:1301.0708; J. Cao, C. Han, L. Wu, J. M. Yang and Y. Zhang, JHEP **1211** 039 (2012) , ArXiv:1206.3865; E. Hardy, ArXiv:1306.1534; H. Baer et al, ArXiv:1306.3148; ArXiv:1306.4183.

31. P. Fayet, Nucl.Phys. **B90**104 (1975) ; R. Barbieri*et al.*, Phys. Rev. **D 75**, 035007 (2007), ArXiv:0607332; U. Ellwanger, C. Hugonie and A. M. Teixeira, Phys.Rept. **496** 1 (2010), ArXiv:0910.1785; M. Maniatis, Int.J.Mod.Phys. **A25** 3505 (2010) ; L. J. Hall, D. Pinner and J. T. Ruderman, JHEP **1204** 131 (2012) , ArXiv:1112.2703; K. Agashe, Y. Cui and R. Franceschini, JHEP **1302** 031 (2013), ArXiv:1209.2115; P. Athron, M. Binjonaid and S.F. King, ArXiv:1302.5291; R. Barbieri *et al.*, Phys. Rev. **D 87** 115018 (2013), arXiv:1304.3670; Phys. Rev. **D 88** 055011 (2013), ArXiv:1307.4937.

32. D. B. Kaplan and H. Georgi, Phys. Lett. **B 136**183 (1984) ; S. Dimopoulos and J. Preskill, Nucl. Phys. **B 199**, 206 (1982); T. Banks, Nucl. Phys. **B 243**, 125 (1984); D. B. Kaplan, H. Georgi and S. Dimopoulos, Phys. Lett. **B 136**, 187 (1984); H. Georgi, D. B. Kaplan and P. Galison, Phys. Lett. **B 143**, 152 (1984); H. Georgi and D. B. Kaplan, Phys. Lett. **B 145**, 216 (1984).; M. J. Dugan, H. Georgi and D. B. Kaplan, Nucl. Phys. **B 254**, 299 (1985).

33. G. F. Giudice *et al.*, JHEP **0706**, 045 (2007), Arxiv:hep- ph/0703164; C. Csaki, A. Falkowski and A. Weiler, JHEP **0809**, 008 (2008), ArXiv:0804.1954; R. Contino, ArXiv:1005.4269; R. Barbieri et al, ArXiv:1211.5085; B. Keren-Zur *et al.*, Nucl. Phys. **B 867**, 429 (2013), ArXiv:1205.5803; G. Cacciapaglia and F. Sannino, ArXiv:1402.0233; M. Carena, L. Da Rold and E. Pontn, JHEP **1406**159 (2014), ArXiv:1402.2987. M. Knig, M. Neubert and D. M. Straub, ArXiv:1403.2756; S. De Curtis, M. Redi and E. Vigiani, JHEP **1406** 071 (2014), ArXiv:1403.3116; D. Espriu. and F. Mescia, ArXiv:1403.7386.

34. R. Contino and G. Servant, JHEP **06** 026 (2008), ArXiv:0801.1679; J. Mrazek and A. Wulzer, Phys. Rev. **D 81**,075006 (2010), G. Dissertori et al, JHEP **1009**019 (2010) , ArXiv:1005.4414; A. De Simone *et al.*, ArXiv:1211.5663; B. Gripaios *et al.*, ArXiv:1406.5957.

35. CMS PAS B2G-12-012.

36. N. Arkani-Hamed and S. Dimopoulos, JHEP **0506**073 (2005), ArXiv:hep-th/0405159; G. F. Giudice and A. Romanino, Nucl. Phys. **B 699**65 (2004) , Erratum-ibid. **B706**, 65 (2005), ArXiv:hep-ph/0406088; N. Arkani-Hamed, S. Dimopoulos, G. F. Giudice and A. Romanino, Nucl. Phys. **B 709**3 (2005) , ArXiv:hep-ph/0409232; M. Binger, Phys. Rev. **D73**095001 (2006) , ArXiv:hep-ph/0408240; D. S. M. Alves, E. Izaguirre and J. G. Wacker, ArXiv:1108.3390; M. E. Cabrera, J. A. Casas and A. Delgado, ArXiv:1108.3867; M. Baumgart, D. Stolarski and T. Zorawski, ArXiv:1403.6118.

37. L. J. Hall and Y. Nomura, JHEP **1003**076 (2010) , ArXiv:0910.2235.

38. G. Giudice and A. Strumia, Nucl. Phys. **B858** 63 (2012), ArXiv:1108.6077; ArXiv:1407.4081.

39. B. Bajc, A. Melfo, G. Senjanovic and F. Vissani; Phys. Rev. **D 73**, 055001 (2006), ArXiv:hep-ph/0510139. S. Bertolini, L. Di Luzio and M. Malinsky, Phys. Rev. D 80, 015013 (2009) ArXiv:0903.4049; S. Bertolini, L. Di Luzio and M. Malinsky, AIP Conf. Proc. **1467**, 37 (2012), ArXiv:1205.5637 and references therein; L. Di Luzio, ArXiv:1110.3210; A. S. Joshipura and

K. M. Patel, Phys. Rev. **D 83**, 095002 (2011); ArXiv:1102.5148. F. Buccella, D. Falcone, C. S. Fong, E. Nardi and G. Ricciardi, Phys. Rev. **D 86**, 035012 (2012), ArXiv:1203.0829.

40. G.F. Giudice, R. Rattazzi and A. Strumia, Phys.Lett. **B715**142 (2012), ArXiv:1204.5465.

41. S. Weinberg, Rev. Mod. Phys. **61** 1 (1989); V. Sahni and A. Starobinsky, Int. J. Mod. Phys. **D 9**373 (2000); S. M. Carroll, Living Rev. Relativity **3** 1 (2001); E. J. Copeland, M. Sami and S. Tsujikawa, Int. J. Mod. Phys. **D15**1753 (2006) ; N. Straumann, Lect. Notes Phys. **721** 327 (2007) ; J. A. Frieman, M. S. Turner and D. Huterer, Ann. Rev. Astron. Astrophys. **46** 385 (2008), ArXiv:0803.0982; R. Bean, ArXiv:1003.4468; S. Bass, ArXiv:1210.3297.

42. S. Weinberg, Phys. Rev. Lett. **59**, 2607 (1987).

43. M. R. Douglas, ArXiv:hep-th/0602266; ArXiv:1204.6626.

44. A.N. Schellekens, ArXiv:0807.3249.

45. N. Arkani-Hamed and S. Dimopoulos, JHEP **0506**, 073 (2005), ArXiv:hep-th/0405159; N. Arkani-Hamed et al, Nucl.Phys. **B709** 3 (2005), ArXiv:hep-ph/0409232; G. Giudice and A. Romanino, Nucl.Phys. **B699**, 65 (2004), Erratum-ibid. **B706**, 65 (2005), ArXiv:hep-ph/0406088; N. Arkani-Hamed, S. Dimopoulos, S. Kachru, ArXiv:hep-ph/0501082; G. Giudice, R. Rattazzi, Nucl.Phys. **B757**, 19 (2006), ArXiv:hep-ph/0606105.

46. G. Giudice, in "Perspectives on LHC Physics", ed. by G. Kane and A. Pierce, World Sci., ArXiv:0801.2562.

47. M. Shaposhnikov, ArXiv:0708.3550; L. Canetti et al, ArXiv:1208.4607.

48. G. F. Giudice, ArXiv:1307.7879.

49. BICEP2 Collaboration, P. A. R. Ade *et al.*, ArXiv:1403.3985; ArXiv:1403.4302.

50. L. Visinelli and P. Gondolo, ArXiv:1403.4594.

51. E. Di Valentino *et al.*, ArXiv:1405.1860.

52. R. Flauger, J. Colin Hill and D. N. Spergel, ArXiv:1405.7351.

53. E. Bulbul *et al.*, ArXiv:1402.2301; A. Boyarsky *et al.*, ArXiv:1402.4119.

54. W. Bonivento *et al.*, ArXiv:1310.1762.

55. A. Salvio and A. Strumia, ArXiv:1403.4226.

Frascati Physics Series Vol. 58 (2014)
Frontier Objects in Astrophysics and Particle Physics
May 18-24, 2014

Hadronic Cross Sections in UHECR Air Showers and Accelerator Measurements

Ralf Ulrich *Karlsruhe Institute of Technology, Germany*
Ralph Engel *Karlsruhe Institute of Technology, Germany*

Abstract

The value of the inelastic cross section of cosmic ray particles with the atmosphere is one of the properties of hadronic collisions that has the largest impact on the fluctuations of the air shower cascade. This provides a very direct relation between measurements of hadronic cross sections at accelerators and fluctuations of extensive air showers. Analysis of cross section data can yield a very extensive understanding, starting from accelerators up to ultra-high energies.

1 Introduction

The most direct connection between measurements performed at accelerators and of hadronic interactions in cosmic ray induced air showers is possible via measurements of the inelastic hadronic cross sections. Given the state of the art

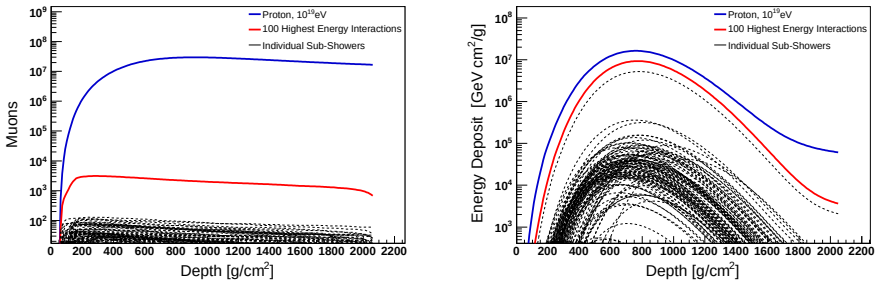

Figure 1: Decomposition of the longitudinal development of air showers, demonstrated exemplary for one proton shower at 10 EeV. The dashed lines indicate the contribution of the 100 highest energetic sub-showers. Left panel: Longitudinal development of the number of muons. Right panel: Longitudinal development of the electromagnetic energy deposit.

experiments, namely the Pierre Auger Observatory [1)], the Telescope Array [2)] and the experiments at the LHC [3)], it it possible to do studies of unprecedented reach.

The general relation of air shower observables to specific characteristics of hadronic interactions must be understood in order to exploit this relation for a measurement based on cosmic ray data. Figure 1 demonstrates this relation for one typical simulated air shower. The muon production in the shower is not significantly affected by the highest energy part of the cascade. For a precise analysis of the muon number in air showers it is, thus, necessary to describe hadronic interaction down to GeV energies. How to do this in a generally self-consistent way is at the moment still a matter of discussion and intensive research. However, the longitudianl shower development and in particular the location of the shower maximum is very well defined by the single most energetic collision in the shower cascade.

For this reason it is possible to perform precise interpretation of the measurement es of the longitudinal shower maximum, even while the muon production in air showers is still far from being understood.

2 Ultra-High Energy Cosmic Ray Measurements

It is a precondition for such studies using cosmic ray data that some minimal information on the nature of cosmic ray particles exists. This is still the most

severe limitation, but there are regions of the parameter space where this does not prevent measurements. Since the analysis of cosmic ray data is only of relevance, if the mass of the primary particle can be restricted, this is the most important task. It can be done most accurately by enhancing the proton fraction in the sample to be analysed. First, a range in primary cosmic ray energies must be selected that has astrophysical arguments for the presence of protons, and furthermore the general compatibility of the data with the assumption of a significant proton component must be given. Second, only the events with a very deep penetration into the atmosphere are selected. Since protons penetrate most deeply of all nuclei this is a very efficient technique to enhance the proton fraction in the sample. This assumes the absence of photons in the dataset, which is given in parts of the energy range where limits on the photon-fraction are $< 1\,\%$ [5].

Excellent preconditions for the study of the measurement of the proton-air cross section are given in the energy range around $10^{18}\,\mathrm{eV}$ to $10^{18.5}\,\mathrm{eV}$. The elongation rate, and the distribution of shower maxima strongly favours a large proton fraction [6], and in this transition region between galactic and extra-galactic cosmic rays, the presence of protons is expected either by the fragmentation of nuclei at higher energies, but also due to a primary proton component accelerated by extra-galactic and galactic accelerators.

This is the range of cosmic ray primaries that is most suited to perform a cross section measurement at ultra-high energies. At higher energies, it is questionable how quickly the proton fraction decreases. More information on the astrophysics behind the extra-galactic cosmic ray component is needed before extending a precise analysis in this direction.

Figure 2 illustrates a compilation of all cosmic ray based measurements.

3 Relation to Accelerator Measurements

In order to relate proton-air to the more fundamental proton-proton data, nuclear effects must be taken into account. There is significant experimental evidence that inclusive properties of nuclear collisions can be scaled from nucleon-nucleon data by taking the number of nucleons in the nuclear system into account. The Glauber/Gribov [7] multiple scattering theory provides a framework for this. However, higher order corrections are not insignificant and must be considered with care. The geometry of the nucleus and nucleon-

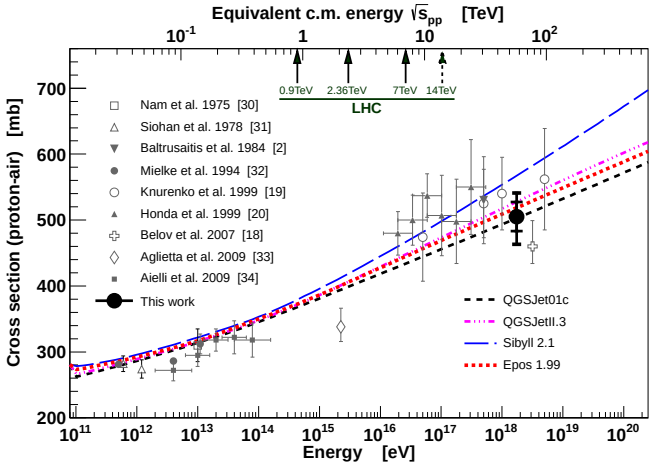

Figure 2: Compilation of measurements of the proton-air cross section from cosmic ray experiments.

nucleon correlations must be used from form factor measurements and models of nuclear structure.

Another very interesting correction is related to the phenomenon of single diffraction. In multiple scattering theory, processes of type $pA \to XA \to pA$, induced by low mass diffraction, produce a screening effect [8].

Thus, the relation between proton-proton and nuclear cross sections contain rich information about the nature of hadronic collisions. Figure 3 shows an overview of measurements of diffraction at accelerators. The experimental situation is not very conclusive. Progress in measurements as well as better theoretical understanding is needed to improve the situation. At the same time this will yield better information on the physics of proton-proton collisions, as well as on the interaction of cosmic ray particles with the atmosphere.

4 Summary

The relation of hadronic interactions in extensive air showers at ultra-high energies to measurements at accelerators is not only defined by the differences in the center-of-mass energies of the collisions. The phase space of the secondary particle production is of similar importance. This is interesting, since it also induces complementarity of cosmic ray and accelerator measurements. This

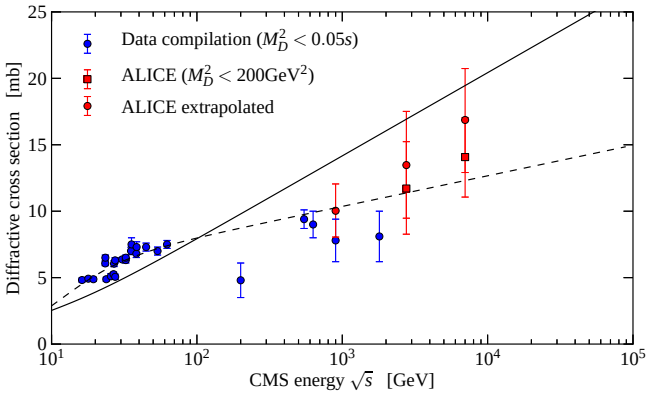

Figure 3: Comparison of measurements of the inelastic proton-proton cross section made at accelerators with data derived from cosmic ray experiments.

brings the additional opportunity to learn about different features of hadronic particle production at wide ranges of center-of-mass energies. However, this is also the reason for the additional challenge for accelerator based measurements that high-x_F secondary particle production, which is what matters in extensive air showers, is experimentally very difficult to access.

Figure 4 compares accelerator data with cosmic ray measurements, after the latter have been corrected for nuclear effects. The general agreement using typical models is very good.

In order to best exploit the complementarity between LHC and ultra-high energy cosmic ray experiments it is, thus, necessary to further improve the data analysis at LHC at low-luminosity using the forward (sub-)detectors. Also the explicit study of proton-oxygen collisions at LHC, and finally the utilization of the LHC beam for a fix target experiment to study large-x_F particle production will all be of paramount importance.

References

1. Pierre Auger Collaboration, NIM A **523** (2004) 50–95.

2. TA Collaboration, Nucl. Phys. Proc. suppl **175-176** (2008) 221–226.

3. ATLAS Collaboration, JINST **3** (2008) S08003; CMS Collaboration,

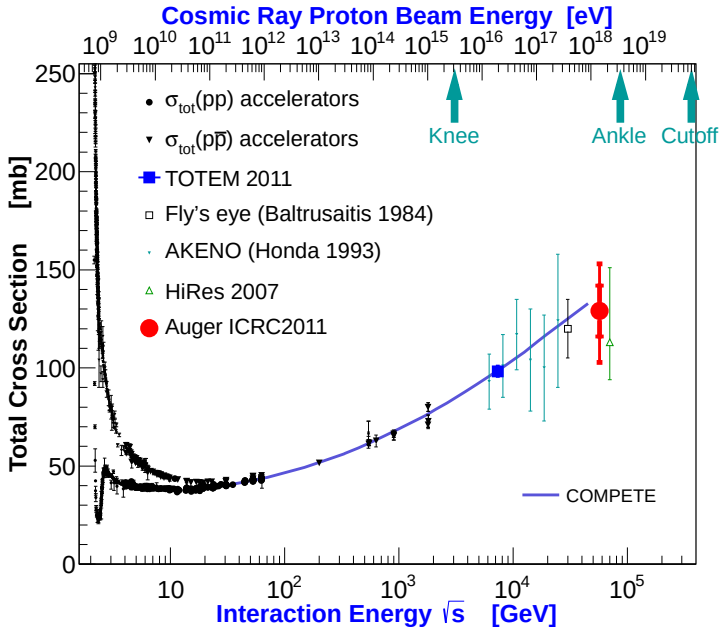

Figure 4: Compilation of inelastic proton-proton cross section measurements from accelerators and cosmic ray experiments. On the bottom the center-of-mass energy is shown, while on top the equivalent cosmic ray energy is indicated.

JINST **3** (2008) S08004. LHCb Collaboration, JINST **3** (2008) S08005. LHCf Collaboration, JINST **3** (2008) S08006. ALICE Collaboration, J. Phys. G **30** (2004) 1517.

4. TOTEM Collaboration, JINST **3** (2008) S08007.

5. Pierre Auger Collaboration, Astropart. Phys. **31** (2009) 399–406.

6. Pierre Auger Collaboration, PRL **104** 091101 (2010) 1986.

7. R. J. Glauber, Phys. Rev. **100** (1955) 242–248; R. J. Glauber and G. Matthiae, Nucl. Phys. B **21** (1970) 135–157; V. N. Gribov, Sov. Phys. JETP **26** (1968) 414–422.

8. M. L. Good and W. D. Walker, Phys. Rev. **120** (1960) 1857–1860.

Frascati Physics Series Vol. 58 (2014)
Frontier Objects in Astrophysics and Particle Physics
May 18-24, 2014

LUNA: FROM SUN TO NOVAE AND BEYOND

Carlo Broggini (the LUNA Collaboration)
INFN, via Marzolo 8, I-35131 Padova

Abstract

One of the main ingredients of nuclear astrophysics is the knowledge of the thermonuclear reactions which power the stars and, in doing so, synthesize the chemical elements. Deep underground in the Gran Sasso Laboratory the cross section of the key reactions of the proton-proton chain and of the Carbon-Nitrogen-Oxygen (CNO) cycle have been measured right down to the energies of astrophysical interest. The main results of LUNA are reviewed and their influence on our understanding of the properties of the neutrino and of the Sun is discussed. We then describe the current LUNA program mainly devoted to the nucleosynthesis of the light elements through the cross section measurement of the most important reactions in the CNO, Ne-Na and Mg-Al cycles. Finally, the future of LUNA towards the study of helium burning is outlined.

1 Introduction

Nuclear astrophysics studies all the reactions which provide the energy to the stars and realize the transmutation of the chemical elements. In particular, the knowledge of the reaction cross-section at the stellar energies is the heart of nuclear astrophysics. Thermonuclear reactions occur in the hot plasma of a star inside an energy window, the Gamow peak, which is far below the Coulomb energy arising from the repulsion between nuclei. In this region the cross section is given by:

$$\sigma(E) = \frac{S(E)}{E}\, exp(-2\,\pi\,\eta), \tag{1}$$

where $S(E)$ is the astrophysical factor (which contains the nuclear physics information) and η is given by $2\,\pi\,\eta = 31.29\,Z_1\,Z_2(\mu/E)^{1/2}$. Z_1 and Z_2 are the nuclear charges of the interacting particles, μ is the reduced mass (in units of amu), and E is the center of mass energy (in units of keV).

Cross sections are extremely small within the Gamow peak. Such smallness makes the star life-time of the length we observe, but it also makes impossible the direct measurement in the laboratory. The rate of the reactions, characterized by a typical energy release of a few MeV, is too low, down to a few events per year, in order to stand out from the laboratory background. Instead, the observed energy dependence of the cross-section at high energies is extrapolated to the low energy region, leading to substantial uncertainties. LUNA, Laboratory for Underground Nuclear Astrophysics, started twenty years ago to run nuclear physics experiments in an extremely low-background environment, the Gran Sasso Laboratory (LNGS), to reproduce in the laboratory what Nature makes inside the stars [1, 2].

2 LUNA at Gran Sasso

Two electrostatic accelerators able to deliver hydrogen or helium beam have been installed in LUNA: first a compact 50 kV "home made" machine [3] and then a commercial 400 kV one [4]. Common features of the two accelerators are the high beam current, the long term stability and the precise beam energy determination. In particular, the 400 kV accelerator is embedded in a tank, a cylinder of 0.9 m diameter and 2.8 m long, filled with an insulating mixture of N2/CO2 gas at 20 bar. The high voltage is generated by an inline Cockcroft-Walton power supply located inside the tank. The radio frequency ion source

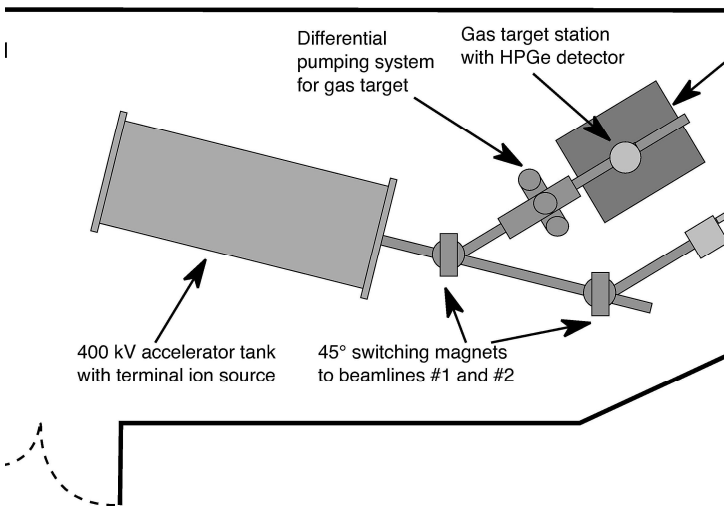

Figure 1: *The LUNA set-up with the 400 kV accelerator*

directly mounted on the accelerator tube can provide beams of hydrogen and He+ over a continuous operating time of 40 days. The ions can be sent into one of two different, parallel beam lines (fig.1), allowing the installation of two different target setups. In the energy range between 150 and 400 keV, the accelerator can provide up to 0.5 mA of hydrogen and 0.25 mA of helium at the target stations, with 0.3 keV accuracy on the beam energy, 100 eV energy spread, and 5 eV per hour long-term stability. The dolomite rock of Gran Sasso provides a natural shielding equivalent to at least 3800 meters of water which reduces the muon and neutron fluxes by a factor 10^6 and 10^3, respectively.

3 ^{3}He burning and solar neutrinos

The initial activity of LUNA has been focused on the ^{3}He(^{3}He,2p)^{4}He cross section measurement within the solar Gamow peak (15-27 keV). Such a reaction is a key one of the hydrogen burning proton-proton chain, which is responsible for more than 99% of the solar luminosity. A resonance in its cross section at the thermal energy of the Sun was suggested long time ago to explain the observed ^{8}B solar neutrino flux. As a matter of fact, such a resonance would decrease the

relative contribution of the alternative reaction ^{3}He(α,γ)^{7}Be, which generates the branch responsible for ^{7}Be and ^{8}B neutrino production in the Sun.

The experimental set-up was made of eight 1 mm thick silicon detectors of 5x5 cm^2 area placed around the beam inside the windowless target chamber filled with ^{3}He at the pressure of 0.5 mbar. The simultaneous detec-

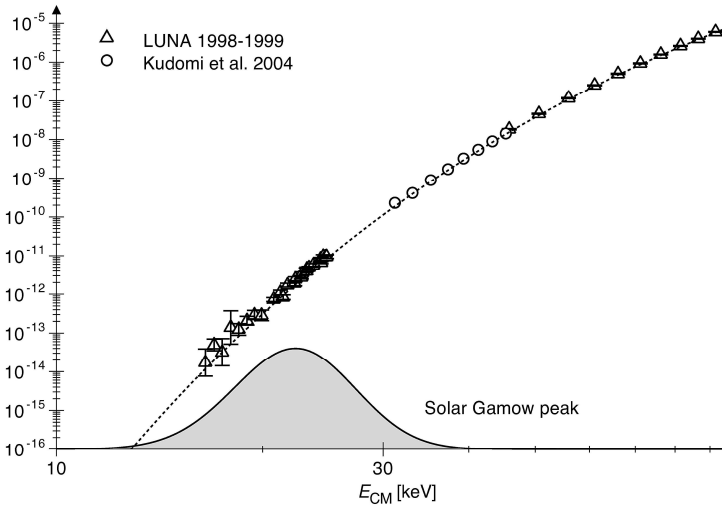

Figure 2: *Astrophysical S(E)-factor of ^{3}He(^{3}He,2p)^{4}He.*

tion of two protons has been the signature which unambiguously identified a ^{3}He(^{3}He,2p)^{4}He fusion reaction. Fig.2 shows the results from LUNA [5] together with higher energy measurements [6, 7, 8]. For the first time a nuclear reaction has been measured in the laboratory at the energy occurring in a star. In particular, at the lowest energy of 16.5 keV the cross section is 0.02 pbarn, which corresponds to a rate of about 2 events/month, rather low even for the "silent" experiments of underground physics. No narrow resonance has been found and, as a consequence, the astrophysical solution of the ^{8}B and ^{7}Be solar neutrino problem based on its existence has been definitely ruled out.

^{3}He(α,γ)^{7}Be, the competing reaction for ^{3}He burning, has been also measured by LUNA both by detecting the prompt γ rays and by counting of the decaying ^{7}Be nuclei with a total uncertainty of 4% [9].

4 The carbon and nitrogen content of the Sun core

^{14}N(p,γ)^{15}O is the slowest reaction of the CNO cycle and it rules its energy production rate. In particular, it is the key reaction to predict the ^{13}N and ^{15}O solar neutrino flux, which depends almost linearly on its cross section.

In the first phase of the LUNA study, data have been obtained down to 119 keV energy with solid targets of TiN and a 126% germanium detector. This way, the five different radiative capture transitions which contribute to the ^{14}N(p,γ)^{15}O cross section at low energy were measured. The total cross section was then studied down to very low energy in the second phase of the experiment by using a 4π BGO summing detector placed around a windowless gas target filled with nitrogen at 1 mbar pressure. At the lowest center of mass energy of 70 keV a cross section of 0.24 pbarn was measured, with an event rate of 11 counts/day from the reaction.

The results obtained first with the germanium detector [10, 11] and then with the BGO set-up [12] were about a factor two lower than the existing extrapolation [13, 14] from previous data [15, 16] at very low energy (fig.3). On the other hand, they were in good agreement with the reanalysis [17] of [16] and with the results obtained with indirect methods [18]. Because of this reduction the CNO neutrino yield in the Sun is decreased by about a factor of two.

In order to provide more precise data for the ground state capture, the most difficult one to be measured because of the summing problem, we performed a third phase of the ^{14}N(p,γ)^{15}O study with a composite germanium detector. This way the total error on the S-factor has been reduced to 8%: $S_{1,14}(0)$=1.57$\pm$0.13 keV barn [19]. This is significant because, finally solved the solar neutrino problem, we are now facing the solar composition problem: the conflict between helioseismology and the new metal abundances (i.e. the amount of elements different from hydrogen and helium) that emerged from improved modeling of the photosphere. Thanks to the relatively small error, it will be possible in the near future to measure the carbon and nitrogen content of the Sun core by comparing the predicted CNO neutrino flux with the measured one. As a matter of fact, the CNO neutrino flux is decreased by about 30% in going from the high to the low metallicity scenario. This way it will be possible to test whether the early Sun was chemically homogeneous, a key assumption of the standard Solar Model [20].

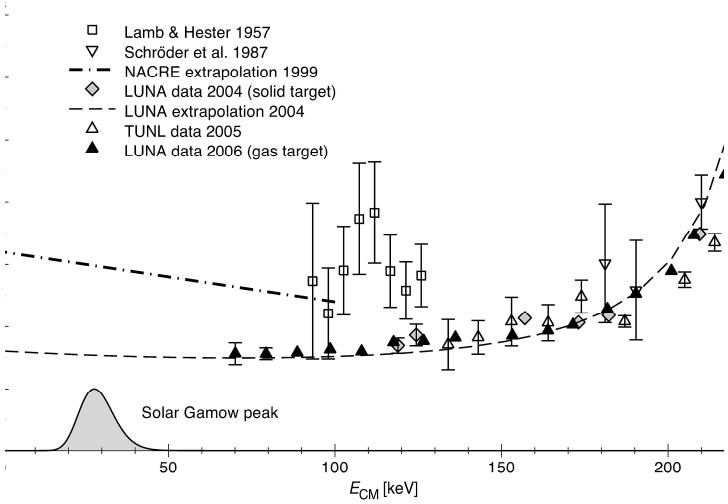

Figure 3: *Astrophysical S(E)-factor of the $^{14}N(p,\gamma)^{15}O$ reaction from direct measurements. The errors are statistical only (the systematic ones are similar.*

The lower cross section is affecting also stars which are more evolved than our Sun. In particular, the lower limit on the age of the Universe inferred from the age of the oldest stellar populations, the globular clusters, is increased by 0.7-1 billion years [21] up to 14 billion years and the dredge-up of carbon to the surface of asymptotic giant branch stars is more efficient [22].

5 Hydrogen burning and beyond

A new and rich program of nuclear astrophysics mainly devoted to CNO, Ne-Na and Mg-Al cycles started a few years ago after the solar phase of LUNA. Of particular interest are those bridge reactions which are connecting one cycle to the next, as $^{15}N(p,\gamma)^{16}O$ [23] and $^{17}O(p,\gamma)^{18}F$ [24], or which are key ingredients of gamma astronomy, as $^{25}Mg(p,\gamma)^{26}Al$ [25], or big-bang nucleosynthesis, as $^{2}H(\alpha,\gamma)^{6}Li$ [26] (LUNA measurements related to big-bang nucleosynthesis are the subject of a dedicated paper in these proceedings). Due to the higher Coulomb barrier of the reactions involved, the cycles become important at temperatures higher than the one of our Sun: hydrogen burning in the shell of

massive stars and Novae explosions (about 30-100, and 100-400 million degrees, respectively). Relatively unimportant for energy generation, these cycles are essential for the 'cooking' of the nuclei up to ^{27}Al. In particular, LUNA is now measuring ^{22}Ne(p,γ)^{23}Na, the reaction of the Ne-Na cycle with the highest uncertainty (up to a factor of 2000 in the region of interest), and ^{17}O(p,α)^{14}N, the reaction closing the second CNO cycle.

After hydrogen burning the natural evolution of LUNA is the study of the next step in the fusion chain towards ^{56}Fe: the helium burning. In particular, ^{12}C(α,γ)^{16}O, the "Holy Grail" of nuclear astrophysics, which determines the abundance ratio between carbon and oxygen, the two key elements to the development of life, and which shapes the nucleosynthesis in massive stars and the properties of supernovae. Equally important are ^{13}C(α,n)^{16}O and ^{22}Ne(α,n)^{25}Mg, the stellar sources of the neutrons which synthesize half of the trans-iron elements through the S-process: neutron captures followed by β decays. This program requires a new 3.5 MV accelerator which has already been financed and which is going to be installed underground in about three years from now in hall C of Gran Sasso.

6 Conclusions

More than twenty years ago LUNA started underground nuclear astrophysics in the core of Gran Sasso and it still remains the unique facility of this kind in the world. The extremely low background has allowed experiments with count rates as low as a few events per year. As a consequence, the important reactions which are responsible for the hydrogen burning in the Sun have been studied for the first time down to the relevant stellar energies. Since a few years LUNA is not focused anymore on the Sun and is studying those hydrogen burning reactions which are responsible for the abundance of the light elements in the Galaxy. The future of LUNA, which is going to start with the installation of a 3.5 MV accelerator underground in Gran Sasso, will be the study of the next step in the fusion chain beyond hydrogen burning: helium burning.

References

1. H. Costantini *et al*, Rep. Prog. Phys. **72**, 086301 (2009).
2. C. Broggini *et al*, Annu. Rev. Nucl. Part. Sci. **60**, 53 (2010).

3. U. Greife Greife *et al*, Nucl. Instrum. Methods A **350**, 327 (1994).
4. A. Formicola *et al*, (2003), Nucl. Instrum. Methods A **507**, 609 (2003).
5. R. Bonetti *et al*, Phys. Rev. Lett. **82**, 5205 (1999).
6. A. Krauss *et al*, Nucl. Phys. A**467**, 273 (1987).
7. M. Dwarakanath and H. Winkler, Phys. Rev. C **4**, 1532 (1971).
8. N. Kudomi *et al*, Phys. Rev. C **69**, 015802 (2004).
9. F. Confortola *et al*, Phys. Rev. C **75**, 065803 (2007).
10. C. Formicola *et al*, Phys. Lett. B **591**, 61 (2004).
11. G. Imbriani *et al*, Eur. Phys. J. A **25**, 455 (2005).
12. A. Lemut *et al*, Phys. Lett. B **634**, 483 (2006).
13. E.G. Adelberger *et al*, Rev. Mod. Phys. **70**, 1265 (1998).
14. C. Angulo *et al*, Nucl. Phys. A **656**, 3 (1999).
15. W.A.S. Lamb and R.E. Hexter, Phys. Rev. **108**, 1304, (1957).
16. U. Schroder *et al*, Nucl. Phys. A **467**, 240 (1987).
17. C. Angulo and P. Descouvement, Nucl. Phys. A **690**, 755 (2001).
18. A.M. Mukhamedzhanov *et al*, Phys. Rev. C **67**, 065804 (2003).
19. M. Marta *et al*, Phys. Rev. C **78**, 022802 (2008).
20. W.C. Haxton and A.M. Serenelli, Astrophysical Journal **687**, 678 (2008).
21. G. Imbriani *et al*, Astronomy and Astrophysics **420**, 625 (2004).
22. F. Herwig and S.M. Austin, Astrophysical Journal **613**, L73 (2004).
23. A. Caciolli *et al*, Astronomy and Astrophysics **533**, A66 (2011).
24. D.A. Scott *et al*, Phys. Rev. Lett. **109**, 202501 (2012).
25. O. Straniero *et al*, Astrophysical Journal **763**, 100 (2013).
26. M. Anders *et al*, Phys. Rev. Lett. **113**, 042501 (2014).

Frascati Physics Series Vol. 58 (2014)
Frontier Objects in Astrophysics and Particle Physics
May 18-24, 2014

Astroparticle Physics with the LHCf Detector at LHC

Alessia Tricomi on behalf of the LHCf Collaboration
University of Catania and INFN Catania, Italy

Abstract

The LHCf detector has been conceived to profit of the unprecedented energies reachable at LHC to provide calibrations of the Monte Carlo models used in High Energy Cosmic Rays (UHECR) Physics through the measurement of the neutral particle spectra produced in the very forward region at LHC. Results of the p-p as well as the p-Pb runs will be shown together with the future plans for the forthcoming run at 13 TeV.

1 Introduction

The origin and properties of UHECR is a long standing question in astroparticle Physics. Dedicated extensive air shower experiments are in place since many years and have strongly contributed to our understanding of High and Ultra High Energy Cosmic Ray Physics. Recently, in particular, the Pierre Auger

Collaboration [1] and the Telescope Array Collaboration [2], thanks to the excellent performance of their hybrid detector arrays, are providing us new exciting observations of UHECRs. Although these recent results have brought a deeper insight in primary cosmic ray properties, still they are largely affected by the poor knowledge of the nuclear interactions in the earth's atmosphere. The average and RMS of the measured depth of the shower maximum (X_{MAX}) are good indicators of the composition of UHECRs [3]. However the predictions of X_{MAX} by air-shower simulations depend on the hadronic interaction model used in the Monte Carlo. A calibration of the energy scale in the $10^{15} \div 10^{17}$ eV energy range accessible to LHC provides crucial input for a better interpretation of primary cosmic ray properties, in the region between the "knee" and the GZK cut-off. The Large Hadron Collider forward (LHCf) experiment was designed with the aim to provide a calibration of the hadronic interaction models in the whole energy range spanned by LHC by measuring the neutral forward particle produced in p-p as well as in p-Ion collisions.

2 The LHCf experiment

The LHCf experiment is composed by two independent position sensitive electromagnetic calorimeters, located on both side of the ATLAS experiment, 140 m away from the LHC-IP1 interaction point, inside the zero-degree neutral absorber (Target Neutral Absorber, TAN). Charged particles from the IP are swept away by the inner beam separation dipole before reaching the TAN, so that only photons mainly from π^0 decays, neutrons and neutral kaons reach the LHCf calorimeters.

Each calorimeter (ARM1 and ARM2) has a double tower structure, with the smaller tower located at zero degree collision angle, approximately covering the region with pseudo-rapidity $\eta > 10$ and the larger one, approximately covering the region with $8.4 < \eta < 10$. Four X-Y layers of position sensitive detectors (scintillating fibers in ARM1, silicon micro-strip detectors in ARM2) provide measurements of the transverse profile of the showers. The two tower structure allows to reconstruct the π^0 decaying in two γs, hitting separately the two towers, hence providing a very precise absolute energy calibration of the detectors. In the range E> 100 GeV, the LHCf detectors have energy and position resolutions for electromagnetic showers better than 5% and 200 μm, respectively. A detailed description of the LHCf experimental set-up and of the expected

physics performances can be found in Ref. [4].

3 Results at $\sqrt{s} = 900$ GeV and 7 TeV pp collisions

The LHCf experiment has succesfully taken data in 2009 and in 2010 until the detector was removed from the TAN region in July 2010 due to the increase of the luminosity above $10^{30}\mathrm{cm}^{-2}\mathrm{s}^{-1}$. In total, 200M shower events were taken in this Phase 1 operation. The energy scale of calorimeters was monitored during the operation by a UV pulse laser and by the peak position of reconstructed invariant mass corresponding to π^0 and the stability was 5%. The energy spectra of forward photons at $\sqrt{s}$ = 900 GeV [5] and 7 TeV [6] have been published together with the π^0 transverse momentum spectrum at $\sqrt{s}$ = 7 TeV [7]. Figure 1 shows the ratios of p_T spectra predicted by DPMJET 3.04 (solid, red), QGSJET II-03 (dashed, blue), SIBYLL 2.1 (dotted, green), EPOS 1.99 (dashed dotted, magenta), and PYTHIA 8.145 (default parameter set, dashed double-dotted, brown) to the combined ARM1 and ARM2 p_T spectra (black dots). Error bars have been taken from the statistical and systematic uncertainties. Among the hadronic interaction models tested in this analysis, EPOS 1.99 [8] shows the best overall agreement with the LHCf data. DPMJET 3.04 [9] and PYTHIA 8.145 [10] show harder spectra than the LHCf data, as well as SIBYLL 2.1 [11], while QGSJET II-03 [12] predicts π^0 spectra that are softer than the LHCf data and the other models. Although no model is able to reproduce the LHCf data perfectly, the LHCf data is in between of model predictions. A similar behaviour is also found in the photon spectra results both at 900GeV and at 7 TeV.

By fitting the p_T spectra in each rapidity bin it is possible to extract the average transverse momentum, $< p_T >$, which results to be consistent with typical values for soft QCD processes. Comparison between the LHCf and UA7 [13] results indicate an $< p_T >$ versus rapidity that is independent of the center of mass energy, in agreement with the expectation of EPOS 1.99, while SYBILL 2.1 tipically gives harder π^0 spectra, namely larger $< p_T >$, and QGSJET II-03 gives softer π^0 spectra, namely smaller $< p_T >$ than the experimental data.

LHCf is now finalizing the analysis of the forward neutron spectra. This measurement is particularly important since it is expected to provide an im-

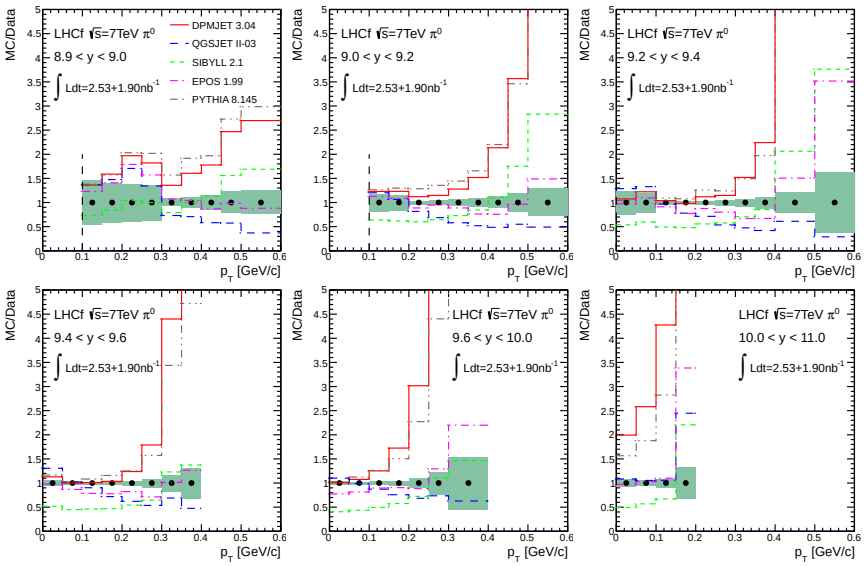

Figure 1: Ratio of the combined ARM1 and ARM2 π^0 p_T spectra to the p_T spectra predicted by various hadronic interaction models. Shaded areas indicate the range of total uncertainties of the combined spectra. Figure from Ref. [7].

portant hint for the problem of cosmic-ray muon excess reported by both Auger [14] and TA [15] Collaborations. This excess could be indeed interpreted in terms of an underestimation of the baryon production in the hadronic interaction models used to derive the CR spectra [16]. The analysis workflow for the neutron energy spectra measurement is similar to the workflow used for the γ analysis, described in [6], however detailed optimization for hadron reconstruction has been carried on [17]. The luminosity has been measured with the help of the LHCf front counter rates, properly normalized with the Van der Meer LHC scan. Particle identification has been carried out by looking at the longitudinal shower development, using two dimensional cuts in the L20% and L90% plane, where L20% and L90% are the longitudinal depths containing 20% and 90% of the total deposited energy, respectively. Hit position has been evaluated by using the transverse shower distribution, measured with the position sensitive layers, to optimally correct the energy measured for the leakage effects.

Figure 2 shows the preliminary energy spectra of forward neutrons measured by the LHCf detector compared with the MC predictions. Due to the

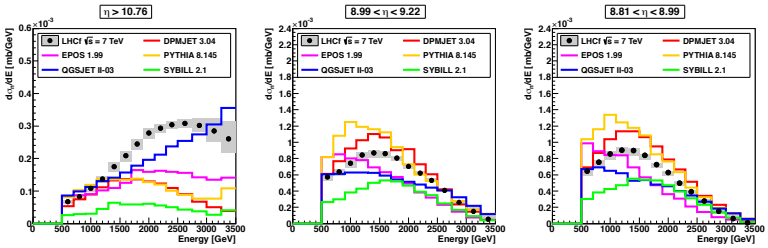

Figure 2: Preliminary neutron spectra measured by LHCf in the $\sqrt{s} = 7$ TeV p-p collisions in the small and large tower. The black markers and gray hatched areas show the combined results of the LHCf Arm1 and Arm2 detectors and the systematic errors, respectively.

limited energy resolution for hadron decay, a detailed unfolding procedure, currently underway, is necessary to extract the final spectra. As a preliminary result of the 7 TeV data analysis LHCf found a higher yield of neutrons in the $\eta > 10.76$ region than any Monte Carlo model but QGSJET II-03.

4 Results in p-Pb collision at $\sqrt{s} = 5.02$ TeV

In early 2013, LHCf took data with p-Pb collisions at the center-of-mass collision energy per nucleon of $\sqrt{s_{NN}} = 5.02$ TeV. Only the Arm2 detector was used for the operations. In most of the operation time, the detector was located on the p-remnant side. The measurements at the proton remnant side of p-Pb collisions at the LHC provide a new information of the nuclear effect in the forward particle production which is particularly important for HECR Physics since the interaction of the primary cosmic rays in the atmosphere occur between proton and nucleus or between nucleus and nucleus, where one of the nucleus is light component [19]. The data have been analysed to extract the π^0 spectra. Half of the forward π^0 production arise from Ultra-Peripheral collisions (UPC). The spectra obtained after the UPC subtraction have been compared with the spectra in p-p collisions at 5.02 TeV, which have been obtained by interpolationg the results at 2.76 TeV and 7 TeV [18]. Results are

also compared with the prediction of EPOS 1.99, DPMJET 3.04 and QGSJET II-03 models, as shown in Fig. 3.

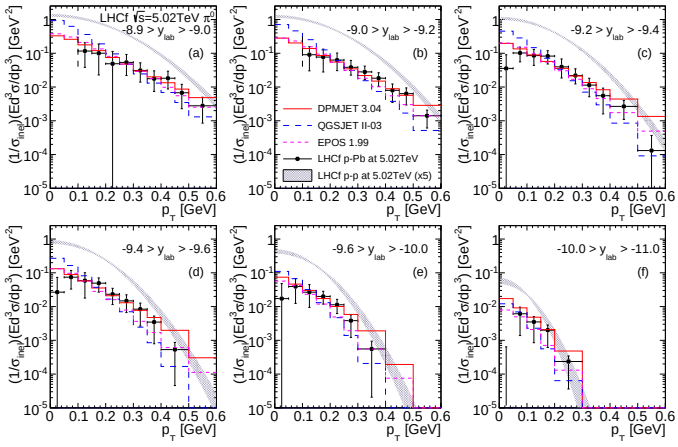

Figure 3: Experimental p_T spectra measured by LHCf in p-Pb collisions at $\sqrt{s_{NN}} = 5.02$ TeV after the subtraction of the UPC component (filled circles). Error bars indicate the total uncertainties incorporating both statistical and systematic uncertainties. Hadronic interaction models predictions and derived spectra for p-p collisions at are also shown.

From the comparison of p-p and p-Pb results the nuclear modification factor, R_{pPb}, has been extracted. It is one of the important effects for modeling interactions between cosmic-rays and atmosphere, since it quantifies the effect of the nuclear medium on the production of forward energetic particles. Figure 4 shows R_{pPb} measured by LHCf compared with the predictions by DPMJET 3.04 (red solid line), QGSJET II-03 (blue dashed line), and EPOS 1.99 (magenta dotted line). The LHCf measurements, although with a large uncertainty which increases with p_T show a strong suppression with R_{pPb} equal 0.1 at $p_T \approx 0.1$ GeV rising to 0.3 at $p_T \approx 0.6$ GeV. All hadronic interaction models predict small values of $R_{pPb} \approx 0.1$, and they show an overall good agreement with the LHCf measurements within the uncertainty.

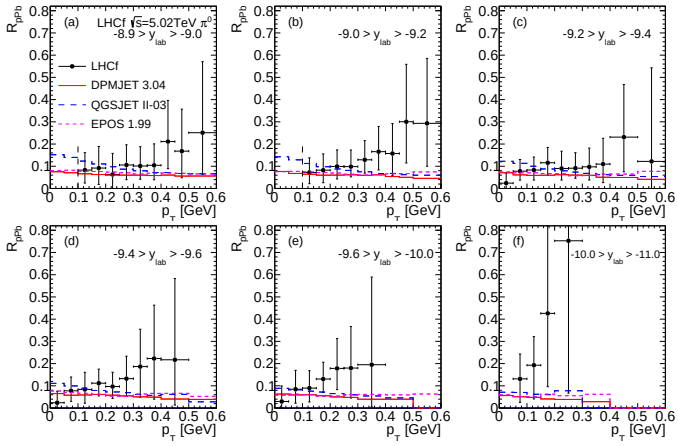

Figure 4: Nuclear modification factor for π^0s as measured by LHCf (black solid circle) compared with the expectaion of DPMJET 3.04 (red solid line), QGSJET II-03 (blue dashed line), and EPOS 1.99 (magenta dotted line). Error bars indicate the total uncertainties incorporating both statistical and systematic uncertainties.

5 Conclusions and Future Plans

The LHCf experiment has successfully completed the Phase 1 operation with $\sqrt{s}$ = 900 GeV and 7 TeV p-p collisions in 2009 and 2010 and published the results of forward photon and π^0 spectra. No hadron interaction model was found to reproduce the LHCf data perfectly, however, some of them have reasonable agreement with data.

LHC will soon restart its operation with p-p collisions at the highest collision energy of $\sqrt{s} = 13$ TeV. Since the radiation dose at $\sqrt{s} = 13$ TeV is about 8 times higher than at 7 TeV, the two calorimeters have been upgraded to optimize their radiation hardness. The plastic scintillators of the calorimeters have been replaced with crystal scintillators of Gd_2SiO_5 (GSO). The SciFi hodoscopes have also been replaced with GSO bar bundles. The LHCf detectors will be re-installed inside the LHC tunnel in the end of 2014. A dedicated run to LHCf with low luminosity is foreseen just before summer 2015.

In addition to the LHC plan, a proposal has been submited to the BNL

PAC to take data with the LHCf detector at RHIC. Data taken in p-Pb collisions in early 2013 and data that will be taken by future operations, $\sqrt{s} = 13$ TeV p-p, p-light nucleus and operations at RHIC, are critical to verify hadron interaction models and to improve our knowlegde of HECR physics.

References

1. G. Rodriguez [Pierre Auger Collaboration], Nucl. Instrum. Meth. A **742** (2014) 261.
2. T. Fujii [Telescope Array Collaboration], EPJ Web Conf. **52** (2013) 06003.
3. [Pierre Auger Collaboration], arXiv:1409.5083 [astro-ph.HE].
4. O. Adriani et al., JINST **3** (2008) S08006.
5. O. Adriani et al., Phys. Lett. **B715** (2012) 298.
6. O. Adriani et al., Phys. Lett. **B703** (2011) 128.
7. O. Adriani et al., Phys. Rev. D **86** (2011) 092001
8. K. Werner et al., Nucl.Phys.Proc.Suppl. **175-176** (2008)
9. F.W. Bopp et al., Phys. Rev. **C77** (2008) 014904.
10. T. Sjöstand, et al., Comput. Phys. Comm. **178** (2008) 852.
11. E.-J. Ahn et al., Phys. Rev. **D80** (2009) 094003.
12. S. Ostapchenko, Phys. Rev. **D83** (2011) 014108.
13. E. Paré et al., Phys. Lett. B **242** (1990) 531.
14. P. Abreu et al. [The Pierre Auger Collaboration], Proc. of 32th Int. Cosmic Ray Conf., Beijing (2011), [arXiv:1107.4804 [astro-ph.HE]].
15. T. Abu-Zayyad, et al. [TA Collaboration], Astrophys. J. 768 (2013) L1
16. T. Pierog and K. Warner, Phys. Rev. Lett. **101** (2008) 171101.
17. K. Kawade et al., JINST **9** (2014) P03016.
18. O. Adriani et al., Phys. Rev. C **89** (2014) 065209.
19. O. Adriani, et al., CERN-LHCC-2011-015. LHCC-I-021 (2011).

Frascati Physics Series Vol. 58 (2014)
Frontier Objects in Astrophysics and Particle Physics
May 18-24, 2014

SNRs AS COSMIC ACCELERATORS

Marco Miceli
INAF-Osservatorio Astronomico di Palermo, Piazza del Parlamento 1, 90134 Palermo, Italy

Abstract

Supernova remnants are considered to be the main source of galactic cosmic rays up to the knee of the cosmic rays energy distribution. I review the increasing set of indications supporting this scenario together with the main open issues.

1 Introduction

The idea of a possible association between supernova remnants (SNRs) and cosmic rays (CRs) dates back to the 1930s, when it was first proposed that the observed flux of CRs can be due to a population of (extragalactic) supernova explosions [5]. Indeed, the current scenario invokes an extragalactic origin only for very energetic CRs, i. e., particles with energies $> 10^{18}$ eV, given that their gyro-radii are larger than the thickness of the Milky Way. On the other hand,

galactic SNRs are considered to be responsible for the acceleration of CRs up to 3 PeV (i. e., the "knee" in the CR spectrum), though it has been proposed that even energies of the order of 10^{18} eV can be achieved in our Galaxy [16].

The simplest argument supporting the association between CRs and SNRs is the energy argument [21], as summarized below. Different estimates of the energy density of CRs concur in providing a value $\epsilon \approx 1-2$ eV cm^{-3} (data from the Voyager and Pioneer spacecrafts indicate [44] $\epsilon = 1.8$ eV cm^{-3}). This value is much higher than that associated with starlight (~ 0.3 eV cm^{-3}), average magnetic field (~ 0.25 eV cm^{-3}), turbulence (~ 0.3 eV cm^{-3}), and thermal energy (~ 0.01 eV cm^{-3}), and this removes many galactic sources from the list of possible accelerators. Considering that the bulk of CR energy is carried by GeV particles with a galactic confinement times of about 1.5×10^7 yr [45], the power needed to sustain the observed CR flux is of $\sim 2 - 3 \times 10^{50}$ ergs per century. The characteristic energy released in a SN explosion is 10^{51} erg and the rate of SN explosions in the Milky Way is of about 2-3 events per century [35]. Therefore SNRs can power the CRs in our Galaxy if they lose just $\sim 10\%$ of their energy in the acceleration process.

2 The acceleration mechanisms

The basic mechanism of particle acceleration is the Diffusive Shock Acceleration (DSA) and relies on the Fermi process [20] applied to SNR shock fronts, where the pre-shock and post-shock medium act as "moving mirrors", thus allowing first-order energy gains in v_{shock}/c for particles scattering back and forth the shock front. This scenario was introduced in a series of papers published in the late 1970s [4, 25, 9, 10, 13] and is described in details in several reviews [15]. Interestingly, this process naturally produces a power law spectrum of particle energies $N(E)dE \propto E^{-s}dE$ with an index $s = (r+2)/(r-1)$, where r is the shock compression ratio. For a high Mach number shock, which is typical of a young SNR, $r = 4$, and then $s = 2$, which is very close to the exponent 2.7 observed for the differential energy spectrum of CRs, the small discrepancy possibly being associated with energy-dependent escape mechanisms.

The timescale of the acceleration process,t_{acc}, is also comparable with the age of the youngest observed SNRs. The value of t_{acc} can be estimated as [18] $t_{acc} = 3/(V_1 - V_2)\ (D_1/V_1 + D_2/V_2)$, where $V_{1,2}$ and $D_{1,2}$ are the upstream / downstream bulk velocities and diffusion coefficients. For a particle with

energy E, the acceleration timescale is $\sim 150(E/(100\text{TeV})$ yr, for $B = 100$ μG and $v_{shock} = 5000$ km/s (typical of a young SNR).

If SNRs lose a significant fraction of their energy to accelerate ultrarelativistic particles, the shock cannot be treated as adiabatic. The loss of energy "deposited" in the CRs and their non-linear back-reaction on the background plasma are predicted to increase the shock compression ratio above the Rankine-Hugoniot limit and decrease the post-shock temperature [17, 26, 14, 43]. This effects is known as "shock modification". Another notable effect consists in the magnetic field amplification [11]: cosmic rays streaming outward produce an electron return current. Electrons are then deflected by the magnetic field, thus originating a turbulent, amplified magnetic field.

3 Synchrotron emission: ultrarelativistic electrons

The direct proof that SNR shocks can accelerate particles up to ultrarelativistic regimes is the ubiquitous presence of synchrotron radio shells in all the galactic SNRs [22]. This emission clearly traces the presence of GeV electrons. Moreover, the detection of synchrotron X-ray emission in SN 1006 [24] and then in other young SNRs [34, 41] has proved that in these sources the electron energy can reach values of the order of 10 TeV. X-ray spatially resolved spectral analysis of the shape of the cutoff in the synchrotron emission of SN 1006 has revealed that the maximum energy that electrons can achieve in the acceleration process is limited by their radiative losses [29, 28]. Similar results have been obtained by analyzing Tycho [30] and RX J1713.7-3946 [37, 46]. These results are promising, because suggest that hadrons, that do not suffer significant radiative losses, may be, in principle, accelerated up to higher energies.

The predicted effects of magnetic field amplification have also been observed in several cases. The thinness of the X-ray synchrotron filaments of young SNRs reveals that $B \sim 100 - 600$ μG [42, 7, 8, 6, 31]. Moreover, in RX J1713.73946 and in Cas A, some knotty X-ray synchrotron emitting regions varies on timescales of a few years, which may be indicative of very short synchrotron cooling times, corresponding to $B \sim 1$ mG [40, 32, 39].

Effects of shock modification have also been observed in SN 1006, where the post-shock density has been found to increase with the efficiency of particle acceleration, thus suggesting an efficient hadron acceleration [27].

4 Gamma-ray emission: leptonic vs. hadronic scenario

The current generation of TeV and GeV observatories has allowed us to reveal the γ-ray emission of a (rapidly growing) number of galactic SNRs. Gamma-ray emission can provide a striking signature of hadron acceleration, being associated with π^0 decay following proton-proton collision due to accelerated hadrons impacting the ambient medium (hadronic scenario). However, it can also be the result of IC scattering from the relativistic electrons on the CMB (and/or dust-emitted IR photons) and nonthermal bremsstrahlung (leptonic scenario). It is not easy to discriminate between these scenarios. For example, the γ-ray emission of RX J1713.7-3946 has been interpreted by different groups as leptonic [19, 33] or hadronic [12], though the Fermi LAT spectrum has almost ruled out the hadronic scenario [1].

Quite surprisingly, while it is difficult to ascertain the origin of the γ-ray emission of young, X-ray synchrotron emitting SNRs (e.g., Vela Jr. [36] or SN 1006 [23]), older SNRs clearly revealed the presence of high energy hadrons, as for W44 [3], W28 [2], and IC 443 [38]. All these middle-aged SNRs interact with dense clouds and the hadronic emission probably originates from CRs leaving the acceleration source and interacting with the dense ambient medium.

5 Acknowledgements

I thank R. Fusco Femiano and G. Mannocchi for their kind invitation to the Vulcano Workshop 2014

References

1. Fermi Collaboration. Observations of the Young Supernova Remnant RX J1713.7-3946 with the Fermi Large Area Telescope. *ApJ*, 734:28, June 2011.

2. Fermi Collaboration. Fermi Large Area Telescope Observations of the Supernova Remnant W28 (G6.4-0.1). *ApJ*, 718:348–356, July 2010.

3. Fermi Collaboration. Gamma-Ray Emission from the Shell of Supernova Remnant W44 Revealed by the Fermi LAT. *Science*, 327:1103–, February 2010.

4. W. I. Axford, E. Leer, and G. Skadron. The acceleration of cosmic rays by shock waves. *International Cosmic Ray Conference*, 11:132–137, 1977.

5. W. Baade and F. Zwicky. Remarks on Super-Novae and Cosmic Rays. *Physical Review*, 46:76–77, July 1934.

6. J. Ballet. X-ray synchrotron emission from supernova remnants. *Advances in Space Research*, 37:1902–1908, 2006.

7. A. Bamba, R. Yamazaki, M. Ueno, and K. Koyama. Small-Scale Structure of the SN 1006 Shock with Chandra Observations. *ApJ*, 589:827–837, June 2003.

8. A. Bamba, R. Yamazaki, T. Yoshida, T. Terasawa, and K. Koyama. A Spatial and Spectral Study of Nonthermal Filaments in Historical Supernova Remnants: Observational Results with Chandra. *ApJ*, 621:793–802, March 2005.

9. A. R. Bell. The acceleration of cosmic rays in shock fronts. I. *MNRAS*, 182:147–156, January 1978.

10. A. R. Bell. The acceleration of cosmic rays in shock fronts. II. *MNRAS*, 182:443–455, February 1978.

11. A. R. Bell. Turbulent amplification of magnetic field and diffusive shock acceleration of cosmic rays. *MNRAS*, 353:550–558, September 2004.

12. E. G. Berezhko and H. J. Völk. Nonthermal and thermal emission from the supernova remnant RX J1713.7-3946. *A&A*, 511:A34+, February 2010.

13. R. D. Blandford and J. P. Ostriker. Particle acceleration by astrophysical shocks. *ApJL*, 221:L29–L32, April 1978.

14. P. Blasi. A semi-analytical approach to non-linear shock acceleration. *Astroparticle Physics*, 16:429–439, February 2002.

15. P. Blasi. The origin of galactic cosmic rays. *A&A Rev.*, 21:70, November 2013.

16. A. M. Bykov and G. D. Fleishman. On non-thermal particle generation in superbubbles. *MNRAS*, 255:269–275, March 1992.

17. A. Decourchelle, D. C. Ellison, and J. Ballet. Thermal X-Ray Emission and Cosmic-Ray Production in Young Supernova Remnants. *ApJL*, 543:L57–L60, November 2000.

18. L. O. Drury. An introduction to the theory of diffusive shock acceleration of energetic particles in tenuous plasmas. *Reports on Progress in Physics*, 46:973–1027, August 1983.

19. D. C. Ellison, D. J. Patnaude, P. Slane, and J. Raymond. Efficient Cosmic Ray Acceleration, Hydrodynamics, and Self-Consistent Thermal X-Ray Emission Applied to Supernova Remnant RX J1713.7-3946. *ApJ*, 712:287–293, March 2010.

20. E. Fermi. On the Origin of the Cosmic Radiation. *Physical Review*, 75:1169–1174, April 1949.

21. V. L. Ginzburg and S. I. Syrovatsky. Origin of Cosmic Rays. *Progress of Theoretical Physics Supplement*, 20:1–83, 1961.

22. D. A. Green. A revised Galactic supernova remnant catalogue. *Bulletin of the Astronomical Society of India*, 37:45–61, March 2009.

23. H.E.S.S. Collaboration. A new SNR with TeV shell-type morphology: HESS J1731-347. *A&A*, 531:A81+, July 2011.

24. K. Koyama, K. Kinugasa, K. Matsuzaki, M. Nishiuchi, M. Sugizaki, K. Torii, S. Yamauchi, and B. Aschenbach. Discovery of Non-Thermal X-Rays from the Northwest Shell of the New SNR RX J1713.7-3946: The Second SN 1006? *PASJ*, 49:L7–L11, June 1997.

25. G. F. Krymskii. A regular mechanism for the acceleration of charged particles on the front of a shock wave. *Akademiia Nauk SSSR Doklady*, 234:1306–1308, June 1977.

26. M. A. Malkov and L. O'C Drury. Nonlinear theory of diffusive acceleration of particles by shock waves. *Reports on Progress in Physics*, 64:429–481, April 2001.

27. M. Miceli, F. Bocchino, A. Decourchelle, G. Maurin, J. Vink, S. Orlando, F. Reale, and S. Broersen. XMM-Newton evidence of shocked ISM in SN 1006: indications of hadronic acceleration. *A&A*, 546:A66, October 2012.

28. M. Miceli, F. Bocchino, A. Decourchelle, J. Vink, S. Broersen, and S. Orlando. The loss-limited electron energy in SN 1006: effects of the shock velocity and of the diffusion process. *ArXiv e-prints*, September 2013.

29. M. Miceli, F. Bocchino, A. Decourchelle, J. Vink, S. Broersen, and S. Orlando. The shape of the cutoff in the synchrotron emission of SN 1006 observed with XMM-Newton. *A&A*, 556:A80, August 2013.

30. G. Morlino and D. Caprioli. Strong evidence for hadron acceleration in Tycho's supernova remnant. *A&A*, 538:A81, February 2012.

31. E. Parizot, A. Marcowith, J. Ballet, and Y. A. Gallant. Observational constraints on energetic particle diffusion in young supernovae remnants: amplified magnetic field and maximum energy. *A&A*, 453:387–395, July 2006.

32. D. J. Patnaude and R. A. Fesen. Small-Scale X-Ray Variability in the Cassiopeia A Supernova Remnant. *AJ*, 133:147–153, January 2007.

33. D. J. Patnaude, P. Slane, J. C. Raymond, and D. C. Ellison. The Role of Diffusive Shock Acceleration on Nonequilibrium Ionization in Supernova Remnant Shocks. II. Emitted Spectra. *ApJ*, 725:1476–1484, December 2010.

34. S. P. Reynolds. Supernova Remnants at High Energy. *ARA&A*, 46:89–126, September 2008.

35. G. A. Tammann, W. Loeffler, and A. Schroeder. The Galactic supernova rate. *ApJS*, 92:487–493, June 1994.

36. T. Tanaka, A. Allafort, J. Ballet, S. Funk, F. Giordano, J. Hewitt, M. Lemoine-Goumard, H. Tajima, O. Tibolla, and Y. Uchiyama. Gamma-Ray Observations of the Supernova Remnant RX J0852.0-4622 with the Fermi Large Area Telescope. *ApJL*, 740:L51, October 2011.

37. T. Tanaka, Y. Uchiyama, F. A. Aharonian, T. Takahashi, A. Bamba, J. S. Hiraga, J. Kataoka, T. Kishishita, M. Kokubun, K. Mori, K. Nakazawa, R. Petre, H. Tajima, and S. Watanabe. Study of Nonthermal Emission from SNR RX J1713.7-3946 with Suzaku. *ApJ*, 685:988–1004, October 2008.

38. M. Tavani, A. Giuliani, A. W. Chen, et al.. Direct Evidence for Hadronic Cosmic-Ray Acceleration in the Supernova Remnant IC 443. *ApJL*, 710:L151–L155, February 2010.

39. Y. Uchiyama and F. A. Aharonian. Fast Variability of Nonthermal X-Ray Emission in Cassiopeia A: Probing Electron Acceleration in Reverse-Shocked Ejecta. *ApJL*, 677:L105–L108, April 2008.

40. Y. Uchiyama, F. A. Aharonian, T. Tanaka, T. Takahashi, and Y. Maeda. Extremely fast acceleration of cosmic rays in a supernova remnant. *Nature*, 449:576–578, October 2007.

41. J. Vink. Supernova remnants: the X-ray perspective. *A&A Rev.*, 20:49, January 2012.

42. J. Vink and J. M. Laming. On the Magnetic Fields and Particle Acceleration in Cassiopeia A. *ApJ*, 584:758–769, February 2003.

43. J. Vink, R. Yamazaki, E. A. Helder, and K. M. Schure. The Relation Between Post-shock Temperature, Cosmic-ray Pressure, and Cosmic-ray Escape for Non-relativistic Shocks. *ApJ*, 722:1727–1734, October 2010.

44. W. R. Webber. A New Estimate of the Local Interstellar Energy Density and Ionization Rate of Galactic Cosmic Cosmic Rays. *ApJ*, 506:329–334, October 1998.

45. N. E. Yanasak, M. E. Wiedenbeck, R. A. Mewaldt, A. J. Davis, A. C. Cummings, J. S. George, R. A. Leske, E. C. Stone, E. R. Christian, T. T. von Rosenvinge, W. R. Binns, P. L. Hink, and M. H. Israel. Measurement of the Secondary Radionuclides ^{10}Be, ^{26}Al, ^{36}Cl, ^{54}Mn, and ^{14}C and Implications for the Galactic Cosmic-Ray Age. *ApJ*, 563:768–792, December 2001.

46. V. N. Zirakashvili and F. A. Aharonian. Nonthermal Radiation of Young Supernova Remnants: The Case of RX J1713.7-3946. *ApJ*, 708:965–980, January 2010.

Frascati Physics Series Vol. 58 (2014)
Frontier Objects in Astrophysics and Particle Physics
May 18-24, 2014

Observations of Gamma-ray Bursts with the *Fermi* Large Area Telescope

Francesco Longo
Dipartimento di Fisica, Università di Trieste
INFN, sezione di Trieste, via Valerio 2, I-34127 Trieste, Italy
Giacomo Vianello, Nicola Omodei
Stanford University (HEPL), 452 Lomita Mall, Stanford, CA, 94205, US
on behalf of the *Fermi*/LAT Collaboration

Abstract

The *Fermi* observatory, with its two instruments, the Gamma-Ray Burst Monitor (GBM) and the Large Area Telescope (LAT), is observing Gamma-ray Bursts (GRBs) with a very large spectral coverage and deep sensitivity, from $\sim$ 10 keV to $>$ 300 GeV. Here we present a review of the main results of the first LAT GRB catalog, containing the 35 GRB detected by the LAT above 100 MeV in the first 3 years of the mission. We also discuss some results on high-energy photons from GRBs obtained with the preliminary Pass 8 new event-level reconstruction. Finally, we present and briefly discuss the LAT observation of the exceptional GRB 130427A.

1 The *Fermi* satellite

Fermi was launched on June 2008, carrying two instruments on board, namely the Gamma-ray Burst Monitor (GBM) [1)], a full sky monitor made of 12 NaI

detectors and two BGO detectors, sensitive respectively in the 8 keV - 1 MeV and 150 keV - 40 MeV energy range, detecting GRBs at a rate of ~ 250/yr; and the Large Area Telescope (LAT) [2], a pair production γ–ray telescope sensitive from 20 MeV to > 300 GeV. The LAT features a field of view of 2.4 sr at 1 GeV, a broad energy range, a low dead time per event (27 μs) and a the largest effective area for gamma-ray space satellites at GeV energies[1]. This allows the LAT to get a larger number of GRB detections at energies $> \sim 20$ MeV ($\sim$ 9 GRBs/year) with respect to its predecessor EGRET (5 GRBs in 10 years) and to AGILE (7 GRBs in 6 years), in rough agreement with the pre-launch expectactions [3].

2 The *Fermi*/LAT GRB catalog

The first *Fermi*/LAT GRB catalog [4] covers 3 years of observations, from August 2008 to July 2011. In such time period *Fermi*/GBM detected ~ 750 GRBs, with around half of them in the LAT field of view. Two detection algorithms were used: a standard likelihood algorithm, providing both detection and localization with < 1 deg accuracy, using the post launch so called "Pass 6 v3 Transient" [5] events above 100 MeV; and a counting analysis using the LAT Low Energy (LLE) [6] class of data, featuring a large effective area starting at $\sim$20 MeV but no localization capability. With the likelihood analysis we detected and localized 28 GRBs, while using the LLE analysis we detected 7 more bursts, for a total of 35 GRBs.

2.1 High-energy emission

While the number of GRBs detected at high-energy by *Fermi*/LAT is a small fraction of the total number of GRBs in the field of view, this sample allows us to uncover unique features of GRBs emerging only at high energies.

2.1.1 Energetics

Since LAT observations are photon-limited rather than background-limited, the detection efficiency is directly related to the counts fluence of the source. This is an important difference with respect to *Fermi*/GBM, which is background

[1]The actual LAT perfomance can be found at this link `http://www.slac.stanford.edu/exp/glast/groups/canda/lat_Performance.htm`

limited and for which the peak flux of the source is more relevant. Of course, the low-energy fluence is highly correlated with the high-energy fluence. The fact that the LAT detects preferentially GRBs with a high low-energy fluence is therefore not surprising. The typical ratio between the high-energy fluence (above 100 MeV) and the low-energy fluence (10 keV - 1 MeV) is ~ 0.1. It is interesting to note that in the catalog there are four *hyper-energetic* bursts for which the ratio exceeds greatly the typical value, being closer or even above 1. The same conclusion can be reached taking the ratio of the rest frame total energy E_{iso} in the two energy bands, which demonstrates that this is not an effect of the distance of these bursts, which are distributed between redshift 0.9 and 4.35.

2.1.2 Delayed and temporally extended emission

The emission above 100 MeV is systematically delayed with respect to the low-energy emission. When using T_{05} as a measure of the onset of the emission for both the 10-300 keV energy range (from [7]) and the 100 MeV - 10 GeV energy range, it is clear that the latter is systematically larger than the former. Also, the duration of the high-energy emission appears to be systematically longer, and features a smooth decaying phase after the end of the low-energy prompt emission. Such decaying phase is well described by a power law in all but three cases, for which we found that a broken power law describes better the data. The time of the temporal decay break is found in all three cases after the end of the low-energy emission, as measured by T_{90}. If we define a *late time decay index* α_L as the index of the power law for the light curves well described by a simple power law, and the index after the break for the three GRBs described by a broken power law, we find that $\alpha_L \sim -1$. This value is foreseen by the standard afterglow model for an adiabatic expansion of the fireball, while a radiative expansion would foresee a decay with an index of 10/7, which is not observed in our data.

2.1.3 High-energy photons

The LAT has observed photons up to 30 GeV coming from bright GRBs, which in the case of high-redshift GRBs can become more than 100 GeV in the rest frame of the progenitor of the burst. This result poses a big challenge for the efficiency of the particle acceleration mechanisms, especially when considering

the fact that some of this high-energy events have been detected within seconds since the start of the low-energy emission. In the context of the standard fireball model [8] the presence of such high-energy photons constrains also the bulk Lorentz factor of the emitting shells to be $\Gamma > 1000$ in some cases, a value much higher than what previously thought. High-energy photons from high redshift GRBs allow also to constrain the opacity of the Universe connected with the interaction of the > 10 GeV γ–rays with optical and UV photons of the Extragalactic Background Light (EBL). In the case of the short GRB 090510, the short time delay observed between low and high-energy events can be used to place tight limits on the energy dependence of the speed of light, which is postulated for example by some quantum gravity theories [9].

2.2 GRBs with Pass 8

Since 2010, the *Fermi*/LAT collaboration is developing a comprehensive revision of the event-level analysis, known as Pass 8 [17]. Using its preliminary achievements, the LAT collaboration re-analyzed the prompt phase of ten bright GRBs previously detected by the LAT, finding four new gamma rays with energies greater than 10 GeV in addition to the seven previously known. Among these four there is a 27.4 GeV gamma-ray from GRB 080916C, which, at a redshift of 4.35, makes it the gamma ray with the highest intrinsic energy (147 GeV) detected so far from a GRB [17].

3 Broad-band spectroscopy

Fermi is an exceptional observatory for GRB spectroscopy (see also [10, 11]). In particular, it has unprecedented spectral coverage, starting around 10 keV up to 300 GeV. We exploited this feature by performing a broad-band spectral analysis of all the GRBs contained in the sample. Before *Fermi* most of the GRB spectra were well described by the empirical Band model [12], which has become the *de-facto* standard model. The spectra of all the brightest bursts inside the LAT FoV present, on the contrary, significant deviations from a Band function, requiring additional components such as power laws, high-energy cutoffs, or both. Other GRBs, observed at low off-axis angles, and with a corresponding high effective area, show deviations as well. We conclude that the empirical Band model seems to be not sufficient to describe all the spectral features of LAT GRBs. Unfortunately, there is no common recipe, and different

components can be required depending on the particular event. This calls for a better broad-band modeling of the spectra of GRBs, opening new questions and prompting new theoretical developments.

4 The afterglow of LAT-detected GRBs

A subsample of LAT-detected GRBs have been studied at other wavelengths, in particular during their afterglow emission. A systematic study published by [13] shows that in many ways the properties of the afterglow of LAT bursts are typical of the general afterglow population, but the ratio between the luminosity of the prompt emission and the luminosity of the afterglow is larger. Therefore, either their prompt emission is more efficient in producing γ-rays, or, conversely, their afterglows are somehow suppressed. In two cases, GRB 090510 and GRB 110731A, Swift and other instruments observed the afterglow when the high-energy extended emission was still detectable by the LAT. A broadband study, from optical wavelengths to γ-rays, showed that the emission is compatible with being from external shocks [14, 15]. In one other case, GRB 100728A, high-energy emission was detected by the LAT only in correspondence with an X–ray flare, which was successfully modeled from X–ray to γ-ray energies as internal shock emission [16].

5 GRB 130427A

The observations of the exceptionally bright GRB 130427A by *Fermi* [18, 19] provide further constraints on the GRB phenomenon and their emission processes. GRB 130427A had the largest fluence, highest observed energy photon (95 GeV), longest γ-ray duration (20 hours), and one of the largest isotropic energy releases ever observed from a GRB. The temporal and spectral analyses of GRB 130427A presented in [18] challenge the widely accepted model that the non-thermal high-energy emission in the afterglow phase of GRBs is synchrotron emission radiated by electrons accelerated at an external shock.

6 Towards the second LAT GRB catalog

The *Fermi* LAT collaboration is actively working to produce the second version of its GRB catalog. This catalog will contain more GRBs, not only due to an extended period of data, but also due to renewed algorithms to search on a

wider angular region centered on GBM GRB trigger positions and to new Pass 8 data selection, with larger effective area both at low and high energies. The recent detections by the LAT are currently maintained and kept updated on the publicly available GRB tables [20, 21].

7 Acknowledgments

The *Fermi* LAT Collaboration acknowledges generous ongoing support from a number of agencies and institutes that have supported both the development and the operation of the LAT as well as scientific data analysis. These include the National Aeronautics and Space Administration and the Department of Energy in the United States, the Commissariat à l'Energie Atomique and the Centre National de la Recherche Scientifique / Institut National de Physique Nucléaire et de Physique des Particules in France, the Agenzia Spaziale Italiana and the Istituto Nazionale di Fisica Nucleare in Italy, the Ministry of Education, Culture, Sports, Science and Technology (MEXT), High Energy Accelerator Research Organization (KEK) and Japan Aerospace Exploration Agency (JAXA) in Japan, and the K. A. Wallenberg Foundation, the Swedish Research Council and the Swedish National Space Board in Sweden.

Additional support for science analysis during the operations phase is gratefully acknowledged from the Istituto Nazionale di Astrofisica in Italy and the Centre National d'Études Spatiales in France.

References

1. C. Meegan *et al*, The Astrophysical Journal **702**, 791 (2009)
2. W.B. Atwood *et al*, The Astrophysical Journal **697**, 1071 (2009)
3. D.L. Band *et al*, The Astrophysical Journal **701**, 1673 (2009)
4. M. Ackermann *et al* , The Astrophysical Journal Supplement **209**, 11 (2013)
5. R. Rando for the *Fermi* LAT Collaboration, arXiv e-print 0907.0626 (2009)
6. V. Pelassa *et al*, arXiv e-print 1002.2617 (2010)
7. W.S. Paciesas *et al*, The Astrophysical Journal Supplement, **199**, 18 (2012)

8. T. Piran, Physics Reports **314**, 575 (1999)
9. V. Vasileiou *et al*, Physical Review D **87**, 12 (2013)
10. A. Goldstein *et al*, The Astrophysical Journal Supplement **199**, 19 (2012)
11. D. Gruber *et al*, The Astrophysical Journal Supplement **211**, 12 (2014)
12. D.L. Band *et al*, The Astrophysical Journal **413**, 281 (1993)
13. J.L. Racusin *et al*, The Astrophysical Journal **738**, 138 (2011)
14. M. De Pasquale *et al*, The Astrophysical Journal Letters**709**, L146 (2010)
15. M. Ackermann *et al*, The Astrophysical Journal **763**, 71 (2013)
16. A.A. Abdo *et al*, The Astrophysical Journal Letters **734**, L27 (2011)
17. W.B. Atwood *et al*, The Astrophysical Journal **774**, 76 (2013)
18. M. Ackermann *et al* , Science **343**, 42 (2014)
19. R. Preece *et al* , Science **343**, 51 (2014)
20. `http://fermi.gsfc.nasa.gov/ssc/observations/types/grbs/lat_grbs/`
21. `http://www.asdc.asi.it/grblat/`

Frascati Physics Series Vol. 58 (2014)
Frontier Objects in Astrophysics and Particle Physics
May 18-24, 2014

THE MAGIC LEGACY TO NEXT GENERATION OF IACTS: RESULTS, RECENT HIGHLIGHTS AND PROSPECTS

Juan Cortina
Institut de Fisica d'Altes Energies, Edifici CN, Campus UAB, 08193 Spain
for the MAGIC collaboration

Abstract

The present generation of Imaging Air Cherenkov Telescopes (IACTs) has greatly improved our knowledge on the Very High Energy (VHE) side of our Universe. The MAGIC IACTs operate since 2004 with one telescope and since 2009 as a two telescope stereoscopic system. I will outline a few of our latest and most relevant results: the surprising gamma-ray factory in the Perseus galaxy cluster with emission from NGC 1275 and the puzzling emission of IC 310; the advances on the identification of the location of emission region in jets of AGNs; the discovery of pulsed emission from the Crab pulsar at VHE, recently found to extend up to 400 GeV and along the "bridge" of the light curve. The results that will be described here and the planned deep observations in the next years will serve as a sound cornerstone for the future of VHE Astrophysics.

1 The MAGIC telescopes

The two MAGIC IACTs were built and are currently operated by a collaboration of institutions in Bulgaria, Croatia, Finland, Germany, Italy, Poland, Japan, Spain, and Switzerland [1].

MAGIC is located at the Roque de los Muchachos Observatory in the island La Palma (Spain). The first single telescope (MAGIC-I) started operations in 2004 and was at the time the largest IACT yet constructed (17m diameter mirror), a fact which translated into a very low energy threshold for VHE γ-ray detection. MAGIC-I featured significant novelties in IACTs, such as the fastest sampling of Cherenkov signals (2 GSps) or active mirror control. Its ultralight carbon fiber frame and mirrors enable very fast repositioning of the telescope (<20 secs for half a turn), a crucial fact to study the prompt emission of GRBs.

The introduction of a second telescope, MAGIC-II, enabled the instrument to perform stereoscopic observations with significantly better sensitivity, and angular and spectral resolutions, starting in Fall 2009. As of today the MAGIC telescopes remain the IACT array with the largest mirrors in the world. MAGIC-II was built essentially as an improved copy of MAGIC-I. The main difference between the telescopes were their cameras and their readout electronics. MAGIC I camera was composed of 577 pixels of two different sizes. On the contrary, the MAGIC II camera was built with 1039 pixels of the same size (0.1°). The readout sampling speed was 2 GSps for both telescopes, but using very different electronics.

During the Summers of 2011-2012 the instrument experienced a thorough upgrade [1)]: the readout was replaced by a homogeneous system based on the DRS4 analog memory sampling chip, a clone of the MAGIC-II camera and L1 trigger were installed in MAGIC-I. The upgrade of the MAGIC-I trigger results in an enlarged trigger area for the system. Besides, since both telescopes are now essentially identical, maintenance and operation are easier.

The threshold energy (peak of the energy distribution of stereo recorded events) of the upgraded telescope has been estimated to be 50 GeV. Fig. 1 shows the sensitivity of the instrument as a function of energy. For energy

[1] An updated list of collaboration members can be found at *http://magic.mpp.mpg.de*

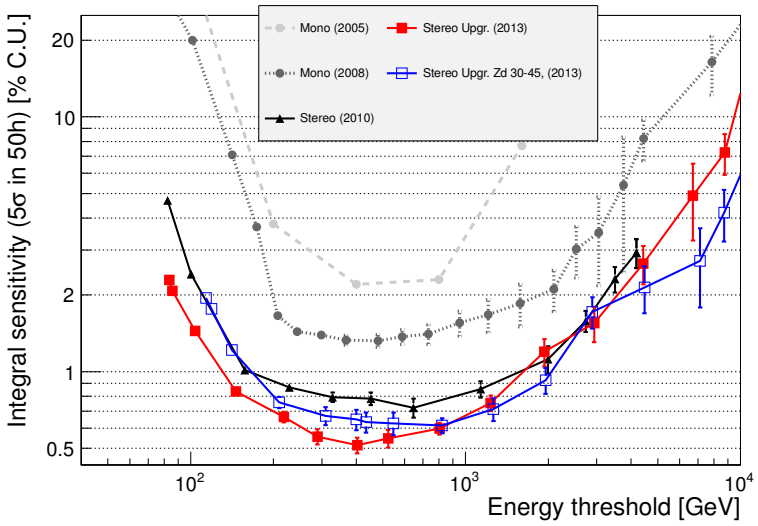

Figure 1: *Integral sensitivity of the current MAGIC Stereo system and previous experimental setups, defined as the flux for which* $N_{\rm excess}/\sqrt{N_{\rm bgd}} = 5$ *after 50 h, and calculated using Crab data. From* 2).

above 300 GeV the sensitivity is 0.76% Crab units. There is a good agreement with the predictions from MC. Respect to single telescope observations, a factor ∼2 improvement in significance is achieved at a few hundred GeV and up to a factor ∼3 at lower energies. The differential sensitivity remains acceptable (10% Crab units) below 100 GeV. Stereo observations result in a significant improvement both in angular and spectral resolutions. An angular resolution of 0.07° is reached at 300 GeV. The best spectral resolution of 16% is reached at a few hundred GeV. Find more details about the instrument's performance in 2).

2 Extragalactic VHE γ-ray physics: not only blazars

Clusters of galaxies are the largest bound structures in our Universe. They are young: in fact they are still forming now. A huge energy budget is available

from gravitational potential of infalling gas (about $10^{61} - 10^{63}$ erg). The observed synchrotron emission in the centers of clusters come from Cosmic Ray (CR) electrons, which are probably accompanied by 100 times more CR protons, because protons are easier to accelerate (as observed in our own galaxy). CR electrons may actually come from CR protons. The density of CR protons inside clusters may be measured using IACTs because CR protons produce γ-rays through π^0 decay.

MAGIC selected the Perseus cluster of galaxies for observations on account of the fact that it is nearby (78 Mpc), i.e. bright in X-rays, and shows a massive cool core and a radio mini-halo. Perseus was not detected at TeV energies after 85 hours of observations [3]. We could set upper limits (ULs) at E>600 GeV. These ULs can be compared to cosmological hydrodynamical simulations with and without the contributions of individual galaxies or to the absolute minimum possible flux assuming that CR electrons are produced by CR protons. They are at the limit of the predictions of the simulations and a factor 3 above the the minimum flux. This allows to estimate the ratio of pressure applied by the CR and pressure produced by the thermal component of the cluster. It is as low as 0.77% - 11.6%. it also enables to limit the magnetic field B in the center of the cluster to B>4-9 μG.

Radiogalaxies (active galaxies displaying a radio jet) generate CR (electron or proton) bubbles in the intergalactic medium. The same process injects magnetic field into the intracluster medium. The total injected energy is huge ($10^{60} - 10^{61}$ erg): it represents a few % of the total energy of accretion into the central supermassive black hole. Relativistic electrons produce synchrotron which can be studied using radiotelescopes, but they also produce VHE γ-rays through Inverse Compton.

In fact radiogalaxies are interesting VHE sources because the emission is not so strongly beamed, i.e. the jet is not as aligned with the line of sight as in blazars, and because they are nearby objects, i.e. we can study them in more detail. IACTs have discovered four radiogalaxies at VHE: Cen-A, M 87, NGC 1275 and IC 310. MAGIC has discovered the last two sources, which actually belong to the same cluster of galaxies: Perseus.

MAGIC, together with HESS and VERITAS, has studied one of the other VHE radiogalaxies: M87. M87 is so close to us (17 Mpc) that many features in the jet can be resolved at longer wavelengths. Flux variations then allow

to identify the source of the VHE emission: IACTs detected in 2007 a bright flare that was simultaneous to the brightening of the radio core [4], indicating that VHE emission originates in the radio core. Unfortunately subsequent simultaneous observations have not shown a similar emission pattern [5].

MAGIC discovered the radiogalaxy IC 310 at VHE [6] during observations of Perseus. A flare was observed in 2011 which revealed that the source is variable from day to day [7]. The observation of a second flare in 2012 showed even faster variability with time scales of 1-10 minutes [8]. Even faster variability has been observed in blazars like Mrk 501 and PKS 2155304, but emission in blazars is doppler-shifted by a larger factor than in a radiogalaxy like IC 310 for which the largest allowed Doppler factor is around 4. The intrinsic variability of the source may in fact be so fast that the emission region is smaller than the event horizon light-crossing time. Hardly any model can accomodate such a small emission region.

3 Pulsars and pulsar wind nebulae

At VHE we study the particles with the highest energy which a pulsar is able to accelerate. MAGIC discovered emission at >25 GeV from the Crab pulsar [9]. VERITAS discovered that the pulsed spectrum extends to >100 GeV [10]. Some months later, MAGIC measured the spectrum of both peaks up to 400 GeV [11]. MAGIC has recently discovered emission from the "bridge" of the light curve at energies exceeding 100 GeV [12]. The presence of the bridge and the fact that both peaks are very narrow is hard to explain within existing models. Aharonian et al [13] for instance propose that VHE γ-rays are not produced inside the magnetosphere but in the wind region. If true, VHE observations would allow to study the wind, which is totally dark at other wavelengths. This model is successful in producing bridge emission but predicts much broader peaks than those measured by MAGIC. Hirotani [14] may be able to reproduce the shape of the light curve assuming that there is an additional toroidal component in the pulsar's magnetic field.

The largest population of sources in the HESS galactic plane survey are Pulsar Wind Nebulae (PWN). Energetically speaking pulsars are CR sources, that is, they spend most of their rotational power in accelerating particles. Photons, especially E<100 MeV, may well be considered as a "sideshow". MAGIC has only detected two PWN at VHE: Crab and 3C 58. These are however

extreme PWN. Crab is the brightest PWN, while 3C 58 is the weakest and least luminous. They are both the least efficient VHE PWN. 3C 58 has in fact a γ-ray luminosity which is as low as 10^{-5} of the pulsar spindown power.

The latest MAGIC spectrum of the Crab Nebula is based on a 70 hour stereo observation spanning from 2009 to 2011 [15]. It extends from 50 GeV up to 30 TeV, with a statistical precision as low as 5% at E<100 GeV. Combined with the Fermi-LAT data, these data yield the most precise measurement of the IC peak so far, at (52.5±2.6) GeV (statistical error only).

The spectrum has been fitted to two different models. A static, constant B-field model [16] predicts however too broad an IC peak. Most probably this implies that the assumption of the homogeneity of the magnetic field inside the nebula is incorrect. A time-dependent model [17] is successful in reproducing the spectral shape under the assumptions of a low magnetic field of less than hundred μG. However, this model fails to provide a good fit of the new spectral data if the observed morphology of the nebula.

3C 58 is a PWN centered in PSR J0205+6449, one of the highest spin-down pulsars in the sky (Edot=2.7×10^{37} erg s^{-1}, or 2% of the Crab pulsar's Edot). The distance and age of this PWN are controversial. The distance may range between 2 and 3.2 kpc. It may be very young and associated to the historical supernova SN1181 or as old as 7000 years. The X-ray thermal emission from the central objects seems to be too weak for a neutron star in this range of ages [18], so it has been speculated that it may not be a simple neutron star, but contain a more exotic sort of matter. Like Crab it shows a torus and a jet in X-rays. Fermi-LAT detected pulsed emission at E<4 GeV and steady emission up to ∼100 GeV.

MAGIC has discovered 3C 58 at VHE after a 85 h observation [19]. Its flux is 0.65% crab, the weakest PWN detected at these energies. For existing models, only a short distance of 2 kpc or a high IR density can reproduce the data from radio to VHE (see Fig. 2). The IR density is probably unrealistically high, so the distance of 2 kpc is favored. The derived magnetic field by all the models fitting the γ-ray data is in any case smaller than 35 μG, very far from equipartition.

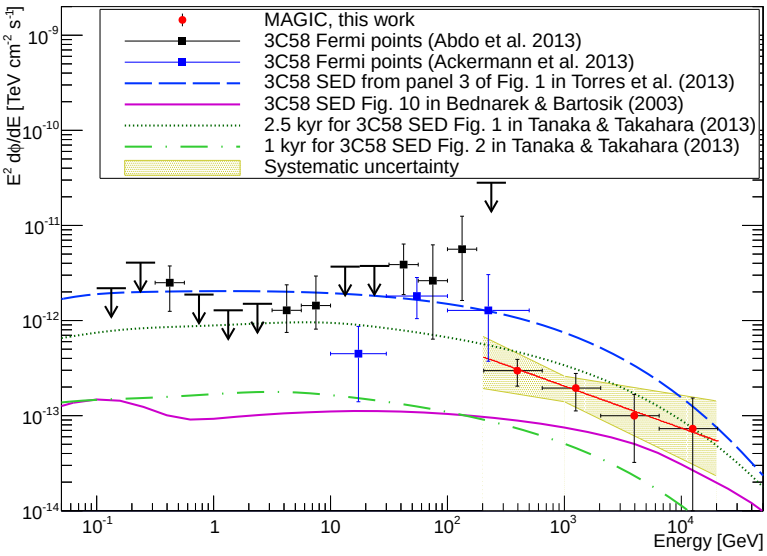

Figure 2: *3C 58 spectral energy distribution in the range between 0.1 GeV and 20 TeV. Red circles are the VHE points reported in this work. The best-fit function is drawn in red and the systematic uncertainty is represented by the yellow shaded area. Black squares and arrows are taken from the Fermi-LAT second pulsar catalog. Blue squares are taken from the Fermi-LAT high-energy catalog. The magenta, clear green dashed-dotted, dark green and blue dashed lines correspond to different models of the source. See* [19] *for details.*

4 Prospects

These were just a few of the latest results of MAGIC. Especially interesting are also the latest constraints on γ-ray emission produced by dark matter annihilation in the dwarf spheroidal Segue [20] or the recent multiwavelength study of PKS 1424+240, which may be the farthest AGN detected at VHE [20].

We plan to operate the telescopes during the next few years, for sure until the first CTA telescope start to operate. Since the current generation of IACTs have already studied most of the obvious candidates for VHE emission, future observations will probably go deeper into relatively few objects. In the last

years we have setup a program of Key Observation Projects to identify and observe the most promising targets.

References

1. D. Mazin for the MAGIC coll., Proc of 33rd ICRC, Id. 1071.
2. In preparation. Also J. Sitarek for the MAGIC coll., Proc of 33rd ICRC, Id. 74.
3. J. Aleksić *et al*, A&A **541**, 99 (2012).
4. V. A. Acciari *et al*, Science **325**, 444 (2009).
5. A. Abramowski *et al*, Ap. J. **746**, Issue 2, 151 (2012).
6. J. Aleksić *et al*, Ap. J. **723** L207 (2010).
7. J. Aleksić *et al*, A&A **563** A91 (2014).
8. J. Aleksić *et al*, submitted for publication.
9. E. Aliú *et al*, Science **322** 1221 (2008).
10. E. Aliú *et al*, Science **334** 69 (2011).
11. J. Aleksić *et al*, A&A **540** A69 (2012).
12. J. Aleksić *et al*, A&A **565** L12 (2014).
13. F. Aharonian *et al*, Nature **482** 507 (2012).
14. K. Hirotani, Ap. J. **733**, L49 (2011). K. Hirotani, Ap. J. **766**, 98 (2013).
15. J. Aleksić *et al*, submitted to JHEAp and arXiv:1406.6892.
16. M. Meyer, D. Horns, H. Zechlin, A&A **523** A2 (2010).
17. J. Martin, D. F. Torres, N. Rea, MNRAS **427** 415 (2012)
18. P. Slane *et al*, Ap. J. **571** L45 (2002).
19. J. Aleksić *et al*, A&A (2014) accepted and arXiv:1405.6074.
20. J. Aleksić *et al*, JCAP **02** 008 (2014).
21. J. Aleksić *et al*, A&A (2014) accepted and arXiv:1401.0464

Frascati Physics Series Vol. 58 (2014)
Frontier Objects in Astrophysics and Particle Physics
May 18-24, 2014

FLARING GAMMA-RAY AGNs

Sara Buson
Università di Padova, Dip. di Fisica e Astronomia "G. Galilei", I-35131 Padova, Italy
INFN, Sezione di Padova, I-35131 Padova, Italy

Abstract

Variability at all wavelengths, from radio to gamma-ray energies, and at time scales from minutes to years, is one of the key signatures of Active Galactic Nuclei (AGNs). These astrophysical sources release a large amount of their energy at gamma rays, in turn making the high-energy band ($>$ 100MeV) a fascinating and crucial domain to study. Recent results and insights gained on AGN physics which have been enabled by the Large Area Telescope on the *Fermi* satellite will be discussed. These results have enabled progress in related astrophysical topics which directly benefit from the better description of the AGN population

1 Introduction

Since its launch in 2008 the *Fermi* satellite has enabled a new frontier in the modern astrophysics extending the study of the variable universe to the high-

energy (HE, > 100 MeV) range [1]. The primary instrument aboard *Fermi* is the Large Area Telescope (LAT), which uses the pair conversion process to detect gamma rays with energies from below 100 MeV to more than 300 GeV.

Looking at the *Fermi* five years sky map in Figure 1 it is evident that a great amount of the detected gamma rays can be related to the diffuse background. Nevertheless, when subtracting this expected background, several gamma-ray excesses are still present and actually found to be tightly connected to astrophysical sources. The latter are mostly persistent sources of extragalactic origin which are collected in the *Fermi* catalog [2].

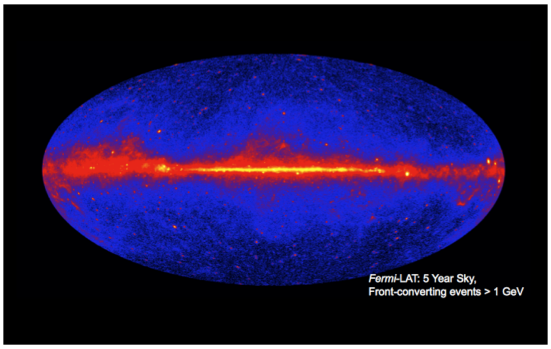

Figure 1: *Fermi* LAT counts map, based on events collected during the first five years of operations, from 100 MeV to 100 GeV.

After more than 5 years of operations *Fermi* LAT has established AGNs as constituting the overwhelming majority of sources populating the gamma-ray sky. The Second LAT AGN catalog accounts for about 1000 objects significantly detected in the 100 MeV $-$ 100 GeV energy band [3]. Within the gamma-ray AGNs, the predominant typology of sources belongs to the blazar class, i.e. AGNs whose relativistic jet of plasma is closely aligned with the line of sight.

Blazars are also the sources that manifest the most dramatic variability in the high-energy band. In sky-survey mode, the LAT observes the entire sky in three hours, making it a suitable tool to follow blazar rapid variations. This all-sky monitor capability of the LAT is complemented by a prompt automatic ground pipelines. The latter enables the release of relevant scientific

information almost in real time.

2 Follow up of transients and flares

Fermi LAT data are analyzed daily thanks to the automatic science processing (ASP) pipeline developed by the *Fermi* LAT team and the great effort of the Flare Advocate duty service [4]. The ASP tool searches for potential flaring activity from known sources and, more generally, from any gamma-ray transients. When new sources are detected or enhanced flux activity by known sources is observed by ASP, they are promptly reported in Astronomer Telegrams (ATels).

Recently, a different approach to search for transients has been developed, which is the Fermi Variability Analysis (FAVA). The FAVA analysis compares the number of gamma rays observed in a given time window to the number of gamma rays expected for the average emission detected from that direction of the sky. The method has been used in weekly time intervals and in two energy ranges, E > 100 MeV and E > 800 MeV. So far it has detected 215 flaring gamma-ray sources[1] with significance of more than 5.5 sigma [5].

3 Results

The prompt individuation of flares and transient sources at gamma rays offers an excellent opportunity to follow them up at other energy bands. In turn, multiwavelength variability studies are an ideal tool to pinpoint AGN physical properties and to test different theories. Several important outcomes were achieved thanks to the synergy with TeV Cherenkov Telescopes. For example, the detection of the Flat Spectrum Radio Quasar (FSRQ), PKS 1222+12 at VHE >100 GeV) was prompted by the detection of a flaring event in the LAT [6]. Detailed studies of the latter revealed the absence of a spectral cutoff in its gamma-ray Spectral Energy Distribution (SED) and located the gamma-ray emission region outside the broad-line region, which would otherwise have absorbed the VHE gamma-rays. Additionally, the observed fast variability challenged the present emission models from jets in FSRQs and the combined *Fermi* LAT and TeV spectral data led us to derive constraints on the density

[1]More information are available at http://www.asdc.asi.it/fava/

of the extragalactic background light (EBL) in the UV-optical to near-infrared range.

Furthermore, *Fermi* has detected also peculiar objects, such as gravitational lensed systems as suggested by [7]. Though the sample is limited, still an interesting variety of properties have been found as well as controversial results. So far, the two best studied at gamma rays are the FSRQs B0218+357 and PKS 1830−211. On the one hand, the former led to the first measurement of gravitational lensed parameters at gamma rays and a competitive limit on the gravitational lens delay [8]. On the other hand the latter, which is also among the brightest *Fermi* AGN, did not display convincing evidence of a lensed signature at gamma rays despite the detection of lensed emission at other wavelengths [9]. Since gravitational lensing is an achromatic process the gamma-ray observations open new questions in the structure and emission mechanism in these sources.

4 Perspectives and future developments

The *Fermi* collaboration is working on a refined event-level analysis, the Pass 8 Instrument Response Functions of the LAT [10], which will have a larger acceptance, a better Point Spread Function at high energies and a wider energy range. This will greatly improve the study of time-domain high-energy astronomy.

More accurate, finer binned light curves will be able to point out any inherent variability. In turn, it will be possible to better constrain the location of the gamma-ray emission region and monitor new features in AGN jets via correlated multi-wavelength studies. Besides, Pass 8 will ensure a significant reduction in background contamination and an increased effective area. The number of detected objects at gamma rays will increase, hence helping to draw an improved, detailed picture of the population.

Looking forward,

Fermi LAT is likely to continue operating for several years and simultaneous operation with the Cherenkov Telescope Array (CTA) is possible. If this occurs, the unprecedented broad-band energy coverage obtained through joint LAT/CTA observations will unveil new insights into the SEDs and variability of AGN. Additional ground-breaking results can be expected in the related study of the extragalactic background light.

5 Acknowledgements

The *Fermi* LAT Collaboration acknowledges support from a number of agencies and institutes for both development and the operation of the LAT as well as scientific data analysis. These include NASA and DOE in the United States, CEA/Irfu and IN2P3/CNRS in France, ASI and INFN in Italy, MEXT, KEK, and JAXA in Japan, and the K. A. Wallenberg Foundation, the Swedish Research Council and the National Space Board in Sweden. Additional support from INAF in Italy and CNES in France for science analysis during the operations phase is also gratefully acknowledged.

References

1. W. B. Atwood, The Large Area Telescope on the Fermi Gamma-Ray Space Telescope Mission ApJ, **697**, 1071 (2009)

2. P. Nolan *et al*, Fermi LAT second source catalog (2FGL), ApJS, **199**, 31 (2012)

3. M. Ackermann *et al*, The Second Catalog of Active Galactic Nuclei Detected by the Fermi Large Area Telescope **743**, 171 (2011)

4. S. Ciprini *et al*, Monitoring the Gamma-ray Sky through 4.5 Years of Fermi LAT Flare Advocate Service arXiv1303.4054 (2013)

5. M. Ackermann *et al*, The Fermi All-sky Variability Analysis: A List of Flaring Gamma-Ray Sources and the Search for Transients in Our Galaxy, ApJ, **771**, 57 (2013).

6. J, Aleksi, *et al*, MAGIC discovery of VHE Emission from the FSRQ PKS 1222+21 ApJL, **730**, L8

7. W. B. Atwood, 2007, in the Les Houches Winter School "The Violent Universe," March 2007, CEA-Saclay

8. C.C. Cheung *et al*, Fermi Large Area Telescope Detection of Gravitational Lens Delayed Gamma-ray Flares from Blazar B0218+357, ApJL, **782**, L14 (2014)

9. A. Abdo *et al*, submitted to ApJ

10. W. B. Atwood *et al*, Pass 8 Toward the Full Realization of the Fermi-LAT Scientific Potential, arXiv1303.3514 (2013).

Frascati Physics Series Vol. 58 (2014)
Frontier Objects in Astrophysics and Particle Physics
May 18-24, 2014

LATEST RESULTS FROM THE ICECUBE NEUTRINO TELESCOPE

Geraldina Golup for the IceCube Collaboration*
Vrije Universiteit Brussel - Inter-university Institute for High Energy Physics

Abstract

The IceCube Neutrino Observatory instruments a cubic kilometer of the Antarctic ice at the South Pole with a three-dimensional grid of light sensors in combination with a square kilometer surface array. The observatory was completed at the end of 2010, but the partially instrumented detector has been taking data since 2005. Several breakthroughs in the field have been accomplished, in particular the first evidence of a flux of high energy neutrinos of extraterrestrial origin and the unexpected lack of a significant signal correlating with Gamma Ray Bursts. We will discuss these results and also cover other recent results such as the observation of atmospheric neutrino oscillations, the latest point source analysis, indirect dark matter searches and future proposed upgrades of the detector.

* http://icecube.wisc.edu

1 Introduction

The IceCube Neutrino Observatory is a unique telescope located at the geographic South Pole whose objective is to open a new observational window to study the Universe: neutrino astronomy. Neutrino detection can help unravel the mystery of the origin of ultra-high energy cosmic rays. Since cosmic rays are charged particles, they are deflected on their path from their sources to Earth by the still poorly known galactic and intergalactic magnetic fields. This, together with the fact that the cosmic ray composition at ultra-high energies is also poorly known, makes it difficult to identify the cosmic ray sources from the arrival directions, as it is not possible to predict the deflection of the cosmic ray trajectories. While being accelerated at their sources, cosmic rays interact with photons and ambient matter producing gamma rays and neutrinos. Gamma rays interact with the cosmic microwave background or the extragalactic background light and have not been detected at Earth above energies of 100 TeV. On the other hand, neutrinos, like gamma rays, have no electric charge so their arrival directions point directly to the position in the sky where they were originated. Thanks to their low interaction cross section, neutrinos have long range, which makes them ideal candidates to study cosmic ray accelerators. The main challenge is to detect them.

2 The IceCube Neutrino Telescope

The IceCube Neutrino Telescope [1)] consists of 5160 optical modules (each one with a photomultiplier tube) deployed on 86 vertical strings buried 1450 to 2450 meters under the surface of the ice. IceCube was designed to look for point sources of neutrinos in the TeV–PeV range to explore the highest energy astrophysical processes. Neutrinos are detected by observing Cherenkov radiation from product particles (muons, particle showers) that are generated when a neutrino interacts through a charge current (CC) or neutral current (NC) process with a nucleus in the ice or the underlying bedrock. A surface detector called IceTop completes the IceCube Observatory. It consists of 81 Cherenkov stations covering an area of 1 km^2 that detect air showers from primary cosmic rays in the 300 TeV to 1 EeV energy range.
Depending on the flavour of the interacting neutrino and the type of interaction, different signatures are expected in the detector. The one with the best angular

resolution (below 1°) is the CC ν_μ interaction where a track is produced as the outgoing muon transverses the detector. Cascades are produced in the detector as a result of CC $\nu_{e,\tau}$ interaction or or all NC neutrino interactions. In this case the angular resolution is poorer (around 10° above 100 TeV). The resolution of the deposited energy for tracks and cascades is around 15% [2] but cascades have a better reconstructed neutrino energy resolution since most of the energy is deposited in the detector, which is not the case for tracks. CC ν_τ interactions could produce among different signatures a so-called 'double-bang' caused by a tau lepton quickly decaying in the ice. This type of interaction has not been observed yet.

3 Search for extra-terrestrial neutrinos

3.1 PeV neutrinos

In an analysis [3] optimized for extremely high energy neutrinos that are produced in the GZK mechanism two neutrinos with energies around 1 PeV were discovered. These two events represent a 2.8σ excess over the expected background in the two years dataset (May 2010 to May 2012). Even though the energies of the events are too low to be GZK neutrinos, this discovery was remarkable since these events were the highest energy neutrinos ever detected until then.

3.2 High Energy Starting Events analysis

With the same data set as the previous analysis, a search for high energy events where the interaction occurs within the detector was designed [4]. The motivation to look at high energy starting events (HESE) is to rule out atmospheric background from cosmic ray showers as much as possible. An atmospheric muon veto was implemented in the data selection. The background events expected from atmospheric muons (mostly sneaking through a dust layer at around 2100 m) was estimated from data using a tagging region and it was found to be 6 ± 3.4 events for the two years data set. The expected background from atmospheric neutrinos was computed to be $4.6^{+3.7}_{-1.2}$ events. After unblinding the data 28 events were observed (including the two PeV neutrinos) with a significance with respect to the reference background of 4.1σ that gave an evidence for the existence of neutrinos beyond the atmospheric origin.

In an update with one more year of data 9 additional events were detected [5] giving a total of 37 events, which now also include one event with a deposited energy of 2 PeV. The total expected atmospheric background for 3 years of data was estimated to be $15.0^{+7.2}_{-4.5}$ events, resulting in a significance of 5.7σ. Two down-going events from the Southern sky have been identified as part of the expected atmospheric muon background. The absence of detected air showers in the remainder of the Southern Hemisphere events, along with their overall rate, high energies, and the preponderance of shower events, generically disfavors any purely atmospheric explanation.

In Fig. 1 we show the energy distribution of the events (left panel) and the

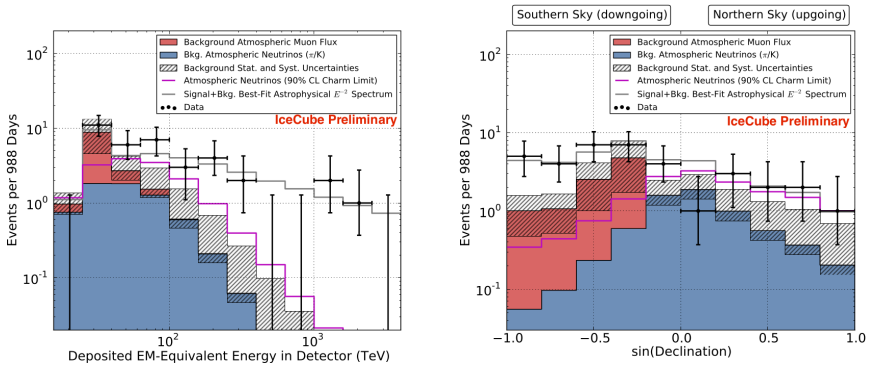

Figure 1: *Energy and declination distributions (left and right panels respectively) for the 3 years data set of the HESE analysis.*

declination distribution (right panel) for the 3 years data set. The energy spectrum of the events is harder than any expected atmospheric background and it is compatible with a benchmark E^{-2} astrophysical model. The best fit for an E^{-2} spectrum is $E^2\phi(E) = (0.95 \pm 0.3) \times 10^{-8}$ GeV cm^{-2} s^{-1} sr^{-1} per flavor (1:1:1). As expected it can be noticed that the distribution is not flat for the Northern Hemisphere since the Earth starts to be opaque to neutrinos at these energies. The Southern Hemisphere distribution is compatible with the expectations of an isotropic flux.

In Fig. 2 the arrival directions of the events in galactic coordinates are plotted. A point source search was performed and no significant signal was found - the cluster of cascades close to the Galactic Center has a p-value of 7%. Moreover,

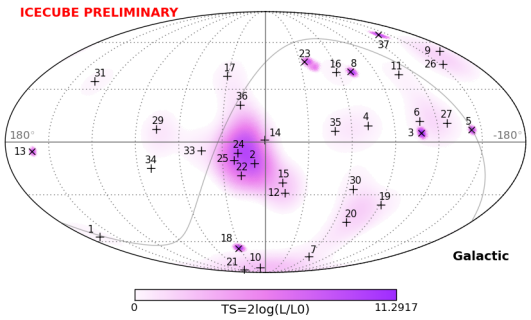

Figure 2: *HESE events sky map in galactic coordinates. Shower-like events are marked with + and those containing muon tracks with ×. The color map shows the test statistic (TS) for the point source clustering test at each location.*

no significant clustering in the arrival times of the events was detected.
To increase the number of starting events (in particular high energy tracks) a high energy extension of the IceCube Telescope is currently being designed. To achieve this goal a large surface array could be added, which would act as a cosmic ray veto and would enlarge the volume for starting tracks; and/or more strings could be deployed, which would enlarge the volume for starting (and ordinary) tracks and would also improve the angular resolution.

3.3 Diffuse up-going ν_μ analysis

A very important confirmation of the previous result has now been detected in a diffuse ν_μ analysis, using two years of data (from May 2010 to May 2012) and only considering up-going neutrino candidates, where an excess of events at energies above 100 TeV has been observed [6]. This excess is compatible with the sum of the atmospheric predictions plus an astrophysical E^{-2} flux with a preliminary significance of 3.9σ and it is consistent with the flux obtained from the HESE analysis.

3.4 Search for Point Sources

The IceCube Collaboration traditionally performs analyses to look for astrophysical neutrino point sources using clean, through-going muons that could

be associated with CC ν_μ interactions. The neutrino candidates data set now includes around 400,000 events in 4 years of data collecting [7]. In the Northern Hemisphere most of the events are atmospheric neutrinos, while in the Southern Hemisphere the triggers are mostly atmospheric muons. Point-like sources of neutrinos in the sky can be identified by searching for clusters of events significantly incompatible with the atmospheric muon and neutrino background. Until now no point source candidates have been detected - the hottest spots in the Northern and Southern Hemisphere have post trial p-values of 22.6% and 44.0% respectively. Declination dependent upper limits to the flux from possible point sources have thus been set.

3.5 Search for neutrinos in coincidence with GRBs

The IceCube Collaboration has searched for neutrinos in coincidence with Gamma Ray Bursts (GRBs), one of the leading candidates for ultra-high energy acceleration. The non-significant observation of neutrinos in coincidence with GRBs [8] has constrained the various models for ultra-high energy cosmic ray production [9], in particular the one where the cosmic rays that escape the acceleration site are neutrons that later decay into protons. Since this result was published, theoreticians have revised their calculations of neutrino emission by GRBs [10]. The current theoretical predictions include now a more detailed particle physics simulation and reduce the signal expectation, but the newly predicted flux is still within the reach of few years of IceCube data.

4 Indirect Dark matter searches

Dark matter searches are being performed at the IceCube Observatory. These are done by trying to detect dark matter particles indirectly by looking for secondary particles (neutrinos) that are produced when they annihilate. Assuming that the halo of our Galaxy is filled with these particles and that they scatter with nuclei in massive objects, some of them will lose enough energy to become gravitationally bound and trapped in the center of these objects. In this way the number density in the center builds up, and thus the annihilation probability increases. Some sources where the number density could be high are the Sun and the Earth. IceCube is producing very competitive results, for instance in Fig. 3 (left panel) where we show the spin dependent limits on the scattering cross section obtained in the search of a signal from the sun [11].

Other targets such as the Galactic Center, the Galactic Halo and dwarf galaxies are being studied and competitive limits on the annihilation cross section are being placed.

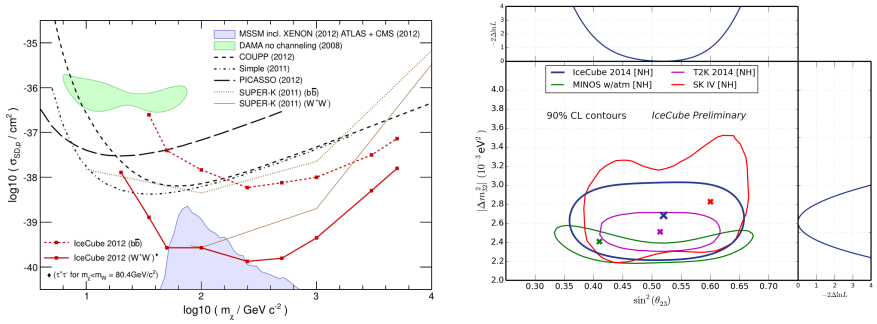

Figure 3: *Left Panel:* 90% *CL upper limits on* σ_{SD} *for hard and soft annihilation channels over a range of WIMP masses. The shaded region represents the allowed MSSM-25 parameter space taking into account accelerator, cosmological and direct DM search constraints. Right Panel: Confidence contours for the atmospheric neutrino oscillation analysis, compared with other experiments.*

5 Neutrino oscillations and PINGU

Another gripping result is that neutrino oscillations have been detected with IceCube at energies between 20 and 100 GeV [12]. Taking advantage of the atmospheric neutrino flux, the disappearance of up-going ν_μ has been observed, rejecting the non-oscillation hypothesis with more than 5σ. In Fig. 3 (right panel) the confidence contour maps in the Δm^2_{32}-$\sin^2(\theta_{23})$ phase space are compared to the results of MINOS, T2K and SuperKamiokande.
Neutrino oscillations in matter differ from those in vacuum, an effect known as MSW (Mikheyev-Smirnov-Wolfenstein) and which is strongest for energies below 10 GeV. This effect depends on the neutrino mass hierarchy - whether it is normal or inverted - and to detect this difference high statistics below 10 GeV is needed. A dense infill is being proposed called PINGU [13], which is among the frontrunners of the competition to determine the neutrino mass hierarchy.

6 Conclusions

The IceCube Neutrino Telescope has marked a first step in the era of neutrino astronomy. There is an increasing evidence for high-energy neutrinos beyond the atmospheric spectrum and future data will provide hints to detect the sources that until now remain unidentified. The IceCube Collaboration is also conducting sensitive indirect dark matter searches and testing neutrino oscillations at higher energies than those studied by reactors and accelerator based experiments. Moreover, the proposed PINGU upgrade could be able to answer the neutrino mass hierarchy problem.

References

1. A. Achterberg *et al*, Astropart. Phys. **26**, 155 (2006).
2. M.G. Aartsen *et al*, JINST **9**, P03009 (2014).
3. M.G. Aartsen *et al*, Phys. Rev. Lett. **111**, 021103 (2013).
4. M.G. Aartsen *et al*, Science **342**, 12412856 (2013).
5. M.G. Aartsen *et al*, Phys. Rev. Lett. in press, ArXiv:1405.5303 (2014).
6. C. Weaver for the IceCube Collaboration, APS April Meeting 2014.
7. M.G. Aartsen *et al*, ArXiv:1406.6757 (2014).
8. R. Abbasi *et al*, Nature **484**, 351 (2012).
9. T. Piran, Rev. Mod. Phys. **76**, 1143 (2004). P. Meszaros, Rept. Prog. Phys. **69**, 2259 (2006).
10. S. Hummer, P. Baerwald, W. Winter, Phys. Rev. Lett. **108**, 231101 (2012).
11. M.G. Aartsen *et al*, Phys. Rev. Lett. **110**, 131302 (2013).
12. M.G. Aartsen *et al*, Phys. Rev. Lett. **111**, 081801 (2013) and J.P. Yañez for the IceCube Collaboration, Neutrino 2014.
13. M.G. Aartsen *et al*, ArXiv:1401.2046 (2014).

Frascati Physics Series Vol. 58 (2014)
Frontier Objects in Astrophysics and Particle Physics
May 18-24, 2014

STATUS OF NEUTRINO OSCILLATIONS AND STERILE NEUTRINOS

Carlo Giunti
INFN, Sezione di Torino, Via P. Giuria 1, I–10125 Torino, Italy

Abstract

We review the status of standard three-neutrino mixing and the results of a global analysis of short-baseline neutrino oscillation data in the extended framework of 3+1 neutrino mixing with a sterile neutrino at the eV scale.

1 Introduction

Neutrino oscillations have been measured with high accuracy in solar, atmospheric and long-baseline neutrino oscillation experiments. Hence, we know without doubt that neutrinos are massive and mixed particles (see Ref. [1]). In this short review we discuss the status of the standard three-neutrino mixing paradigm (Section 2) and the indications in favor of the existence of an additional sterile neutrino given by anomalies found in some short-baseline neutrino oscillation experiments (Section 3).

2 Three-Neutrino Mixing

Solar neutrino experiments (Homestake, GALLEX/GNO, SAGE, Super-Kamiokande, SNO, Borexino) measured $\nu_e \to \nu_\mu, \nu_\tau$ oscillations generated by the solar squared-mass difference $\Delta m^2_{\rm SOL} \simeq 7 \times 10^{-5}\,{\rm eV}^2$ and a mixing angle $\sin^2\vartheta_{\rm SOL} \simeq 0.3$. The KamLAND experiment confirmed these oscillations by observing the disappearance of reactor $\bar\nu_e$ with average energy $\langle E\rangle \simeq 4\,{\rm MeV}$ at the average distance $\langle L\rangle \simeq 180\,{\rm km}$.

Atmospheric neutrino experiments (Kamiokande, IMB, Super-Kamiokande, Soudan-2, MACRO, MINOS) measured ν_μ and $\bar\nu_\mu$ disappearance through oscillations generated by the atmospheric squared-mass difference $\Delta m^2_{\rm ATM} \simeq 2.3\times10^{-3}\,{\rm eV}^2$ and a mixing angle $\sin^2\vartheta_{\rm ATM} \simeq 0.5$. The K2K and MINOS long-baseline experiments confirmed these oscillations by observing the disappearance of accelerator ν_μ with $\langle E\rangle \simeq 1.3\,{\rm GeV}$ and $3\,{\rm GeV}$ at distances $L \simeq 250\,{\rm km}$ and $730\,{\rm km}$, respectively.

The Super-Kamiokande atmospheric neutrino data indicate that the disappearance of ν_μ is likely due to $\nu_\mu \to \nu_\tau$ transitions, in agreement with the observation of $\nu_\mu \to \nu_\tau$ events in the OPERA long-baseline accelerator experiment.

The two independent solar and atmospheric Δm^2's are nicely accommodated in the standard framework of three-neutrino mixing in which the left-handed components of the three active flavor neutrino fields ν_e, ν_μ, ν_τ are superpositions of three massive neutrino fields ν_1, ν_2, ν_3 with masses m_1, m_2, m_3: $\nu_{\alpha L} = \sum_{k=1}^{3} U_{\alpha k}\nu_{kL}$, for $\alpha = e, \mu, \tau$. The unitary mixing matrix can be written in the standard parameterization in terms of three mixing angles ϑ_{12}, ϑ_{23}, ϑ_{13} and a CP-violating phase[1] δ:

$$U = \begin{pmatrix} c_{12}c_{13} & s_{12}c_{13} & s_{13}e^{-i\delta} \\ -s_{12}c_{23} - c_{12}s_{23}s_{13}e^{i\delta} & c_{12}c_{23} - s_{12}s_{23}s_{13}e^{i\delta} & s_{23}c_{13} \\ s_{12}s_{23} - c_{12}c_{23}s_{13}e^{i\delta} & -c_{12}s_{23} - s_{12}c_{23}s_{13}e^{i\delta} & c_{23}c_{13} \end{pmatrix}, \quad (1)$$

where $c_{ab} \equiv \cos\vartheta_{ab}$ and $s_{ab} \equiv \sin\vartheta_{ab}$. It is convenient to choose the numbers labeling the massive neutrinos in order to have

$$\Delta m^2_{\rm SOL} = \Delta m^2_{21} \ll \Delta m^2_{\rm ATM} = \frac{1}{2}\left|\Delta m^2_{31} + \Delta m^2_{32}\right|, \quad (2)$$

[1]For simplicity, we do not consider the two Majorana CP-violating phases which contribute to neutrino mixing if massive neutrinos are Majorana particles, because they do not affect neutrino oscillations (see Ref. [1]).

parameter	h.t.	b.f.	1σ range	2σ range	3σ range	r.u.
$\Delta m^2_{\rm S}/10^{-5}\,{\rm eV}^2$		7.54	7.32 – 7.80	7.15 – 8.00	6.99 – 8.18	3%
$\sin^2\vartheta_{12}/10^{-1}$		3.08	2.91 – 3.25	2.75 – 3.42	2.59 – 3.59	5%
$\Delta m^2_{\rm A}/10^{-3}\,{\rm eV}^2$	NH	2.44	2.38 – 2.52	2.30 – 2.59	2.22 – 2.66	3%
	IH	2.40	2.33 – 2.47	2.25 – 2.54	2.17 – 2.61	3%
$\sin^2\vartheta_{23}/10^{-1}$	NH	4.25	3.98 – 4.54	3.76 – 5.06	3.57 – 6.41	11%
	IH	4.37	4.08 – 6.10	3.84 – 6.37	3.63 – 6.59	11%
$\sin^2\vartheta_{13}/10^{-2}$	NH	2.34	2.16 – 2.56	1.97 – 2.76	1.77 – 2.97	9%
	IH	2.39	2.18 – 2.60	1.98 – 2.80	1.78 – 3.00	9%

Table 1: Best fit (b.f.) values of the neutrino mixing parameters obtained in the global analysis of neutrino oscillation data presented in Ref. [2] in the framework of three-neutrino mixing with the two hierarchy types (h.t.): normal hierarchy (NH) and inverted hierarchy (IH). The relative uncertainty (r.u.) has been obtained from the 3σ range divided by 6.

with $\Delta m^2_{kj} = m^2_k - m^2_j$. Then, there are two possible hierarchies for the neutrino masses: the normal hierarchy (NH) with $m_1 < m_2 < m_3$ and the inverted hierarchy (IH) with $m_3 < m_1 < m_2$.

With the conventions in Eqs. (1) and (2), we have $\vartheta_{\rm SOL} = \vartheta_{12}$ and $\vartheta_{\rm ATM} = \vartheta_{23}$. Moreover, the mixing angle ϑ_{13} generates ν_e disappearance and $\nu_\mu \to \nu_e$ transitions driven by $\Delta m^2_{\rm ATM}$, which can be observed in long-baseline neutrino oscillation experiments.

In 2011 the T2K experiment reported the first indication of long-baseline $\nu_\mu \to \nu_e$ transitions, followed by the MINOS experiment. Recently, the T2K Collaboration reported a convincing 7.5σ observation of $\nu_\mu \to \nu_e$ transitions through the measurement of 28 ν_e events with an expected background of 4.92 ± 0.55 events.

The most precise measurement of the value of ϑ_{13} comes from the measurement of $\bar\nu_e$ disappearance in the Daya Bay reactor experiment: $\sin^2 2\vartheta_{13} = 0.090^{+0.008}_{-0.009}$. This result has been confirmed by the data of the RENO and Double Chooz reactor experiments. Hence, we have a robust evidence of a non-zero value of ϑ_{13}. It is very important, because it opens promising perspectives for the observation of CP violation in the lepton sector and matter effects in long-baseline oscillation experiments, which could allow to distinguish the normal and inverted neutrino mass hierarchies.

The three-neutrino mixing parameters can be determined with good precision with a global fit of neutrino oscillation data. In Tab. 1 we report the results of the latest global fit presented in Ref. [2]. One can see that all the oscillation parameters are determined with precision between about 3% and 11%. The largest uncertainty is that of ϑ_{23}, which is known to be close to maximal ($\pi/4$), but it is not known if it is smaller or larger than $\pi/4$. For the Dirac CP-violating phase δ, there is an indication in favor of $\delta \approx 3\pi/2$, which would give maximal CP violation, but at 3σ all the values of δ are allowed, including the CP-conserving values $\delta = 0, \pi$.

3 Beyond Three-Neutrino Mixing: Sterile Neutrinos

The completeness of the three-neutrino mixing paradigm has been challenged by the following indications in favor of short-baseline neutrino oscillations, which require the existence of at least one additional squared-mass difference $\Delta m^2_{\rm SBL} \gg \Delta m^2_{\rm ATM}$:

1. The reactor antineutrino anomaly, which is an about 2.8σ deficit of the rate of $\bar{\nu}_e$ observed in several short-baseline reactor neutrino experiments in comparison with that expected from a new calculation of the reactor neutrino fluxes.

2. The Gallium neutrino anomaly, consisting in a short-baseline disappearance of ν_e measured in the Gallium radioactive source experiments GALLEX and SAGE with a statistical significance of about 2.9σ.

3. The LSND experiment, in which a signal of short-baseline $\bar{\nu}_\mu \to \bar{\nu}_e$ oscillations has been observed with a statistical significance of about 3.8σ.

In this review, we consider the 3+1 neutrino mixing scheme in which there is an additional massive neutrinos at the eV scale and the masses of the three standard massive neutrinos are much smaller. Since from the LEP measurement of the invisible width of the Z boson we know that there are only three active neutrinos (see Ref. [1]), in the flavor basis the additional massive neutrino corresponds to a sterile neutrinos, which does not have standard weak interactions.

In the 3+1 scheme, the effective probability of $\nu_\alpha \to \nu_\beta$ transitions in short-baseline experiments has the two-neutrino-like form

$$P_{\nu_\alpha \to \nu_\beta} = \delta_{\alpha\beta} - 4|U_{\alpha 4}|^2 \left(\delta_{\alpha\beta} - |U_{\beta 4}|^2\right) \sin^2\left(\frac{\Delta m^2_{41} L}{4E}\right) , \qquad (3)$$

where U is the mixing matrix, L is the source-detector distance, E is the neutrino energy and $\Delta m^2_{41} = m^2_4 - m^2_1 = \Delta m^2_{\rm SBL} \sim 1\,{\rm eV}^2$. The electron and muon neutrino and antineutrino appearance and disappearance in short-baseline experiments depend on $|U_{e4}|^2$ and $|U_{\mu 4}|^2$, which determine the amplitude $\sin^2 2\vartheta_{e\mu} = 4|U_{e4}|^2|U_{\mu 4}|^2$ of $\nu_\mu \to \nu_e$ transitions, the amplitude $\sin^2 2\vartheta_{ee} = 4|U_{e4}|^2\left(1 - |U_{e4}|^2\right)$ of ν_e disappearance, and the amplitude $\sin^2 2\vartheta_{\mu\mu} = 4|U_{\mu 4}|^2\left(1 - |U_{\mu 4}|^2\right)$ of ν_μ disappearance.

Since the oscillation probabilities of neutrinos and antineutrinos are related by a complex conjugation of the elements of the mixing matrix (see Ref. [1]), the effective probabilities of short-baseline $\nu_\alpha \to \nu_\beta$ and $\bar\nu_\alpha \to \bar\nu_\beta$ transitions are equal.

Global fits of short-baseline neutrino oscillation data have been presented recently in Ref. [3, 4]. These analyses take into account the final results of the MiniBooNE experiment, which was made in order to check the LSND signal with about one order of magnitude larger distance (L) and energy (E), but the same order of magnitude for the ratio L/E from which neutrino oscillations depend. Unfortunately, the data of the MiniBooNE experiment do not allow us to confirm or reject the LSND $\bar\nu_\mu \to \bar\nu_e$ signal because the experiment had too large backgrounds. Moreover, the ν_e and $\bar\nu_e$ MiniBooNE data show an excess in the low-energy bins which is widely considered to be anomalous because it is at odds with neutrino oscillations.

In the following we summarize the results of the 3+1 analysis of short-baseline data presented in Ref. [4] of the following three groups of experiments:

(A) The $\nu_\mu \to \nu_e$ and $\bar\nu_\mu \to \bar\nu_e$ appearance data of the LSND, MiniBooNE, BNL-E776, KARMEN, NOMAD, ICARUS and OPERA experiments.

(B) The ν_e and $\bar\nu_e$ disappearance data described in Ref. [5], which take into account the reactor and Gallium anomalies.

(C) The constraints on ν_μ and $\bar\nu_\mu$ disappearance obtained from the data of the CDHSW experiment, from the data of atmospheric neutrino oscillation

	LOW	HIG	noMB	noLSND
$\chi^2_{\rm min}$	291.7	261.8	236.1	278.4
NDF	256	250	218	252
GoF	6%	29%	19%	12%
$(\chi^2_{\rm min})_{\rm APP}$	99.3	77.0	50.9	91.8
$(\chi^2_{\rm min})_{\rm DIS}$	180.1	180.1	180.1	180.1
$\Delta\chi^2_{\rm PG}$	12.7	4.8	5.1	6.4
$\rm NDF_{PG}$	2	2	2	2
$\rm GoF_{PG}$	0.2%	9%	8%	4%
$\Delta\chi^2_{\rm NO}$	47.5	46.2	47.1	8.3
$\rm NDF_{NO}$	3	3	3	3
$n\sigma_{\rm NO}$	6.3σ	6.2σ	6.3σ	2.1σ

Table 2: Results of the 3+1 fit of short-baseline data [4] taking into account all MiniBooNE data (LOW), only the MiniBooNE data above 475 MeV (HIG), without MiniBooNE data (noMB) and without LSND data (noLSND). The first three lines give the minimum χ^2 ($\chi^2_{\rm min}$), the number of degrees of freedom (NDF) and the goodness-of-fit (GoF). The following five lines give the quantities relevant for the appearance-disappearance (APP-DIS) parameter goodness-of-fit (PG). The last three lines give the difference between the χ^2 without short-baseline oscillations and $\chi^2_{\rm min}$ ($\Delta\chi^2_{\rm NO}$), the corresponding difference of number of degrees of freedom ($\rm NDF_{NO}$) and the resulting number of σ's ($n\sigma_{\rm NO}$) for which the absence of oscillations is disfavored.

experiments, from the MINOS neutral-current data and from the analysis of the SciBooNE-MiniBooNE data.

Table 2 summarizes the statistical results. In the LOW fit all the MiniBooNE data are considered, including the anomalous low-energy bins, which are omitted in the HIG fit. There is also a noMB fit without MiniBooNE data and a noLSND fit without LSND data.

From Tab. 2, one can see that in all fits which include the LSND data the absence of short-baseline oscillations is disfavored by about 6σ, because the improvement of the χ^2 with short-baseline oscillations is much larger than the number of oscillation parameters.

The goodness-of-fit in the LOW analysis is significantly worse than that in the HIG analysis and the appearance-disappearance parameter goodness-of-fit is much worse. This result confirms the fact that the MiniBooNE low-energy

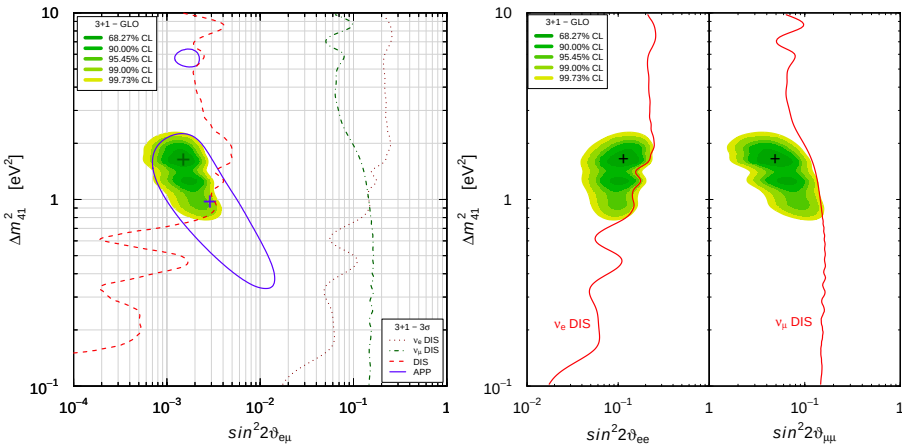

Figure 1: Allowed regions in the $\sin^2 2\vartheta_{e\mu}$–Δm^2_{41}, $\sin^2 2\vartheta_{ee}$–Δm^2_{41} and $\sin^2 2\vartheta_{\mu\mu}$–$\Delta m^2_{41}$ planes obtained in the global (GLO) HIG fit [4] of short-baseline neutrino oscillation data compared with the 3σ allowed regions obtained from $\nu_\mu \to \nu_e$ short-baseline appearance data (APP) and the 3σ constraints obtained from ν_e short-baseline disappearance data (ν_e DIS), ν_μ short-baseline disappearance data (ν_μ DIS) and the combined short-baseline disappearance data (DIS). The best-fit points of the GLO and APP fits are indicated by crosses.

anomaly is incompatible with neutrino oscillations, because it would require a small value of Δm^2_{41} and a large value of $\sin^2 2\vartheta_{e\mu}$, which are excluded by the data of other experiments (see Ref. [4] for further details). Therefore, we think that it is very likely that the MiniBooNE low-energy anomaly has an explanation which is different from neutrino oscillations and the HIG fit is more reliable than the LOW fit.

Figure 1 shows the allowed regions in the $\sin^2 2\vartheta_{e\mu}$–Δm^2_{41}, $\sin^2 2\vartheta_{ee}$–Δm^2_{41} and $\sin^2 2\vartheta_{\mu\mu}$–$\Delta m^2_{41}$ planes obtained in the HIG fit of Ref. [4]. These regions are relevant, respectively, for $\nu_\mu \to \nu_e$ appearance, ν_e disappearance and ν_μ disappearance searches. Figure 1 shows also the region allowed by $\nu_\mu \to \nu_e$ appearance data and the constraints from ν_e disappearance and ν_μ disappearance data. One can see that the combined disappearance constraint in the $\sin^2 2\vartheta_{e\mu}$–Δm^2_{41} plane excludes a large part of the region allowed by $\nu_\mu \to \nu_e$ appearance data, leading to the well-known appearance-disappearance tension

quantified by the parameter goodness-of-fit in Tab. 2.

It is interesting to investigate what is the impact of the MiniBooNE experiment on the global analysis of short-baseline neutrino oscillation data. With this aim, the authors of Ref. [4] performed two additional 3+1 fits: a noMB fit without MiniBooNE data and a noLSND fit without LSND data. From Tab. 2 one can see that the results of the noMB fit are similar to those of the HIG fit and the exclusion of the case of no-oscillations remains at the level of 6σ. On the other hand, in the noLSND fit, without LSND data, the exclusion of the case of no-oscillations drops dramatically to 2.1σ. In fact, in this case the main indication in favor of short-baseline oscillations is given by the reactor and Gallium anomalies which have a similar statistical significance. Therefore, it is clear that the LSND experiment is still crucial for the indication in favor of short-baseline $\bar{\nu}_\mu \to \bar{\nu}_e$ transitions and the MiniBooNE experiment has been rather inconclusive.

In conclusion, the results of the global fit of short-baseline neutrino oscillation data presented in Ref. [4] show that the data can be explained by 3+1 neutrino mixing if the low-energy MiniBooNE anomaly is omitted. Moreover, the crucial indication in favor of short-baseline $\bar{\nu}_\mu \to \bar{\nu}_e$ appearance is still given by the old LSND data and the MiniBooNE experiment has been inconclusive. Hence new better experiments are needed in order to check this signal.

References

1. C. Giunti and C. W. Kim, *Fundamentals of Neutrino Physics and Astrophysics* (Oxford University Press, Oxford, UK, 2007), ISBN 978-0-19-850871-7.

2. F. Capozzi, G. L. Fogli, E. Lisi, A. Marrone, D. Montanino and A. Palazzo, Phys.Rev. **D89**, 093018 (2014).

3. J. Kopp, P. A. N. Machado, M. Maltoni, and T. Schwetz, JHEP **1305**, 050 (2013).

4. C. Giunti, M. Laveder, Y. Li, and H. Long, Phys.Rev. **D88**, 073008 (2013).

5. C. Giunti, M. Laveder, Y. Li, Q. Liu, and H. Long, Phys. Rev. **D86**, 113014 (2012).

Frascati Physics Series Vol. 58 (2014)
Frontier Objects in Astrophysics and Particle Physics
May 18-24, 2014

ARE THE ICECUBE NEUTRINO EVENTS EXTRATERRESTRIAL OR CAN BE OF ATMOSPHERIC ORIGIN?

A.A. Petrukhin
National Research Nuclear University MEPhI
(Moscow Engineering Physics Institute),
115409, Moscow, Russia

Abstract

Cascade showers with PeV energies observed in the IceCube experiment gave a powerful pulse to discussions of their possible extraterrestrial neutrino origin. The reason is very simple. The expected flux of atmospheric neutrinos is very small to generate such events. But if to take into account a possibility of formation of a new state of matter in nucleus-nucleus interactions of cosmic rays with energies of about 10^{16} eV and above, the picture may drastically change. Calculations show that in this case the muon and neutrino spectra would be much harder than it is usually assumed and could explain the appearance of such cascade showers. The energy spectrum of muons measured in BUST and IceCube experiments at energies above 100 TeV showed a significant excess of the measured number of muons in comparison with calculations based on the traditional approach. In this case, the events observed in the IceCube can be generated by atmospheric neutrinos, and their registration can be the evidence in support of the formation of the new state of matter at very high energies.

1 Introduction

The search for extraterrestrial sources of high energy neutrinos is one of the main tasks of the IceCube experiment. And several events [1)] that could only be caused by interactions of neutrinos with PeV energies have been registered (fig. 1). The probability of formation of cascades with such energies by other particles is vanishingly small, and the flux of neutrinos of atmospheric origin from known sources of their generation is clearly insufficient to explain the observed number of events. Neutrino production in the decays of pions, kaons and other light mesons at such energies is strongly suppressed due to a significant increase in their lifetime with the energy growth. Decays of charmed and other heavier particles in principle can explain the necessary neutrino flux, but for that very large yield of such particles is required.

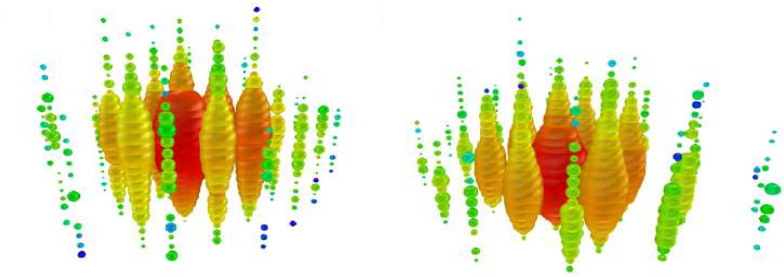

Figure 1: *PeV cascade showers from neutrinos observed in the IceCube* [1)].

Therefore it is rightful to consider the inclusion of a new process of interaction, which can lead to a dramatic increase in the number of produced muons and neutrinos. As of such a process, the mechanism of formation of blobs of quark-gluon matter with a large orbital momentum [2)], which leads to appearance of a centrifugal barrier with a height inversely proportional to the mass of particles emitted from that blob, may be considered. As a result, the probability of emission of the light quarks is significantly suppressed and for heavy particles (such as the top quark) there is practically no barrier.

The paper provides a quantitative estimation of the possible neutrino flux from the new mechanism of hadron interaction, which may explain the appearance of events registered in the IceCube, and discusses the possibility of

independent evaluation of the flux of ultrahigh-energy muons, detected in the IceCube from the upper hemisphere at various zenith angles.

2 Muon and neutrino flux in atmosphere

The results of theoretical calculations of muon flux in the atmosphere are presented in many publications and differ from one another, but in general give a picture shown in fig. 2 [3]. The point is that the muon energy spectrum measured in various experiments imposes serious restrictions on the possibilities of manipulating of parameters of hadron interactions used in the calculations. Though the results of these experiments indicate some excess of muons with energies above 10 TeV in comparison with calculations (fig. 2), its value is not significant and was usually explained by some overestimation of muon energy in the corresponding experiments, especially taking into account the indirect character of the used methods of muon energy estimation.

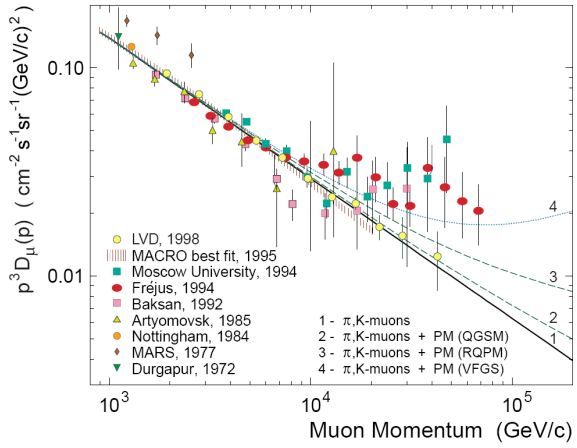

Figure 2: *Differential energy spectrum of cosmic ray muons* [3].

Appearance of the model of formation of quark-gluon matter blobs with the large orbital momentum dramatically changed the situation. In this case there are two major changes in the behaviour of the muon components of cosmic rays in the atmosphere [4]: firstly, the excess of muon bundles in extensive air showers appears, and secondly, the inclusive energy spectrum of muons in

the energy region above 100 TeV changes strongly. If a new state of matter decays into very heavy particles, e. g. into top-anti-top pair, which in their turn decay into W-bosons and b-quarks, then an additional muon flux appears. For illustration, in fig. 3 the contribution of this process in cosmic ray muon energy spectrum is shown. As the figure shows, the number of muons and correspondingly neutrinos with PeV energies increases by almost two orders of magnitude and becomes sufficient to explain the events observed in IceCube.

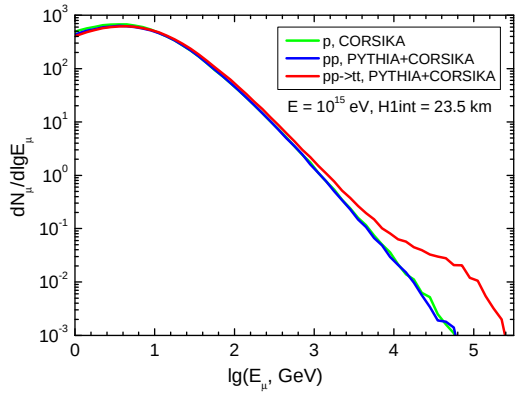

Figure 3: *Energy spectrum of muons from t-quark decay, for a fixed primary energy* 10^{15} *eV.*

3 How to check the proposed approach?

Between the energy spectra of muons and neutrinos there is some connection, caused by the processes of their formation. Energy spectra of muons and neutrinos from the decays of pions at high energies, where the muon decay can be neglected, are similar. In the decays of kaons and other heavier particles the ratio between μ and ν changes, though not very noticeable. In the decays of W-bosons the situation is much different as the decay probabilities in any lepton pair: electron, muon and tau – are practically equal, and in the first approximation the total muon flux must be two-three times less than the total neutrino flux. However, this flux is sufficient for its registration on different setups.

The first result on the measurement of the energy spectrum of muons at energies above 100 TeV was obtained in the experiment conducted at the Baksan Underground Scintillation Telescope (fig. 4) [5]. Though statistics in this energy region is low, nevertheless all registered events are quite clear and convincing. This result was in fact confirmed in the IceCube experiment. An excess of muons with energies above 100 TeV was registered at different zenith angles (fig. 5) [6].

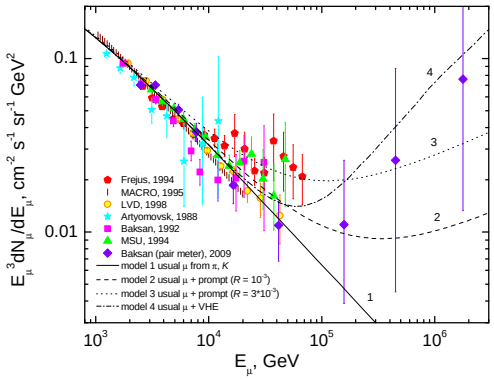

Figure 4: *Data from Baksan Underground Scintillation Telescope (the dark diamonds)* [5].

The other model prediction – the appearance of an excess of muon bundles in EAS, which in most studies was interpreted as a heavier mass composition of primary cosmic rays (PCR) – was experimentally confirmed. But with the energy growth its value exceeded the predictions even for pure iron primary flux. The results of muon bundles study at NEVOD-DECOR setup [7] and Pierre Auger Observatory [8] are presented in figs. 6 and 7 correspondingly.

So, various experiments confirm the predictions of the new model of nucleus-nucleus interaction. But to finally prove this it is necessary to obtain the cosmic ray muon energy spectrum above 100 TeV with higher statistics. For that it is expedient to use the method of registering of electron-positron pairs (pair meter technique), which allows to estimate the energy of almost every muon, unlike the method of detection of cascade showers caused by bremsstrahlung, which probability is $\sim 10^{-2}$. Naturally for the successful

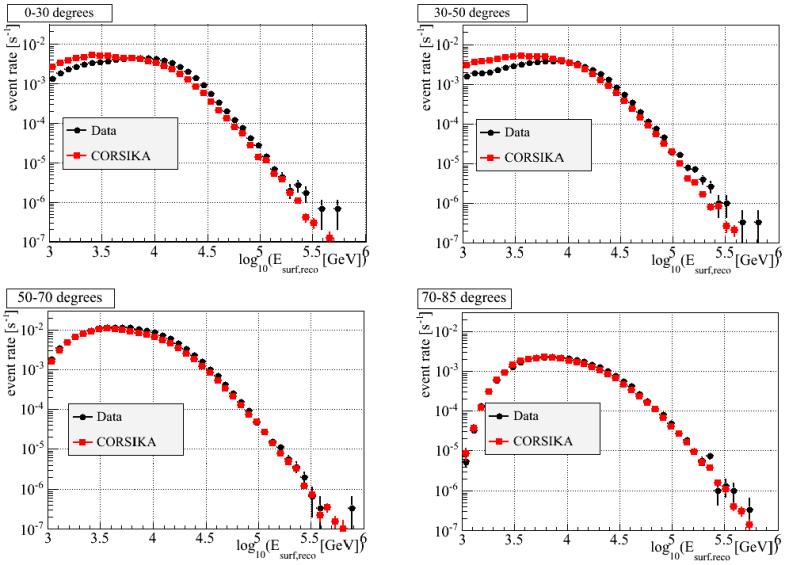

Figure 5: *Cascade shower spectra from muons registered in IceCube at different zenith angles* [6].

application of this method to the analysis of experimental data it is necessary to solve a number of methodical issues related to the large multiplicity of detected muons and to the structure of IceCube (large distances between measuring modules, downward orientation of photomultipliers). However, a large volume of the detector and a high statistics of the experimental data allow to hope that this problem will be solved, and the energy spectrum of muons will be obtained up to PeV energies.

4 Conclusion

If it is shown that the energy spectrum of muons changes its behavior in the energy region above 100 TeV and muons with energy of PeV are registered, then, naturally, the assumption of astrophysical origin of neutrinos which caused PeV cascade showers will be incorrect. But in this case these events confirm the existence of a new state of matter, which is formed in the PeV energy region in nucleus-nucleus interactions. Maybe it will not be a blob of quark-gluon

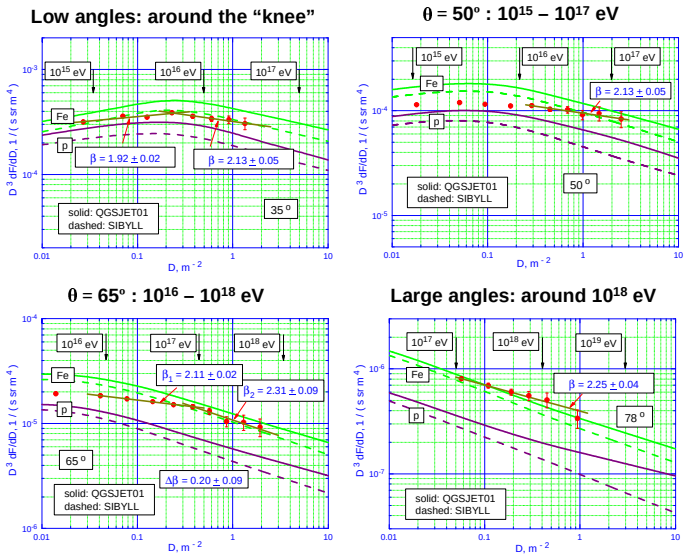

Figure 6: *Local muon density spectra measured in NEVOD-DECOR* [7].

matter with a large orbital momentum, but something else. In any case, a new state of matter should explain the changes in the neutrino (and muon) energy spectrum in the energy region above 100 TeV, the appearance of muon bundles excess growing with PCR energy, as well as anomalies observed in hadron experiments (halos, alignment, penetrating cascades, Centauros, etc.). As shown in [2], the model of formation of quark-gluon blobs with a large orbital momentum allows to explain all unusual phenomena observed in cosmic rays, including changes in the EAS energy spectrum and interpretation of changes in the mass composition of PCR from a unified point of view.

5 Acknowledgements

Author thanks A.G. Bogdanov and R.P. Kokoulin for fruitful discussions and the help in preparation of this paper. This work has been supported by Ministry of Education and Science of the Russian Federation and the Leading Scientific School grant NSh-4930.2014.2.

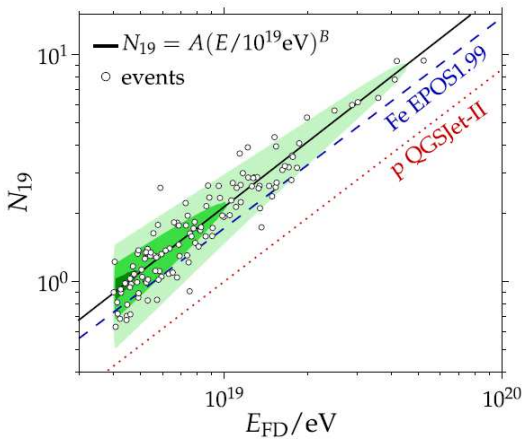

Figure 7: *Results of muon component investigations in the Auger experiment for inclined EAS* [8].

References

1. M.G. Aarsten *et al*, PRL **111**, 021103 (2013).
2. A.A. Petrukhin, in: Proceedings of the Vulcano Workshop 'Frontier Objects in Astrophysics and Particle Physics', p.497 (ed. F. Giovanelli, G. Mannocchi, 2006).
3. E.V. Bugaev *et al*, Phys. Rev. D **58**, 05401 (1998); arXiv:hep-ph/9803488 v3, Jan 2000.
4. A.A. Petrukhin, NIM **A742**, 228 (2014).
5. A.G. Bogdanov *et al*, Astropart. Phys. **36**, 224 (2012).
6. P. Berghaus and C. Xu, Atmospheric muon spectrum from catastrophic energy losses in IceCube. Talk presented at 32nd Int. Cosmic Ray Conf., Beijing, 2011.
7. O. Saavedra *et al*, J. Phys.: Conf. Ser. **409**, 012009 (2013).
8. G. Rodriguez, EPJ Web of Conf. **53**, 07003 (2013).

Frascati Physics Series Vol. 58 (2014)
Frontier Objects in Astrophysics and Particle Physics
May 18-24, 2014

RESULTS FROM THE PAMELA SPACE EXPERIMENT

Emiliano Mocchiutti on behalf of the PAMELA Collaboration
INFN, Sezione di Trieste, I-34149 Trieste, Italy

Abstract

Launched on 15^{th} June 2006, the PAMELA apparatus is still collecting data more than doubling the expected life time. A review of the most significant results obtained by PAMELA will be presented with particular emphasis on the precision of the measurements addressing the issue of systematic and statistical errors. Moreover, results about the ongoing analyses about solar modulation and solar flares will be discussed.

1 Introduction

PAMELA[1] is a satellite borne experiment built to study the cosmic rays. In this work the results obtained after almost eight years of data taking are reviewed.

[1]The PAMELA Collaboration: O. Adriani, G.C. Barbarino, G.A. Bazilevskaya, R. Bellotti, M. Boezio, E.A. Bogomolov, M. Bongi, V. Bonvicini,

2 Physics goals and instrument description

The PAMELA physics goal is the measurement of the cosmic ray spectra at 1 Astronomical Unit (AU). Its 70 degrees quasi–polar orbit makes it particularly suited to study items of galactic, heliospheric and trapped nature. PAMELA has been mainly conceived to perform high–precision spectral measurement of antiprotons and positrons and to search for antinuclei, over a wide energy range. Besides the study of cosmic antimatter, the instrument setup and the flight characteristics allow many additional scientific goals to be pursued [1)]. The instrument is installed inside a pressurized container attached to the Russian Resurs–DK1 Earth–observation satellite that was launched into Earth orbit on June 15^{th} 2006 from the Baikonur cosmodrome in Kazakhstan. The mission has been extended from the foreseen three years to the actual unlimited acquisition, till at least December 31^{st} 2015. PAMELA was first switched on June 21^{st} 2006 and it has been collecting data continuously since July 11^{th} 2006 for more than 40 TB of collected data. To date about 2900 days of data have been analyzed, corresponding to more than one billion recorded triggers. A schematic overview of the PAMELA apparatus is shown in fig. 1. The apparatus is ∼1.3 m high, has a total mass of 470 kg and an average power consumption of 355 W. It comprises the following subdetectors, arranged as shown in figure (from top to bottom): a time–of–flight system (TOF – S1, S2, S3); a magnetic spectrometer; an anticoincidence system (AC – CARD, CAT, CAS); an electromagnetic imaging calorimeter; a shower tail catcher scintillator (S4) and a neutron detector. The central components of PAMELA are a permanent magnet and a tracking system composed of six planes of double–sided silicon sensors, which form the magnetic spectrometer. This device is used to

S. Bottai, A. Bruno, F. Cafagna, D. Campana, R. Carbone, P. Carlson, M. Casolino, G. Castellini, A. Danilchenko, C. De Donato, C. De Santis, N. De Simone, V. Di Felice, V. Formato, A.M. Galper, U. Giaccari, A.V. Karelin, S.V. Koldashov, S. Koldobskiy, S.Y. Krutkov, A.A. Kvashnin, A.N. Kvashnin, A. Leonov, V. Malakhov, L. Marcelli, M. Martucci, A.G. Mayorov, W. Menn, M. Mergè, V.V. Mikhailov, E. Mocchiutti, A. Monaco, N. Mori, R. Munini, G. Osteria, F. Palma, B. Panico, P. Papini, M. Pearce, P. Picozza, C. Pizzolotto, M. Ricci, S.B. Ricciarini, R. Sarkar, M. Simon, R. Sparvoli, P Spillantini, Y.I. Stozhkov, A. Vacchi, E. Vannuccini, G.I. Vasilyev, S.A. Voronov, Y.T. Yurkin, G. Zampa, N. Zampa, V.G. Zverev

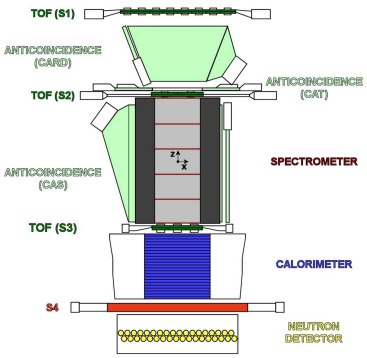

Figure 1: *Schematic view of the PAMELA apparatus.*

determine the rigidity (momentum divided by charge) and the charge of particles crossing the magnetic cavity. The rigidity measurement is done through the reconstruction of the trajectory based on the impact points on the tracking planes and the resulting determination of the curvature due to the Lorentz force. The direction of bending of the particle (*i.e.* the discrimination of the charge sign) is the key method used to separate matter from anti–matter. The sampling imaging calorimeter is used for particle identification. The high granularity of the calorimeter and the use of silicon strip detectors provide detailed information on the longitudinal and lateral profiles of particle interactions as well as a measure of the deposited energy. More technical details about the entire PAMELA instrument and launch preparations can be found in [2].

3 Particle measurements

Due to their abundance, the measurement of primary cosmic rays is easier with respect to the anti–particle measurements. Sample selection is very efficient and the main effort is put in the estimation of systematic uncertainties.

3.1 Protons and helium nuclei spectra

Precise measurements of proton and helium nuclei fluxes are needed to understand the acceleration and subsequent propagation of cosmic rays in the Galaxy. The results reported by PAMELA [3] in the rigidity range 1 GV –

1.2 TV, Fig. 2 on the left, show that the spectral shapes of these two species cannot be well described by a single power law. Moreover, the proton over helium fraction result shows that the spectral indexes of these two particle fluxes is different. This latter result is in a very good agreement with preliminary AMS measurement presented at the ICRC in 2013 (Rio de Janeiro, Brazil). These data challenge the current paradigm of cosmic-ray acceleration in supernova remnants followed by diffusive propagation in the Galaxy. The es-

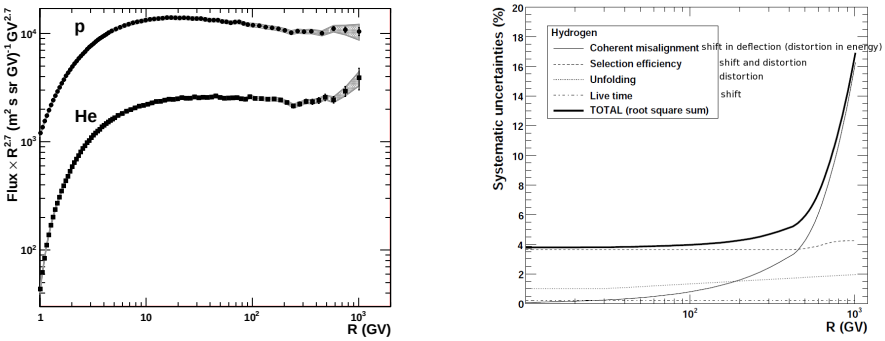

Figure 2: *On the left, proton and helium nuclei flux measured with PAMELA as function of the rigidity; shaded area represent the estimated systematic error. On the right, systematic uncertainties estimated for the PAMELA proton and helium nuclei flux.*

timation of systematic uncertainties is a crucial issue for this high statistic flux measurements. In the case of PAMELA, the estimated systematics are shown in figure 2, right panel. PAMELA results were tested for internal consistency, leading to the published results. The effect of the systematic uncertainties on the resulting spectrum, distortions or shift, are written in the figure.

3.2 Negative electron spectrum

The PAMELA apparatus is able to separate negative electrons from positrons up to about 600 GeV [4]. The capabilities of the PAMELA detectors permit also to contrain and estimate accurately any systematic effect due to the energy measurement. In fact the energy of electrons can be determined using two

independent detectors: the spectrometer and the electromagnetic calorimeter. The resulting flux can be easily described by a single power law, even if a certain hardening of the spectrum may be present at high energies. This interesting feature seems to be in agreement with the positron fraction measurement.

3.3 Nuclei

Light nuclei up to Oxygen are detectable with the dE/dx measured by the scintillator of the TOF system. It is possible to study with high statistics the secondary/primary cosmic ray nuclear and isotopic abundances such as B/C, Be/C, Li/C and ^{3}He/^{4}He. These measurements can constrain existing production and propagation models in the galaxy, providing detailed information on the galactic structure and the various mechanisms involved. The B/C ratio as function of kinetic energy per nucleon measured by PAMELA is in good agreement with previous measurements [5].

4 Anti–particle measurements

The main task of PAMELA is to measure the antimatter components of the cosmic–ray. At high energy, main sources of background in the antimatter samples result from spillover (protons in the antiproton sample and electrons in the positron sample) and from like–charged particles (electrons in the antiproton sample and protons in the positron sample).

4.1 Antiproton to proton ratio

Electrons in the antiproton sample can be easily rejected by applying conditions on the calorimeter shower topology, while the main source of background originates from spillover protons. In order to reduce the spillover background and accurately measure antiprotons up to the highest possible energy, strict selection criteria were imposed on the quality of the fit. To measure the antiproton–to–proton flux ratio the different calorimeter selection efficiencies for antiprotons and protons were estimated. The difference is due to the momentum dependent interaction cross–sections for the two particles. These efficiencies were studied using both simulated antiprotons and protons, and proton samples selected from the flight data. In this way it was possible to normalize the simulated proton and therefore the antiproton selection efficiency.

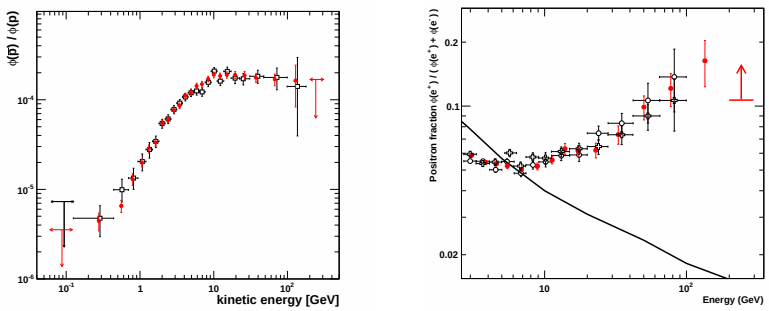

Figure 3: *Left panel: the antiproton-to-proton flux ratio obtained by PAMELA. Right panel: the PAMELA positron fraction compared to the standard model prediction for secondary positron production. Different symbols represent PAMELA published data sets.*

The left panel of fig. 3 shows the antiproton–to–proton flux ratio measured by the PAMELA experiment [6, 7]. Only statistical errors are shown since the systematic uncertainty is less than a few percent of the signal, which is significantly lower than the statistical uncertainty. The PAMELA data are in excellent agreement with recent data from other experiments, the antiproton–to–proton flux ratio increases smoothly with energy up to about 10 GeV and then levels off. The data follow the trend expected from secondary production calculations and our results are sufficiently precise to place tight constraints on secondary production calculations and contributions from exotic sources [6].

4.2 Positron fraction

Protons are the main source of background in the positron sample and excellent positron identification is needed to reduce the contamination at a negligible level. The method used to obtain the published results is the proton background estimation method. This approach consists in keeping a very high selection efficiency and in quantifying the residual proton contamination by the mean of a so–called "spectral analysis" [8, 9]. Results are shown in the right panel of fig. 3 where PAMELA data [8, 9, 10] are compared to the standard model theoretical prediction for secondary positron production. The PAMELA data

are in excellent agreement with AMS measurement [11]. The positron fraction cannot be described by the standard model of secondary production [12], black line in fig. 3, right panel. The rise at E>10 GeV seems a very difficult feature to be reproduced by a pure secondary component without using an unrealistic soft electron spectrum and ad hoc tuning of the other parameters [13], suggesting the existence of other primary sources [14].

5 Other measurements

5.1 Solar modulation galactic cosmic rays

Since protons and helium nuclei are detected by PAMELA with very high statistics it is possible to precisely study time variations and transient phenomena during the 23rd solar minimum and 24rd solar maximum. A long term measurement of the proton, electron and nuclear fluxes at 1 AU provides information on propagation phenomena occurring inside the heliosphere. As already mentioned, the possibility to measure the anti–particle spectra allow also charge dependent solar modulation effects to be studied. The proton flux as measured by PAMELA in different time intervals shows an increasing flux of galactic cosmic rays corresponding to a decreasing solar activity [15] between years 2006 and 2009. Studies are on-going to precisely determine the proton flux in the time interval from the solar minimum to the solar maximum.

5.2 Solar energetic particles

Due to the period of solar minimum few significant solar events with energy high enough to be detectable were registered. The observation of solar energetic particle (SEP) events with a magnetic spectrometer permit several aspects of solar and heliospheric cosmic ray physics to be addressed for the first time [16].

6 Conclusions

PAMELA is continuously taking data and the mission is planned to continue until the satellite will stay in orbit. An analysis for positron flux till low energy (down to 100 MeV), and for solar flares is in progress and will be the topic of future publications.

7 Acknowledgment

We would like to acknowledge contributions and support from: Italian Space Agency (ASI), Deutsches Zentrum für Luft– und Raumfahrt (DLR), The Swedish National Space Board, Swedish Research Council, Russian Space Agency (Roskosmos, RKA). R. S. wishes to thank the TRIL program of the International Center of Theoretical Physics, Trieste, Italy that partly sponsored his activity.

References

1. P. Picozza *et al.*, *Proceedings of 20th ECRS, Lisbon – Portugal 2006.*
2. P. Picozza *et al.*, Astrophys. J., **27** (2007) 296.
3. O. Adriani *et al.*, Science, **332** (2011) 69.
4. O. Adriani *et al.*, Phys. Rev. Lett., **106** (2011) 201101.
5. O. Adriani *et al.*, to appear on Astrophys. J. (2014).
6. O. Adriani *et al.*, Phys. Rev. Lett., **102** (2009) 051101.
7. O. Adriani *et al.*, JETP Lett., **69** (2012) 621.
8. O. Adriani *et al.*, Nature, **458** (2009) 607.
9. O. Adriani *et al.*, Astropart. Phys., **34** (2010) 1.
10. O. Adriani *et al.*, Phys. Rev. Lett., **111** (2013) 081102.
11. M. Aguilar *et al.*, Phys. Rev. Lett., **110** (2013) 141102.
12. I. Moskalenko and A. Strong, Astrophys. J., **493** (1998) 694.
13. T. Delahaye, F. Donato, N. Fornengo, J. Lavalle, R. Lineros, P. Salati and R. Taillet, Astro–Ph/0809.5268 Preprint (2008).
14. P. D.Serpico, Phys. Rev. D, **79** (2009) 021302.
15. O. Adriani *et al.*, Astrophys. J., **765** (2013) 91.
16. O. Adriani *et al.*, Astrophys. J., **742** (2011) 102.

Frascati Physics Series Vol. 58 (2014)
Frontier Objects in Astrophysics and Particle Physics
May 18-24, 2014

SPECTRA OF ASTROPHYSICAL PARTICLES AT ULTRA HIGH ENERGY AND THE AUGER DATA

Roberto Aloisio
INAF - Osservatorio Astrofisico di Arcetri, Firenze, Italy
Gran Sasso Science Institute (INFN), L'Aquila, Italy

Abstract

We use a kinetic-equation approach to describe the propagation of ultra high energy cosmic ray protons and nuclei comparing theoretical results with the observations of the Pierre Auger Observatory.

1 Introduction

After more than hundred years from the discovery of Cosmic Rays (CR), performed through the first balloon flight of Victor F. Hess in 1912, we have unveiled and understood most of the fundamental aspects of this fascinating phenomenon. In the energy range that spans from few GeV/n up to 10^3 TeV/n a self consistent scenario that accommodates CR composition, propagation and sources was developed in the last 30 years, the so-called standard model of galactic CR (for a review see [1)] and references therein). At the

highest energies, in the regime of Ultra High Energy Cosmic Rays (UHECR) with $E > 10^{17}$ eV, the situation becomes much more unclear. The origin of UHECR, with observed energies up to 10^{20} eV, has been challenging our theoretical understanding since long time and a clear solution of the problem is still lacking.

At energies in the range $10^{17} \div 10^{19}$ eV the propagation of UHE particles is extended over cosmological distances with a typical path length of the order of Gpc. Therefore the particle's energy is affected by the cosmological expansion of the universe that results in an adiabatic process of energy loss. Together with cosmology the propagation of UHECR is affected by the interaction with astrophysical radiation fields: the Cosmic Microwave Background (CMB) and the background field constituted by infra-red, visible and ultra-violet radiation that we will call collectively: Extragalactic Background Light (EBL). The first background is the well known cosmic radiation fossil of the big bang, with a black body spectrum degraded nowadays to a temperature of 2.7 °K. The EBL radiation field is produced by astrophysical objects at present and past cosmological epochs and subsequently modified by red-shift and dilution due to the expansion of the Universe.

As stated above the propagation of UHECR extends over cosmological distances, thus the cosmological evolution of the backgrounds has a non negligible role in the propagation of UHECR. While the cosmological evolution of the CMB is analytically known, the evolution with red-shift of the EBL field should be inferred from observations at different red-shifts through specific models [2]. These models are in good agreement in the low red-shifts regime ($z < 4$), which is the most important in the physics of UHECR, while show significant differences in the high red-shift regime ($z > 4$). These differences have a small impact on the expected UHECR flux and composition they affect only the production of cosmogenic neutrinos (see [3] and references therein). Being this issue outside the aims of the present paper we will not enter this discussion here using the recipe of Stecker [2] to model the EBL radiation field and its cosmological evolution.

Let us now briefly recall the dominant interactions channels of UHECR with the background radiation, with particular emphasis on their imprints on the expected flux. We will restrict the discussion to charged particles, being the possibility of photons as UHECR very unlikely as follows from experimental

observations [4].

The propagation of UHE nucleons[1] is affected only by the interaction with the CMB radiation field [5, 6]. There are two spectral signatures that can be firmly related to the propagation of protons through this background: pair-production dip [7], which is a rather faint feature caused by the pair production process: $p+\gamma_{CMB} \rightarrow e^+ + e^- + p$, and a sharp steepening of the spectrum caused by the pion photo-production: $p + \gamma_{CMB} \rightarrow \pi + p$ called Greisen-Zatsepin-Kuzmin (GZK) cut-off [8]. The GZK cutoff position is roughly defined by the energy where the pair-production and the photo-pion production energy loss become equal, namely at $E_{GZK} \simeq 50$ EeV [9].

The propagation of UHE nuclei, apart from CMB, is affected also by the EBL. The interaction processes that condition the propagation of UHE nuclei are pair production, that involves only the CMB background [6, 10, 11], and photo-disintegration. The latter is the process in which a nucleus of atomic mass number A because of the interaction with CMB and EBL looses one or more nucleons $A + \gamma_{CMB,EBL} \rightarrow (A - nN) + nN$, being n the number of nucleons lost by the nucleus [5, 6, 10, 11].The photo-disintegration of nuclei, together with the pair production process, produces a steepening in the observed spectrum. The exact position of the flux suppression depends only on the nuclei species, being a consequence of the interaction with the CMB field thus free from the uncertainties connected with the EBL [5, 6, 10, 11].

From the experimental point of view the observations of UHECR are far from being clear with different experiments claiming contradictory results. The HiRes and, nowadays, the Telescope Array (TA) experiments show a proton dominated composition till the highest energies with a clear observation of the proton pair-production dip and GZK cut-off [12, 13]. Chemical composition observed by HiRes and TA is coherent with such picture showing a pure proton dominated spectrum starting from energies $E \simeq 10^{18}$ eV till the highest energies. The experimental picture changes taking into account the Auger observations. The spectrum observed by Auger[2] shows a behavior not clearly

[1]Hereafter we will refer only to protons because, as discussed in [3, 5, 6], the decay time of neutrons is much shorter than all the other time scales involved in the propagation of UHE particles.

[2]Here we consider the Auger data published in 2011, the new results published in 2013 do not change the picture presented here [14].

understood in terms of the proton pair-production dip and GZK cut-off [15]. This spectral behavior could be a signal of a substantial nuclei pollution in the spectrum, which is confirmed by the Auger observations on chemical composition that show a progressively heavy composition toward the highest energies, this tendency starts already at $E > 4 \times 10^{18}$ eV [16].

In the present paper we will restrict our analysis only to the Auger data discussing the assumptions on the sources of UHECR that enable a good description of the flux [15] and chemical composition [16] observed by Auger. This analysis is performed without a formal fitting procedure, based on some likelihood method, that would be rather time consuming given the analytic computation scheme used. The main goal of this paper, based on the analysis presented in [14], is to give an overall picture, inferring general rules about the possible sources of UHECR.

The paper is organized as follows: in the next session 2 we will focus on the Auger data discussing the source models that better reproduce observations in terms of both flux and chemical composition, we will conclude in section 3 discussing the main outcomes of our study.

2 Auger Observations

Following the discussion recently presented in [14] we will use the theoretical framework based on the kinetic approach for the propagation of UHE particles, that was introduced in [9] for protons and in [5, 6] for nuclei. As in [14], we will assume that the spectrum of the accelerated particles at the sources has a power law behavior in energy and the sources are homogeneously distributed in the Universe with no cosmological evolution. Through this simplified theoretical approach we will compare Auger data on flux and chemical composition with theoretical predictions finding interesting general consequences on source models.

The most commonly used shower observables to study the composition of UHECR are the mean value of the depth of shower maximum $\langle X_{max} \rangle$ and its dispersion $\sigma(X_{max})$. As was first discussed in [17], the combined analysis of $\langle X_{max} \rangle$ and $\sigma(X_{max})$ is more sensitive to chemical composition and provides less model dependent results. However, inferring chemical composition of UHECR from these observables is subject to some level of uncertainty because their conversion to mass relies on shower simulations codes which depend on

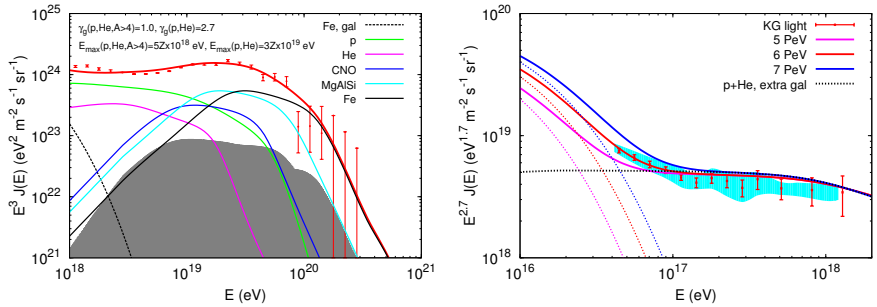

Figure 1: *[Left Panel] Flux of UHECR obtained with two classes of sources as described in the text in comparison with the flux observed by Auger* [15]. *[Right Panel] Low energy tail of the light UHECR component in comparison with the KASCADE-Grande data on the light component in the high energy tail of galactic cosmic rays* [18].

the assumptions on the hadronic interaction models. These models, while give the same fit to low energy accelerator data, provide different results of the high energy extrapolations needed in UHECR physics (for a review see [19]) and references therein).

To determine $\langle X_{max} \rangle$ and $\sigma(X_{max})$ we will use the results published in [20] that provide a simple recipe to compute these two quantities, given a specific choice of the hadronic interaction model used to simulate the shower development in the atmosphere. In [20] four different MC schemes were considered: EPOS 1.99, Sibyll 2.1, QGSJet 1 and QGSJet 2 [21]. In the following we will present results on $\langle X_{max} \rangle$ and $\sigma(X_{max})$ as shadowed regions that constrain the results of the four different MC schemes cited, this way of presenting the results is useful to show the uncertainties connected with the hadronic interaction model chosen. Therefore, in our analysis we will use three observables, i.e. flux $J(E)$, $\langle X_{max} \rangle$ and $\sigma(X_{max})$, to constrain theoretical models, i.e. injection power law index γ_g, source emissivity $\mathcal{L}_0$ and injection ratios of different nuclei species.

In figures 1 (left panel) and 2 we show our results. As discussed in [14], in order to reproduce the chemical composition observed by Auger it is needed to assume that heavy elements are injected at the source with a very flat injection

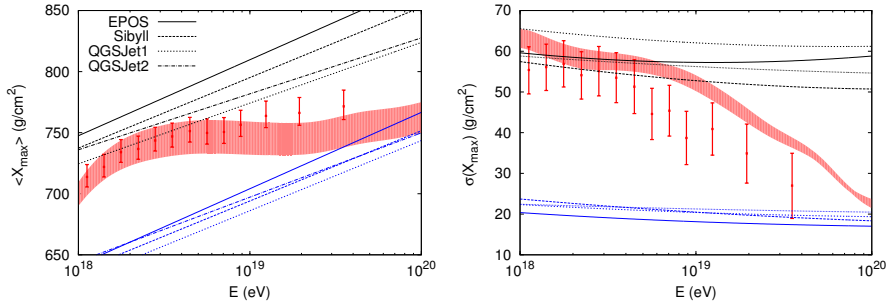

Figure 2: *Mean value of the depth of shower maximum* $\langle X_{max} \rangle$ *and its dispersion* $\sigma(X_{max})$ *as measured by Auger* [16] *and in our calculations with the same choice of parameters as in figure 1. The shadowed red band corresponds to the uncertainties due to the MC scheme adopted (see text).*

spectrum $\gamma_g < 1.5$, while light elements (p+He) should be injected with a steep spectrum $\gamma_g > 2.5$. This result directly follows from the Auger observation of a chemical composition that is proton dominated at low energies ($< 3 \div 4 \times 10^{18}$ eV) and smoothly drifts toward a heavier composition at higher energies. From the heavy composition at high energies, assuming a rigidity dependent approach $E^Z_{max} = Z E^p_{max}$, follows that the maximum acceleration energy for protons cannot be larger than few $\times\ 10^{19}$ eV, in figure 1 (left panel) and 2 we have assumed $E^p_{max} = 5 \times 10^{18}$ eV in the case of sources providing heavy nuclei and $E^p_{max} = 3 \times 10^{19}$ eV in the case of sources injecting only light elements.

This result on the maximum energy surely represents a sort of change of paradigm in the physics of UHECR. While in the past a lot of theoretical efforts were made to model a very high maximum energy ($> 10^{20}$ eV), nowadays, after the Auger observations, the situation seems changed with a required maximum energy for protons well below 10^{20} eV.

In figures 1 (left panel) and 2 we assumed a source emissivity of the light component, with an injection power law $\gamma_g = 2.7$ and composed only by proton and Helium, as $\mathcal{L}_0(p, He) = 7 \times 10^{49}$ erg/Mpc^3/yr (above 10^7 GeV/n) with an injection ratio $Q^{He}_{acc} = 0.1 Q^p_{acc}$. The second component, with a flat injection $\gamma_g = 1.0$ and contributing p, He, CNO, MgAlSi and Fe, has an emissivity of $\mathcal{L}_0 = 1.5 \times 10^{44}$ erg/Mpc^3/yr (above 10^7 GeV/n) with a ratio of the injected

elements as

$$Q_{He}^{\rm acc} = 0.2 Q_p^{\rm acc},\ Q_{CNO}^{\rm acc} = 0.06 Q_p^{acc},\ Q_{MgAlSi}^{\rm acc} = 0.03 Q_p^{acc},\ Q_{Fe}^{\rm acc} = 0.01 Q_p^{acc}.$$

The total fluxes of p and He are plotted as thick continuous green and magenta lines respectively, obtained as the sum of the two contributions to p and He spectra from the two classes of sources considered. At EeV energies sources providing also heavy nuclei give a very small contribution to the flux of p and He, in this energy range the flux of light elements (p+He) is contributed mainly by sources with steep injection. The flux of secondary nuclei, products of the photo-disintegration process, is plotted through the grey shadowed area. For each injected primary specie the total flux (primary plus secondaries) is plotted with continuos colored lines as labeled. In the left panel of figure 1 the end of the proton spectrum coincides with the maximum energy reached in the sources, while the spectra of nuclei are ended by photo-disintegration on the EBL. Together with the extragalactic CR components, in the left panel of figure 1 we also plot the tail of the galactic (iron dominated) CR spectrum (black dotted line) as computed in [22].

The hard injection spectra required to fit the Auger data might be reminiscent of models of the origin of UHECRs associated to acceleration in rapidly rotating neutron stars [23], although hard spectra are a more general characteristic of acceleration scenarios where regular electric fields are available (e.g. unipolar induction and reconnection).

An additional component of extragalactic light nuclei with a generation spectrum much steeper than the one used for heavy nuclei can be introduced making use of the recent data collected by the KASCADE-Grande (KG) collaboration, which show the existence at sub-EeV energies of a light (p+He) component with a spectral index $\gamma_g = 2.79 \pm 0.08$ [18] attributed to extragalactic sources. Therefore, our hypothesis is compatible with the experimental results of KG, as shown in the right panel of figure 1 where we plot the KG data points together with the systematic uncertainties (shaded area). The rapidly falling dotted lines in figure 1 (right panel) show the Galactic (p+He) spectrum as computed in [22], with a maximum energy of protons of 5, 6 and 7 PeV (see labels). The roughly constant black dotted line shows the flux of extragalactic light CRs as calculated above, based on the fit to the Auger data. The

solid lines indicate the sum of the galactic and extra galactic light components, showing a remarkable agreement with the KG data.

3 Conclusions

In this paper we took the Auger data on the spectrum and chemical composition of UHECRs at face value and tried to infer as much physical information as possible. The evidence that CRs in the energy region $1 \div 5 \times 10^{18}$ eV are dominated by light elements may be considered rather solid as it follows from data on $\langle X_{max} \rangle$ and its dispersion for the three largest UHECR detectors, Auger [16], TA [12] and HiRes [13]. Most of the debate on mass composition concentrates upon data at energies $\geq 5 \times 10^{18}$ eV.

Here we showed that the spectrum and chemical composition observed by Auger require hard injection spectra for the heavy component as also discussed in [24]. Moreover, we found that the maximum acceleration energy for nuclei of charge Z should be relatively low, namely $\simeq 5Z \times 10^{18}$ eV. From the theoretical point of view the hard injection spectrum is interesting in that it suggests an acceleration mechanism not based on the diffusive shock acceleration paradigm.

The most disappointing consequence of the hard injection spectra is that the Auger spectrum can only be fitted for energies $\geq 5 \times 10^{18}$ eV, while lower energy CRs imply a different explanation. Filling this gap requires the introduction of an ad hoc CR component and we showed here that such component must be composed of extragalactic light nuclei (p+He) with an injection spectrum with a slope $\gamma_g \simeq 2.7$. The most straightforward implication of this fact is that the transition from galactic to extragalactic CRs must be taking place at energies $\leq 10^{18}$ eV rather than at the ankle.

Remarkably this light component has a spectrum and flux which are compatible with the recently detected flux of light nuclei in the energy region $10^{16} \div 10^{18}$ eV by KASCADE-Grande [18]. These data show an ankle-like feature at $\simeq 10^{17}$ eV, that may be tentatively associated to the transition to extragalactic protons. The disappointing complexity of the viable explanations for the spectrum and chemical composition of Auger are probably the sign that the injection spectra needed to fit the data are themselves the result of a more complex phenomenology. An instance of this could be the propagation in extragalactic magnetic fields and/or phenomena that occur inside the sources that may also potentially affect the spectra of nuclei injected on cosmological

scales and possibly preferentially select high energy nuclei.

Acknowledgements

The author warmly thanks A.F. Grillo for joint work on the subject of UHECR and his presentation at the Vulcano Conference. The author also thanks V.S. Berezinsky and P. Blasi with whom part of the results presented here were obtained.

References

1. V. Ptuskin, Astrop. Phys. **39** (2012) 44.
2. F.W. Stecker, M.A. Malkan and S.T. Scully, Astrophys. J. **648** (2006) 744; T. M. Kneiske, T. Bretz, K. Mannheim and D.H. Hartmann, Astron. Astrophys. **413** (2004) 807.
3. D. Allard, Astropart. Phys. **39** (2012) 33.
4. J. Abraham et al. Astropart.Phys. **31** (2009) 399; V. Scherini, Nucl.Instrum.Meth. **A630** (2011) 226.
5. R. Aloisio, V. Berezinsky and S. Grigorieva, Astropart. Phys. **41** (2013) 73.
6. R. Aloisio, V. Berezinsky and S. Grigorieva, Astropart.Phys. **41** (2013) 94.
7. V. Berezinsky, A.Z. Gazizov and S.I. Grigorieva, Phys.Rev. **D74** (2006) 043005.
8. K. Greisen, Phys.Rev.Lett. **16** (1966) 748; G.T. Zatsepin and V.A. Kuzmin, JETP Lett. **4** (1966) 78.
9. V.S. Berezinsky and S.I. Grigor'eva, Astron.Astrophys. **199** (1988) 1.
10. R. Aloisio, D. Boncioli, A. Grillo, S. Petrera, and F. Salamida, JCAP **10** (2012) 007.
11. R. Aloisio, V. Berezinsky and A. Gazizov, Astropart.Phys. **39** (2012) 129.
12. C. C. Jui et al, J.Phys.Conf.Ser. **404** (2012) 012037; Y. Tsunesada, arXiv:1111.2507.

13. R. Abbasi et. al., Phys.Rev.Lett. **92** (2004) 151101; R. Abbasi et. al., Phys.Rev.Lett. **100** (2008) 101101.

14. R. Aloisio, P. Blasi and V. Berezinsky, JCAP **10** (2014) 020.

15. P. Abreu, arXiv:1107.4809; F. Salamida, Pierre Auger collaboration (2011), contribution to the 32nd International Cosmic Ray Conference.

16. J. Abraham et. al., Phys.Rev.Lett. **104** (2010) 091101.

17. R. Aloisio, V. Berezinsky, P. Blasi and S. Ostapchenko, Phys. Rev. **D77** (2008) 025007.

18. W. Apel et. al., Phys.Rev.Lett. **107** (2011) 171104; W. Apel, J. Arteaga-Velzquez, K. Bekk, M. Bertaina, J. Blmer, et. al., Phys.Rev. **D87** (2013) 081101.

19. R. Engel, D. Heck and T. Pierog, Ann.Rev.Nucl.Part.Sci. **61** (2011) 61.

20. P. Abreu et al, JCAP **02** (2013) 026.

21. T. Pierog and K. Werner, Phys.Rev.Lett. **101** (2008) 171101; E.J. Ahn, R. Engel, T.K. Gaisser, P. Lipari and T. Stanev, Phys.Rev. **D80** (2009) 094003; N. N.Kalmykov, S.S. Ostapchenko and A.I. Pavlov, Nucl.Phys.Proc.Suppl. **52B** (1997) 17; S.S. Ostapchenko, Phys.Rev. **D74** (2006) 014026.

22. R. Aloisio and P. Blasi, JCAP **07** (2013) 001.

23. P. Blasi, R. I. Epstein and A. V. Olinto, Astrophys.J. **533** (2000) L123; J. Arons, Astrophys.J. **589** (2003) 871; K. Fang, K. Kotera, and A. V. Olinto, Astrophys.J. **750** (2012) 118; K. Fang, K. Kotera, and A. V. Olinto, JCAP **1303** (2013) 010.

24. A. M. Taylor, Astroparticle Physics **54** (2014) 48.

Frascati Physics Series Vol. 58 (2014)
Frontier Objects in Astrophysics and Particle Physics
May 18-24, 2014

MEASUREMENT OF THE COSMIC RAY ENERGY SPECTRUM WITH ARGO-YBJ

Giuseppe Di Sciascio on behalf of the ARGO-YBJ Collaboration
INFN, Sezione di Roma Tor Vergata, Italy

Abstract

The ARGO-YBJ detector, located at high altitude in the Cosmic Ray Observatory of Yangbajing in Tibet (4300 m asl, about 600 g/cm^2 of atmospheric depth) provides the opportunity to study, with unprecedented resolution, the cosmic ray physics in the primary energy region between 10^{12} and 10^{16} eV. The preliminary results of the measurement of all-particle and light-component (i.e. protons and helium) energy spectra between approximately 5 TeV and 5 PeV are reported and discussed. The study of such energy region is particularly interesting because not only it allows a better understanding of the so called 'knee' of the energy spectrum and of its origin, but also provides a powerful cross-check among very different experimental techniques. The comparison between direct measurements by balloons/satellites and the results by surface detectors, implying the knowledge of shower development in the atmosphere, also allows to test the hadronic interaction models currently used for understanding particle and cosmic ray physics up the highest energies.

1 Introduction

There is a general consensus that Galactic cosmic rays (hereafter CRs) up to the "knee" ($\sim$3–4$\cdot 10^{15}$ eV) originate in Supernova Remnants (SNRs) accelerated by the first order Fermi mechanism in shock waves. The theoretical modelling of this mechanism can reproduce the measured spectra and composition of CRs. Recent measurements carried out by the balloon-borne CREAM experiment [1, 2] show that the proton and helium spectra from 2.5 to 250 TeV are both flatter compared to the lower energy measurements. In particular, the proton spectrum in this energy range is found harder than the value obtained by fitting many previous direct measurements [3]. The evolution of the proton and helium spectra and their subtle differences can be an indication of the contribution of different populations of CR sources operating in environments with different chemical compositions [4].

In the knee region the measurements of the CR primary spectrum are carried out only by EAS arrays and the current experimental results are conflicting. In the standard picture the "mass of the knee" is light being due to the steepening of the p and He spectra [5]. However, different experiments attribute the "mass of the knee" to higher nuclei. A hybrid measurement carried out exploiting the Cherenkov light yield detected by the EAS-TOP experiment (located at 2000 m a.s.l.) at different core distances in EAS and the high energy underground muons sampled by the MACRO experiment, has been used to infer the helium flux at 80 TeV, resulting twice larger than that obtained by JACEE [6, 7]. The EAS-TOP/MACRO analysis implies a decreasing proton contribution to the primary flux well below the observed knee in the primary spectrum. Such considerations can be described through the ratios of the three components at 250 TeV, that can be expressed as: $J_p : J_{He} : J_{CNO} = (0.20\pm0.08) : (0.58\pm0.19) : (0.22\pm0.17)$ [7]. In addition, also the results of the Tibet ASγ and the BASJE experiments, located at 4300 m a.s.l and at 5200 m a.s.l. respectively, favour a heavier composition because the proton component is no more dominant at the knee [8, 9]. Indications for a substantial fraction of nuclei heavier than helium at 10^{15} eV have been obtained in old measurements of delayed hadrons [10], as well as by the CASA-MIA collaboration [11].

The knowledge of the primary proton spectrum is fundamental to understand the cosmic rays acceleration mechanisms and the propagation processes in the Galaxy. A careful measurement of the proton spectrum in the energy

region from TeV to 10 PeV is the key component for understanding the origin of the knee. In addition, precise knowledge of its flux may allow one to calculate the yield of rare secondary CRs as antiprotons and positrons and establish the expected fluxes of the atmospheric neutrinos.

A measurement of the CR primary energy spectrum (all-particle and light component) in the energy range few TeV – 10 PeV is under way with the ARGO-YBJ experiment (for a description of the detector and a report of the latest physics results see [12]). To cover this wide energy range different 'eyes' have been used:

- *'digital readout'*, based on the strip multiplicity, in the few TeV – 200 TeV energy range [13];
- *'analog readout'*, based on the particle density in the shower core region, in the 100 TeV – 10 PeV range;
- *'hybrid measurement'*, carried out by ARGO-YBJ and a wide field of view Cherenkov telescope, in the 100 TeV - PeV region [14].

The results concerning the all-particle and the light component (p+He) spectra obtained with the analog readout are summarized in the following. The results obtained with the 'hybrid measurement' are described in [14, 15].

2 Measurement of the CR light component (p+He) spectrum

A measurement of the primary CR light (p+He) component energy spectrum has been carried out in the energy range 5 – 200 TeV exploiting the *digital read-out* of the ARGO-YBJ experiment, i.e. the picture of the EAS provided by the strip/pad system. With this analysis for the first time a ground-based measurement of the CR spectrum overlaps data obtained with direct methods for more than one energy decade, thus providing a solid anchorage to calibrate the energy scale of EAS arrays approaching the knee region.

The ARGO-YBJ spectrum, reconstructed with an unfolding technique based on the Bayesian approach, agrees remarkably well with the values obtained by adding up the p and He fluxes measured by CREAM both concerning the total intensities and the spectral index. The value of the spectral index of the power-law fit to the ARGO-YBJ data is -2.61±0.04, which should be compared with γ_p = -2.66±0.02 and γ_{He} = -2.58±0.02 obtained by CREAM [2].

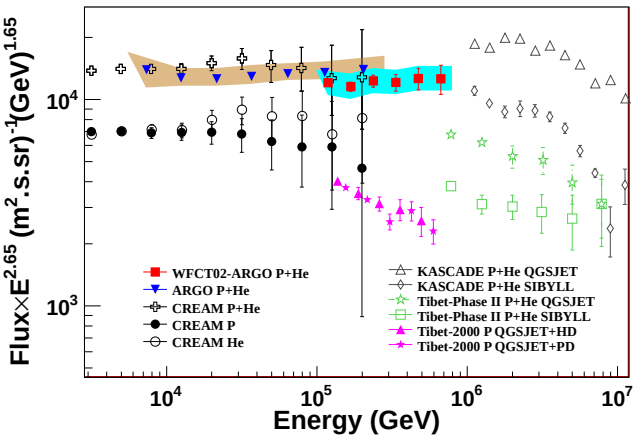

Figure 1: Light component (p+He) energy spectrum of primary CRs measured by ARGO-YBJ compared with other experimental results. The ARGO-YBJ 2012 data refer to the results published in [13]. The results obtained by ARGO-YBJ/WFCTA hybrid measurement are shown by the filled red squares [14].

The present analysis does not allow the determination of the individual p and He contribution to the measured flux, but the ARGO-YBJ data clearly exclude the RUNJOB results [16, 17]. Details can be found in [13].

This measurement has been extended to higher energies exploiting an *hybrid measurement* with a prototype of the future Wide Field of view Cherenkov Telescope Array (WFCTA) of the LHAASO project [18]. The idea is to combine in a multiparametric analysis two mass-sensitive parameters: the particle density in the shower core measured by the analog readout of ARGO-YBJ and the shape of the Cherenkov footprint measured by WFCTA [14]. For a detailed description of the technique see [14, 15].

The light component energy spectra measured by ARGO-YBJ up to about 600 TeV with the digital and the hybrid systems are shown in the Fig. 1. The hybrid spectrum can be described by a single power-law with a spectral index of -2.63 $\pm$ 0.06 up to about 600 TeV. A systematic uncertainty in the absolute flux of 15% is shown by the shaded area. The error bars show the statistical errors only. The absolute flux at 400 TeV is $(1.79\pm0.16)\times10^{-11}$ GeV^{-1} m^{-2} sr^{-1} s^{-1}. This result is consistent for what concern spectral index and absolute flux with

the measurements carried out by ARGO-YBJ below 200 TeV and by CREAM. The flux difference is about 10% and can be explained with a difference in the experiments energy scale of $\pm 3.5\%$ [14].

This result is very important to fix the energy scale of the experiment. Below 10 TeV the absolute energy scale of ARGO-YBJ is calibrated at 10% level exploting the westward displacement of the Moon shadow under the effect of the GMF [19]. Above this energy the overposition with CREAM allows to compare both energy scales: the agreement is at a few percent level.

3 All-particle Energy Spectrum in the PeV energy region

The measurement of the CR energy spectrum up to 10 PeV is under way exploiting the RPC charge readout of the ARGO-YBJ detector which allows to study the structure of the particle density distribution in the shower core region up to particle densities of about $10^4/\mathrm{m}^2$ [20, 21].

The study of the lateral density function (LDF) at ground is expected to provide information on the longitudinal profile of the showers in the atmosphere, that is to estimate their development stage, or *age*, which is related to X_{max}, the atmospheric depth at which the cascade reaches its maximum size. This implies the possibility of selecting showers within given intervals of X_{max} or, equivalently, of X_{dm}, the distance of the shower maximum from the detector.

The shower development stage in the atmosphere, as observed at a fixed altitude (the detection one), depends on the energy of the interacting primary. For fixed energy, it depends on the nature of the primary: heavy primaries interact higher in the atmosphere, thus giving showers which, on average, reach their maximum at a larger distance from the detector than a lighter primary of the same energy. For this reason, the combined use of the shower energy and age estimations can ensure a sensitivity to the primary mass, thus giving the possibility of selecting a light (p+He) event sample with high efficiency.

Various observables were considered and analyzed in order to find a suitable estimator of the primary CR energy. Among them, according to MC simulations, N_{p8}, the number of particles detected within a distance of 8 m from the shower axis, resulted well correlated with energy, not biased by the finite detector size and not much affected by shower to shower fluctuations [22]. Therefore, the analysis is carried out in terms of different N_{p8} intervals to

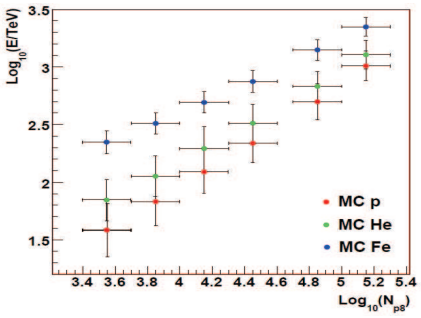

Figure 2: Truncated size N_{p8} as a function of the primary energy for shower induced by different nuclei.

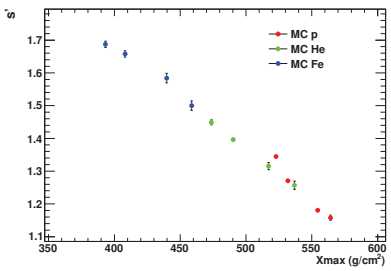

Figure 3: The age parameter s' resulting from the fits of the average LDF of simulated p, He and Fe samples (in each N_{p8} bin) vs the corresponding X_{max} average values.

select event samples corresponding to different primary energies. Nevertheless, as shown in Fig. 2, this truncated size is a mass-dependent energy estimator parameter.

In order to have a mass-independent parameter we fitted the LDFs of triggered showers (up to about 10 m from the core) event-by-event, for different N_{p8} intervals and different shower initiating primaries, with a suitable function to get the shape parameter s' (see [23]) for details). From these studies we find that, for a given primary, the s' value decreases when N_{p8} (i.e. the energy) increases, this being due to the observation of younger (deeper) showers at larger energies. Moreover, for a given range of N_{p8}, s' increases going from proton to iron, as a consequence of a larger primary interaction cross section. Both dependencies are in agreement with the expectations, the slope s' being correlated with the shower age, thus reflecting its development stage. This outcome has two important implications, since the measurements of s' and N_{p8} can both (i) help constraining the shower age and (ii) give information on the primary particle nature.

Concerning the first point, we show in Fig. 3 the s' values as obtained from the fit of the average LDFs, for each simulated primary type and N_{p8} interval, as a function of the corresponding X_{max} average value. As can be seen, the shape parameter s' depends only on the development stage of the shower,

independently from the nature of the primary particle and energy. That plot expresses an important universality of the LDF of detected EAS particles in terms of the lateral shower age. The LDF slope s' is a X_{max} average value estimator mass-independent. This implies the possibility to select most deeply penetrating showers (and quasi-constant X_{dm} intervals) at different zenith angles, an important point for correlating the exponential angular rate distribution with the interaction length of the initiating particle [24]. Obviously shower-to-shower fluctuations introduce unavoidable systematics, whose effects can be anyway quantified and taken into account.

The second implication is that s' from the LDF fit very close to the shower axis, together with the measurement of the truncated size N_{p8}, can give information on the primary particle nature, thus making possible the study of primary mass composition and the selection of a light component data sample.

Assuming an exponential absorption after the shower maximum, we get the size at maximum (N_{p8}^{max}) by using N_{p8} and s' measurements for each event: $N_{p8}^{max} \approx N_{p8} \cdot exp[(h_0 sec\theta - X_{max}(s'))/\lambda_{abs}]$. A suitable choice of the absorption lenght λ_{abs} (=120 g/cm^2) allows to get N_{p8}^{max} a parameter correlated with primary energy in an almost linear and mass independent way, providing an energy estimator with a Log(E/TeV) resolution of 0.10–0.15 (getting better with energy).

As described in [20, 21], with the RPC charge readout we took data with 4 different gain scales to explore the particle density range $\approx$20 – 10^4 particles/m^2. In this preliminary analysis the results obtained with the two intermediate gain scales (so-called G1 and G4) are presented.

Selecting quasi-vertical events ($\theta < 15^\circ$) in terms of the truncated size N_{p8} with the described procedure we reconstructed the CR all-particle energy spectrum shown in the Fig. 4 in the energy range 100 – 3000 TeV. In the plot a $\pm$15% systematic uncertainty, due to hadronic interaction models, selection criteria, unfolding algorithms, aperture calculation and energy scale, is shown by the shaded area. The statistical uncertainty is shown by the error bars. As can be seen from the figure, the two gain scales overlap making us confident about the event selection and the analysis procedure. The ARGO-YBJ all-particle spectrum is in fair agreement with the parametrizations provided by Horandel [3] and Gaisser-Stanev-Tilav [25], showing evidence of a spectral index change at an energy consistent with the position of the knee.

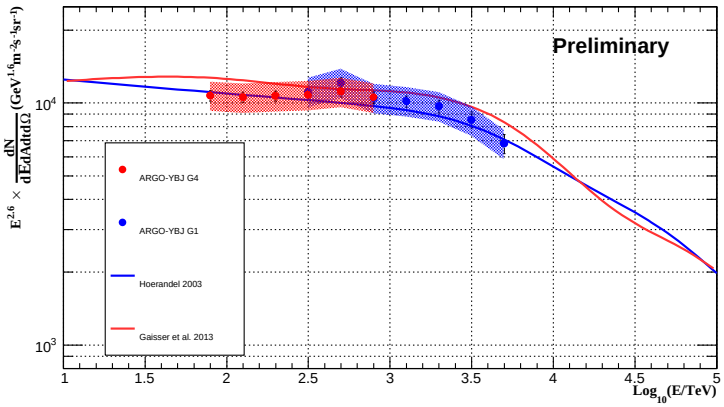

Figure 4: All-particle energy spectrum of primary CRs measured by ARGO-YBJ. Quasi-vertical events ($\theta < 15°$) recorded with two different gain scales (G1 and G4) are plotted. The systematic uncertainty is shown by the shaded area and the statistical one by the error bars. The parametrizations provided by Horandel [3)] and Gaisser-Stanev-Tilav [25)] are shown for comparison.

4 Observation of the knee in the (p+He) energy spectrum

The measurement of the light component energy spectrum has been extended up to PeVs exploiting three different approaches.

(1) A selection of events in the $s' - N_{p8}$ space allowing to get a light (p+He) component sample of showers with a contamination of heavier nuclei of about 15% (see Fig. 5).

(2) A Bayesian unfolding technique similar to that applied to reconstruct the CR energy spectrum up to 200 TeV. A similar event selection based on the particle density on the central carpet, slightly modified to take into account larger showers recorded with the RPC charge readout, selects a light component event sample with a contamination of heavier nuclei less than 15%.

(3) The ARGO-YBJ/WFCTA hybrid measurement with a different selection procedure which increases the aperture of a factor 2.4 (see [15)] for a detailed description of the method and a discussion of the results).

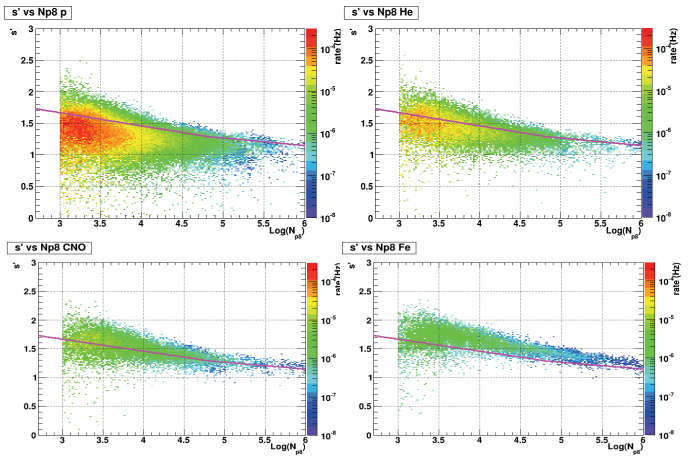

Figure 5: Relation between the LDF shape parameter s' and the truncated size N_{p8} for different nuclei. Showers have been sampled with energy spectra according to Horandel [3]. The p+He selection cut is shown by the lines.

The energy spectrum of the p+He component measured by ARGO-YBJ with the different methods is summarized in the Fig. 6. The systematic uncertainty is shown by the shaded area and the statistical one by the error bars.

As can be seen, all three different analysis show evidence of a knee-like structure starting from about 650 TeV. With respect to a single power-law with a spectral index –2.62 the deviation is observed at a level of about 6 s.d. . The results obtained with the analysis of RPC charge readout data are in fair agreement. These results agree with the ARGO-YBJ/WFCTA hybrid measurement within systematic uncertainty. For comparison, the parametrizations of the light component provided by Horandel [3] and Gaisser-Stanev-Tilav [25] are shown by the blue and red dashed lines, respectively. A Horandel-like spectrum with a modified knee at Z×1 PeV is also shown.

The all particle and the light component energy spectra measured by ARGO-YBJ are compared to a compilation of different experimental results in the Fig. 7.

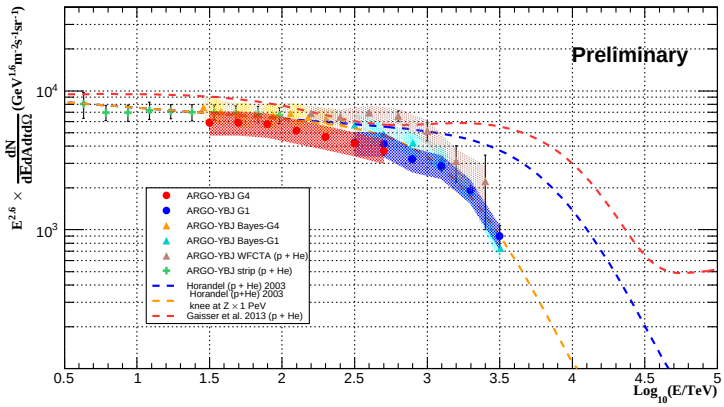

Figure 6: Light (p+He) component energy spectrum of primary CRs measured by ARGO-YBJ with three different analysis. Data recorded with two different gain scales (G1 and G4) are plotted. The systematic uncertainty is shown by the shaded area and the statistical one by the error bars. The parametrizations provided by Horandel [3] and Gaisser-Stanev-Tilav [25] are shown for comparison. A Horandel-like spectrum with a modified knee at Z×1 PeV is also shown.

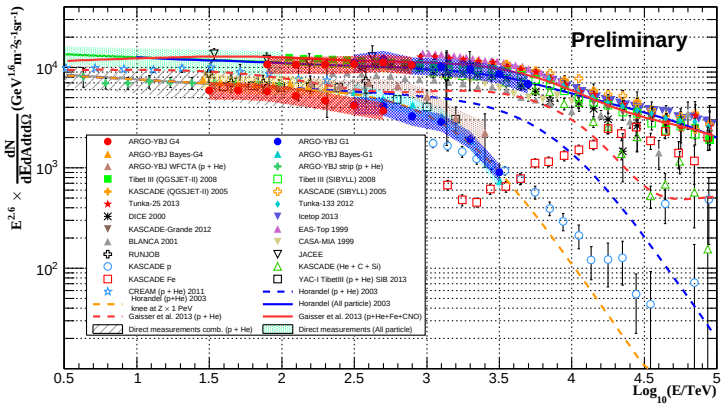

Figure 7: All particle and light (p+He) component energy spectra of primary CR measured by ARGO-YBJ and compared to different experimental results. The parametrizations provided by Horandel [3] and Gaisser-Stanev-Tilav [25] are shown for comparison. A Horandel-like spectrum with a modified knee at Z×1 PeV is also shown.

5 Conclusions

The CR energy spectrum has been studied by the ARGO-YBJ experiment in a wide energy range (TeVs $\rightarrow$ PeVs) exploiting different approaches. The Moon shadow technique and the overposition with the CREAM data allow to fix the absolute energy scale of ARGO-YBJ up to 4% level. The all-particle spectrum measured in the energy range 100 – 3000 TeV is in good agreement with well-known parametrizations, making us confident about the selection and reconstruction of the analog data. The light component (p+He) has been reconstructed with high resolution up to about 5 PeV. The ARGO-YBJ results show a clear indication of a knee-like structure starting at about 650 TeV. Improvements of event selection with the full statistics is under way to extend the measurement up to 10 PeV. Preliminary results obtained with the last analog gain scale (able to extend the energy range of the charge readout by a factor of 2 at least) are consistent with the results presented in this paper.

References

1. H.S. Ahn et al., Astrophys. J. Lett.**714**, L89 (2010).
2. Y.S. Yoon et al., Astrophys. J.**728**, 122 (2011).
3. J.H. Hörandel, Astropart. Phys. **19**, 193 (2003).
4. D. Caprioli et al., Astropart. Phys. **34**, 447 (2011).
5. W.D. Apel et al., Astropart. Phys. **31**, 86 (2009).
6. K. Asakimori et al., Astrophys. J.**502**, 278 (1998).
7. M. Aglietta et al., Astropart. Phys. **21**, 223 (2004).
8. M. Amenomori et al., Phys. lett. B **632**, 58 (2006).
9. H. Tokuno et al., Astropart. Phys. **29**, 453 (2008).
10. H. T. Freudenreich et al., Physics Rev. D **41**, 2732 (1990).
11. M.A.K. Glasmacher et al., Astropart. Phys. **12**, 1 (1999).
12. G. Di Sciascio et al., Proc. TAUP 2013, ArXiv:1407.8462.

13. B. Bartoli et al., Physics Rev. D **85**, 092005 (2012).

14. B. Bartoli et al., Chinese Phys. C **38**, 045001 (2014).

15. Z. Cao et al., these proceedings.

16. A.V. Apanasenko et al., Astropart. Phys. **16**, 13 (2001).

17. V.A. Derbina et al., Astrophys. J. Lett.**628**, L41 (2005).

18. Z. Cao et al., Chinese Phys. C **34**, 249 (2010).

19. B. Bartoli et al., Physics Rev. D **84**, 022003 (2011).

20. S. Mastroianni et al.in Proc. 33rd ICRC, (Rio de Janeiro, 2013) **ID: 1035** (http://143.107.180.38/indico/contributionListDisplay.py?confId=0).

21. B. Bartoli et al., The analog RPC Detector of the ARGO-YBJ Experiment, to appear in Astropart. Phys. .

22. I. De Mitri et al., in Proc. 33rd ICRC, (Rio de Janeiro, 2013) **ID: 0779** (http://143.107.180.38/indico/contributionListDisplay.py?confId=0).

23. A. Surdo et al., in Proc. 33rd ICRC, (Rio de Janeiro, 2013) **ID: 0781** (http://143.107.180.38/indico/contributionListDisplay.py?confId=0).

24. G. Aielli et al., Physics Rev. D **80**, 092004 (2009).

25. T.K. Gaisser at al., Frontiers of Physics **8**, 748 (2013).

Frascati Physics Series Vol. 58 (2014)
Frontier Objects in Astrophysics and Particle Physics
May 18-24, 2014

The knee of the proton spectrum at 630 TeV

Zhen Cao
(for the ARGO-YBJ Collaboration and the LHAASO Collaboration)
Institute of High Energy Physics, 19B Yunquan St. Beijing, 100049, China

Abstract

Using the hybrid technique with the ARGO-YBJ resistive plate chamber (RPC) array and the imaging Cherenkov telescope (ICT) at 4300m a.s.l., we carry out a measurement of energy spectrum of cosmic ray proton and helium nuclei. The fully covered RPC array measures the shower geometry and the lateral distribution of shower particles in 3 m from the shower core and the wide field of view telescope measures the shower energy and the shape of the shower image. An algorithm based on the measured shower parameters is developed to select protons and helium nuclei out of the well reconstructed showers with a purity better than 92%. A clear break of the spectrum is observed below 1 PeV with a significance of 5.9σ. The knee of the cosmic ray proton spectrum is discovered at (630±87) TeV almost model independently. Combining the sum of the proton spectrum and helium spectrum by CREAM, the spectrum of mixed protons and helium nuclei by ARGO-YBJ and the hybrid measurement, the $H\&He$ spectrum is found to be a power law with single index of -2.62±0.01

from 2 TeV to 630 TeV. All fluxes are consistent within 10% among the three experiments, implying that the energy scale is fixed within 4%.

1 Introduction

The knee of cosmic ray spectrum is a highly complicated issue which is far to be resolved experimentally [1]. As summarized in Fig.1 of reference [2], the difference between "all cosmic ray" fluxes measured by numerous experiments is greater than 100% around the knee which also has a big uncertainty of nearly one order of magnitude in its energy from few hundred TeV to few PeV, such as the difference between CASA-MIA [3] and KASCADE [4] concerning the knee of the proton spectrum. The spectral indices are also different between measurements. Such a big discrepancy has evolved into a long standing puzzle that makes very difficult to develop any precise theory about the cosmic ray acceleration and propagation through our galaxy. The maximum energy of cosmic rays in their cosmos accelerators and the injection spectra are relevant issues here. Experimentally, the problem behind the huge discrepancy is the highly entangled uncertainties in energy measurement, which suffers from both unknown energy scale and nearly totally unknown mixture of nuclei from proton to iron, and the shower detecting efficiency estimation which is also composition and interaction model dependent. The ultimate way to solve the problem is to independently measure the spectra of individual nuclei in the energy range that contains the knees of all components. The energy scale must be calibrated independently. Space or balloon borne experiments have made significant progresses, such as CREAM [5], PAMELA [6] and AMS02 [7]. The charge of every cosmic ray event is well measured. Due to many experimental constraints, AMS02 measures the spectra up to 2 TeV/nucleus and CREAM measures the spectra up to 200 TeV, which have important overlaps with the measurements by AMS02 except the proton spectrum. With a difference less than 10% (could be smaller in the final AMS02 publication), the two experiments which are calibrated at test beams provide important calibration information for both the absolute flux of each species and the energy scale. Limited by its exposure, CREAM measurements suffer from large statistical uncertainty above 50 TeV for proton and helium spectra and at even lower energies for heavier nuclei. At the 4300 m above the sea level, ARGO-YBJ [8] manages a selection of mixed

sample of proton and helium ($H\&He$) covering the most of the energy range of the CREAM experiment above 5 TeV. For this special sample, the energy scale can be calibrated by using the displacement of the moon shadow in the geomagnetic field as a function of the particle energy [9]. It turns out that the agreement of the mixed proton and helium fluxes between the two experimental measurements implies that the energy scales are consistent within 4% which is smaller than the systematic uncertainties. The combined spectrum of protons and helium nuclei is found to be a single-index power law with the index of -2.62 ± 0.01 and the flux of $(1.95 \pm 0.16) \times 10^{-11}\ GeV^{-1}\ m^{-2}\ s^{-1}\ sr^{-1}$ at 400 TeV. Using a hybrid technique with the ARGO-YBJ detector array [10] and a wide field of view Cherenkov imaging telescope [11], as one of the prototype detectors of the LHAASO project [12], the measurement of the $H\&He$ spectrum is extended to a few PeV. A clear bending of the spectrum is observed. The hybrid experiment, the selection of the $H\&He$ sample, the shower energy measurement and the further analysis for the knee of the proton spectrum are described in the following sections.

2 The Hybrid Experiment

Hybrid air shower events are those whose cores are fallen inside the fully covered ARGO-YBJ array of $76m \times 72m$ (1 meter from the edges of the array) resistive plate chambers (RPC) and arrival directions are in the effective field of view (FoV) of the telescope, i.e. a cone of 6° respect to the main axis of the telescope which has a physical FoV of 14° × 16° pointing to 30° from the zenith. This defines an aperture of 163 $m^2 sr$. For high energy showers ($\geq$ 100 TeV), they are detected almost with the full efficiency, particularly for the $H\&He$ events according to the simulation for the hybrid experiment. This minimizes the uncertainty of the cosmic ray flux measurement. The hybrid observation had been carried out in three winters in 2010, 2011 and 2012. Above a threshold of about 100 TeV, 8218 high quality events are collected in the exposure of 7.28×10^5 seconds.

The RPCs, measuring particle density up to 20000/m^2 at which the readout electronics saturates, form an unique array that measures nearly every secondary particles in the showers. The shower core location is very well measured with an error of 1.2 m and arrival direction with an error $< 0.3°$. Besides, the secondary particles close to the core (within 10 meters) are mainly produced

in the hadronic interactions at low heights and hardly affected by the multiple Coulomb scattering. On the most hit RPC in every event, the recorded number of particles in a proton shower is clearly larger than that of an iron shower at the same energy. The particular RPC data are therefore very useful in determining the composition of the shower. The shower images are well contained in the FoV of the telescope with such accurate geometry of showers that passed all criteria described elsewhere [13]. The total number of Cherenkov photons in the shower image serves as a shower energy estimator by taking into account the decreasing with the distance from the shower. Moreover, it is well known that the images of showers at same distance from the telescope are more elongated for lighter composition. These features of the hybrid measurement, enables an analysis of showers for its composition before knowing the shower energy.

This feature allows us to disentangle the dependence of the shower energy estimator to the shower composition. As shown in Figure 1 for the specific case of using the total number of Cherenkov photons in the shower image, a bias up to 60% in shower energies could be avoided if the composition is known prior the energy reconstruction. For a mixed sample, the energies of iron showers in the data set could be underestimated by 27% if $H\&He$ showers is reconstructed correctly at 630 TeV (upper panel), or the proton energies could be overestimated by 39% in the other extreme case (lower panel). With any accuracy better than 60%, one may not be able to resolve a meaningful energy spectrum for "all particles". In other words, to measure the spectrum with a required accuracy of about 20%, as the typical resolution for individual species, the separation between mass groups is essential.

3 $H\&He$ Shower Selection and the Energy Measurement

The approach described in this paper is based on an algorithm that enables the selection for the specific mass group, e.g. the $H\&He$ group, out of the all well reconstructed events by using the two composition sensitive parameters mentioned above, then the shower energy is determined with the corresponding response function for the specific mass group.

To select the $H\&He$ showers, one of the sensitive parameters is the number of secondary particles on the most hit RPC in a shower, denoted as N_{max}. It must be a function of the shower size, which can be indicated by using the density of Cherenkov photons at the core, denoted as N_0^{pe}. The photon density

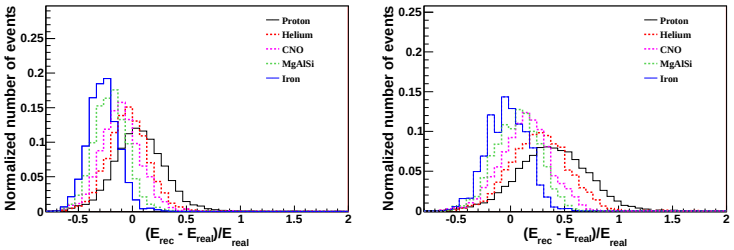

Figure 1: *The cosmic ray energy response functions in the measurements by the hybrid technique using the total number of Cherenkov photons in the shower images. The composition dependence of the energy reconstruction algorithm is illustrated here by using two extreme cases. In the upper panel, the response functions for all 5 mass groups are shown in an algorithm favoring the H&He mass group around 630 TeV. The lower is for the algorithm that is favoring the mass groups of Fe and Mg/Al/Si around 1 PeV.*

is estimated using the total number of photons in the shower image measured by the Cherenkov telescope with an impact parameter R_p from the shower axis. An exponential distribution of the Cherenkov photon density as a function of R_p is assumed in the estimation according to the shower simulation. The two measured parameters are found well correlated as shown in Figure 2. With an assumption of the composition evenly distributed among the 5 mass groups, one can see a clear separation between species. The correlation reflects the shower energy dependence. A energy dependent cut indicated by the straight line filters out the *H&He* samples with a purity of 92% below 700 TeV assuming some realistic composition models [14, 15].

The other mass sensitive parameter is associated with the shape of the shower image in the Cherenkov telescope as mentioned above. Quantitative description of the elongation of the shower image using the ratio between the photon density weighted average length and width, L/W, has a clear dependence of the distance from the shower axis to the telescope, R_p, due to a pure geometric reason. Taking the advantage of the precise shower geometry measured by the RPC array, the relationship between L/W and R_p is established for individual mass group and the separation between the groups is rather clear as plotted in Figure 2, as well. Here a weak energy dependence in the ratio

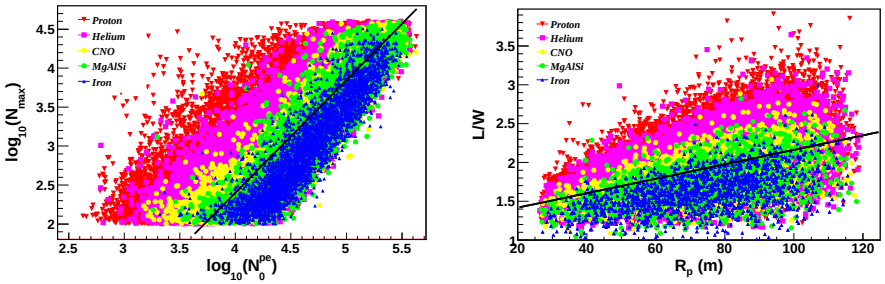

Figure 2: *Two composition sensitive parameters measured by the RPC array and the Cherenkov telescope, respectively. In the left panel, the number of charged shower particles in the most hit RPC as a function of the shower size which is estimated by using the density of number of Cherenkov photons at the core. In the right panel, the ratio between the length and the width of the shower Cherenkov image is shown as a function of the impact parameter R_p. It is a pure geometrical effect for each mass group which is indicated using different color. The straight lines indicate the cuts for selecting the $H\&He$ samples used in the analysis.*

L/W is already corrected also using N_0^{pe}. A R_p dependent cut as shown by the straight line filters out the $H\&He$ samples with the same purity. Adding all selected events together, the overall detecting efficiency for the $H\&He$ events is about 72%, constant over the range above 200 TeV.

Applying the selecting algorithm to the data set results in a nearly constant aperture of 121 m^2sr. The ratio between the proton and helium events is approximately 1:0.8. The contamination of the nuclei heavier than helium is estimated according to different composition models using the detailed simulation including the response of the hybrid experimental instruments.

The shower energy E reconstructed using N_0^{pe} has a symmetric resolution function combining the two components together with H:He=1:0.8. As shown in the upper panel of Figure 1, there exists a systematic shift of $\pm$5% for helium and proton component, respectively. As a function of the shower energy, the systematic bias is less than 2% and the resolution varies from 27% to 23% over a wide range from 100 TeV to 8 PeV. This feature of the energy estimator using the total number of Cherenkov photons, which is an accumulation of the photons produced in all stages of the shower development, guarantees a

distortion-free measurement of the energy distribution. It is suitable for an investigation for any structure of the energy spectrum as long as the scale of the structure is greater than 25%, namely a bin of 0.2 in $log_{10}E$.

4 Energy Spectrum of $H\&He$ and the Knee of the Proton Spectrum

A more strict cut for 97% purity of the $H\&He$ sample is applied on the well constructed event set of 8218 showers. This yields a much smaller aperture of $\sim 50m^2sr$ with a $H\&He$ selection efficiency of 30%, but a precise measurement of the spectrum below 700 TeV [13] which fits well with a single-index power law. It is consistent with the previous measurements by CREAM [5] and ARGO-YBJ [8] in the overlap energy range from 100 to 200 TeV. The measurement thus serves as a calibration for both energy scale and absolute flux, i.e. the energy scale is fixed within 3.5% which is sufficient to explain the difference of 9% between the observed fluxes.

The measurement with the larger aperture described in this paper is shown in Figure 3. The energy range is extended to 8 PeV. A clear break of the spectrum is observed around 630 TeV. Below the break, newly measured fluxes in 4 energy bins agree with the previous measurement in [13] which has a higher purity. Same as the previous ones, they fit well with a single index power law, $1.82 \times 10^{-11}(E/400TeV)^{-2.62}GeV^{-1}m^{-2}sr^{-1}s^{-1}$. Extending this spectrum to higher energies as an a priory hypothetic flux, the observed deficit above the break has a significance of 5.9σ. Although the contamination of heavy nuclei is well under control below the break, i.e. less than 8%, it becomes very severe above the break. On one hand, the contamination gradually increases with energy according to most of models, such as Horandel [14] and H4a [15]. On the other hand, the break causes the $H\&He$ rapidly reducing with energy, so that the heavy showers dominates the last bin above 3.2 PeV in the selected samples. The contamination is subtracted from the observed events by assuming the fluxes of heavy nuclei using Horandel's model. A systematic uncertainty introduced by the assumption is estimated by using different composition models. Combining other uncertainties in both energy scale and detecting efficiency such as the photometric calibration of the telescope, the weather condition, the shower reconstruction quality cut and the RPC analog read-out calibration, the total systematic uncertainty is estimated and plotted as the shaded area in Figure 3.

It is clear that we have observed the "knee" of the spectrum of $H\&He$ around 630 TeV. A more interesting question is how much we could learn from the observation, particularly about the knee of the proton spectrum. Such a further analysis requires more assumptions about the primary fractions of proton and helium nuclei, how do the spectra break at their own "knees" and of course where are the knees. The real question is what is the model independent knowledge after so many assumptions being introduced in the analysis. The philosophy in such an analysis is trying to keep the assumptions as general as possible. For the composition, many experiments at lower energies imply that the protons are nearly same as helium in the energy range under investigation. They also indicate that the spectrum of helium is getting harder in the energy range, therefore the helium nuclei may be more than protons, e.g. the CREAM experiment. The ratio between protons and helium nuclei is, therefore, assumed to be 1:1 or 1:1.3 below the break. For sake of simplicity, the H-spectrum and the He-spectrum are assumed to have the same spectral indices below or above their knees. On the assumptions about the bending of the individual spectra of protons and helium nuclei, we test four cases. They are broken power law with rigidity-independent knees, rigidity-proportional knees, mass-proportional knees and rigidity independent exponential cut-off model. To fit the observed $H\&He$ spectrum in Figure 3 with those assumed components, no experimental issue has to be taken into account except the difference of the selecting efficiency between the proton showers and the helium showers. In Figure 3, all the fitting results are plotted in two panels, i.e. the left is for H:He=1:1 and the right is for 1:1.3.

To summarize the analysis, we make a chart in Table 1. In the first column of the analysis results, the bending energies of the proton spectra are listed in TeV. They clearly show that the observed bending of the $H\&He$ spectrum is due to the knee of the proton spectrum. The contribution of the bending of the helium spectrum to the $H\&He$ spectrum is either the same as the protons (case 1, dot-dashed line in Figure 3) or an irresolvable little kink in the spectrum (case 2, solid line), or an apparent discrepancy (case 3, dashed line) but it cannot be significantly ruled out by the data. Here the H spectrum is the same as that is in case 2. The similar situation is for the cut-off model (case 4, dotted line). The statistical shortage can be explained by the χ^2 per degree of freedom in the hypothesis tests in the second column. Given the statistics,

Table 1: *Summary of the analysis. For each composition models in columns, four models of bending of the spectra at their knees are under testing. The results show energies of the knee of the p-spectrum in TeV in the first column and the χ^2 per degree of freedom for the test with the observed data in the second column. For the last knee model, the energy is the cut-off energy, E_c in the cut-off factor e^{-E/E_c}.*

knee model	H:He=1:1	H:He=1:1.3
rigidity-independent power-law	640, 0.4	640, 0.4
rigidity-proportional knees w/ power-law	631, 0.4	631, 0.4
mass-proportional knees w/ power-law	631, 0.8	631, 1.1
rigidity-independent cut-off	4930 , 2.1	4930, 2.1

the selection purity and efficiency in the current experiment, we nevertheless can safely claim that the proton spectrum knee occurs at (630±87) TeV. There actually exists an extreme case, in which the proton spectrum does not bend at all and the observed bending is purely due to the helium. This case may be too much deviated from the existing knowledge, although we are not able to rule out it.

About the spectra of protons or helium nuclei above the break, two items prevent us to make a concrete conclusion. One is the contamination of the heavy nuclei. As discussed in the early part of the paper, the energy reconstruction procedure is not available for a highly mixed samples. The other is that even between the protons and helium nuclei, the ratio is totally unknown. In other words, the assumption of having the same power law functional form and the same index is totally pre-determined. The conclusion is that there is no constraint on the individual proton and helium spectra above the break. Therefore, the energy of 630 TeV as the knee of the p-spectrum is the only safe claim of the analysis based on the observed broken $H\&He$ spectrum.

5 Acknowledgements

Thanks to all members of the ARGO-YBJ Collaboration and of the LHAASO Collaboration. This paper is a report of the collaboration work over years of operation of the telescopes and the RPC array at the Yangbajing observatory (Tibet, China). In particular, appreciations to Dr. Shoushan Zhang who carries out the whole spectrum analysis using the hybrid data set. Especially, I

greatly appreciate the hard work of the observatory team who made the both instruments working properly during the long operation periods. This work is supported in China by NSFC (Contract No. 10975145 and No. 11075170), the Knowledge Innovation Fund (H85451D0U2) of IHEP, the Chinese Ministry of Science and Technology, the Chinese Academy of Science, and the Key Laboratory of Particle Astrophysics, CAS, and in Italy by the Istituto Nazionale di Fisica Nucleare (INFN), and the Ministero dell'Istruzione, dell'Università e della Ricerca (MIUR).

References

1. J. Blümer *et al*, Progress in Particle and Nuclear Physics 63, 293 (2009).
2. J.R. Hörandel, Modern Physics Letter A, 22, 1533 (2007).
3. M.A.K. Glasmacher *et al*, Astroparticle Physics 12, 1 (1999).
4. T. Antoni *et al*, Astroparticle Physics 24, 1 (2005).
5. Y. S. Yoon *et al*, Astrophys. J. 728, 122 (2011).
6. O. Adriani *et al*, Science, 332(6025):69-72 (2011).
7. S. Ting, Highlight Presentation on ICRC-2013 in Rio de Janeiro, Brazil., https://143.107.180.38/indico/getFile.py/access?contribId=1259%sessionId=2 &resId=0 &materialId=slides&confId=0, the proceedings are in press on Brazilian Journal of Physics.
8. B. Bartoli *et al*, Physical Review D 85, 092005 (2012).
9. B. Bartoli *et al*, Physical Review D 84 022003 (2011).
10. G.Aielli *et al*, Nucl. Instrum. Methods Phys. Res. A 562, 92 (2006).
11. S.S. Zhang *et al*, Nucl. Instr. and Meth. A 629, 57 (2011).
12. Z. Cao *et al*, Chinese Physics C 34, 249 (2010).
13. B. Bartoli *et al*, Chinese Physics C, Vol. 38, 045001 (2014).
14. J.R. Hörandel, Astroparticle Physics 19, 193 (2003).
15. T.K. Gaisser *et al*, Astroparticle Physics 35, 801 (2012).

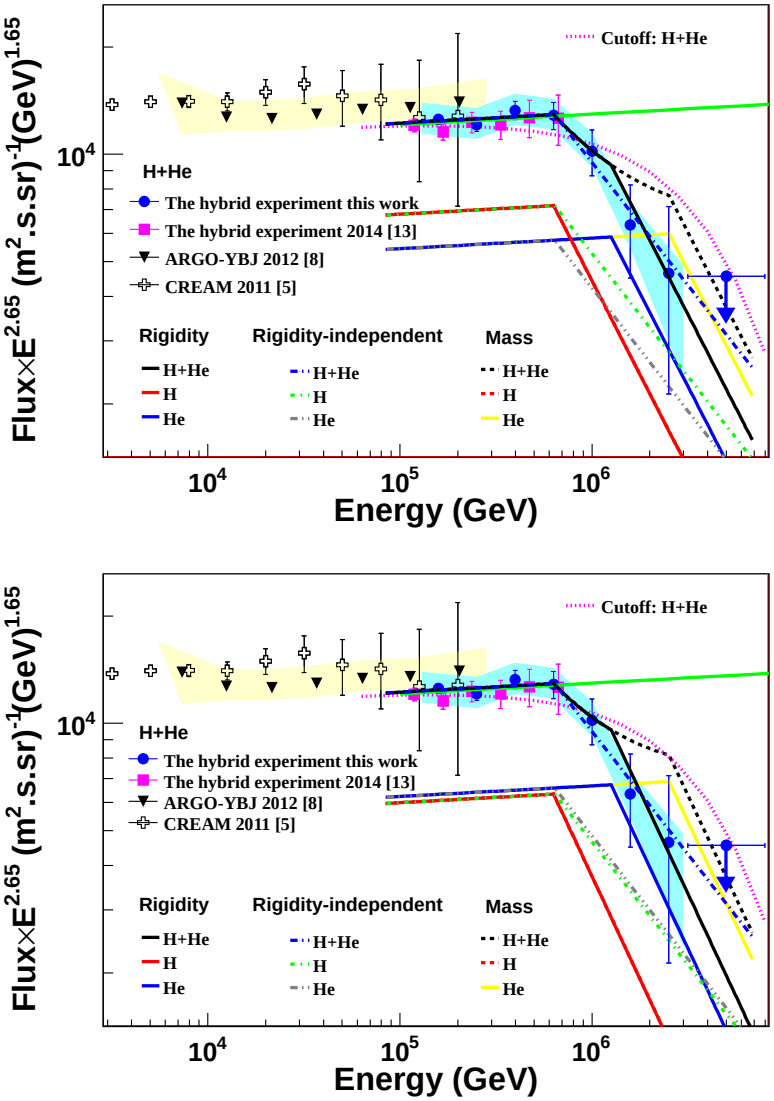

Figure 3: *The energy spectrum of cosmic ray H&He from 2 TeV to 8 PeV. The filled circles represent the new measurement in this paper using the hybrid technique. Combining the previous hybrid measurement below 700 TeV (squares), the ARGO-YBJ measurement using the digital readout of the RPC array (triangles) and the sum of the proton and helium spectra by CREAM (open crosses), the observation clearly shows a simple power law with a single index up to 630 TeV and a break with a 5.9σ deviating from a simple power law spectrum. The bars attached to the points are statistical errors. Systematic errors are represented as shaded areas around the data. Lines indicate composition models that fit the data in two cases of assumptions on the ratios between H and He. The left is for 1:1 and the right is for 1:1.3, see text for details.*

Frascati Physics Series Vol. 58 (2014)
Frontier Objects in Astrophysics and Particle Physics
May 18-24, 2014

The heavy knee and the light ankle observed with KASCADE-Grande

A. Haungs, W.D. Apel, K. Bekk, J. Blümer, H. Bozdog,
F. Cossavella, K. Daumiller, P. Doll, R. Engel, J. Engler, B. Fuchs,
H.J. Gils, D. Heck, D. Huber, T. Huege, D. Kang, H.O. Klages,
K. Link, M. Ludwig, H.J. Mathes, H.J. Mayer, J. Milke, J. Oehlschläger,
S. Ostapchenko, N. Palmieri, T. Pierog, H. Rebel, M. Roth, H. Schieler,
S. Schoo, F.G. Schröder, H. Ulrich, A. Weindl, D. Wochele, J. Wochele
KIT - Karlsruher Institut für Technologie, Germany,
J.C. Arteaga-Velázquez
Univ Michoacana, Inst de Física y Matemáticas, Morelia, Mexico
M. Bertaina, E. Cantoni, A. Chiavassa, F. Di Pierro
Dipartimento di Fisica, Università degli Studi di Torino, Italy
I.M. Brancus, A. Ghergel-Lascu, B. Mitrica, M. Petcu, G. Toma
Horia Hulubei NIPNE, Bucharest, Romania
C. Morello, G.C. Trinchero
Osservatorio Astrofisico di Torino, INAF Torino, Italy
V. de Souza
Uni São Paulo, Inst de Física de São Carlos, Brasil
D. Fuhrmann, R. Glasstetter, K.-H. Kampert
Fachbereich Physik, Universität Wuppertal, Germany
C. Grupen
Department of Physics, Siegen University, Germany
J.R. Hörandel
Dept of Astrophysics, Radboud Univ Nijmegen, The Netherlands
P. Łuczak, J. Zabierowski
National Centre Nuclear Research, Dpt of Astrophysics, Lodz, Poland
O. Sima
Dpt. of Physics, University of Bucharest, Bucharest, Romania

contact email: haungs@kit.edu

Abstract

Investigations of the energy spectrum as well as the mass composition of cosmic rays in the energy range of PeV to EeV are important for understanding both, the origin of the galactic and the extragalactic cosmic rays. The multi-detector arrangement of KASCADE and its extension KASCADE-Grande was designed

for observations of cosmic ray air showers in this energy range. Most important result from KASCADE is the proof that the knee feature at several PeV is due to a decrease in the flux of light atomic nuclei of primary cosmic rays. Recent results of KASCADE-Grande have now shown two more spectral features: a knee-like structure in the spectrum of heavy primaries at around 90 PeV and a hardening of the spectrum of light primaries at an energy of 120 PeV.

1 KASCADE-Grande

Extensive air showers (EAS) are generated when high-energy cosmic particles enter the Earth's atmosphere. Forward-boosted secondary particles as well as emitted light during the development of the EAS in various frequency ranges form the detectable products. Main parts of the experiment are the Grande array spread over an area of $700 \times 700\,\mathrm{m}^2$, the original KASCADE array covering $200 \times 200\,\mathrm{m}^2$ with unshielded and shielded detectors, a large-size hadron calorimeter, and additional muon tracking devices (fig. 1, right panel). The radio antenna field LOPES [1)] and the microwave experiment CROME [2)] completed the experimental set-up of KASCADE-Grande.

KASCADE-Grande stopped finally the active data acquisition of all its components end of 2012 and is now decommissioned. The collaboration, however, continues the detailed analysis of nearly 20 years of high-quality air-shower data. Moreover, with KCDC, the KASCADE Cosmic-ray Data Center, we provide to the public the edited data via a customized web page (see section 4).

The estimation of energy and mass of the primary particles is based on the combined investigation of the charged particle, the electron, and the muon components measured by the detector arrays of Grande and KASCADE. The multi-detector experiment KASCADE [3)] (located at 49.1°n, 8.4°e, 110 m a.s.l.) was extended to KASCADE-Grande in 2003 by installing a large array of 37 stations consisting of $10\,\mathrm{m}^2$ scintillation detectors each. KASCADE-Grande [4)] provided an area of $0.5\,\mathrm{km}^2$ and operated jointly with the existing KASCADE detectors. While the Grande detectors were sensitive to charged particles, the KASCADE array detectors measured the electromagnetic component and the muonic component separately. These muon detectors enabled to reconstruct the total number of muons on an event-by-event basis also for Grande triggered events.

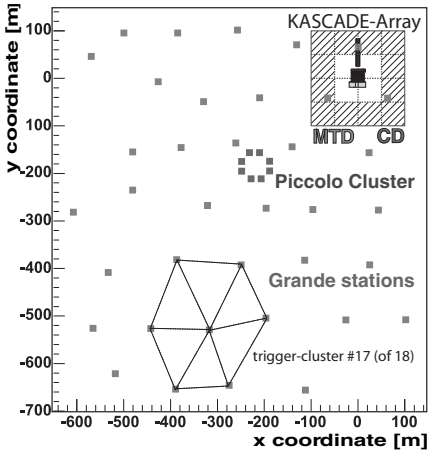

Figure 1: Layout of the KASCADE-Grande experiment: The original KASCADE, the distribution of the 37 stations of the Grande array, and the small Piccolo cluster for fast trigger purposes are shown. The outer 12 clusters of the KASCADE array consist of μ- and e/γ-detectors, the inner 4 clusters of e/γ-detectors, only.

2 The all-particle energy spectrum

In first steps of the data analysis, we reconstructed the all-particle energy spectrum. By combining both observables and using the hadronic interaction model QGSJet-II, a composition independent all-particle energy spectrum of cosmic rays is reconstructed in the energy range of 10^{16} eV to 10^{18} eV for the Grande data within a total uncertainty in flux of 10-15% [5]. The spectrum is in the overlapping region in agreement with the earlier published spectrum by KASCADE [6].

Despite the overall smooth power law behavior of the resulting all-particle spectrum, there are some structures, which do not allow to describe the spectrum with a single slope index (fig. 2). The justification of the 'knee' at a few times 10^{15} eV is given since many years. But now, there is also a clear evidence that just above 10^{16} eV the spectrum shows a 'concave' behavior, which is significant with respect to the systematic and statistical uncertainties. Another feature in the spectrum is a small break, i.e. knee-like feature at around 10^{17} eV.

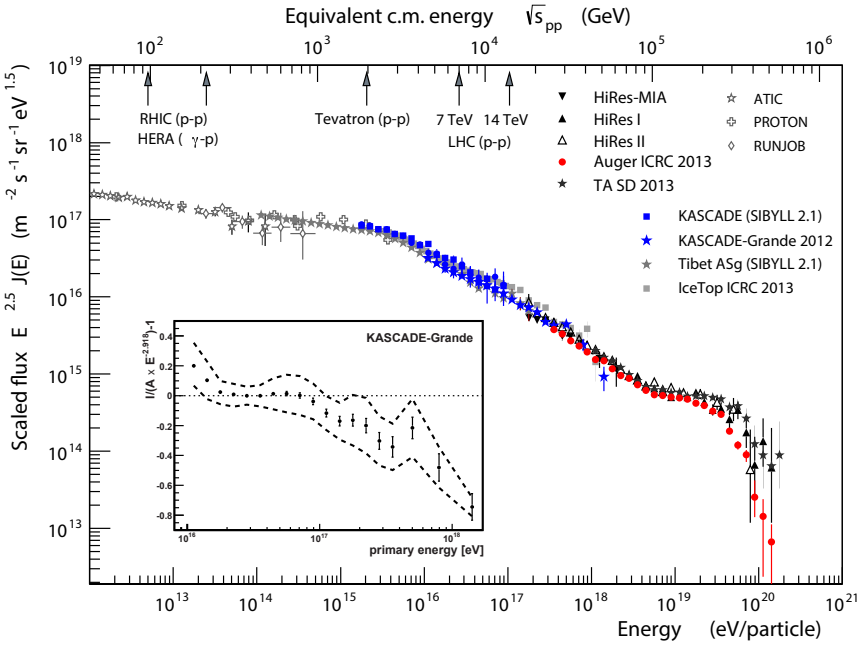

Figure 2: The all-particle energy spectrum obtained with KASCADE and KASCADE-Grande based on the QGSJet-II model and unfolded, i.e. corrected for the reconstruction uncertainties. Shown are the spectra in comparison with results of other experiments. In addition, the corresponding interaction energy at accelerators are indicated. The inlet displays the measured spectrum of KASCADE-Grande in a way to better see the spectral features.

This slight slope change occurs at an energy where the rigidity dependent, i.e. charge dependent, knee of the iron component would be expected.

3 Composition

The basic goal of the KASCADE-Grande experiment is the determination of the chemical composition in the primary energy range $10^{15} - 10^{18}$ eV by reconstructing individual mass group spectra. Structures observed in these individual spectra provide strong constraints to astrophysical models of origin and propagation of high-energy cosmic rays. Already in 2005 KASCADE could

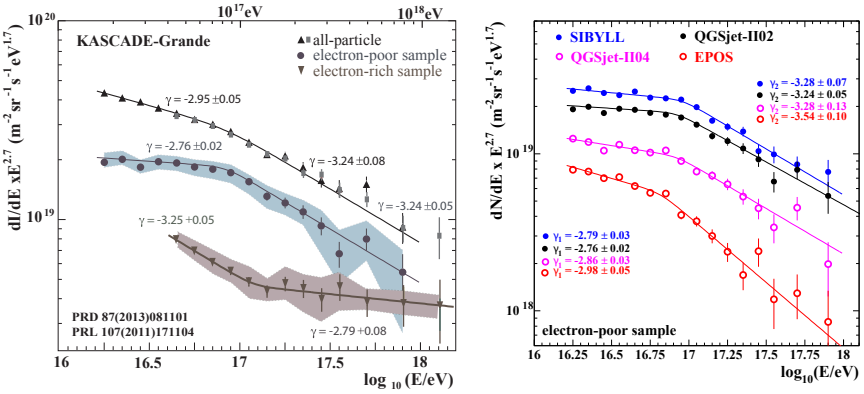

Figure 3: Left: All-particle, electron-poor, and electron rich energy spectra from KASCADE-Grande. Right: Reconstructed energy spectra of the heavy primary component for four hadronic interaction models. The error bars show the statistical uncertainties; fits on the spectra and resulting slopes before and after the heavy knee are also indicated.

prove [6] (confirmed by different approaches [7]) that the knee is caused by a decrease of the light mass group of primary particles and not by medium and heavy primary particles.

With KASCADE-Grande we investigated such individual mass group spectra also at higher primary energies. Using the reconstruction of the energy spectrum by correlating N_{ch} and N_{μ} on an event-by-event basis, the mass sensitivity is minimized by means of the parameter $k(N_{ch}, N_{\mu})$. However, the evolution of k as a function of energy keeps track of the elemental composition, and allows an event-by-event separation between light, medium and heavy primaries, at least. Using k as separation parameter for different mass groups, where the values of k are normalized with help of simulations, directly the energy spectra of the mass groups are obtained [8, 9]. All the simulations for the described analyses are performed with the air-shower simulation package CORSIKA [10] allowing simulations based on various hadronic interaction models. The application of this methodical approach to shower selection and separation in various mass groups were performed and cross-checked in different ways, where figure 3, left panel, shows the main results:

Knee-like feature in the heavy component of primary cosmic

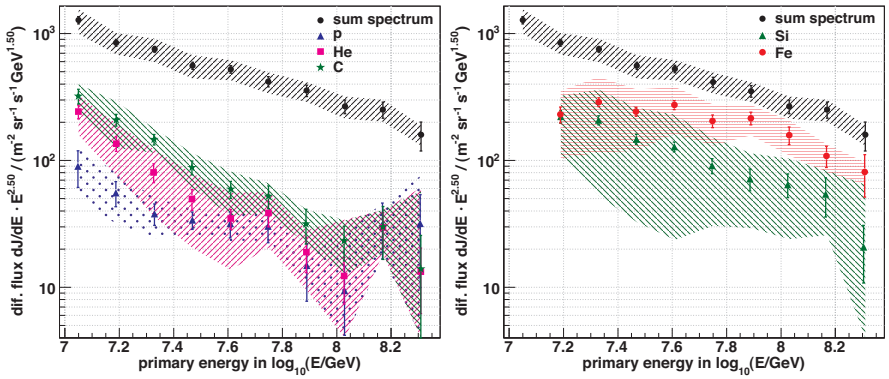

Figure 4: The unfolded energy spectra for elemental groups of cosmic rays, represented by protons, helium, and carbon nuclei (left panel) as well as by silicon and iron nuclei (right panel), based on KASCADE-Grande measurements. The all-particle spectrum, which is the sum of all five individual spectra, is also shown. The error bars represent the statistical uncertainties, while the error bands mark the maximal range of systematic uncertainties.

rays: The reconstructed spectrum of the electron-poor events, i.e. the spectrum of heavy primaries, shows a distinct knee-like feature at about $8 \cdot 10^{16}$ eV. Applying a fit of two power laws to the spectrum interconnected by a smooth knee results in a statistical significance of 3.5σ that the entire spectrum cannot be fitted with a single power law. The change of the spectral slope is $\Delta\gamma = -0.48$ from $\gamma = -2.76 \pm 0.02$ to $\gamma = -3.24 \pm 0.05$ with the break position at $\log_{10}(E/eV) = 16.92 \pm 0.04$. Applying the same function to the all-particle spectrum results in a statistical significance of only 2.1σ at the same energy and a change of the spectral slope from $\gamma = -2.95 \pm 0.05$ to $\gamma = -3.24 \pm 0.08$. Hence, the selection of heavy primaries enhances the knee-like feature that is already present in the all-particle spectrum. The analysis was repeated on basis of different hadronic interaction models [11]. Despite the fact, that the relative abundance of the heavy particles varies significantly dependent on the model in use, the spectral feature of the knee is visible in all the spectra (fig. 3, right panel).

This 'heavy' knee is confirmed by a detailed KASCADE-like unfolding analysis applied to the data of the Grande array [12]. In Fig. 4, the unfolded differential energy spectra of lighter primaries (protons as well as helium and

carbon nuclei, left panel), and the spectra of heavier ones (silicon and iron nuclei, right panel) are depicted. In addition, all five unfolded spectra are summed up to the all-particle flux. The shaded band indicates the methodical uncertainties, while the error bars represent the statistical error originating from the fact that only vertical showers are used. With increasing energy, the heavy component becomes the dominant contributor to the cosmic ray composition. This agrees with the results of KASCADE [6], where a reduction of the light component beyond the first knee was found. The spectra of lighter primaries are rather featureless within the given uncertainties. In the iron spectrum, however, there is a slight bending discernible at around 1×10^{17} eV.

Ankle-like feature in the light component of primary cosmic rays: An ankle-like feature was observed in the spectrum of the electron-rich events (Fig. 3), i.e. light elements of the primary cosmic rays, at an energy of $10^{17.08 \pm 0.08}$ eV. At this energy, the spectral index changes by $\Delta\gamma = 0.46$ from $\gamma_1 = -3.25 \pm 0.05$ to $\gamma_2 = -2.79 \pm 0.08$. Applying again a fit of two power laws to the spectrum results in a statistical significance of 5.8σ that the entire spectrum cannot be fitted with a single power law. It is worth to mention that the changes in the spectrum of heavy primaries and in the spectrum of light elements are not connected by a bias in the separation or reconstruction procedures, as well as due to a dependence of the hadronic interaction model, which was checked in detail [11]. Due to differences in the high energy hadronic interaction models regarding the number of produced muons, it is also not possible to tell if the shown spectrum of light particles consists mainly of protons and helium primaries or if it is an almost pure proton spectrum. For simulations using the QGSJet-II-2 model, however, the reconstructed spectrum of light elements well reproduces a combined proton and helium spectrum.

4 The KASCADE Cosmic-ray Data Center KCDC

The KASCADE/KASCADE-Grande experiment was a large-area detector for the measurement of cosmic ray air showers lasting for more than 20 years and financed by taxes. The aim of this particular project is the installation and establishment of a public data center for high-energy astroparticle physics. In the research field of astroparticle physics, such a data release is a novelty, whereas the data publication in astronomy has been established for a long time. There-

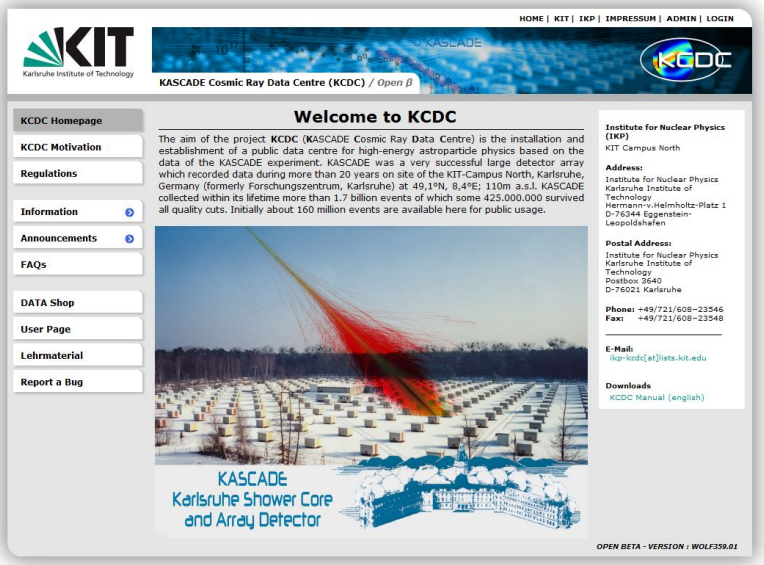

Figure 5: Title page of the website of KCDC, the KASCADE Cosmic-ray Data Center.

fore, there are no completed concepts, how the data can be treated/processed so that they are reasonably usable outside the collaboration. The first goal of KCDC is to make the data from the KASCADE experiment available to the community. A concept for this kind of data center (software and hardware) is already developed, implemented, and already released as a platform to external users (fig. 5). The project faces thereby open questions, e.g. how to ensure a consistent calibration, how to deal with data filtering and how to provide the data in a portable format as well as how a sustainable storage solution can be implemented. In addition, access rights and license policy play a major role and are considered. Users are invited to visit KCDC under `https://kcdc.ikp.kit.edu`.

5 Summary

In summary, after separating the KASCADE-Grande measured events into a light and a heavy component, a knee-like feature is identified in the spectrum

of the heavy component, and an ankle-like feature is observed in the spectrum of the light component. Whereas the 'heavy-knee' occurs at an energy where the rigidity dependent knee of the iron component is expected, the 'light-ankle' might indicate an early transition from galactic to extragalactic origin of cosmic rays. The KASCADE-Grande collaboration has started to provide the entire data set to the public within the project KCDC, the KASCADE Cosmic Ray Data Center.

6 Acknowledgments

KASCADE-Grande is supported by the BMBF and the 'Helmholtz Alliance for Astroparticle Physics - HAP' of Germany, the MIUR and INAF of Italy, the Polish Ministry of Science and Higher Education and the Romanian Authority for Scientific Research (PNII-IDEI grants 271/2011 and 17/2011).

References

1. H. Falcke et al. - LOPES, Nature 435 (2005) 313.
2. R. Smida et al. - CROME, EPJ Web Conf. 53 (2013) 08010.
3. T. Antoni et al. - KASCADE, NIM A **513** (2003) 429.
4. W.-D. Apel et al. - KASCADE-Grande, NIM A **620** (2010) 202.
5. W.-D. Apel et al. - KASCADE-Grande, Astropart. Phys. **36**, 183 (2012).
6. T. Antoni et al. - KASCADE, Astropart. Phys. **24**, 1 (2005).
7. W.-D. Apel et al. - KASCADE-Grande, Astropart. Phys. **34**, 476 (2011).
8. W.-D. Apel et al. - KASCADE-Grande, PRL **107**, 171104 (2011).
9. W.-D. Apel et al. - KASCADE-Grande, PRD **87**, 081101(R) (2013).
10. D. Heck et al., report Forschungszentrum Karlsruhe, FZKA 6019 (1998).
11. W.-D. Apel et al. - KASCADE-Grande, Adv. Space Res. **53**, 1456 (2014).
12. W.-D. Apel et al. - KASCADE-Grande, Astropart. Phys. **47**, 54 (2013).

Frascati Physics Series Vol. 58 (2014)
Frontier Objects in Astrophysics and Particle Physics
May 18-24, 2014

THE PIERRE AUGER OBSERVATORY: RESULTS, OPEN QUESTIONS AND FUTURE PROSPECTS

Antonella Castellina[1], for the Pierre Auger Collaboration[2]
(1) Osservatorio Astrofisico (INAF), Università and Sezione INFN, Torino, Italy
(2) Observatorio Pierre Auger, Malargüe, Argentina
(Full author list : http://www.auger.org/archive/authors_2014_05.html)

Abstract

The Pierre Auger Observatory is collecting ultra high energy cosmic rays to study their origin and nature. A review of selected analyses is presented, with emphasis given to the measure of the energy spectrum and mass composition. The interpretation of the results obtained so far opens new questions which will be addressed by the foreseen upgrade of the Observatory.

1 Introduction

The sources, nature and propagation properties of the ultra high energy ($E \geq 10^{18}$ eV) cosmic rays are still a matter of debate, despite the $\simeq$100 years since their discovery. Their energy spectrum shows two particularly interesting regions: the *ankle*, from $\simeq 10^{18}$ to 10^{19} eV, which is expected to host the transition from galactic to extragalactic cosmic rays, and the region above few 10^{19} eV,

where a *suppression* in the cosmic ray spectrum is expected, mainly due to the interaction of extragalactic protons with the CMB photons. The origin of these features is still debated and different scenarios can be built, e.g. ascribing them to the interaction of cosmic rays with the intergalactic radiation fields, the sources distribution or their inner characteristics [1, 2, 3, 4]. Combined data on the particles energy, nature and arrival direction are mandatory to get new insights in this problem and disentangle the different hypotheses.

The Pierre Auger Observatory has been explicitly designed for this aim. Its concept is that of a hybrid detector , consisting of a large Surface Detector array (SD [5]) and of 27 Fluorescence Detectors (FD [6]). The SD is made of 1660 water Cherenkov stations, spread over a total area of $\simeq 3000$ km^2 on a 1.5 km grid in Malargüe, province of Mendoza, Argentina; it measures the lateral density distribution of charged particles at ground and their temporal distribution in each station. The FD overlooks this region from four sites located along the perimeter, each with 6 FD telescopes and can record the fluorescence light produced as the shower crosses the atmosphere, thus measuring its longitudinal profile. A small area of $\simeq 30$ km^2, the *Infill*, is instrumented with 71 SD with additional muon detectors on a 750 m grid and with 3 FD with elevated field of view to lower the energy threshold of the Observatory down to 10^{17} eV. A set of high quality instruments are installed in the field to monitor the atmospheric conditions; on line and long term performances of the detectors and data quality are monitored continuously (see [8] and refs. therein). The overall uptime and efficiency of the SD is above 98%, while a duty cycle of $\simeq 13\%$ characterises the FD, which can operate only in clear moonless nights. Thanks to the possibility of combining the information from the two types of detectors, the reconstruction capabilities are enhanced with respect to the individual detectors.

2 Energy spectrum

Four different data sets are used in Auger to construct the energy spectrum: the SD vertical and horizontal sets (below and above 60° respectively), the Infill and the hybrid data; for each of them, the exposure is carefully evaluated thanks to our monitoring systems. Exploiting the hybrid data set (consisting of all events detected by both the SD and FD), it is possible to obtain the energy calibration directly from the data [9]. About 130 000 events have been combined through

a maximum likelihood method; both FD and SD share the same systematic uncertainty on the energy scale, which amounts to 14% [10]. The resulting spectrum is shown in Fig.1. The unprecedented statistics allows to clearly identify the two main features of the *Ankle*, at $\log(E/\mathrm{eV}) = (18.72 \pm 0.01 \pm 0.02)$, and of the *Cutoff*, at $\log(E_{1/2}/\mathrm{eV}) = (19.63 \pm 0.01 \pm 0.01)$.
$E_{1/2}$ is the energy at which the flux falls at half the value expected from a simple extrapolation of the power law; the significance of the suppression is more than 20 σ.

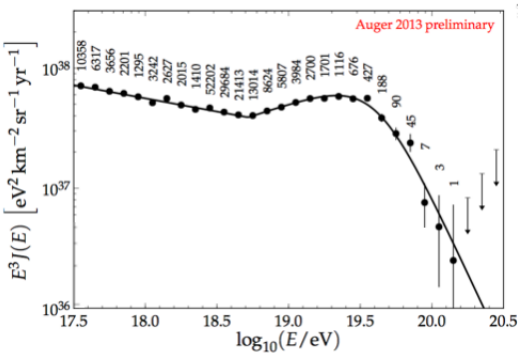

Figure 1: *The Auger energy spectrum after combining different SD and hybrid data sets* [11].

3 The nature of the primaries

Different observables can be used to obtain information on the primary composition. The most direct one is related to the depth of maximum development of the longitudinal profile of the showers, measured by the FD.
A difference of $\simeq 100$ g cm^{-2} is observed between the $\langle X_{\mathrm{max}} \rangle$ of showers generated by protons and iron nuclei, the latter developing higher in atmosphere. A narrower distribution (smaller RMS(X_{max})) is furthermore obtained from heavy nuclei as compared to light ones. $\langle X_{\mathrm{max}} \rangle$ is related to the depth of the first interaction of the primary and to the subsequent development of the shower; for this reason, the interpretation in terms of composition is complicated by the large uncertainties in the hadronic interaction models used in the simulations. Having been corrected for the detector resolution, $\langle X_{\mathrm{max}} \rangle$ and its RMS can be directly compared to the predictions of different models, as shown in Fig.2 [8]. As shown, all models predict a constant elongation rate

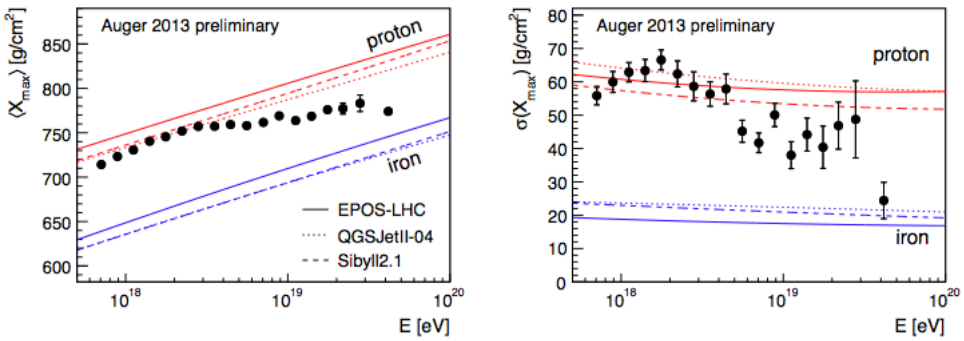

Figure 2: $\langle X_{\rm max}\rangle$ *and its RMS as a function of energy, compared to the predictions of the most recent, post-LHC, air shower simulations using different hadronic interaction models (see text).*

as a function of energy for pure compositions. This is at variance with our measurements, which clearly show a change of slope at few EeV. If we assume that no change in hadronic interactions comes into play at these energies, our data show evidence for a composition getting heavier above the ankle region. Different information can be extracted from $\langle X_{\rm max}\rangle$ and its RMS: the former is related only to the mean logarithmic mass $\langle lnA\rangle$, the latter includes both the shower to shower fluctuations and the dispersion in the mass distribution during propagation. The derived $\langle lnA\rangle$ and its variance are shown in Fig.3 ([8]) and refs.therein); there is a clear change from light to medium-heavy composition, although slow as suggested by the low values of $\sigma^2_{\ln A}$.

The nature of the primaries can be studied with more statistics exploiting SD data. Starting from the temporal distribution of the signals in the stations, it is possible to reconstruct the muon longitudinal profile and derive the depth of maximum development of the muon component. In the frame of the same interaction model, both $\langle X_{\rm max}\rangle$ and $\langle X^{\mu}_{\rm max}\rangle$ can be converted to $\langle lnA\rangle$, hopefully converging to a coherent result. As shown in Fig.4, there is a discrepancy in the EPOS-LHC case, which could be most probably explained as a collective effect of nuclei in atmosphere (as compared to *pp* interactions at LHC). As for QGSJetII-04, the good agreement is only apparent, as this model does not accurately reproduce the rapidity gap distribution of LHC data [8]. From these considerations, although insufficient to exclude specific models, it appears that UHECR data have the power to constrain high energy interaction models in unexplored energies and kinematic regions.

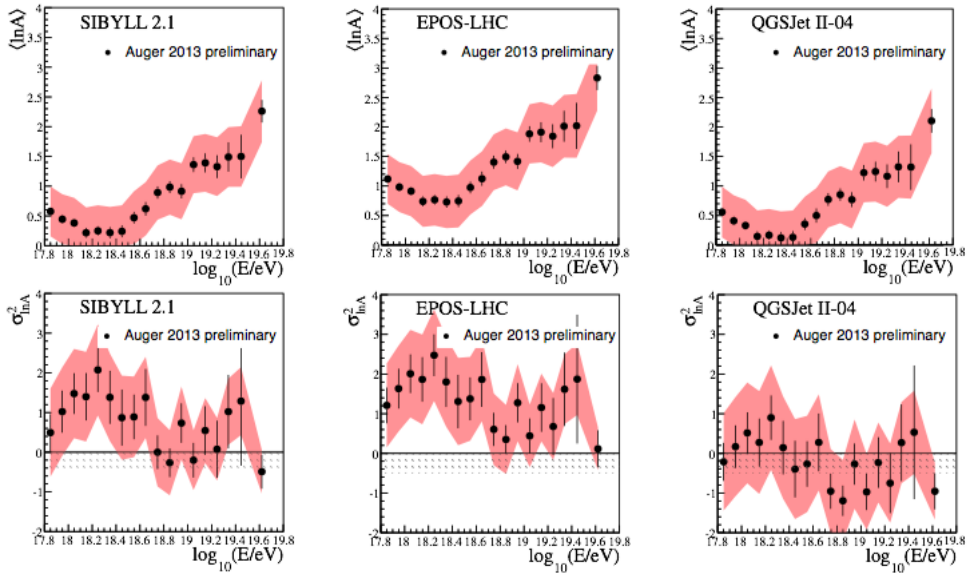

Figure 3: *$\langle lnA \rangle$ and $\sigma^2_{\ln A}$ as derived from Auger data using various hadronic interaction models. Red bands: systematic uncertainties. ([8] and refs.therein).*

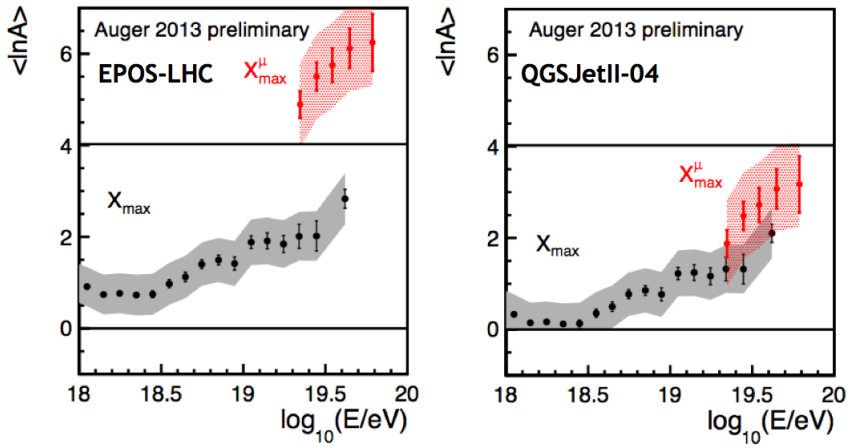

Figure 4: *Comparison of the $\langle lnA \rangle$ obtained from $\langle X_{\max} \rangle$ and $\langle X^{\mu}_{\max} \rangle$ for EPOS-LHC (left) and QGSJetII-04 (right) ([8] and refs.therein).*

4 Anisotropy in arrival directions

A key observable to obtain information about the sources and nature of UHE cosmic rays is the spatial distribution of their arrival directions. At these energies, the particles are most probably extragalactic; if the observed flux suppression can be attributed to propagation effects, they would be limited by a "GZK horizon" of about 100 Mpc.
A correlation between the arrival directions of the highest energy cosmic rays (above 50 EeV) and the positions of the nearby AGN from the Véron-Cetty-Véron (VCV) catalogue was reported in 2007 [14]. The most recent update of this search is shown in Fig.5; the current estimate of the fraction of correlation is $(33 \pm 5)\%$, against a 21% expected under the hypothesis of isotropy.

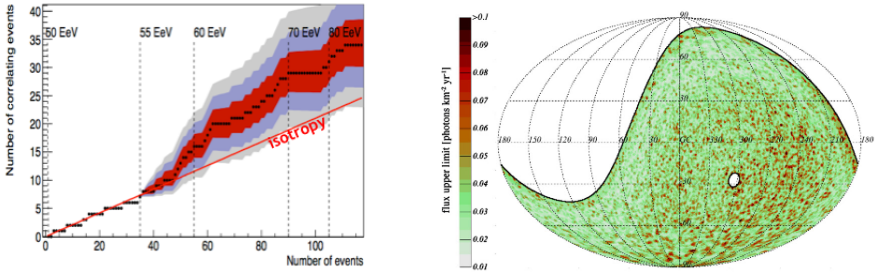

Figure 5: *Auger events correlating with the positions of AGN from the VCV catalogue, in an energy ordered plot (left)* [8]. *Celestial map of photon flux upper limits in photons* $km^{-2}yr^{-1}$ *in Galactic coordinates (right)* [15].

Scenarios in which EeV cosmic ray protons are emitted by non-transient sources in the Galaxy can be constrained by looking at possible point sources of EeV photons. Using hybrid events, a search in the energy range $10^{17.3}$ to $10^{18.5}$ eV was performed, leading to an energy flux upper limit of less than 0.25 eV cm^{-2}s^{-1} in every direction (assuming a photon spectral index of -2) [15].
We could not find detectable point sources of EeV neutral particles; however, Galactic sources of EeV cosmic rays could still be present if e.g. they were transient, or too weak to be detected.
The results from the present study complement those from the targeted search for fluxes of neutrons above 1 EeV [16].

5 Future prospects

During the last 10 years, the Auger data analyses have led to major breakthroughs in the study of cosmic rays spanning over four orders of magnitude in energy (from 10^{17} to above 10^{20} eV). Different models have been built trying to reproduce our results (see e.g. [7]), but the many unknowns about source distribution, composition, galactic and extragalactic magnetic fields, etc. prevent the emergence of a consistent picture. As described above, many questions have been answered, at the same time leading to more questions and thus to a well defined science case for the future.

• Auger was built to answer the fundamental question about the existence or absence of the flux suppression. From our analysis, the cutoff is now established at $E_{1/2} = 10^{19.63}$ eV with a significance of more than 20 σ. However, the cutoff energy is lower than expected from the GZK effect, and the composition results show a trend toward heavier mass with increasing energy. An alternative explanation for the cutoff would be the reaching of the maximum energy available for particle acceleration in the sources. It is thus mandatory to elucidate the origin of the flux suppression, thus providing fundamental information on the astrophysical sources of UHE cosmic rays. The direct detection of cosmogenic photons or neutrinos would be direct evidence of the GZK.

• The observed correlation between the highest energy events and the positions of the VCV AGNs points to the possible presence of a sub-dominant fraction of protons above 50 EeV (below 15%). The clear detection of such component would be of the greatest importance to evaluate the physics potential of future detectors of cosmic rays, neutrinos and $\gamma-$rays. At the lower end of the considered energy region, while the ankle has been clearly seen, the composition is light, although the anisotropy stays below few % and no steady sources of Galactic protons have been detected. Extreme assumptions on the Galactic magnetic fields could reconcile the two results.

• Although not discussed above, important information have been obtained from Auger about hadronic interactions in an energy and kinematic region not explorable by man-made accelerators. A fundamental objective for the future is that of studying hadronic multiparticle production in air showers; new constraints on new phenomena, e.g. Lorentz invariance violation, can be obtained.

The Auger Collaboration is now proposing an upgrade which will add composition and hadronic interaction sensitive information through the disentangling of the muonic and electromagnetic components of extensive air showers. Different options are under scrutiny to fulfill the scientific goals; several years of high quality data taking are foreseen with the upgraded Observatory.

References

1. V. Berezinsky *et al.*, Phys. Lett. **B612**, 147 (2005).
2. D. Allard *et al.*, JCAP **0810**, 033 (2008).
3. A. M. Taylor *et al.*, Phys. Rev. **D84**, 105007 (2011).
4. N. Shaham and T. Piran, Phys. Rev. Lett. **110**, 021101 (2013).
5. The Pierre Auger Collaboration, Nucl. Instr. Meth. **A613**, 29 (2010).
6. The Pierre Auger Collaboration, Nucl. Instr. Meth. **A620**, 227 (2010).
7. R. Aloisio *et al.*, arXiv:1312.7459.
8. A. Letessier-Selvon for the Pierre Auger Collaboration, in Proc. 33rd ICRC, Rio de Janeiro, Brazil (2013); arXiv:1310.4620.
9. R. Pesce for the Pierre Auger Collaboration, in Proc. 32nd ICRC, Beijing, China, **2** (2011) 214; arXiv:1107.4809.
10. V. Verzi for the Pierre Auger Collaboration, in Proc. 33rd ICRC, Rio de Janeiro, Brazil (2013); arXiv: 1307.5059.
11. A. Schulz, for the Pierre Auger Collaboration, in Proc. 33rd ICRC, Rio de Janeiro, Brazil (2013); arXiv: 1307.5059.
12. The Pierre Auger Collaboration, JCAP **02** 026 (2013).
13. M. Settimo for the Pierre Auger Collaboration, in Proc. of Photon 2013, PoS **062** (2013).
14. The Pierre Auger Collaboration, Science **318** 938 (2007).
15. The Pierre Auger Collaboration, ApJ **789** 160 (2014).
16. The Pierre Auger Collaboration, ApJ Lett. **789** L34 (2014).

Frascati Physics Series Vol. 58 (2014)
Frontier Objects in Astrophysics and Particle Physics
May 18-24, 2014

Large Scale Distribution of Arrival Directions of Cosmic Rays Detected at the Pierre Auger Observatory Above 10 PeV

Raffaella Bonino for the Pierre Auger Collaboration*
Osservatorio Astrofisico di Torino (INAF), Università di Torino and Sezione INFN, Torino, Italy

**Av. San Martín Norte 304, 5613 Malargüe, Argentina*
(Full author list: http://www.auger.org/archive/authors_2014_05.html)

Abstract

Searches for large-scale anisotropies in the distribution of arrival directions of cosmic rays with energies above 10 PeV detected at the Pierre Auger Observatory are presented. Although no significant deviation from isotropy is revealed at present, some of the measurements suggest that future data will provide hints for large-scale anisotropies over a wide energy range. Assuming that the cosmic ray anisotropy is dominated by dipole and quadrupole moments in the EeV-energy range, some consequences of the present upper limits on their amplitudes are presented.

1 Introduction

To understand CRs nature and origin large scale anisotropy studies are complementary to measurements of energy spectrum and mass composition. The

transition from a galactic to an extragalactic origin should in fact induce a significant change in CRs large scale angular distribution. In particular, if they are still galactic at EeV energies, a %-level modulation is expected (the predicted amplitude varies significantly according to the chosen galactic magnetic field, composition and distribution of sources [1]). On the other hand, if CRs are already extragalactic at 10^{18} eV, no structure except for a CMB-dipole is expected, with an anisotropy amplitude of the order of ~ 0.6 % [2].

A measurable dipole is regarded as a likely possibility in many scenarios of CR origins at EeV energies (e.g. as a signature of their escape from Galaxy or a Compton-Getting effect, in case of extragalactic origin). Otherwise, an excess along a plane would show up as a prominent quadrupole moment, plausible scenario in case of emission of light EeV CRs from sources preferentially located in the galactic disk or in the super galactic plane at higher energies.

Using the large amount of data collected by the Surface Detector array of the Pierre Auger Observatory [3], results of first harmonic analyses of the right ascension distribution performed in different energy ranges above 10 PeV are presented here. A thorough search for large scale anisotropies in terms of dipoles and quadrupoles as a function of both the declination and the right ascension is presented as well.

2 First harmonic analysis in Right Ascension

Thanks to the joint data acquired by both the infill array with 750 m spacing and the regular array with 1.5 km spacing, in this analysis we use the full energy range above 10^{16} eV. The data set analyzed here covers the whole period from 1 January 2004 up to the end of 2012.

2.1 Analysis methods

The statistics accumulated in the EeV energy range allows one to be sensitive to intrinsic anisotropies with amplitudes down to the 1% level. This requires determination of the exposure of the sky and of various acceptance effects at a corresponding accuracy. Possible spurious modulations of experimental or atmospheric origin should thus be taken into account or, alternatively, methods which are not sensitive to these effects should be used.

The first kind of approach could be implemented with a "modified Rayleigh analysis" [4], i.e. the classical Rayleigh formalism slightly modified to account

for non-uniform exposure. Each event is weighted with the inverse of the integrated number of unitary cells at the local sidereal time of the event. Energy assignment is then corrected for weather and geomagnetic effects [5, 6], which could represent other sources of systematic effects.

Below 1 EeV weather effects have a significant impact also on the detection efficiency and hence spurious variations of the counting rates are amplified. We adopt in this case the differential "East-West method" [7]. It exploits the differences in the number of counts between the eastward and the westward arrival directions at a given time. Since the instantaneous exposure for events coming from E or W is the same, this difference allows us to remove, at first order, effects of experimental or atmospheric origin without applying any correction, although at the price of a reduced sensitivity. The amplitude and phase can thus be calculated by using the standard first harmonic analysis slightly modified to account for the subtraction of the W sector to the E one.

2.2 Amplitude of the first harmonic

The Rayleigh amplitude measured by any observatory can be used to reveal (or infer) anisotropies projected on the Earth equatorial plane. All the amplitude values are thus divided by the mean value of the cosine of the declination of the observed sky, giving a direct measurement of the component of the dipole in the equatorial plane. The obtained amplitudes are shown in the left panel of Fig. 1, the dashed line in the plot represents the upper values of the amplitude which may arise from fluctuations in an isotropic distribution at 99% C.L..

In the energy ranges 1-2 and 2-4 EeV the measured amplitudes of (1.0±0.2)% and (1.4±0.5)% have a probability to arise by chance from an isotropic distribution of about 0.03% and 0.9%, while above 8 EeV the measured amplitude of (5.9±1.6)% has chance probability of only 0.1%. Since several energy bins were searched, these numbers do not represent absolute probabilities and constitute just interesting hints for large scale anisotropies that will have to be further scrutinized with enlarged statistics.

Upper limits at 99% C.L. on the amplitudes have thus been derived and are shown in the right panel of Fig. 1, together with previous results from other experiments and with some predictions for the anisotropies arising from models of both galactic and extragalactic CR origin (see [8] for more details). The bounds reported here already exclude the particular model with an antisym-

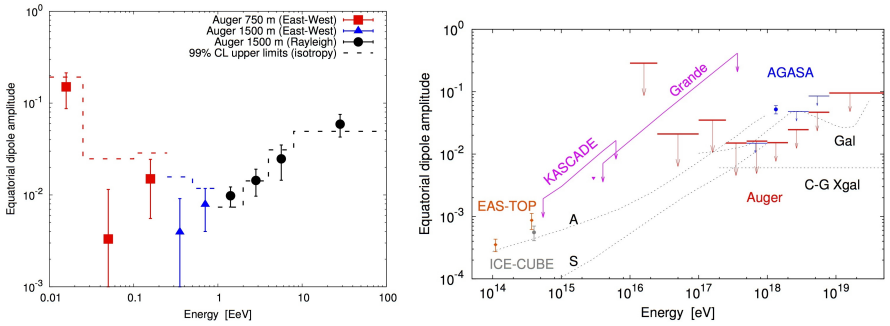

Figure 1: *Left: Equatorial dipole amplitude as a function of energy. Right: Upper limit at 99%C.L. for the equatorial dipole amplitude as a function of energy. Predictions from different models are also displayed (see text).*

metric halo magnetic field (A) above 0.25 EeV and the *Gal* model at few EeV energies, and are starting to become sensitive to the predictions of the model with a symmetric field (S).

2.3 Phase of the first harmonic

The Pierre Auger Collaboration has already reported the intriguing possibility of a smooth transition from a common phase of 270° (compatible with the right ascension of the Galactic Center 268.4°) in the first two bins below 1 EeV to a phase of 100° above 5 EeV [8]. The left panel in Fig. 2 shows this smooth transition in the phase derived with data from 1 January 2004 to 31 December 2010 for the larger array and from 12 September 2007 to 11 April 2011 for the infill. It has been already pointed out that this consistency of phases in adjacent energy intervals is expected with a smaller number of events than the detection of amplitudes standing out significantly above the background noise in the case of a real underlying anisotropy.

This behaviour motivated us to design a prescription with the intention of establishing at 99% C.L. whether this consistency in phases in adjacent energy intervals is real. Once an exposure of $21\,000\,\mathrm{km^2\,sr\,yr}$ is accumulated by the regular array from 25 June 2011 on, and applying the same first harmonic analysis described here, a positive anisotropy signal will be claimed within a global threshold of 1% if a constancy of phase below 1 EeV and/or a transition

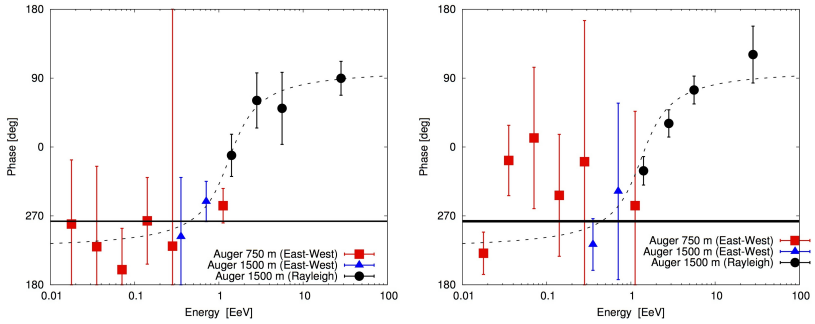

Figure 2: *Phase of the first harmonic as a function of energy with data acquired before (left) and after (right) the beginning of the prescription. The continuous and the dashed lines shown in both plots are the fit defined in* [8].

at ∼1 EeV are observed with the infill and the regular array, respectively.

To report the midterm status of the prescription, the phase of the first harmonic is shown in the right panel of Fig. 2 with data since 25 June 2011 (starting date of the prescription) up to 31 December 2012. At this stage, the values derived from the infill data are still affected by large uncertainties, whereas, the overall behavior of the points derived from the analysis with the regular array shows good agreement with the prescribed curve. The final result of the prescription is expected for 2015, once the required exposure is reached.

3 Spherical harmonic analysis

The analysis presented in the previous section benefits from the almost uniform directional exposure in right ascension of a ground-based observatory operating with high duty cycle, but is not sensitive to a dipole component along the Earth rotation axis. In this section we present a comprehensive search in all directions for any dipole or quadrupole patterns significantly standing out above the background noise [9], whose components are functions of both the right ascension and the declination.

Due to the steepness of the energy spectrum, any mild bias in the estimate of the shower energy with time or zenith angle can lead to significant distortions of the event counting rate above a given energy. The influence of atmospheric

conditions and geomagnetic field, the most important effects on shower size, have thus been studied in detail and taken into account [5, 6]. In searching for anisotropies, it is also critical to know accurately the directional exposure of the Observatory, i.e. to accurately determine the operational time of the detector, the geometric aperture and the detection efficiency.

Any angular distribution over the sphere $\Phi(\mathbf{n})$ can be expanded in terms of spherical harmonics, $\Phi(\mathbf{n}) = \sum_{\ell \geq 0} \sum_{m=-\ell}^{\ell} a_{\ell m} Y_{\ell m}(n)$, where $\mathbf{n}$ denotes a unit vector taken in equatorial coordinates. Due to the non-uniform and incomplete coverage of the sky at the Pierre Auger Observatory, the estimation of coefficients $a_{\ell m}$ is possible only by assuming a $\ell_{\max}$. The resolution deteriorates by a factor larger than 2 each time $\ell_{\max}$ is incremented by 1. With our present statistics, this prevents the recovery of each coefficient with good accuracy as soon as $\ell_{\max} \geq 3$, which is why we restrict this analysis to dipole and quadrupole searches only.

Assuming that the angular distribution of cosmic rays is modulated by a dipole and a quadrupole, we reconstructed the amplitudes of both moments: the case of a pure dipole is presented in the left panel of Fig. 3. The 99% C.L. upper bounds on the amplitudes that would result from fluctuations of an isotropic distribution are indicated by the dotted line. One can see, similarly to the results presented in the previous section, interesting hints for large scale anisotropies that will have to be further scrutinized with independent data. The corresponding reconstructed directions in orthographic projection with the associated uncertainties are shown in the right panel of Fig. 3 as a function of the energy. All reconstructed declinations are in the equatorial southern hemisphere and the phases in right ascension are smoothly aligned as a function of the energy, as already pointed out in the previous section.

Upper bounds on the dipole and quadrupole amplitudes have been obtained at the 99% C.L. and are shown as a function of energy in Fig. 4, along with generic estimates of the amplitudes expected from stationary galactic sources distributed in the disk considering two extreme cases of primaries: protons and iron nuclei. The expected amplitudes are calculated by considering the Bisymmetric Spiral Structure model with anti-symmetric halo field and a turbulent field generated according to a Kolmogorov power spectrum. Unless the strength of the galactic magnetic field is much higher than in the picture used here, the upper limits on dipole and quadrupole amplitudes challenge

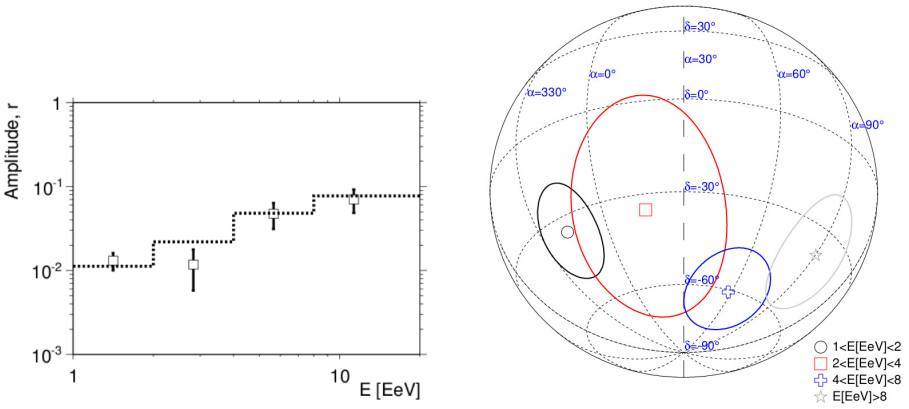

Figure 3: *Left: Amplitude of the dipole as a function of energy. The dotted line stands for the 99% C.L. upper bounds that would result from fluctuations of an isotropic distribution. Right: Directions of the dipole with corresponding uncertainties (circles).*

an origin of CRs from galactic stationary sources distributed in the disk and emitting predominantly light particles in all directions at EeV energy ranges.

4 Auger-TA joint analysis

Full-sky coverage allows the measurement of the spherical harmonic coefficients in an unambiguous way. This can be achieved by combining data from observatories located in both the northern and southern hemispheres. A combined analysis using data recorded at the Telescope Array and the Pierre Auger Observatory has been performed and will be reported in a near future [10].

5 Conclusions

Searches for evidence of large scale anisotropy in the CRs arrival directions have been pursued by the Auger Collaboration. No statistically significant deviation from isotropy is revealed within the systematic uncertainties, even though there are interesting hints for large scale anisotropies that will have to be further scrutinized with independent data. An intriguing phase transition in

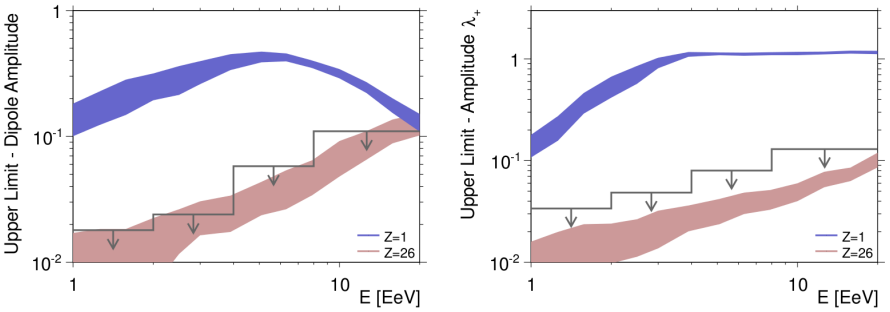

Figure 4: *99% C.L. upper limits on dipole and quadrupole amplitudes as a function of energy. Some generic anisotropy expectations are also shown (see text and* [9] *for more details).*

right ascension has been observed with increasing energy and will be specifically tested through a prescribed test.

Acknowledgements The successful installation, commissioning and operation of the Pierre Auger Observatory would not have been possible without the strong commitment and effort of the technical and administrative staff in Malargüe.

References

1. V. Ptuskin *et al.*, A&A **268**, 726 (1993); J. Candia *et al.*, JCAP **0305**, 003 (2003); G. Giacinti *et al.*., JCAP **07**, 031 (2012).
2. A.M. Hillas, PhLA **24**, 677 (1967); V.S. Berezinsky *et al.*, PhRvD **74** 043005 (2006) and APh **21**, 617625 (2004).
3. A. Castellina, these proceedings, VULCANO Workshop 2014 (2014).
4. S. Mollerach and E. Roulet, JCAP **0508**, 004 (2005).
5. Pierre Auger Collaboration, APh **32**, 89 (2009).
6. Pierre Auger Collaboration, JCAP **11**, 022 (2011).
7. R. Bonino *et al.*, ApJ **738**, 67 (2011).
8. Pierre Auger Collaboration, APh **34**, 628 (2011)
9. Pierre Auger Collaboration, ApJS **203**, 34 (2012); ApJL **762**, L13 (2013).
10. Pierre Auger and Telescope Array Collaborations, paper submitted to ApJ

Frascati Physics Series Vol. 58 (2014)
Frontier Objects in Astrophysics and Particle Physics
May 18-24, 2014

UHECR AND GRB NEUTRINOS: AN INCOMPLETE REVOLUTION?

Daniele Fargion
Physics Dept., Univ. "La Sapienza" and INFN Rome1, Rome, Italy
P.G. De Sanctis Lucentini
Gubkin Russian State University of Oil and Gas, Moskow, Russian Federation
P. Oliva
University Niccolò Cusano, Via Don Carlo Gnocchi, 3, Rome.

Abstract

At highest energy edges the Ultra High Energy Cosmic Ray, **UHECR** and PeVs neutrino, **UHE**ν, should soon offer new exciting astronomy. The fast and somehow contradictory growth of hundreds of antagonist models attests the explosive vitality of those new astronomy frontiers. No conclusive understanding on the *UHECR* and *UHE* neutrino source is at hand. The earliest expectation of *GRBs* as the main *UHE*ν sources explained by a single shot Fireball model has been rejected. The source of *UHECR* as the expected *GZK* ones within few tens Mpc from our Super-Galactic Plane has been quite disproved. Alternative models on Gamma Ray Burst, **GRB**, for instance the long life precessing Jets, together with the newly updated records by *AUGER*, *TA* and *ICECUBE* are nevertheless offering a partial understanding and an early hint for a point source correlations along our galaxy and toward *Cen A*, the nearest extragalactic *AGN*.

1 The Cosmic Ray Century

A century ago the radioactivity was used to probe the atomic nature. The same radioactivity was discovered around us, made by electrons (β), helium nuclei (α) and photons (γ). Apparently the radioactivity seems being generated by terrestrial matter: In fact as one rises from the ground level it starts to decline.

In those days Victor F. Hess proved through hot-air balloon ascensions that the radioactivity after few kilometers grows up to tens or even hundred times more than at sea level: the cosmic radioactivity rules at highest sky; consequently the idea of a cosmic rays nature ***CR*** was born. Nowadays we are aware of the motley nature of the *CR*, mostly composed by charged particles as proton, Helium and other nuclei and with the presence of electrons and positrons; we can say that *CR* are well representative of our solar system element composition.

Photons and Neutrinos are shining too. Photons, with energy from X to $TeVs$, are well observed. Neutrinos not, mainly because of the *CR* atmospheric neutrino secondary pollution and because of the extreme weak neutrino interaction. Cosmic Ray energies ranges in an almost steady power law for nearly eleven order of magnitude from GeV to ZeV energy. They are mostly stopped at twenty kilometers of altitude, or ten meter water equivalent, by our safe and protective atmosphere. Moreover charged *CR* are smeared by terrestrial, solar and galactic magnetic fields leading to confused homogeneous rain with no apparent source imprint. We are blind within such a smooth *CR* rain. No source, no astronomy *"at sight"*. In some sense the existence of large scale galactic magnetic fields smearing *CR* is testimony of the cosmic magnetic monopole absence, the celebrated *Parker's bound* on galactic magnetic monopoles.

To be more accurate, at sea level we feel only a part of such smooth *CR* secondaries, traces made by scattering fragments of nucleons-nuclei raining from the high atmosphere: muons, gammas and electron pairs, as well as secondary neutrinos, for this reason called *atmospheric neutrinos*. These are the neutrino noises that hide a more rare underline neutrino astronomy. The most powerful *CR*, $TeVs$–$PeVs$–$EeVs$–$ZeVs$, are observed at sea level by their catastrophic pair-production chain, leading to a tree-like air-shower whose top vertex is the primary *CR* event and whose late ramification are the million or thousand of billion secondaries pairs leptons (with only few hadrons).

To observe such *UHECR* there are both water Cherenkov array detector

(surface detectors in km^2 array) or Fluorescence Telescope array, tracking air-shower lightening in the dark nights, as in *AUGER*, *HIRES*, *TA* experiments. At $TeVs \div PeVs$ energies, *CR* air showering might blaze by Cherenkov flash for large optical telescope arrays such as Hess, Veritas, Magic or large scintillator and water arrays such as ARGO and Milagro as well as for ice and ICECUBE. These telescope experiments found in last decade a large number of $TeVs$ point sources partially coincident with γ $GeVs$ Fermi satellite signals; the array ones, ARGO and Milagro, and ICECUBE found a remarkable anisotropy in the $TeVs$ *CR* sky, with a tens degree window size, whose source is puzzling; we suggested an *UHECR* radioactive beamed imprint, mostly galactic, and its decay in flight as a possible source [21]. We also try to find here *UHECR* and *UHE*ν correlation as discussed and summarized in Fig 1.

Charged particles in *CR* at higher and higher energies may be accelerated on star flare, Supernova explosion shells, jets either in micro (as *GRBs*, *SGRs*) and/or in macro sites (as in AGN nuclei and Quasars) as well as in brightest Radio Galaxies or even more along additional candidate places [29]. We are all hunting for the *CR* sources nature since a century, with yet no definitive success. *UHECR* and *UHE*ν might point to them. Two main *UHE*ν models arose in last a few years proposing respectively a Galactic and an Extragalactic origination and defending the *UHECR* and *UHE*ν traces within different arguments. As a matter of fact, in last decade we all hoped to reveal soon their origination by their extreme component, the *UHECR*, hundred billions times more energetic than lower $GeV \div TeV$ *CR*, and possibly un-deflected.

The *UHECR* nucleons, while crossing in random walk our μ Gauss magnetic fields, have to fly within narrow angle $\delta_{rm-p} \simeq 2.5^\circ$. No such a clustered multiplet has been found (see Fig1) out of a remarkable exception of a triplet yet to be discussed. The *UHECR* following AUGER composition data might be light nuclei, He-like; in that case the incoherent random angle bending along the galactic plane and arms, crossing along the whole Galactic disk of 20 kpc, arriving in different alternating spiral arm fields and within a characteristic coherent length of 2 kpc, for He nuclei becomes $\delta_{rm-He} \simeq 16^\circ$ [21], well consistent with observed *UHECR Cen A* clustering, (see Fig. 1). On the contrary *UHECR* might be (at least partially, as AUGER showering signature did suggest) also heavy nuclei, as Fe, Ni,Co and so on, to explain by their bending, the extreme spread of few *UHECR* events along Vela, that is the nearest and

brightest Gamma pulsar in the sky, (see Fig. 1).

2 The one shoot Fireball failure versus *GRB* precessing jet

The *UHEν* signature was expected to be associated in time with several *GRB*, sources or with *BL Lac* flaring sources; other candidate proposed were the Star-Burst galaxy and the Radio Galaxies. The most popular Fire-ball model of *GRB* one huge shoot event, with or without a fountain jet, has been disproved. It should be noted that if *GRB* are not one shoot event but a long life jet [9)] decaying in power law of hours-day scale time $I \simeq I_o \left(\frac{t}{10^4\,\mathrm{s}}\right)^{-1}$, than its precessing blazing time for their neutrinos should not longer be correlated with the short gamma-X blazing time (constraint, the latter, assumed of second-minute in Fireball model times).

Indeed, in precessing *GRBs* Jet model it has been assumed since long ago a wider time scale to embrace also the otherwise mysterious *GRBs* precursors, as well as *SGRs* and statistical Jet solid angle [9) 11)]. These observed precursor may be both gamma and neutrino events; such precursor neutrinos are indeed observed in a few *GRB* events: a 109 TeV neutrino, within 0.2° of GRB091230A, with a localization uncertainty of 0.2°, and with detection time 14 hours before the gamma trigger; a 1.3 TeV neutrino 1.9° off GRB090417B, with localization uncertainty of 1.6°, and detection time 2249 seconds before the trigger; a 3.3 TeV neutrino 6.1° off GRB090219, with a localization uncertainty of 6.1°, and detection time 3594 seconds before the trigger.

These three observed *GRB*-neutrino precursor neutrino event, unexplained in fireball one-shoot model, may be a few percent of all the *UHEν* events in ICECUBE. Additional *GRBs* might be at higher redshift and they may be part of the ICECUBE *UHEν* sources if one enlarge the *GRB*-neutrino time windows; however also AGN jet and local galactic *UHEν* may play a role. As we shall show a few correlated *UHEν* and *UHECR* may be present inside galactic plane as well as few smeared clustering in tens *TeV* γ *CR* anisotropy and spread multiplet in tens *EeV* *UHECR* around Cen-A may trace the *UHECR* astronomy, see details in Fig. 1. It should be noted that if *UHE* neutrino will cluster in a spread tail group of events one might advocate either *UHECR* scattering along galactic gas (as for the Fermi bubble traced by its observed γ fountain), or one may suggest the radioactive (light and heavy) *UHECR* decay in flight, offering a possible correlation to *UHECR* $10^{18} \div 10^{20}$ eV clustering and the large scale

Milagro-Argo-ICECUBE TeVs-PeVs γ anisotropy [20) 21)].

3 The *UHE* neutrino flavor metamorphosis

Let us remind that neutrino are neutral and always un-deflected; (to be more precise, in cosmology for neutrinos with mass in expanding universe, once they became non relativistic neutrinos they might be bent by gravity too; this effect may play a minor role in largest scale dark matter density growth and large scale formation). Therefore the $UHE\nu$ may offer a new Astronomy. However, as we mentioned, at low (less than tens TeV) energies, neutrinos are polluted by abundant (CRs fragments) smeared atmospheric neutrino noise that hides any underlying astrophysical neutrino point-source. Let us remind that atmospheric GeV neutrinos while being mostly born at a ratio $(\nu_e : \nu_\mu : \nu_\tau = 1 : 2 : 0)$ by proton-proton scattering interactions chain in atmosphere, once at hundred $GeV \div TeVs$, they become ruled, at sea level, by muons neutrinos $(\nu_e : \nu_\mu : \nu_\tau \simeq 0.1 : 1 : 0)$; this occurs because the relativistic pion (and Kaon) still decay, feeding muons and anti-muons neutrinos while their muon decay, the main road to electron flavor birth, is inhibited by a longer muon lifetime. Therefore, electron (and rarest charmed born tau flavor) presence at hundred $GeV \div TeVs$ are rare (less than 10%); most signals (at hundred $GeV \div TeVs$) are muon neutrino tracks as observed by inner ICECUBE experiment, the Deep Core, in the last years.

Here we don't discuss the atmospheric muon neutrino conversion and partial suppression by flavor mixing that is tuned at GeV energies and led to the neutrino Pontecorvo Maki Nakagawa Sakata mixing matrix in last two decades. To consider the flavor mixing and possible experiment along the Earth see [23)]. However at higher energies (above tens $TeV \div PeV$) the extraterrestrial signals might (and indeed do) overcome the softer atmospheric neutrino noise (mainly because the astrophysical hardest spectra). In fact those extraterrestrial signals, while being expected to be born in general by $p + p$ or $p + \gamma$ in flux ratio $(\nu_e : \nu_\mu : \nu_\tau \simeq 1 : 2 : 0)$, because of the mixing and because of the large galactic distances may oscillate and converted into electron and tau neutrino flavor component. The outcome in a first approximation leads to a final equipartition flavor flux: $(\nu_e : \nu_\mu : \nu_\tau = 1 : 1 : 1)$, because of the complete flavor de-coherence mixing in flight. These ruling shower signals have been observed by last 3 years ICECUBEvevent data. The dominant ν_e and ν_τ interaction are mainly elec-

tromagnetic leading to Cherenkov spherical shower in ice. These majority of spherical shower events (28) are four times more abundant than muon tracks (7). This may sound contradictory keeping in mind that a third of these 35 events should be atmospheric muon or neutrino noise [18] (in principle all of them noise signals should mainly show up as muons, too many respect the 7 observed ones); however because a very different detector flavor acceptance it maybe still (barely) consistent with $(\nu_e : \nu_\mu : \nu_\tau = 1 : 1 : 1)$ [26] [6], once considering also the Neutral Current contribute.

Therefore the best hope and probe of a new $UHE\nu$ astronomy is the recent neutrino sudden flavor change at tens $TeV \div PeVs$ energy [6], but all showering cascades are smeared in their arrival direction ($\pm 15^\circ$) and they are making inconclusive any map correlation. Then a more directional astronomy is needed, as the one made by muon tracks. Additional such signals are able to open an $UHE\nu$ astronomy: they are in-written into few tens TeV energy (crossing in ICECUBE) muons at horizons [24]. The first estimate of nearly 40 of such events offer hope for soon novel astronomy. Unfortunately the recent published ($TeV \div PeVs$) – not only those above tens of $TeV \div PeVs$ – muon crossing inside the ICECUBE were painting a puzzling random map, not favoring any known or expected γ X source [18].

A more restrictive filtering of those events (muon crossing above few tens TeV) may be more telling for extraterrestrial nature, but such a selection has not been done yet [24]. We must remind that an anti-neutrino electron $\bar{\nu_e} + e$ peak resonance may tag and reveal a different neutrino sky volume. Indeed the Glashow resonance peak may rise by $\bar{\nu_e} + e \to W^-$ at $E_{\bar{\nu_e}} = 6.3$ PeV [27], but this has not been observed (yet), while observing 2 PeV cascade shower. This is suggesting either a sudden softening in the PeV neutrino spectra [6] or a smooth interchange (around ten TeV energy) between a soft power-law in atmospheric neutrino with a harder extraterrestrial neutrino power-law within a fine-tuned parameters (apt to avoid the expected Glashow signal as well as its ideal τ double bang signature) [28]. The powerful ν_τ discover via its first bang inside a rock (mountain or Earth) and its consequent τ escape outside in air, decaying in an amplified τ airshower, is a very promising adjoint neutrino astronomy at highest energy range $PeVs \div EeV$, first foreseen more than 15 years ago [12] and today widely searched in different large experimental array [4] [3] [1] (the so called "Earth skimming neutrinos" [13] that were more properly earlier named

as "Horizontal Upward Tau Airshower" [12]).

4 The *UHECR* fly undeflected: an *UHECR* Astronomy?

We expected that *UHECR* might flight straight because of their energetic rigidity, at best for *UHECR* proton. They survive the Lorentz bending and smoothing occurring for lower (up to EeV) *CR*. Such *UHECR*, well above EeV, are extremely rare, but their interaction at high altitude in atmosphere makes their explosive pair-production tree air-shower along their fall, proliferous and amplified into extended wide area (tens km square size). Their detection may be tested by wide spread km distance array, each detector even of minor volume (few square meter swimming-pool for Cherenkov detection) on the ground. Such experiments like Flys' Eye, AGASA, Hires, Auger and TA were located in last two decades over hundreds or several thousands km square area. These *UHECR* (if nucleon or even nuclei) might exhibit a cut off (within nearly 2% of cosmic radius) because of the "Cosmic Black Body Radiation" opacity, mostly by $p + \gamma \rightarrow \Delta \rightarrow \pi +$ nucleon interaction, the so-called photon-pion GZK cut off [30]. Their consequent GZK neutrinos (at EeV energies) are not observed yet and cannot feed the mentioned ICECUBE events. A more severe distance cut occur to *UHECR* nuclei propagation because of their fragility by photon-nuclei dissociation; moreover light and heavy nuclei are partially or totally bent while crossing the galaxy. Therefore their maps might trace only nearby local Universe well within $1 - 2\%$ percent of cosmic size. To escape the near Universe size (GZK size bounded, in case of *UHECR* clustering at far extragalactic edges) one may consider the *UHE* neutrinos at ZeV hitting the relic cosmic ones via Z-resonance (in analogy to Glashow W resonance) [10]: the Z *UHE* decay into nucleons or anti-nucleons might be the final trace explaining *UHECR* correlation well above GZK bounded universe; this proposal found much interest and it will be actual if *UHECR* are correlated with guaranteed AGN above GZK distances. *UHECR* neutron are also expected but well confined within one Mpc ($E_n \simeq 10^{20}$ eV) size while *UHE* photons ($E_\gamma \simeq 10^{18} \div 10^{20}$ eV) are bounded within a few tens Mpc. No such *UHECR* neutron or photon source or clustering has been found (yet). *UHE* neutrino might test most of the far and secret Universe edges, but they may observe also nearby galactic sources. The simplest solution of *UHECR* (nearby Local Super-galactic plane) and of *UHE* neutrino (expected to be traces of *GRBs*) have been in a very recent years

fallen away. New galactic and extragalactic candidate source have been considered, somehow with much dispute and disagreement in the scientific arena. Therefore *UHECR* either nucleon or nuclei must arise in a small (tens Mpc) or even narrow (few Mpc) Universe, possibly in sharp astronomy (for proton) or in a smeared clustering map (for light nuclei or nearest galactic heavy nuclei). The last AUGER maps showed only marginal smeared clustering and a rarest remarkable triplet [31]. see Fig. 1. As we will show elsewhere

5 Conclusions

The difficult puzzle of *UHECR* astronomy and the *UHE* neutrino maps may soon be matched by cooperative test and overlapping. There are often unexplainable delay (three years) in *UHECR* (AUGER) data release. Nevertheless the sources as nearest AGN Cen A, rise as a remarkable smeared clustering of *UHECR* events in AUGER ($E_{UHECR} > 6 \cdot 10^{19}$ eV as well in rare overlapping tens *EeV* long chain events foreseen [20], and observed [2] [21]; they may be well understood if they are mostly made by He nuclei and its fragments. The nearest brightest γ pulsar Vela is also suspected to be correlated with a train of *UHECR* events (mostly if heavy Ni, Co nuclei, possibly radioactive ones), and a doublet of ICECUBE neutrinos (see Fig. 1, event n. 3 (a muon) and n.6 (a shower) in ICECUBE [17]) as well as a remarkable *TeVs* ICECUBE *CR* anisotropy [21]; Cen-X3 and Cygnus region is also rising in ARGO *TeVs* anisotropy [21] and in a very rich (7) recent *UHECR* multiplet clustering containing also new TA and old Hires events: they are a remarkable clustering showing a nearby source connection. The most surprising narrow triplet is grown over a recent rarest (highest energy) doublet [31], by an additional third event (by last TA *UHECR* data); other triplet and quadruplet point to unknown sources not far from galactic plane; they are possibly showing a cooperative galactic and extragalactic source role; we offered here a first attempt in this difficult map understanding (see Fig. 1). We believe that with care and with needed time we are going to disentangle (within the fog of such noisy high energy sky) the first sources shining from our near and far Universe; we believe that most UHECR are related to precessing jet beaming, galactic and extragalactic in tuned and equatable ratio (see also [25]), and *UHECR* as well as *UHE*ν are not commonly found along any contemporaneous γ explosive or flaring event (GRB,AGN), because of a different timing of the jet blazing beam

inner cones. The hardest *UHEν* jet might be found in most distant *GRB* and AGN blazing whose timing may be often pre-cursed (or rarely delayed) respect gamma flaring or burst. On the contrary *UHECR* are mostly galactic and in nearest Universe. Few sources (UHECR-UHEν) overlap within nearest Milky Way sources or within rarest AGN candidate. The dramatic absence of Virgo cluster both on AUGER and TA map maybe solved by lightest nuclei opacity above few Mpc flight. Lightest UHECR nuclei are still offering a first smeared novel astronomy that we tried to disentangle here.

6 In memory

This article is devoted to Daniele Habib greatest linguist and translator, who disappeared in these days half a century ago.

References

1. Y. Aita et al. ApJ 736 L12,(2011);
2. Auger Coll., 32ND INT.COSMIC RAY CONF., BEIJING,p-9-13. 2011
3. Auger Coll. Advances in High Energy Physics, vol. 2013, Article ID 708680
4. X. Bertou et.all Astropart. Phys., 17,183,(2002);
5. Courier, 31 May 2012, (http://cerncourier.com/cws/article/cern/49675)
6. D.Fargion,P.Paggi; Nuclear Inst. and Methods in Physics Research, A 753C (2014), pp. 9-13.
7. ICECUBE Collab. Arxiv:1311.6519, Science, v.342, Nov. 2013.
8. Enberg R., Reno M.H., Sarcevic I.Phys. Rev. D 78, 043005 (2008);
9. D.Fargion, Astron.Astrophys.Suppl.Ser.138:507-508,1999;
10. D.Fargion, B. Mele, A. Salis, ApJ, 517:725 733, 1999;
11. D.Fargion, Memorie della Societa Astronomica Italiana Vol. 83 n. 1, 2012, 312-318. D.Fargion, M.Grossi,Nuovo Cim.C28:809-812,2005; Chin.J.Astron.Astrophys. 6S1 (2006) 342-348;

12. D.Fargion,et al.26th ICRC,He 6.1.09,p.396-398(1999). D.Fargion , ApJ, 570, 909,(2002); D. Fargion , et all. ApJ, 613, 1285, (2004);

13. J. L. Feng1,et al.Phys. Rev. Lett. 88, 161102 (2002);

14. Gaisser T.K.,Honda M. Ann.Rev.Nucl.Part.Sci.52:153-199,(2002)

15. Gora14)Gora D. et all., 10.1016/j.astropartphys.2014.06.005, (2014); D. Fargion et al. Journal of Physics: Conf. Series,110,6, (2008); NIMA, p. 146-150.10.1016/j.nima.2008.01.028 (2008)

16. Hill G., ICECUBE Coll., Neutrino 2014,Boston, June 2nd, (2014)

17. ICECUBE Collaboration, arXiv:1405.5303

18. ICECUBE Collaboration, arXiv:1406.6757

19. C.Kopper, ICECUBE coll;Rencontres de Moriond EW (2014);

20. D.Fargion, Progress in Particle and Nuclear Physics 64,363-365,(2010):

21. D.Fargion, Nuclear Inst. and Methods in Physics Research, A (2012), pp. 174-179

22. D.Fargion, D.D'Armiento,J. Phys. G: Nucl. Part. Phys. 39 (2012)

23. D.Fargion et al.ApJ. Volume 758 Number 1, 758, 3 (2012);

24. D.Fargion, arXiv:1404.5914;

25. P. Padovani,, E. Resconi,arXiv:1406.0376

26. F. Vissani, G. Pagliaroli, F. L. Villante, arXiv:1306.0211 , (2013)

27. S.L. Glashow, Phys. Rev. **118**, 316 (1960).

28. J. Learned, S. Pakvasa, **ApJ** 32671995.

29. P. Mszros;(2014) arXiv:1407.5671.

30. Greisen, K. Physical Review Letters 16 (17): 748,750, (1966); Zatsepin, G.T, Kuz'min, V.A.*Zh. Eks. Teor. Fiz., Pis'ma Red.***4** *(1966)144*

31. S.V. Troizky, Pis'ma v ZhETF, vol. 96, iss. 1, pp. 14,17; (2012)

32. Ke Fang et all. arXiv:1404.6237

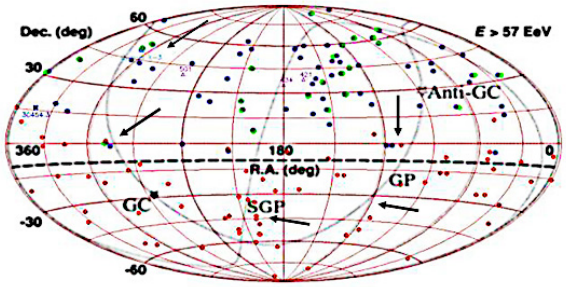

Figure 1: *The UHECR map in equatorial coordinate following AUGER detector (South) and TA (in North)* [32]. *There are few clustering tagged by five arrows: the most left and north one point toward a TA-Hires multiplet along Cen-3X, one of the location of gamma anisotropy at TeV by Milagro-Argo detectors; the next arrow point toward the remarkable UHECR made by highest doublet (TA-AUGER) UHECR found recently* [31] *where a new third UHECR has been just found this year by TA; the probability to occur such an event is well below* 10^{-4} *; a third arrow on the center-right side point on to a clustering along a nearest AGN, Cen-a not far from the largest energetic 2 PeV event number n.*35 *in ICECUBE over a doublet around the Cen A cluster, where an additional twin overlapping multi-plet occurs at* 20 *EeV energy see* [2]*; the fourth arrow point to the nearest and brightest Gamma Pulsar, Vela, related to an aligned AUGER triplet event; the fifth arrow point to a doublet by TA and a singlet by AUGER, an additional single by Hires UHECR events nearby a well collimated UHE neutrino muon found by ICECUBE event n.*5*; all these five region are candidate of UHECR and possibly UHE neutrino sources, mostly galactic.*

Frascati Physics Series Vol. 58 (2014)
Frontier Objects in Astrophysics and Particle Physics
May 18-24, 2014

ARE COSMIC RAYS STILL A VALUABLE PROBE OF LORENTZ INVARIANCE VIOLATIONS IN THE AUGER ERA?

Roberto Aloisio
INAF Arcetri,Firenze, Italy and Gran Sasso Science Institute (INFN), L'Aquila, Italy
Denise Boncioli, Aurelio F. Grillo
INFN Laboratori Nazionali del Gran Sasso, Assergi , Italy
Piera L. Ghia
CNRS/IN2P3 - LPNHE Paris
Armando di Matteo,
INFN and Physics Department, Università di L'Aquila, L'Aquila, Italy
Sergio Petrera
Physics Department, Università di L'Aquila, INFN and Gran Sasso Science Institute, L'Aquila, Italy
Francesco Salamida
CNRS/IN2P3 - IPN Orsay

Abstract

Relativistic Invariance might be modified by Quantum Gravity effects. The interesting point which emerged in the last fifteen years is that remnants of possible Lorentz Invariance Violations could be present at energies much lower than their natural scale, and possibly affect Ultra High Energy Cosmic Rays phenomena. We discuss their status in the view of recent data from the Pierre Auger Observatory.

1 Introduction

Relativistic Invariance is the fundamental space-time symmetry. If General Relativity and Quantum Mechanics can be reconciled, space-time could be subject to quantum fluctuations and the Lorentz Invariant space-time could emerge as a semiclassical limit of Quantum Gravity (QG). Lorentz Invariance

Violations (LIV) can therefore be possible. Although these effects may only be very small, it has been shown in the last two decades that measurable effects can be present even at energies much lower than the Quantum Gravity scale. In particular possible LIV effects could show themselves in Ultra High Energy Cosmic Rays (UHECR) phenomena.
The possibility of putting extremely strong limits on, at least some, LIV parameters from UHECRs detection was firstly quantitatively discussed in [1] and later on refined in many ways. Consequently, as soon as the evidence of the suppression in the spectrum of UHECRs around $5 \cdot 10^{19}\ eV$ became undisputable, based on results from HiRes [2] and Auger [3], limits on those violating parameter were derived. A discussion and references can be found in [4].
Here we discuss the status of these bounds in the light of recent interpretation of measurements by the Pierre Auger Observatory [5] (see e.g. Aloisio 2013 [6]) for which the observed suppression in the spectrum might be due to the maximum cosmic ray acceleration energy at the sources rather than to an effect of their propagation in extra-galactic space.

2 Lorentz Invariance Violations: effects on UHECR propagation

The aim of this paper is purely phenomenological and a general discussion of LI violating terms that can affect UHECR physics is out of its scope [4] [7]. To parametrize departures from relativistic invariance we follow here the approach of [1], which amounts to assuming that the relation, connecting the energy and momentum of a particle (dispersion relation), is modified as:

$$E_i^2 - p_i^2 = m_i^2 \Rightarrow \mu_i(E, p, m_P) \approx m_i^2 + \frac{f_i}{m_P^n} E_i^{2+n} \tag{1}$$

where $p = |\overrightarrow{p}|$, μ is an arbitrary function of momenta and energy, $m_P \approx 2 \cdot 10^{28}\ eV$ is the possible scale where QG effects become important and f_i, which can have both signs, parametrizes the strength of LIV for particle i. The last equality reflects the fact that LI is an exceedingly good approximation of the physics we know, so that modifications are expected to be quite small, making an expansion of the LIV dispersion relation in terms of $1/m_P$ appropriate. In practical terms, only $n = 1, 2$ will be relevant [1].
The right hand side of eq.1 is invariant when $f = 0$. We will assume normal conservation of energy and momentum. Finally we assume that, in nuclei, LIV

only affects nucleons: this implies that, for a nucleus of atomic number A, effectively $m_p \to Am_P$. From eq.1 it is clear that the correction term is always much smaller than both (E^2, p^2) even for $E \approx 10^{20}\ eV$. However, as soon as[1] $p \geq (m_i^2 m_P^n/|f_i|)^{1/(2+n)}$ the correction becomes larger than the mass of the particle, and this can lead to very important effects [1)]. We consider here how LIV affects the threshold energy for the Greisen [8)], Zatsepin, Kuzmin [9)] process $p\gamma_{bkg} \to (p,n)\pi$, where γ_{bkg} is a photon of Cosmic Microwave Background or Infrared radiation. The threshold for this process, in a LIV world, is modified:

$$E_{GZK} \approx \frac{m_p m_\pi}{2\omega_\gamma} \Rightarrow E_{GZK} \approx \frac{\mu(E_p, p_p, m_p, m_P)\mu(E_\pi, p_\pi, m_\pi, m_P)}{2\omega_\gamma} \qquad (2)$$

(ω_γ being the energy of the background photon). The last equation has to be solved for $E_p = E_{GZK}$. For our simplified treatement, we will assume that f_i are the same for all the hadrons.

The most interesting case is for $f \leq 0$. As soon as f moves from zero towards negative values the threshold energy at first slightly increases, but for $f < -2.5 \cdot 10^{-14}$ $(n = 1)$ $[f < -3 \cdot 10^{-6}$ $(n = 2)]$, eq.2 has no longer real solutions [1)]: the photo-pion production reaction is no longer kinematically allowed and protons propagate freely in the Universe.

For nuclei, for which the relevant process of interaction on the universal backgrounds is photo-disintegration, an equation corresponding to eq.2, with $m_P \to Am_P$, can be written. The modification of the thresholds is similar to that for protons.

Limits on LIV parameters derived from the observed steepening of the spectrum of UHECRs have been reported in literature [10) 11)].

These limits, however, depend crucially on the assumption that the observed flux suppression is originated by the propagation of UHECRs. Auger composition data combined with those on the all-particle spectrum might indicate a different scenario, as illustrated for example by Blasi [12)]. According to [12)] the two first moments of the distribution of X_{max}, the depth in atmosphere where the shower reaches its maximum development, may indicate that the flux suppression is due to the end of cosmic ray acceleration at the source, implying also a very hard injection spectrum, incompatible with Fermi acceleration mechanism. In this framework propagation would have little, if any, effects on

[1]Since at the leading LIV order $E \approx p$ we will use them without distinction.

experimental observables.
It is therefore worthwhile to verify if LIV can be still bound in this scenario.
To simulate LIVs we have propagated UHECRs switching off the interactions

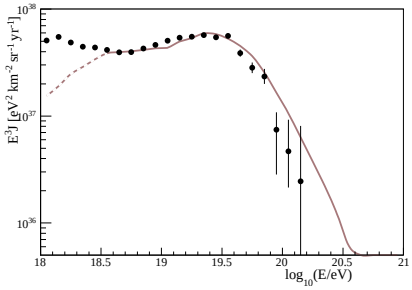

Figure 1: *The all particle flux compared with the LIV case in the text.*

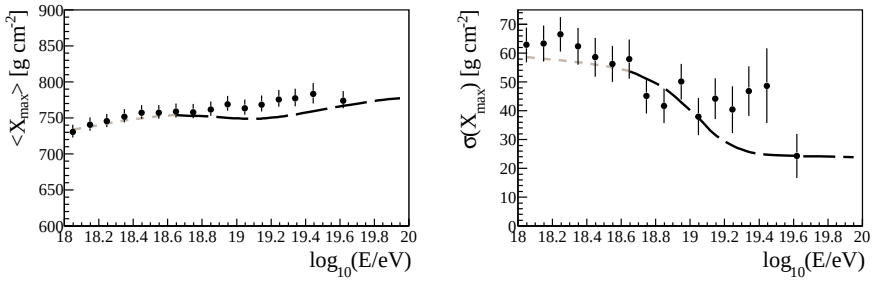

Figure 2: $\langle X_{max} \rangle$ *and its dispersion* $\sigma(X_{max})$ *as reconstructed from the LIV simulation described in this paper.*

with background photons, only accounting for energy losses due to the expansion of the Universe. To account for these losses we used a simplified version of SimProp [13], with maximum source rigidity $R_{max} = 5 \cdot 10^{18}$ V and fixed $\gamma = 2$, consistent with Fermi acceleration. The source model used is the minimal, "standard" one, *i.e.* equal sources, uniformily distributed in comoving volume throughout the whole Universe, without evolution effects, emitting all nuclei in a rigidity dependent way.
The simulation is consistent with LIV as soon as f is sufficiently negative so

that Eq. (2) has no real solution. The produced fluxes and composition qualitatively reproduce both Auger spectrum and composition behaviour as shown in fig.1 and fig.2.
This has an important consequence: the present data from the Pierre Auger observatory, interpreted in the simple framework above[2] do not allow to constrain LIV effects as parametrized by modified dispersion relations (eq.1,2).
It is however obvious that the above statement *cannot* be taken as evidence of LIV, since many other astrophysical/particle physics explanations can be considered. For instance the source model is too simple. On the other hand possible sources with hard spectrum have been proposed [12]. Moreover, changes in the hadronic cross sections above LHC energies cannot be excluded, and would modify UHECR interactions. Finally, for completeness, we note that the Telescope Array Collaboration has reported indications of a proton-dominated cosmic ray composition [14]. With the current statistics, Telescope Array data cannot discriminate between the proton and Auger-like composition [15]. A proton composition would invalidate the conclusion that data are compatible with LIV, if the reported spectrum suppression is due to propagation.

3 Lorentz Invariance Violations: other effects on UHECR Physics

In principle, *all* aspects of UHECR physics can be modified by LIV.
For instance, LIV can affect the cosmic ray acceleration processes, and also the energy losses during acceleration. Since in the example of LIV propagation in the above section we considered $\gamma = 2$, we can assume standard Fermi acceleration.
With respect to acceleration itself changes might be possible since (at UHE) $E \neq p$ due to LIV. However we already commented that this modification is very small and only relevant near the QG scale. Moreover, even in the case of relativistic shocks the Lorentz factor of the shock is much smaller than that of the accelerated particles, and therefore LIV effects on the shock itself are not expected.
For (synchrotron) energy losses at the source there might be a more important

[2]Note however that this framework, as also indicated for instance in [6] can only fit the data above $4 \cdot 10^{18} eV$ and a different component is needed at lower energies.

effect because, since ($f_i < 0$) the group velocity of nuclei reaches a maximum value $< c$, the Lorentz factor of, say, a proton is bounded and the energy lost in photons is limited [16]. This point will be discussed in a forthcoming paper. More important effects are expected in the interactions of UHE particles in the atmosphere and in the decay of secondary particles. These effects can make some parts of the kinematical space unallowed for the processes and therefore make some reaction impossible. With respect to the modification of the thresholds discussed in the previous Section, an important difference is that these processes might be affected by (unknown) LIV dynamics. However, since we are interested in *conservative* bounds, we do not consider this problem here. In the next two subsections we will discuss, in a unified kinematical approach, the effects on particle decays, hence atmospheric showering, and interactions of nuclei in the atmosphere.

3.1 LIV effects on particle decays and showering

Consider the most important decay for atmospheric showering, $\pi^0 \to \gamma\gamma$. We construct, both for the initial particle and the final state, the quantity $s = (\sum p_i^\mu)^2$. When $f = 0$ (LI) s is an invariant and can be computed in any reference frame; if $f \neq 0$ (LIV) this is not the case but energy-momentum conservation implies that this quantity should be equal between initial and final states, if computed in the same reference frame. Now the crucial point is that, with $f < 0$ there is no guarantee that this quantity is still positive. For the above decay, from the equality $s_{ini} = s_{fin}$ we obtain:

$$m_\pi^2 + \frac{1}{m_P^n}(f_\pi E_\pi^{2+n} - f_\gamma(E_{\gamma_1}^{2+n} + E_{\gamma_2}^{2+n})) - 2(E_{\gamma_1}E_{\gamma_2} - p_{\gamma_1}p_{\gamma_2}) = 2p_{\gamma_1}p_{\gamma_2}(1-\cos\theta_{1,2}) \tag{3}$$

Since there are very strong limits [17] on f_γ we will assume it to be zero. The right hand side of eq.3 is non negative, while the left hand one can become negative for large enough E_π. Therefore neutral pions do not decay if $E_\pi > (m_P^n m_\pi^2/|f_\pi|)^{\frac{1}{2+n}}$. To test this effect we have generated 100000 atmospheric showers with CONEX [18] imposing the same condition for all particle decays. The results of this simulation are presented in figs.3,4. In particular, in fig.3 the air shower longitudinal development, in the case of standard LI development (for protons and iron primaries), is compared to the LIV case for different masses. Since the energy of the pions is related to the energy per

nucleon of the incident nucleus, the LIV threshold moves to higher energies for heavier nuclei.
In fig.4, left panel, the expectation for $\langle X_{max} \rangle$ vs energy for LI shower development (solid lines) and LIV case (dashed lines) is reported, while the right panel presents the average number of muons vs primary energy in LI and LIV cases. This number has been normalized to the average number of muons in standard LI proton showers to better show the effect of LIV.
The suppression of the (neutral) pion decays makes these particles interact, thus increasing the amount of muons in the extensive air shower. Moreover the position of the shower maximum moves to higher altitudes as the electromagnetic part of the shower consumes faster. From the observational point of view this makes nuclei (and protons) primaries looking heavier than they are in reality. These changes in the shower development will also affect the results reported in the previous section, since the knowledge of the shower developement is a necessary ingredient to perform the comparison with experimental data. Detailed study is underway and will be presented in a further publication.

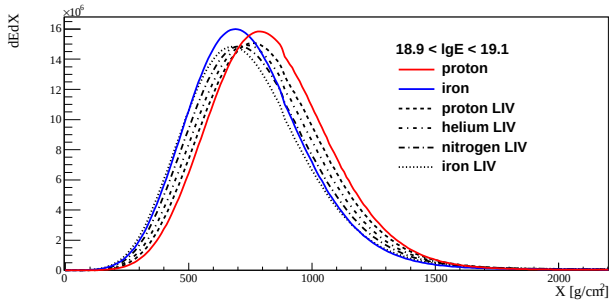

Figure 3: *Extensive Air Shower longitudinal development simulated with CONEX. Red and blue solid line represents the case of standard LI shower development respectively for protons and iron primaries. The dashed lines represent the LIV cases for different masses.*

3.2 LIV effects on interactions

The interactions of UHECR nuclei can also be affected by LIV. To discuss these effects, we follow here the same approach of the previous subsection, and

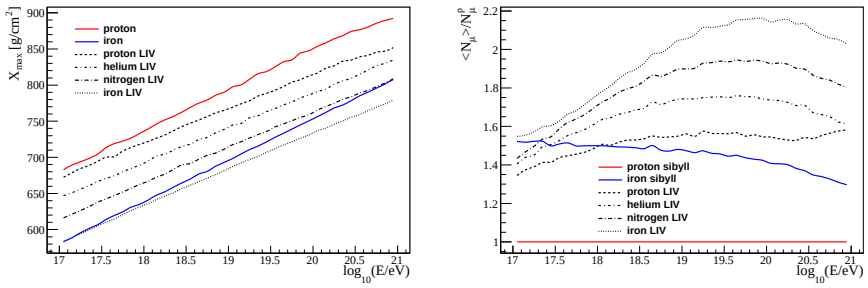

Figure 4: *Left panel: Expectation for* $\langle X_{max} \rangle$ *vs energy for LI shower development (solid lines) and LIV case (dashed lines). The LIV effect at the highest energies is to make shower appear heavier than they are in reality. Right panel: Average number of muons vs primary energy in LI and LIV cases. This number has been normalized to the average amount of muons in standard LI proton showers to better show the effect of LIV.*

consider for instance the reaction $p_{CR}p_{air} \to p_1 p_2 + n_\pi \pi$.

$$\begin{aligned} s_{ini} &= (p^\mu_{CR} + p_{Air})^2 = 2m^2 + 2(p^\mu_{CR} p^\mu_{Air}) + \frac{f}{m_p} E^3 \\ &\approx 2m^2 + 2E_{CR} m + \frac{f}{m_p} E^3_{CR} \end{aligned} \tag{4}$$

having neglected LIV for the nucleons of the atmospheric nuclei. If $f < 0$ and $E_{CR} > \sqrt{2m(m + m_P)/(-f)} \approx 5 \cdot 10^{18}\ eV\ (f = -1)$ then $s_{ini} < 0$.
Of course there can be cancellations, since also in the right of the reaction there will be (negative) LIV terms. However, given the energy dependence of the LIV term, an exact cancellation is only possible in the elastic case ($n_\pi = 0$) and if the CR proton does not lose energy.
The equality $s_{ini} = s_{fin}$ implies, in the case $n_\pi = 0$ taken as an example:

$$2mE_{CR} + \frac{f}{m_p}(E^3_{CR} - E^3_1 - E^3_2) - 2(E_1 E_2 - p_1 p_2) = 2(p_1 p_2 (1 - \cos\theta_{12})) \tag{5}$$

Again the right hand side of eq.5 is non negative by construction. On the other hand, if $f < 0$ the left hand side can be negative for large enough E_{CR}. Numerically one finds that as soon as $E_{CR} \geq 10^{19}\ eV,\ (f = -1)$, the left hand side becomes negative apart in a very small kinematical region so that the reaction is not allowed. This means for instance that if we clearly detect

at ground (the interaction of) a proton with primary energy of $E = 10^{20}\ eV$ we can set a limit for $f \geq -5 \cdot 10^{-3}$.
These effects will also affect the shower developement. As above, only detailed simulation can describe the overall effect.

4 Conclusions

In this note we have presented a discussion on the status of bounds on Lorentz Invariance Violations parameters at the light of most recent spectrum and composition data from the Pierre Auger Observatory [3, 5]. If the data are interpreted as indicating that the spectrum of UHECRs is limited at the sources [6], it turns out that the very strong limits that were previously derived [10, 11], from the presence of the GZK flux suppression, do not apply any longer. This does not affect other limits, derived from the mere existence of UHECRs [19]. Clearly this fact cannot be interpreted as evidence for LIV since there are possible astrophysical/particle physics explanations of the data.
We have then analyzed other aspects of UHECR physics that can be affected by LIV, in particular effects on interaction on the atmosphere and shower developement: LI violating interactions and decay can induce modifications of the normal physics which dictates the production of secondary particles that are detected in UHECRs experiments. The effects of these modifications are in principle detectable (and falsifiable) in an experiment like the Pierre Auger Observatory: in order to understand if this can be done effectively, however, detailed simulations are needed and are under way.

5 Acknowledgements

We would like to acknowledge many useful discussions with our colleagues of the Pierre Auger Collaboration. We also thank G. Amelino-Camelia, S.Liberati and F.Mendez for discussions in an early part of this work, and T. Pierog for help in modifying CONEX.

References

1. R. Aloisio, P. Blasi, P. L. Ghia, A. F.Grillo, Phys.Rev. **D62** 053010 (2000) and references therein

2. The HiRes Collaboration, Nuc. Phys. B (Proc. Suppl.) **212-213** 74-78 (2011)

3. The Pierre Auger collaboration, Physics Letters **B 685** 239-246 (2010)

4. S. Liberati, arXiv:1304.5795 and references therein

5. The Pierre Auger Collaboration, Physical Review Letters **104** 091101 (2010); an update has been presented at ICRC 2013, arXiv:1307.5059

6. R. Alosio, P. Blasi, V. Berezinsky, arXiv:1312.7459

7. A. Kostlecky and N. Russel, arXiv:0801.0287v7

8. K. Greisen, Phys. Rev. Lett. **16** 748 (1966)

9. G.T. Zatsepin, V.A. Kuzmin, Pisma Zh. Eksp. Teor. Fiz. **4** 114 (1966)

10. T. Jacobson, S. Liberati, D. Mattingly Annals Phys. **321** 150-196 (2006)

11. A. Saveliev, L. Maccione, G. Sigl JCAP **1103** 046 (2011)

12. P. Blasi, arXiv:1403.2967

13. R. Aloisio et al., JCAP **1210** 007 (2012), arXiv:1204.2970

14. Telescope Array Collaboration, Nuclear Instruments and Methods in Physics Research, Section A, **742** 29-34 (2014)

15. W. Hanlon for the Pierre Auger and Telescope Array Collaborations, Proc. of 33rd Int. Cosmic Ray Conf., Rio de Janeiro, Brazil, arXiv:1310.0647

16. T. Jacobson, S. Liberati, D. Mattingly, Nature **424** 1019-1021 (2003)

17. see e.g. : H.Vankov, T.Stanev, Phys. Lett. **B 538** 251-256 (2002)

18. T. Bergmann, et al. Astropart. Phys.**26** 420-432 (2007)

19. F.R. Klinkhamer and M.Risse, Phys.Rev.**D77** 016002 (2008)

Frascati Physics Series Vol. 58 (2014)
Frontier Objects in Astrophysics and Particle Physics
May 18-24, 2014

High-energy Gamma Rays detection with the AMS-02 electromagnetic calorimeter

F. Pilo for the AMS-02 ECAL Group
INFN Sezione di Pisa, Italy

Abstract

The AMS-02 experiment, operating on the International Space Station since May 2011, is designed for a 10-20 years long mission, studying the fluxes of different cosmic ray components in the high energy range 1-2000 GeV. Identification of electrons, positrons and photons is provided by the Electromagnetic Calorimeter (ECAL), a fine-grained lead-scintillating fibre sampling calorimeter that provides an excellent reconstruction of the electromagnetic shower energy as well as a precise three-dimensional imaging of the longitudinal and lateral shower development.

Thanks to the 3D shower reconstruction capability, ECAL allows a stand-alone determination of the incoming particle direction, with unprecedented angular resolution. The AMS-02 sub-detectors located above the ECAL provide rejection of charged background. As a result, ECAL is able to identify high energy photons coming from galactic and extragalactic sources. The AMS-02 photon detection strategy will be discussed.

1 γ-rays dection in AMS-02

Detecting high energy γ-rays, one of the less abundant components of cosmic rays, is a primary task of the Alpha Magnetic Spectrometer (AMS-02). This general purpose detector operates continuously on the International Space Station (ISS) since May 2011 and aims to identify and measure the spectra of the cosmic rays components with so far unreached precision in the energy window from 1 GeV to a few TeV [1)]. The core of the experiment, the spectrometer, consists of a silicon tracker inside a permanent magnet determining the momentum of charged particles, and four planes of time of flight counters (TOF), measuring the particle velocity. The particle charge is redundantly measured by the tracker, the TOF and a ring imaging Cerenkov detector (RICH) below the magnet. A transition radiation detector (TRD), located on top of the detector, and an electromagnetic calorimeter (ECAL) at the bottom, complete the set of sub-detectors that together provide high capability of discriminating the hadronic component of cosmic rays from the electromagnetic one.

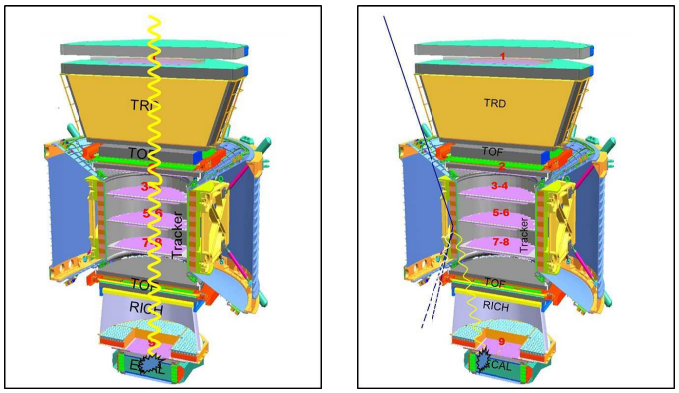

(a) (b)

Figure 1: *a) AMS-02 single photon detection mode. b) Example of background source: π^0 particles generated in interaction of primary protons with the AMS-02 material.*

Thanks to the versatile detector configuration, γ-rays can be identified

using two independent and mutually exclusive methods. In *conversion mode* gamma-rays are identified by tracking back the e^+e^- pairs generated in the gamma conversion happened somewhere in the material upstream of the magnet. In *single photon mode*, the photons are directly detected in the ECAL using all the other sub-detectors located above the calorimeter as a veto to suppress charged backgrounds (see figure 1b for an example of background event). Clearly with this second technique the calorimeter has a key role not only measuring the photon energy, but also determining the incoming particle direction, and generating the trigger for the whole experiment.

2 The electromagnetic calorimeter

The sensitive volume of the ECAL consists of a multilayer sandwich of lead foils and scintillating fibers with a square cross section of 648x648 mm^2 and a thickness of 166.5 mm corresponding to 17 radiation lengths [2]. The calorimeter is subdivided in nine superlayers, each 18.5 mm thick and made of 11 grooved, 1 mm thick lead foils interleaved with ten layers of 1 mm diameter scintillating fibers. In each superlayer, the fibers run in one direction only. The 3D imaging capability of the detector is obtained by stacking superlayers alternately with fibers parallel to the x and y axes (five and four superlayers, respectively). The fibers are coupled on one end to multi-anode photomultipliers arranged so that the size of the basic light collection area is 9x9 mm^2 giving the detector a very high read-out granularity.

The detector commissioning, with the test beam at CERN Super Proton Synchrotron (SPS) [3] and the following in-orbit checks, confirmed that the ECAL completely fulfills the design specifications. In particular, the detector shows a very good energy resolution, below 20% for energies above 50 GeV and a deviation from linearity smaller that 1% in the energy range between 8 and 180 GeV, with the major source of non-linearity being the rear energy leakage, an effect that is easily correctable up to the TeV (see Fig. 2b).

The angular resolution in the reconstruction of the particle incoming direction is measured in two independent ways: using both data from electron beams and electrons collected during the flight, comparing the direction reconstructed by the tracker with the one estimated by ECAL. In both cases the assumption that a shower initiated by an electron is compatible with a shower initiated by a photon in the ECAL has been verified and eventually corrected

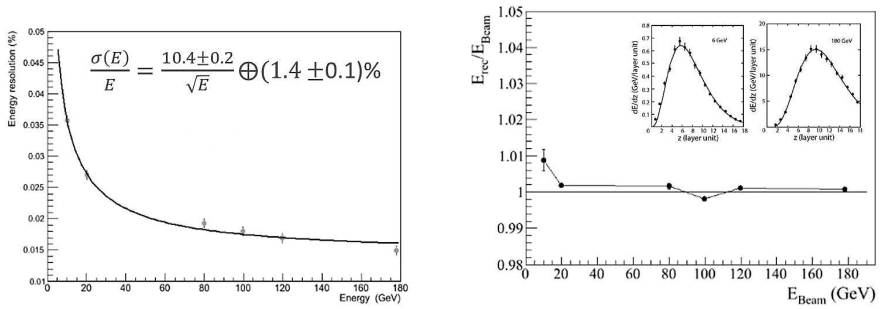

(a) (b)

Figure 2: *a) The ECAL energy resolution measured at test beam. b) The linearity of the detector response, better than 1% for energies up to 180 GeV.*

using the Monte Carlo experiment simulation. As pointing accuracy is a fundamental figure of merit in γ astrophysics, allowing to discriminate between point sources and diffuse emission, the unique 3D imaging capabilities of the ECAL have been deeply exploited in the development of the algorithms for direction reconstruction. In particular the best results were obtained measuring the position of the shower axis from the fit of the lateral development of the electromagnetic shower. Figure 3a shows the angular resolution defined by the three-dimensional angular opening with respect to the tracker track direction that contains 68% of the events, as a function of energy: it is better than 1° above 40 GeV and slightly improves with the inclination of the incoming particle.

Designing the ECAL stand-alone trigger [4], major efforts were spent to recover the efficiency down to the lowest possible energy while containing the acquisition rate and the power consumption. In particular the system has been designed to be almost 100% efficient on high energy deposits (above 10 GeV) and as highly efficient as possible at low energies; to produce a trigger rate below 100 Hz; to have low sensitivity to external conditions (temperature, solar activity ...) and high robustness, assuring good performances even in case of a broken PMTs (hot or dead) or of global gain fluctuations; to require a power consumption below 15 Watt and components weight below 5 kg. The basic idea to fulfill all these requirements is to build up a trigger with a granularity of 1 PMT (18x18 mm^2). The signals of the last dynode of the PMT's of

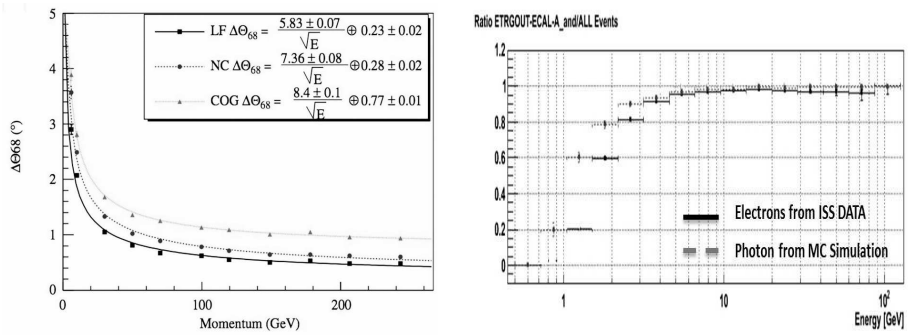

(a) (b)

Figure 3: *a) The ECAL 3D angular resolution according to different algorithms of shower axis position reconstruction: the best results are obtained using a parameterization of lateral shower development (LF). b) Standalone trigger efficiency measured on electrons and photons as a function of particle energy.*

the 6 central superlayers are sent as input to a set of comparators and the outputs combined to produce the first decision level of the trigger, i.e. the "fast trigger": usually for each view (x and y) at least 2 (out of 3) superlayers must have at least one photomultiplier above threshold. These thresholds, one for each superlayer, have been optimized using the AMS-02 Monte Carlo to obtain more than 90% efficiency on 2 GeV photons, enhancing the rejection of hadronic background with a longitudinal profile resembling the electromagnetic shower one. If the fast trigger request is satisfied, the incoming particle direction is roughly evaluated by taking, for each view, the average position of the fired PMTs: the angular distance of the barycenters of the 2 most distant superlayers is requested to be inside 20° in order to produce the final trigger decision, the "level 1" trigger. This reduces the trigger rate rejecting background particles entering the calorimeter from outside the ECAL field of view.

Data taking operations in space demonstrated that the ECAL stand alone trigger, thanks to its flexible configuration and reliable design, can easily accommodate the required performances. The transfer function of the comparators has been reconstructed from flight data showing the correct behavior with an effective applied threshold within a few percent with respect to the design value; only few channels got lost after the launch. To evaluate the trigger efficiency

we first use a highly pure electron sample triggered by the TOF and passing inside the detector field of view; then the results have been used to tune the Monte Carlo simulation and to finally estimate the efficiency on photons. This resulted to be completely in agreement with the expectations, being about 80% at 2 GeV and reaching 99% at 10 GeV (see figure 3b). For an average polar orbit the trigger rate is contained in about 120 Hz (approximately 10% of total AMS-02 rate).

3 Photon identification

The first step of the photon identification strategy consists in an event preselection requiring the presence of one shower in the ECAL, a reconstructed incoming direction inside the upper TOF plane active area, very low activity in the sub-detectors upstream the calorimeter. Among the remaining candidates the main background source consists of protons and electrons reaching ECAL from the lateral and the rear sides, generating a shower whose axis is wrongly reconstructed: to clearly identify the γ-rays a very high rejection power (of the order of 10^6) is required. This is obtained using boosted decision tree (BDT) methods combining the variables describing the 3D electromagnetic shower shape in ECAL with the variables measuring the activity in other AMS sub-detectors, like the energy deposit in the 4 TOF layers, the time difference between the TOF hits closest to shower axis in the four TOF layers, the number of TRD tracks and the minimum TRD track distance from shower axis. Two BDT's classifiers, one to reject electrons and one for protons, were trained separately using both data and Monte Carlo simulations: the photon candidates are finally selected applying tight cuts on both the two estimators as shown in figure 4a.

Figure 4b shows the level of background rejection reached applying the full selection algorithm; even considering the feeble flux out of the galactic plane the expected contamination above 30 GeV is lower than 10%: it's possible to look at the high energy gamma sky and search for high energy sources. For the *single photon mode* detection the corresponding AMS-02 effective area (defined as the surface integral of the detection efficiency as a function of energy and incoming direction) is shown in figure 4c as a function of $cos\theta$, where θ is the particle inclination angle, and $log_{10}(E/GeV)$.

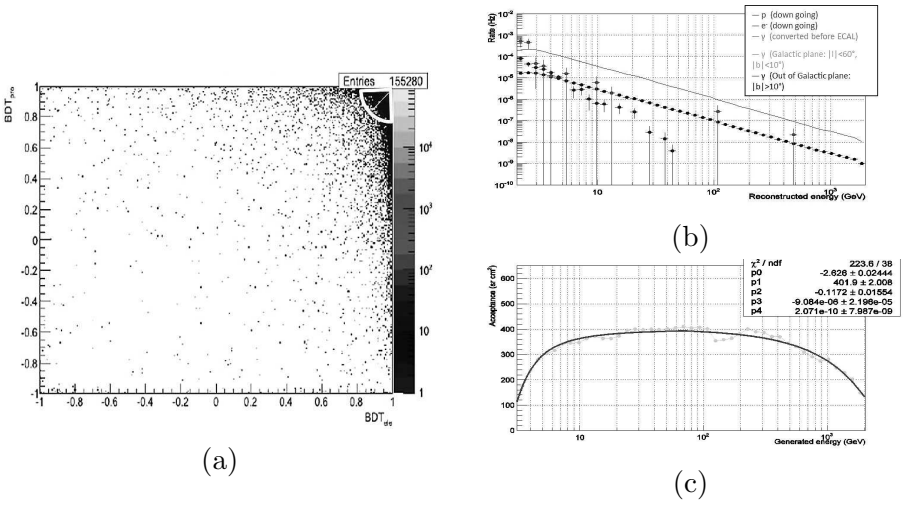

Figure 4: *a) BDT classifiers applied to photons. Two BDTs trained on electrons and protons are combined in a unique classifier, the "BDT radius" which defines the circular sector of good candidates. b) The background rate applying the selection procedure. Since the geomagnetic cut-off is not considered, the background is overestimated below 10 GeV. c) The differential effective area as a function of cosθ and* $log_{10}(E/GeV)$.

4 Conclusion

The AMS-02 electromagnetic calorimeter is an imaging calorimeter operating in space since May 2011. The high granularity guarantees excellent performances for both lepton/hadron separation and pointing. These characteristics, along with the robust and fully configurable standalone trigger, allow the ECAL to directly detect γ particles. By means of accurate discriminant analysis tecniques, the level of background can be sufficently contained, as confirmed by the sky map (see figure 5) obtained with photon candidates applying the correction for the detector exposure. In the map, the galactic plane, as well as the brightest *gamma*-rays sources like Vela, Geminga, Crab and Cygnus, are clearly visible. In the future, thanks to the very long data taking time foreseen for AMS-02, more results are expected in particular in the investigation of structures in the photon spectrum, where the very good calorimeter energy resolution will play a key role.

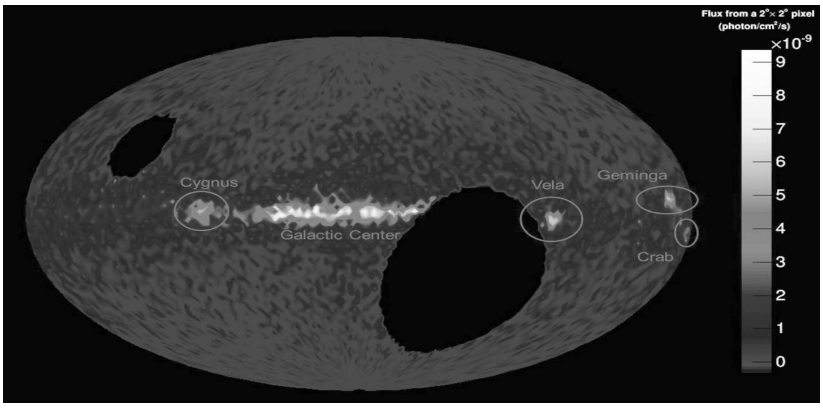

Figure 5: *Gamma all-sky map for energy above 5 GeV in* $2^\circ x 2^\circ$ *pixels in galactic coordinates. The map is obtained for a period of 24 month of data taking, correcting for the exposure of the instrument (the two empty ovals correspond to regions out of the AMS field of view).*

References

1. M. Aguilar *et al*, Phys. Rev. Lett. **110**, 14 (2013).

2. S. Rosier-Lees *et al*, J.Phys.Conf.Ser **404** (2012).

3. C. Adloff *et al*, Nucl.Instrum.Meth **A714** (2013).

4. F. Cadoux *et al*, Nuclear Science, IEEE Transactions on **55**, 2 (2008).

Frascati Physics Series Vol. 58 (2014)
Frontier Objects in Astrophysics and Particle Physics
May 18-24, 2014

HIGH-ENERGY ATMOSPHERIC PHYSICS AND TERRESTRIAL GAMMA-RAY FLASHES

Martino Marisaldi
INAF IASF Bologna, Via Gobetti 101, 40129 Bologna, Italy,
INFN sezione di Bologna, Viale B. Pichat 6/2, 40129 Bologna, Italy,
Birkeland Centre for Space Science, Allegaten 55, N-5007 Bergen, Norway

Abstract

Thunderstorms have been recently established as the most energetic natural particle accelerators on Earth. Starting from the early work by Wilson in 1925 suggesting the acceleration of electrons up to relativistic energies in thunderstorms electric fields, it took about 75 years to build up a sufficiently large observational frame and reach a general consensus on the existence of this phenomenon. The most violent manifestation of this process are Terrestrial Gamma-ray Flashes, sub-millisecond bursts of gamma-rays with energy up to several tens of MeV produced in thunderstorms and typically detected from space by detectors designed for high-energy astrophysics. First discovered in 1994 by the BATSE instrument onboard the NASA CGRO spacecraft, TGFs are now entering a golden age thanks to the wealth of observations delivered by the AGILE, RHESSI and Fermi satellites. Despite a general consensus on the underlying physical mechanism, several questions are still open, namely on the TGF-lightning relation, the maximal energy, and the pervasiveness of the phenomenon. In addition to TGFs observed from space, impulsive bursts

of radiation as well as long-lasting emissions have been observed by detectors onboard research airplanes and deployed on ground, suggesting that the production of energetic radiation within thunderstorms is a much more pervasive phenomenon than previously thought.

1 Introduction to high-energy atmospheric physics

In recent years it has been established that thunderstorm environment is the site of energetic particle acceleration, capable to produce and accelerate electrons, positrons, photons and neutrons with energies up to several tens of MeV. In fact, thunderstorms are the most energetic natural particle accelerators on Earth, see [1] for a recent extensive review. The production of energetic radiation in thunderstorms was first foreseen in the work by C.T.R. Wilson in 1925 [2], describing the mechanism of runaway electron production in air. A free electron in air, in the presence of an external electric field, may gain more energy by the ambient field than the energy lost by friction force with the air molecules. The requirement for the electron is to be energetic enough so that the Bethe-Bloch equation describing the friction force in air at the electron energy is decreasing, and the ambient field is above a certain threshold level, which is about one tenth of the conventional breakdown field and is close to the maximum electric field observed in thunderstorms. When these initial conditions are satisfied, the electron gains energy as long as it's moving within the field region, and can become relativistic. Energetic electrons can then undergo photon production by Bremsstrahlung in air, then photons can further produce energetic electrons and positrons by Compton scattering and pair production, and eventually neutrons by photo-production. Successive theoretical development [3] showed that runaway electrons interacting with air molecules by Møller scattering can produce knock-on electrons with sufficient energy to run into the runaway regime as well, therefore starting an avalanche multiplication process (Relativistic Runaway Electron Avalanche, RREA) that greatly enhance the total number of energetic particles.

It took almost 75 years to reach a general consensus on the effective manifestation of this mechanism, since the early experimental evidences were controversial. It is now established that significant X- and gamma-ray fluxes can be produced by thunderstorms on different time scales, from minute-

long quasi-stationary fluxes (gamma-ray glows or Terrestrial Ground Enhancements, TGEs) to sub-millisecond bursts of gamma-rays (Terrestrial Gamma-ray Flashes, TGFs). Although the production of runaway electrons is believed to be at the basis of all these phenomena, the conditions at the acceleration site (field magnitude and spatio-temporal behaviour, source size) appear to be different.

The first unambiguous observation of a long duration emission of hard X-rays associated to thunderstorm came in 1985 [4] with pioneering aircraft observations. Later, balloon measurements provided information on both ionizing radiation and electric fields inside active thunderstorms [5]. Recent airplane observations of gamma-ray glows were reported by the ADELE experiment [6], suggesting that RREA mechanism is responsible for this emission. Unambiguous ground based observations of long duration X- and gamma-ray emissions were first reported in 2000 [7], followed by a wealth of observations mostly carried out on Japan winter thunderstorms [8] or high-altitude sites [9]. Although aircraft observations suggest the RREA mechanism to be at the basis of the glow phenomenon [6], ground-based observations point out the possible contribution of charged cosmic rays, whose spectrum is modified by the thunderstorm electric field and overcomes the RREA contribution to the gamma-ray flux above few tens of MeV [10].

2 Terrestrial Gamma-ray Flashes

In addition to long duration emissions, gamma-rays emission from thunderstorms can take the form of sub-millisecond, bright bursts of gamma radiation extended up to several tens of MeV in energy and associated to lightning activity, known as Terrestrial Gamma-ray Flashes (TGFs). Since their discovery in the early nineties by the Burst and Transient Source Experiment (BATSE) detector on-board the NASA Compton Gamma-ray Observatory (CGRO) [11], a wealth of observations have been provided by the three currently operative space instruments capable of TGF detection: the Reuven Ramaty High Energy Solar Spectroscopic Imager (RHESSI) [12], the Gamma-ray Burst Monitor (GBM) on-board the *Fermi* satellite [13] and Astrorivelatore Gamma ad Immagini LEggero (AGILE) [14, 15, 16, 17, 18, 19]. In addition to space observations, one TGF has been observed onboard an aircraft by the ADELE experiment [20], and recently a claim for ground observation of TGFs has been

reported [21].

Although runaway electrons are believed to be at the basis of the TGF phenomenon, it has been shown [22] that the RREA mechanism alone acting on seed electrons produced by natural radioactive background or extensive air showers is not enough to account for the high fluence observed from space. Two competing models have thus emerged to overcome this theoretical limitation: either the relativistic electron flux is further enhanced by the Relativistic Feedback mechanism [23] acting within the large-scale electric field of thunderstorms, or the multiplication and acceleration of electrons takes place in the high field region associated to the tip of upward propagating lightning leaders [24]. This latter scenario implies a tight link between TGFs and lightning propagation, and seems to be supported by recent observations based on ground-based radio observations [25] and optical measurements from satellite [26].

3 Outlook: a global perspective

The study of TGFs and related phenomena is now carried out mostly on a local perspective, i.e. trying to understand the single event source mechanism and properties. This is basically unavoidable since many pieces of the puzzle to understand these phenomena are still missing. However, it is worth looking at these phenomena also from a global perspective, trying to understand their potential contribution to the coupling between atmospheric layers and, eventually, their impact on climate. This is even more important now that recent studies have suggested that observed TGFs might be just the tip of the iceberg and these phenomena may be much more pervasive than previously expected.

Considering the Earth global energy budget, of the 341 W/m^2 delivered on average by incoming solar irradiance, about 28% is transferred from the Earth's surface to the atmosphere as sensible heat (energy transfered by conduction and convection, 17 W/m^2) and latent heat (80 W/m^2) [27]. This energy transfer is driven by winds that carry heat and moisture out of the surface and ultimately drive atmospheric circulation and thunderstorm activity. This energy powers the $\approx$ 2000 thunderstorms active on average every second on Earth, which act as electric current generators keeping charged the surface-ionosphere capacitor and ultimately driving the Earth global electric circuit (GEC) [28]. Given the finite conductivity of the atmosphere, the surface-ionosphere capac-

itor would discharge in a finite time if the charging provided by thunderstorms were not at play. Indeed, the observed fair weather current of ≈ 2 pA/m^2 requires an average energy flux of 5×10^{-7} W/m^2 to maintain the average +250 kV potential difference between the ionosphere and Earth surface steady on the long term. This is indeed a tiny fraction (about 5×10^{-9}) of the total energy flux available from sensible and latent heat, but it is sufficient to maintain the GEC active. A larger, but still small fraction of energy is dissipated by lightning activity in thunderstorms. There are ≈ 44 lightning flashes per second on average on Earth [29], each of them dissipating about $10^9 - 10^{10}$ J [30], corresponding to $0.3 - 3 \times 10^{-3}$ W/m^2 average energy flux. The vast majority of this energy is delivered as heat and kinetik energy associated to the mechanical blast wave. However, how much energy is released in the radio-frequency and high-energy channel (relativistic electrons and gamma-rays) is regarded as one of the top ten questions in lightning research [31]. Given the TGF intensity observed from space and the transport of photons from the production region close to thundercloud top through the atmosphere, one may estimate the average TGF energy at the source to be of order 10 kJ. If every lightning is associated to a TGF [32], the total energy flux delivered in the TGF channel would be $\approx 3 \times 10^{-9}$ W/m^2. Again, this is a very small fraction (about 3×10^{-11}) of the total energy flux available. However, this crude estimate does not consider gamma-ray glows, for which the paucity of measurements does not allow a reasonable estimate of the average energy flux. In principle, these long duration emissions, despite less bright than TGFs, thanks to the larger spatial extension and quasi-stationary behaviour may deliver a larger amount of energy in the high-energy channel. Although the energy delivered in the high-energy channel is a very small fraction of the total available energy, we cannot neglect its contribution to the coupling between the atmosphere and the ionosphere and eventually as a feedback factor for climate processes. The long interaction length of this radiation (the minimum cross section for gamma-rays in air is at ≈ 20 MeV) makes gamma-rays a suitable mean for coupling the top of the troposphere and the ionosphere, tens of kilometers above.

Climate is a highly complex and interconnected system, where all variables at play couple together in a non-linear fashion. In this scenario, even factors accounting for a small fraction of the total available energy budget can give a feedback with substantial amplification of the effects. For example, galac-

tic cosmic rays flux at Earth accounts for about 10^{-9} the total solar irradiance, equivalent to that of starlight. Although the influence of cosmic rays on climate is still under debate, there is a growing set of observations suggesting a correlation between galactic cosmic rays flux and climate variation at the centuries - millennia time scales [33]. The proposed mechanism for providing the required substantial feedback to the climate system is the influence of ionizing radiation on aerosol nucleation and the formation of cloud condensation nuclei [34]. This feedback ultimately influences cloud coverage and the rediative balance, hence the climate [35].

Although the rough estimate of the energy flux delivered as ionizing radiation by thunderstorms and reported above is a factor ≈ 30 lower than that due to galactic cosmic rays, it is worth exploring the possibility that such energy flux may provide a feedback to climate as well. Unlike cosmic rays, ionizing radiation from thunderstorms would be an *internal* forcing agent, directly linked to thunderstorm activity. Ionizing radiation produced by thunderstorms may act on aerosol nucleation exactly like cosmic rays, moreover it can affect the GEC by directly modifying the air conductivity by ionization, both locally, close to the production region, and at a larger distance, given the large interaction length. To address this issue it is mandatory to assess a better estimate of the total amount of energy delivered as ionizing radiation, increasing the amount of observations for both TGFs and long duration glows, both at ground level, airplane, balloon and satellite altitude. Important information will come from the two forthcoming space missions ASIM and TARANIS, specifically designed for the observation of TGFs and related phenomena.

4 Acknowledgements

AGILE is a mission of the Italian Space Agency (ASI), with co-participation of INAF (Istituto Nazionale di Astrofisica) and INFN (Istituto Nazionale di Fisica Nucleare). This work was carried out in the frame of the ASI-INAF agreement I/028/12/0. This study was supported by the European Research Council under the European Unions Seventh Framework Programme (FP7/2007-2013)/ERC grant agreement n. 320839 and the Research Council of Norway under contracts 208028/F50, 216872/F50 and 223252/F50 (CoE).

5 References

References

1. J.R. Dwyer *et al*, Space Sci. Rev., **173**, 133 (2012).
2. C.T.R. Wilson, Proc. Camb. Philos. Soc., **22**, 534 (1925).
3. A.V. Gurevich, Phys. Lett. A, **165**, 463 (1992).
4. M. McCarthy and G.K. Parks, Geophys. Res. Lett., **12**, 393 (1985).
5. K.B. Eack *et al*, J. Geophys. Res., **101**, 29637 (1996).
6. N. Kelley *et al*, EGU General Assembly Conference Abstracts, **15**, 9650 (2013).
7. M. Brunetti *et al*, Geophys. Res. Lett., **27**, 1599 (2000).
8. H. Tsuchiya *et al*, J. Geophys. Res., **116**, D09113 (2011).
9. A. Chilingarian *et al*, Phys. Rev. D, **83**, 062001 (2011).
10. A. Chilingarian *et al*, Atmospheric Research, **114**, 1 (2012).
11. G.J. Fishman *et al*, Science, **264**, 1313 (1994).
12. D.M. Smith *et al*, Science, **307**, 1085 (2005).
13. M.S. Briggs *et al*, J. Geophys. Res., **118**, 3805 (2013).
14. M. Marisaldi *et al*, J. Geophys. Res., **115**, A00E13 (2010).
15. M. Marisaldi *et al*, Phys. Rev. Lett., **105**, 128501 (2010).
16. M. Tavani *et al*, Phys. Rev. Lett., **106**, 018501 (2011).
17. F. Fuschino *et al*, Geophys. Res. Lett., **38**, L14806 (2011).
18. M. Tavani *et al*, Nat. Hazards Earth Syst. Sci., **13**, 1127 (2013).
19. M. Marisaldi *et al*, J. Geophys. Res., **119**, 1337 (2014).
20. D.M. Smith *et al*, J. Geophys. Res., **116**, D20124 (2011).

21. R. Ringuette *et al*, J. Geophys. Res., **118**, 7841 (2013).

22. J.R. Dwyer *et al*, J. Geophys. Res., **113**, D10103 (2008).

23. J.R. Dwyer, J. Geophys. Res., **117**, A02308 (2012).

24. S. Celestin and V.P. Pasko, J. Geophys. Res., **116**, A03315 (2011).

25. S.A. Cummer *et al*, Geophys. Res. Lett., **38**, L14810 (2011).

26. N. Østgaard *et al*, Geophys. Res. Lett., **40**, 2423 (2013).

27. K.E. Trenberth *et al*, Bull. Amer. Meteor. Soc., **90**, 311 (2009).

28. M.J. Rycroft *et al*, J. Atmos. Solar Terrestrial Physics, **62**, 1563 (2000).

29. H.J. Christian *et al*, J. Geophys. Res., **108**, 4005 (2003).

30. V.A. Rakov and M.A. Uman, Lightning Physics and Effects, Cambridge (2003).

31. J.R. Dwyer and M.A. Uman, Physics Reports, **534**, 147 (2013).

32. N. Østgaard *et al*, J. Geophys. Res., **534**, 147 (2013).

33. J. Kirkby *et al*, Surveys in Geophysics, **117**, A03327 (2012).

34. J. Kirkby *et al*, Nature, **476**, 429 (2011).

35. R.G. Harrison, Surveys in Geophysics, **25**, 441 (2004).

Frascati Physics Series Vol. 58 (2014)
Frontier Objects in Astrophysics and Particle Physics
May 18-24, 2014

THE GAMMA-400 MISSION

Valter Bonvicini
INFN Sez. di Trieste, I-34149 Trieste, Italy
on behalf of the GAMMA-400 collaboration*

Abstract

GAMMA-400 is a new space mission scheduled to be launched at the end of the current decade on-board the Russian space platform Navigator. The

* A.M. Galper, N.P. Topchiev, O. Adriani, R.L. Aptekar, I.V. Arkhangelskaja, A.I. Arkhangelskiy, L. Bergstrom, E. Berti, G. Bigongiari, S.G. Bobkov, M. Boezio, E.A. Bogomolov, S. Bonechi, M. Bongi, S. Bottai, K.A. Boyarchuk, G. Castellini, P.W. Cattaneo, P. Cumani, G.L. Dedenko, C. De Donato, V.A. Dogiel, Ch. Fuglesang, M.S. Gorbunov, Yu.V. Gusakov, B.I. Hnatyk, V.V. Kadilin, V.A. Kaplin, A.A. Kaplun, M.D. Kheymits, V.E. Korepanov, J. Larsson, A.A. Leonov, V.A. Loginov, F. Longo, P. Maestro, P.S. Marrocchesi, V.V. Mikhailov, E. Mocchiutti, A.A. Moiseev, N. Mori, I.V. Moskalenko, P.Yu. Naumov, P. Papini, M. Pearce, P. Picozza, A.V. Popov, A. Rappoldi, S. Ricciarini, M.F. Runtso, F. Ryde, R. Sarkar, O.V. Serdin, R. Sparvoli, P. Spillantini, S.I. Suchkov, M. Tavani, A.A. Taraskin, A. Tiberio, E.M. Tyurin, M.V. Ulanov, A. Vacchi, E. Vannuccini, G.I. Vasilyev, Yu.T. Yurkin, N. Zampa, V.N. Zarikashvili, V.G. Zverev

experimental apparatus is designed for simultaneous detection of gamma and cosmic rays in a broad energy range: 100 MeV − 3 TeV for photons, 1 GeV - 20 TeV for electrons and positrons, and up to $10^{15} - 10^{16}$ eV for p and He. The characteristics of the instrument are optimized to address some of the most impelling science topics, such as search for signatures of dark matter, studies of Galactic and extragalactic gamma-ray sources, Galactic and extragalactic diffuse emission, gamma-ray bursts, as well as high-precision measurements of the spectra of cosmic-ray electrons + positrons and nuclei.

1 Origin and evolution of the project

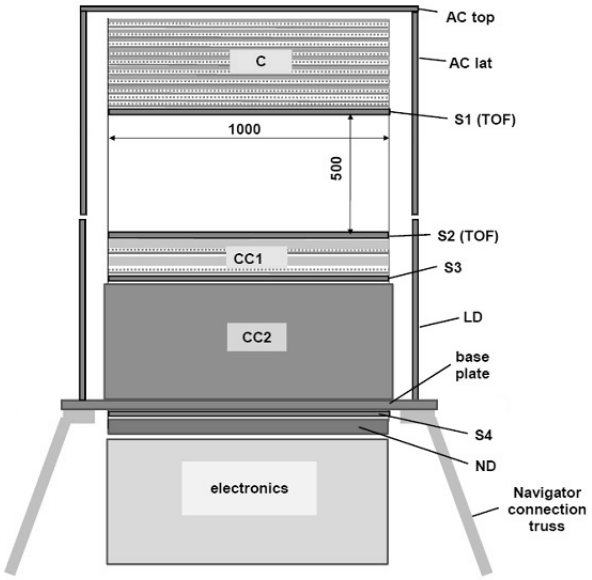

Figure 1: *Schematic view of the baseline. From top to bottom: the tracker (C), anticoincidence system (AC top and lat), time-of-flight system (S 1 to 4), calorimeter (CC1 and CC2), charge identification system on the side of the calorimeter (LD) and neutron detector (ND). The values are in mm.*

GAMMA-400 [1)] is a Russian space mission, approved by the Russian Space Agency RKA-ROSCOSMOS, with an international contribution. The

apparatus will be installed on the platform Navigator and, apart from the detectors shown in fig. 1 and described in the next section, will comprise also six gamma-ray burst monitor Konus-FG and two magnetometers.
The launch is currently scheduled by 2020 and the mission is expected to have a lifetime of at least 7 years. The orbit will initially be highly eccentric (apogee 300000 km, perigee 500 km) with an inclination of 51°. After 5 months the orbit will become more circular with an average radius of about 200000 km. This high altitude orbit will allow GAMMA-400 to make long, continuous observation of specific regions of the celestial sphere, without Earth occultation.
During the past years, the collaboration between the Russian and Italian group focused on the development of a dual instrument, capable of studying not only gamma-rays and electrons, as originally intended, but also cosmic-rays protons and nuclei.

2 The apparatus

The apparatus [2)] is composed by a converter/tracker and a calorimeter, described in the following. Plus, in order to discriminate the high charged particles background from the gamma-rays, a neutron detector as well as an anticoincidence and a time-of-flight system are foreseen. A charge identification system will be placed on the sides of the calorimeter to discriminate between the different nuclear species.
The tracker and the calorimeter are widely spaced ($\sim$ 50 cm). This substantial distance helps to improve the angular resolution at high energy. The top 2 X_0 of the calorimeter are composed by interleaved planes of CsI slabs and Silicon strip planes. At high energy, where the multiple scattering is negligible, the long lever arm between the hits on these Silicon planes and the hits in the tracker facilitate the reconstruction of the incoming direction of the gamma-ray.

2.1 Converter/Tracker

The main purposes of the tracker are to convert the incoming gamma-ray inside the inert material and detect the created pair inside the Si.
The GAMMA-400 tracker, whose schematic view is shown in fig. 2, is designed as a four tower detector. Each tower is composed by ten planes, each of which has two layers of single-sided Si microstrip, for the x/y view respectively. The read-out of strips is analogue. The Si sensors make use of the capacitive charge

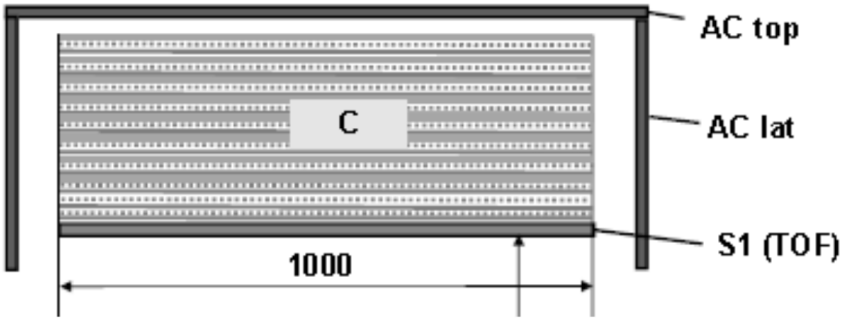

Figure 2: *Schematic view of the tracker.*

division, helping to reduce the number of read-out channels while maintaining an excellent position resolution. The strip pitch is 80 μm with one every three strips read-out. The read-out pitch is thus 240 μm. Five sensors, square tiles of $\sim$9.7$\times$9.7 cm^2, are arranged in a ladder. Each plane is composed by five of these ladders.

The first eight planes of the tracker comprise a Tungsten layer, absent in the last two planes, to ensure the conversion of the gamma-ray. The thickness of each of the first eight planes is $\sim$ 0.1 X_0.

The performance of GAMMA-400, compared those of Fermi-LAT, are presented in fig. 3. The results for the angular resolution at low energy are improved by the use of the analogue read-out, which ensures a lower error on the position with respect to the digital read-out. At high energy, the use of the long lever arm between the tracker and the Si planes in the calorimeter permits to reach an angular resolution better than 0.1° from 10 GeV and better than 0.02° starting from 100 GeV.

2.2 Calorimeter

The calorimeter is composed by an array of 28$\times$28$\times$12 cubes of CsI(Tl), each of side 3.6 cm. This novel concept for the detector permits to reconstruct the shower created from particles coming not only from the top, but also from the sides of the calorimeter. The planar geometrical factor is therefore very high

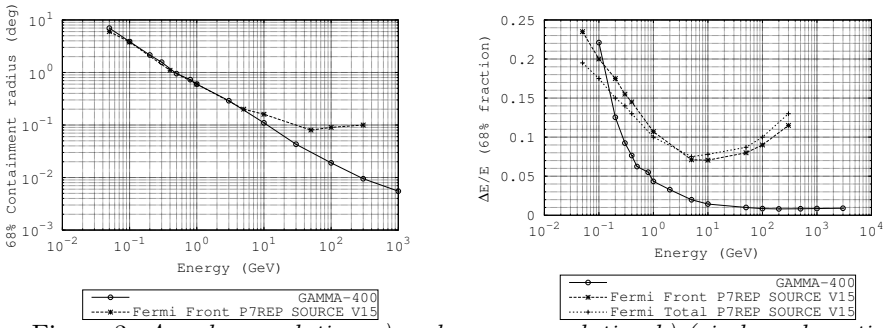

Figure 3: *Angular resolution a) and energy resolution b) (circle and continuous line) compared to the performance of Fermi-LAT (front in dashed line and stars, total in dotted line and cross hair).*

($\sim$10 m^{2}sr). The effective geometrical factor, result of the implementation of the necessary cuts, in the 100 GeV - 1 TeV energy range is equal to $\sim$3.4 m^{2}sr for electrons and $\sim$3.3 m^{2}sr for protons. The total radiation length is 54.6×54.6×23.4 X_0 while the interaction length is 2.5×2.5×1.1 λ_I.

The possibility to reconstruct the shower of particles coming also from the sides of the detector can be exploited to improve significantly the total effective area of the instrument. The large geometrical factor of the calorimeter alone can also be exploited for gamma-ray physics. In this case the angular resolution, while not sufficient for a precision study the sources, can nonetheless be useful to provide a trigger to other instruments to perform multiwavelength studies of the same source. In the case of a transient phenomenon (e.g. AGN flare), the position of the flaring source could be used to repoint on-ground telescopes, which have a limited field-of-view.

The energy resolution for gamma-rays, thanks also to the depth and performance of the calorimeter, reaches 1% at 100 GeV. The expected energy resolution for electrons will be of 1% at TeV energies, while the hadronic energy resolution for protons will be $\sim$ 35%.

A prototype of the calorimeter has already been built. It consists of 14 layers, nine crystals each. The prototype has been tested at CERN SPS with protons and deuterium.

3 Physics with GAMMA-400

GAMMA-400 has been optimized to detect the three main component of the cosmic radiation: gamma-rays from 50 MeV up to TeV, electrons up to ∼20 TeV and protons and nuclei up to the "knee" (few PeV/nucleon).

3.1 Photons

For what concerns the gamma-rays, the main scientific objective of GAMMA-400 will be the search of a possible signal related to Dark Matter annihilation or decay. This search, to be performed looking to the Galactic Center, Dwarf Spheroidal Galaxies and satellites such as galaxy clusters, will rely on the excellent angular and energy resolutions of GAMMA-400. The improvement in energy resolution will not only permit the detection of the lines resulting from by the $\gamma\gamma$ annihilation channel of the Dark Matter candidate, but also the detection of features in the spectrum. Some of this features, if present, could help to discriminate between different candidates [3].

Apart from the search for Dark Matter signal, GAMMA-400 will study also astrophysical sources such as supernova remnants, Active Galactic Nuclei, pulsars and pulsar wind nebulae and gamma-ray bursts, thanks also to the very wide field-of-view of the Konus-FG. GAMMA-400 will help in the detection of new candidates of these sources, in the discrimination against the background and the study of their high energy spectrum.

GAMMA-400 will also be used as a trigger for transients to be used for observation from the ground, thanks to the large field-of-view guaranteed by the calorimeter.

3.2 Electrons

High energy electrons have a high energy loss rate, proportional to E^2, thus a limited lifetime. TeV electrons must be accelerated at less than 1 kpc away from Earth. Therefore, by studying the spectrum of TeV electrons, one can have insight on the acceleration mechanism inside nearby sources. Thanks to its high energy resolution, GAMMA-400 will be able to detect spectral features [4] in the all-electron spectrum.

3.3 Nuclei

The knee origin is still an open question in cosmic-rays physics. Up to now, measurements could only be performed with balloons or detectors on the ground. GAMMA-400, thanks to its very deep and wide calorimeter, will be able to detect protons and nuclei up to the knee. Being a space-borne experiment, it will be able to study directly the knee, without any previous interaction of the particles with the atmosphere. Thanks to its Geometrical Factor and energy resolution, GAMMA-400 will shed light on the cosmic-rays acceleration mechanism, propagation and composition.

4 Conclusions

The GAMMA-400 mission represents a unique opportunity to perform simultaneous measurements of photons, electrons and nuclei with unprecedented accuracy, thanks to its highly performing tracker and calorimeter. It will provide in-depth investigations on some of the most challenging physics items, such as: Dark Matter search using gamma-ray and high-energy electron spectra, the cosmic-ray origin, production and acceleration to the highest energies and the flux and elemental composition of nuclei in the knee region. The synergy with ground-based Cerenkov-arrays (such as CTA) and other wavelength instruments, will ensure a continuation of the effort of the Fermi mission, after its ending, in the multiwavelength study of gamma-ray sources.

References

1. Galper, A. M. *et al*, Status of the GAMMA-400 Project, Adv. Space Res. **51**, 297-300 (2013).
2. Galper, A. M. *et al*, The Space-Based Gamma-Ray Telescope GAMMA-400 and its Scientific Goals in: Proceedings of the International Cosmic-Ray Conference (Brazil, Rio de Janeiro, 2013)
3. Bergström, L. , 130 GeV fingerprint of right-handed neutrino dark matter, Phys. Rev. D **10**, 86 (2012).
4. Kobayashi, T. *et al*, The Most Likely Sources of High-Energy Cosmic-Ray Electrons in Supernova Remnants, ApJ, **601**, 340-351 (2004).

Frascati Physics Series Vol. 58 (2014)
Frontier Objects in Astrophysics and Particle Physics
May 18-24, 2014

The CALET mission on the International Space Station

Paolo Maestro
Department of Physical Sciences, Earth and Environment
University of Siena, via Roma 56, 53100 Siena (Italy)
for the CALET collaboration

Abstract

The CALorimetric Electron Telescope (CALET) is an astroparticle physics experiment currently under preparation to be installed on the International Space Station. Its main scientific goal is to search for possible clues of the presence of astrophysical sources of high-energy electrons nearby the Earth or signatures of dark matter, by measuring accurately the electron spectrum up to several TeV. CALET will also investigate the mechanism of cosmic-ray (CR) acceleration and propagation in the Galaxy, by performing direct measurements of the energy spectra and elemental composition of CR nuclei from H to Fe up to several hundreds of TeV, and the abundance of trans-iron elements at few GeV/amu up to about Z=40. The instrument consists of two layers of segmented plastic scintillators to identify the particle charge, a thin tungsten-scintillating fiber calorimeter providing accurate particle tracking, and a thick crystal calorimeter to measure the energy of CRs with excellent resolution and electron/hadron separation up to the multi-TeV scale. In this paper, we will review the status of the CALET mission, the instrument configuration and its performance, and the expected measurements of the different components of the cosmic radiation in 5 years of observations.

1 Introduction

CALET (CALorimetric Electron Telescope) is a space-based detector developed by a Japanese led international collaboration to directly measure the high-energy cosmic radiation on the International Space Station (ISS). CALET is scheduled to be launched in JFY[1]2014 by the Japanese rocket HTV (H-IIA Transfer Vehicle) and robotically installed on the Japanese Experiment Module Exposure Facility (JEM-EF) on ISS. The CALET mission will address many of the outstanding questions of High-Energy Astrophysics, such as the origin of cosmic rays (CR), the mechanism of CR acceleration and galactic propagation, and the existence of dark matter and nearby CR sources, by measuring accurately the fluxes of CR electrons, γ rays and nuclei in a wide energy window from few GeV up to the TeV region [1)].

2 The CALET instrument and its performance

The CALET instrument consists of a Total AbSorption Calorimeter (TASC), a finely segmented pre-shower IMaging Calorimeter (IMC), and a CHarge Detector (CHD) (Fig. 1). The TASC is a homogeneus calorimeter made of 192 Lead Tungstate (PWO) "logs" ($20\times19\times320$ mm^3) arranged in 12 layers. The logs in the top layer are readout by photomultiplier tubes (PMTs), while a dual photodiode/avalanche-photodiode system is used for the readout of the remaining layers. The TASC is specifically designed to measure the energy of the incident particle with excellent energy resolution: $\sim$2% for $e^{\pm}$ and γ rays above 100 GeV, $\sim$40% for 1 TeV protons and $\sim$30% for nuclei above few hundreds of GeV/amu. Moreover, exploting its shower imaging capabilities, a proton rejection $>10^5$ can be achieved, sufficient to keep the proton contamination below a few percent in the observation of CR electrons in the TeV region [2)].

The IMC consists of 7 tungsten plates interleaved with double layers of 1 mm^2 cross-section scintillating fibers (SciFi), arranged in belts along orthogonal directions and readout by multianode PMTs, and is capped by an additional

[1]Japanese Fiscal Year

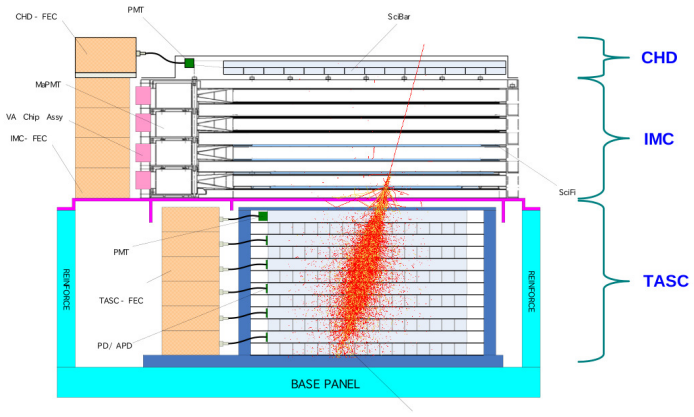

Figure 1: *Schematic view of CALET. The picture of a simulated shower is superimposed.*

SciFi layer pair. Its surface area is 45×45 cm^2 and its total thickness ∼3 radiation lengths (X_0). The IMC fine granularity allows to measure precisely the incident particle trajectory (with angular resolution better than 1°), identify the starting point of the shower and separate the incident from backscattered particles.

The charge of the CR nuclei is measured via the Z^2 dependence of the specific ionization loss in a double layered, segmented, plastic scintillator array (CHD) positioned above the IMC. Each layer is composed of 14 scintillator paddles (3.2×1.0×44.8 cm^3) each readout by a PMT. Taking advantage of its excellent charge resolution (∼0.1 electron charge units (e) for B, ∼0.2e for Fe) [3, 4], CHD can resolve individual chemical elements from Z=1 to Z=40.

The total thickness of the instrument is equivalent to 30 X_0 and 1.3 proton interaction length, the total weight is 650 kg. The effective geometrical factor of CALET for high-energy electrons and nuclei is ∼1200 cm^2 sr.

Prototypes of the CHD, IMC and TASC detectors were extensively tested at CERN in 2012 with beams of accelerated muons, electrons from 10 to 290 GeV, and protons from 30 to 400 GeV, and in 2013 with beams of ion fragments at 13 and 30 GeV/amu respectively, produced by the spallation of a primary Pb beam at onto a Be target. Results of the data analysis clearly demonstrate that the measured detector perfomance meets the design specifications [5].

3 CALET science goals

3.1 Acceleration and propagation of CR nuclei

It is nowadays generally accepted that CRs are accelerated in blast waves of supernova remnants (SNRs), which are the only galactic candidates known with sufficient energy output to sustain the CR flux. Recent measurements of γ-ray emission from several SNRs [6, 7, 8] provided evidence for hadronic CR acceleration in SNR shocks. However several questions remain unanswered. For instance, it is not clear if diffusive shock acceleration occurs in isolated SNR or in multiple remnants embedded in a turbulent stellar association; if there are different astrophysical sites associated with different energy or element regimes; if the knee in the all CR-particle spectrum is due to a rigidity-dependent limit, above which the diffusive shock acceleration becomes inefficient; how the shock is modified by the dynamical interaction with the accelerated particles [9]. In order to enhance our knowledge of these physical processes, direct measurements of the CR chemical composition and individual energy spectra of CR nuclei, more accurate than the currently available ones and approaching the PeV energy region, are needed. CALET will be able to identify CR nuclei with individual element resolution and measure their energies in the range from a few tens of GeV to several hundreds of TeV. In 5 years of data taking on the ISS, it is expected to extend the proton energy spectrum up to ∼900 TeV, the He spectrum up to 400 TeV/amu (Fig. 2) and measure the energy spectra of the more abundant heavy nuclei with sufficient statistical precision up to ∼20 TeV/amu for C and O and 9-10 TeV/amu for Ne, Mg, Si and Fe. These data would allow to measure accurately the spectral shape of the most abundant CR elements and investigate the presence of possible spectral break in the flux of nuclei as the one recently reported by CREAM [10] and PAMELA [11], but not confirmed by AMS-02 [12].

Information on the CR propagation in the galaxy may be obtained by measuring the ratio of abundances of CR secondary-to-primary elements (like B/C or sub-Fe/Fe), which is known to decrease, following a power-law in energy $E^{-\delta}$, where δ is the propagation index. This is a key parameter and its accurate measurement is crucial to derive the spectrum at the source by correcting the observed spectral shape for the energy dependence of the propagation term. The B/C data at low energies (<100 GeV/amu) favor $\delta \approx 0.6$ which is some-

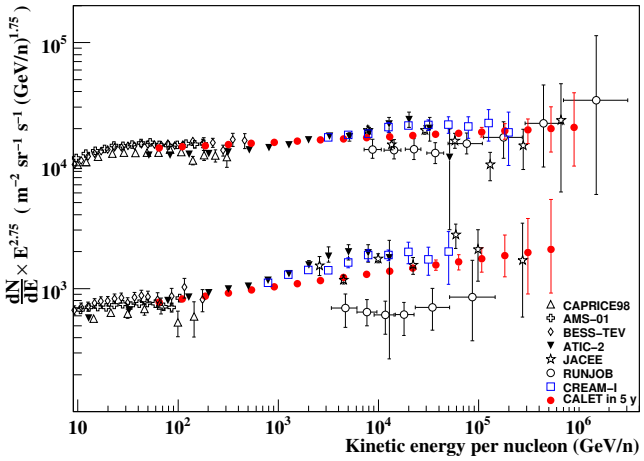

Figure 2: *Expected CALET measurement (red dots) of the energy spectra of proton and He after 5 years of observation on the ISS, compared with a compilation of direct measurements.*

what steeper than the trend observed in high energy (100-1000 GeV/amu) data which seem to flatten to $\delta \approx 0.4$. However the high-energy measurements provided by balloon experiments [13, 14] suffer from statistical limitations and large systematic errors, stemming from the corrections for the nuclei produced by CR interaction with the residual atmospheric overburden at flight altitude and do not allow to constraint tightly the value of δ and discriminate among different propagation models. Taking advantage of its long exposure in space and the absence of atmosphere, CALET will provide new data to improve the accuracy of the present measurements above 100 GeV/amu and extend them above 1 TeV/amu (Fig. 3).
Moreover, exploiting the CHD particle identification capability, CALET will measure the abundances of ultra-heavy CRs at few GeV/amu in the $26<Z\leq40$ charge range with an expected statistics ∼2-4 times larger than TIGER [15].

3.2 CR electrons: astrophysical sources and dark matter

Unlike the hadronic component of CRs, electrons, during their diffusion in the Galaxy, suffer radiative energy losses proportional to their squared energy.

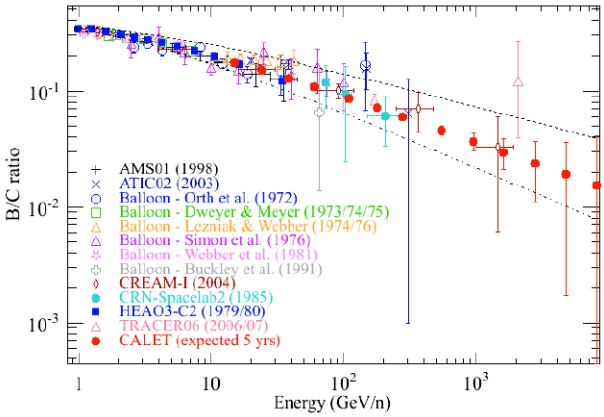

Figure 3: *A compilation of the B/C ratio as a function of energy per nucleon and the expectation for CALET after 5 years of observations (red dots).*

Thus TeV electrons observed at Earth likely originated in sources younger than 10^5 years and <1 kpc far from the Solar System. Since the number of such nearby SNRs is limited (e.g.: Vela, Monogem, Cygnus Loop remnants, and few others), the electron energy spectrum around 1 TeV could exhibit spectral features and, at very high energies, a measurable anisotropy in the electron arrival directions would be expected, due to the locality of the possible sources. An alternative explation for the features recently observed in the electron spectrum by the balloon-borne experiment ATIC [16] and the increase in the positron fraction measured by the space-based detectors PAMELA [17], Fermi [18] and AMS-02 [19] is that they could be signatures of decay or annihilation of dark matter particles. Thanks to its excellent energy resolution, electron/hadron discrimination power, and long exposure in space, CALET will be able to perform a precision measurement of the electron spectral shape from few GeV up to 10 TeV, as shown in Fig. 4, where the expected statistics of CALET after 5 years of observation is estimated according to an empirical model of the eletron+positron flux, including a source contribution from dark matter or a nearby pulsar, and fitting simultaneously the observed positron and electron data [20].

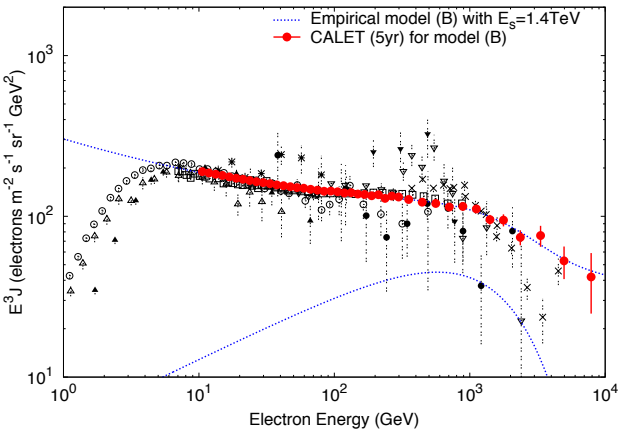

Figure 4: *A compilation of measurements of the electron spectrum compared with the expectation for CALET after 5 years of observation (red dots). The blue dotted line represents an empirical model parametrizing the e^- and e^+ fluxes as the sum of individual power-law spectra and a common single power-law spectrum with an exponential cutoff, describing a source contribution from dark matter or a nearby pulsar (shown by the overlaid fit projection)* [20].

3.3 Gamma rays: sources and transients

The excellent energy resolution and background rejection capability of the CALET instrument will allow to perform energy-resolved measurements of the diffuse γ-ray emission and study the spectral shape of more than 100 bright sources at high latitude from the Fermi LAT catalog [21]. Moreover CALET will be capable of searching for possible sharp lines from annihilation of dark matter particles in the diffuse spectrum. Dedicated $LaBr_3(Ce)$ and BGO scintillating crystals will complement the calorimetric instrument in the detection γ-ray bursts and X-ray transients in the energy range from 7 keV to 20 MeV [22].

4 Conclusions

The CALET instrument is currently under preparation to be launched to ISS-JEM in JFY 2014. In a mission life of 5 years, it will perform precision measurements of electrons, nuclei, and γ-rays at the high energy frontier, providing valuable information for a better understanding of the origin and nature of dark

matter and the mechanisms of acceleration and transport of CRs in the galaxy.

References

1. S. Torii *et al.*, Nucl. Instr. And Meth. A **630**, 55 (2011)
2. Y. Akaike *et al.*, Adv. Space Res. **45**, 690 (2010)
3. P.S. Marrocchesi, Proc. of 33^{rd} ICRC 0362 (2013)
4. P.S. Marrocchesi, Proc. of IEEE-TNS (Seoul) N31-3 (2013)
5. Y. Akaike, Proc. of 33^{rd} ICRC 0726 (2013)
6. F.A. Aharonian *et al.*, Nature **432**, 75 (2004)
7. M. Tavani *et al.*, ApJ. Lett. **710**, L151 (2010)
8. A.A. Abdo *et al.*, Science **327**, 1103 (2010)
9. P. Blasi *et al.*, Phys.Rev.Lett. **109**, 061101 (2012)
10. H.S. Ahn *et al.*, ApJ **714**, L89 (2010)
11. O. Adriani *et al.*, Science **332**, 69 (2011)
12. S. Haino, Proc. of 33^{rd} ICRC 1265 (2013)
13. H.S. Ahn *et al.*, Astropart. Phys. **30**, 133 (2008)
14. A. Obermeier *et al.*, ApJ **752**, 69 (2011)
15. B.F. Rauch, Proc. of 33^{rd} ICRC 0819 (2013)
16. J. Chang *et al.*, Nature **456**, 362 (2008)
17. O. Adriani *et al.*, Nature **458**, 607 (2009)
18. A.A. Abdo *et al.*, Phys. Rev. Lett. **102**, 181101 (2009)
19. M. Aguilar *et al.*, Phys. Rev. Lett. **110**, 141102 (2013)
20. K. Yoshida *et al.*, Proc. of 33^{rd} ICRC 0735 (2013)
21. A.A. Moiseev, Proc. of 33^{rd} ICRC 0627 (2013)
22. K. Yamaoka *et al.*, Proc. of 33^{rd} ICRC 1007 (2013)

Frascati Physics Series Vol. 58 (2014)
Frontier Objects in Astrophysics and Particle Physics
May 18-24, 2014

AERA - The Auger Engineering Radio Array

Raphael Krause[1] for the Pierre Auger Collaboration[2]
[1] *III. Physikalisches Institut A, RWTH Aachen University, Aachen, Germany*
[2] Observatorio Pierre Auger, Av. San Martín Norte 304, 5613 Malargüe, Argentina
Full author list: http://www.auger.org/archive/authors_2014_05.html

Abstract

Extensive air showers originating from ultra high energy cosmic rays exhibit emission of electromagnetic signals in the radio frequency range. Together with other detection techniques, radio measurements deliver complementary information on the electromagnetic shower component with a duty cycle close to 100 %. The Auger Engineering Radio Array (AERA) is located within the Pierre Auger Observatory in Argentina which is the world's largest detector for cosmic rays. It offers a well calibrated environment to test and develop future detector techniques and is therefore an optimal location for AERA. Currently, AERA constitutes the largest radio cosmic ray setup consisting of 124 autonomous radio stations and covering an area of 6 km^2. In 2011 continuous data taking has started with several thousand cosmic ray events recorded so far. In measurements of air showers simultaneously with radio, fluorescence light and particle detectors, the sensitivity of the radio detection to cosmic ray properties such as arrival direction, energy and composition is being investigated.

1 Introduction

Until today there are still open questions about ultra high energy cosmic rays (UHECR), e.g. what are their sources, how do they propagate to Earth through the universe and what is their chemical composition?
If a primary UHECR hits the Earth's atmosphere it interacts inelastically with an air nucleus and produces billions of secondary particles in the form of an extensive air shower. With a cosmic ray flux of only one particle per square kilometer per year at energies higher than $E \approx 10^{18}\,\mathrm{eV}$, large ground-based detectors, e.g. the Pierre Auger Observatory, are needed to observe these secondary particles.
The Pierre Auger Observatory, located near Malargüe in Argentina, is the largest cosmic ray experiment worldwide. Two different baseline detector methods, fluorescence and surface detectors, cover an area of $3000\,\mathrm{km}^2$. [1)]
When an air shower traverses the atmosphere of the Earth nitrogen molecules are excited. When they de-excite, fluorescence light in the ultra violet regime is emitted isotropically and measured by 27 fluorescence telescopes of the observatory. The longitudinal shower profile, which provides information about the arrival direction and energy of the primary cosmic ray, is measured with the fluorescence detectors. Furthermore, the longitudinal shower profile is a measure of the composition of UHECRs. The fluorescence detector (FD) is restricted to measure only in clear and moonless nights. This leads to a duty cycle of the fluorescence detectors of about 13 %.
The surface detector (SD) array of the Pierre Auger Observatory observes secondary cosmic ray particles which reach ground level. It consists of 1660 water-Cherenkov detectors. With the surface detectors it is possible to measure the lateral shower profile which provides information about the arrival direction and energy of the primary cosmic ray. The duty cycle of the surface detectors is close to 100 %.
During the development of extensive air showers within the Earth's atmosphere, electromagnetic radiation in the radio frequency range is emitted. With the Auger Engineering Radio Array (AERA) the Pierre Auger Observatory is enhanced with the radio detection technique. The radio signal of an extensive air shower provides information about the arrival direction and energy of the cosmic ray as well as about the longitudinal and lateral shower development. AERA has the potential of a duty cycle close to 100 %.

2 Radio Emission Processes in Extensive Air Showers

There are two main radio emission processes in extensive air showers. The first emission process is the geomagnetic emission process. Charged secondary particles are deflected in the Earth's magnetic field due to the Lorentz force and form a radiating dipole perpendicular to the shower axis. The emitted electric field is polarized into the vector product of the incoming direction $\vec{e}_{\mathrm{r}}$ of the extensive air shower and the Earth's magnetic field $\vec{B}$: $\vec{E} \propto \vec{e}_{\mathrm{r}} \times \vec{B}$. The electric field amplitude scales with $|\vec{E}| \propto |\vec{B}| \sin(\alpha)$, where α describes the angle between shower axis and the Earth's magnetic field.
The second emission process is the charge excess process. Secondary particles knock out electrons of air molecules. The electrons propagate along with the shower front and positively charged air molecules remain. Moreover, secondary produced positrons annihilate with electrons of air molecules and again positively charged air molecules remain. Due to these charge excess effects, a dipole along the shower axis results in a radio signal polarized radially towards the shower axis. [2)]
The full electric field vector $\vec{E}_{\mathrm{theo}}$ can be described as a superposition of both radio emission processes, geomagnetic $\vec{e}_{\mathrm{geo}}$ and charge excess $\vec{e}_{\mathrm{ce}}$, where a describes the relative strength of the charge excess in relation to the geomagnetic effect:

$$\vec{E}_{\mathrm{theo}} \propto \sin(\alpha)\, \vec{e}_{\mathrm{geo}} + a\, \vec{e}_{\mathrm{ce}} \tag{1}$$

3 The Auger Engineering Radio Array

The Auger Engineering Radio Array (AERA) is located in the north-west of the Pierre Auger Observatory within the SD array. The layout of AERA is shown in the right picture of fig. 1. AERA is overlooked by the fluorescence telescopes of Coihueco and is set up close to the low energy extensions AMIGA [3)] and HEAT [4)] of the Pierre Auger Observatory. Therefore, it is located in a perfect environment to develop new detector techniques as well as to compare and combine different techniques to investigate UHECRs. AERA covers an area of about $6\,\mathrm{km}^2$ and consists of 124 radio stations.

The scientific goals of AERA are to investigate the VHF radio emission processes of extensive air showers and to measure primary cosmic ray properties, e.g. the arrival directions and energies as well as their composition.

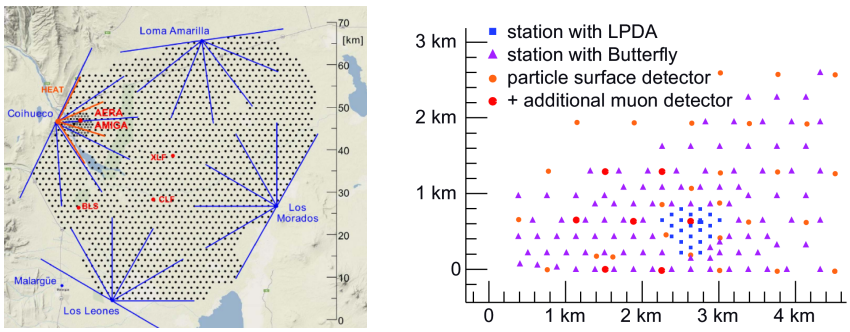

Figure 1: *a) Layout of the Pierre Auger Observatory. The position of the* 1660 *surface water-Cherenkov detectors are marked as gray dots and the field of view of* 27 *fluorescence detectors at the edge of the SD array as blue and orange lines. b) Layout of AERA within the SD array. The radio stations are set up on a regular grid with three different spacings of* 150 m, 250 m *and* 375 m.

4 AERA - Radio Stations

Since 2011 AERA has taken data with 24 radio stations (AERA24) equipped with logarithmic periodic dipole antennas (LPDA). AERA was extended with 100 radio stations using a different antenna type (bow-tie dipole) called the butterfly antenna [5)] in 2013. In the near future further butterfly radio stations will be set up to extend the array. Both radio station types are autonomous solar-powered stations. They consist of two, east-west and north-south polarized antennas. The antennas are aligned with an accuracy of less than 1 ° to the magnetic north. This allows precise measurements of the electric field polarization. The LPDA consists of nine dipole arms. The size of a fully assembled LPDA is 4.25 m × 4.25 m × 3.9 m. The butterfly radio station is designed to reduce production costs and to realize an easier deployment. Technically, the butterfly antenna exhibits a better signal to noise ratio and a smaller group delay than the LPDA [6)]. The size of a fully assembled butterfly antenna is 2.28 m × 2.28 m × 1.65 m. Both radio station types are shown in fig. 2.
The antennas are connected to low-noise amplifiers. The measured radio signal is amplified by 18 dB (LPDA) or 26 dB (butterfly) respectively. [5)] A filter amplifier restricts the frequency bandwidth of the antenna stations to between 30 MHz and 80 MHz. The data are digitized with a sampling rate of 200 MHz.

Figure 2: *Photos of the AERA radio stations a) logarithmic periodic dipole radio station b) butterfly radio station. The butterfly antenna is located underneath the parabolic wifi antenna.*

5 Calibration of the AERA Radio Stations

The electric field of an extensive air shower is measured as a voltage trace from the radio antennas. To reconstruct the electric field vector a calibration of the antenna characteristics is necessary. The vector effective length (VEL) $\vec{H}$ is a measure of the directional sensitivity of the antenna depending on the incoming direction θ, ϕ and the frequency f of the signal and describes the relation between the measured voltage trace U and the incoming electric field $\vec{E}$,

$$U(\theta, \phi, f) = \vec{H}(\theta, \phi, f) \cdot \vec{E}(\theta, \phi, f). \tag{2}$$

For the electric field reconstruction the Auger software framework Offline [7] is used. The VEL used for the electric field reconstruction is simulated with the software called NEC2 [8]. The simulated VEL is based on a complete model of a radio station. Besides the antenna itself the influence of all conducting elements of the radio station are taken into account.
To investigate the influence of ground conditions and to verify the simulated VEL, measurements have been performed at AERA. The VEL is determined by measuring the transmission between a calibrated transmitting antenna and a

fully assembled radio station using a vector network analyzer. In the frequency range from 30 MHz to 80 MHz the distance R between the transmitting antenna and the radio station has to be larger than 25 m to guarantee far field conditions. Therefore, the transmitting antenna is fixed underneath a GPS-controlled flying drone, a so-called octocopter. The setup is shown at the left side of fig. 3. In the right picture of fig. 3 the measured and simulated horizontal VEL component of a fully assembled butterfly radio station are compared with each other at a frequency of $f = 55$ MHz. Agreement between simulation and measurement at the level of 20 % is visible.

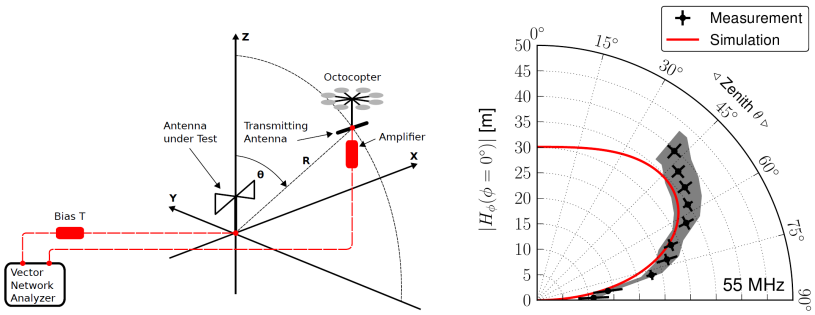

Figure 3: *a) radio station calibration setup* [9] *b) measured and simulated horizontal vector effective length component of a butterfly radio station at* $f = 55$ MHz. *Systematic uncertainties are indicated by the gray band* [9].

6 AERA - Measurements

The well calibrated AERA radio stations allow the three dimensional electric field vector to be reconstructed with a good precision. Therefore, data of AERA24 with at least three triggered radio stations and a zenith angle smaller than 55 ° that has been measured in coincidence with the surface detector array of the Pierre Auger Observatory are investigated. The left picture of fig. 4 shows a comparison between the measured polarization and the expected polarization for the dominating geomagnetic emission process. Only small differences between measurement and model prediction are visible. Measured and expected polarization show a good agreement. However, a more detailed analysis reveals a second order component radially polarized towards the shower

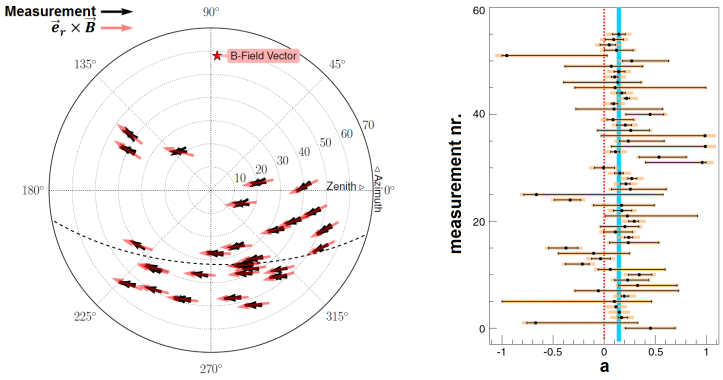

Figure 4: *a) measured (black) and expected geomagnetic (red) electric field polarization* [10] *b) several measurements at AERA determine the relative charge excess component in average to* $a = (14 \pm 2)\,\%$ [11].

axis as explained in sec. 2. With AERA the mean relative strength of this component has been measured to be $a = (14 \pm 2)\,\%$ [11] (right picture of fig. 4).

In the following, the reconstruction of the primary cosmic ray energy by measuring the radio signal of an extensive air shower is presented. The measured electric field strength is corrected for geomagnetic and charge excess effects by scaling the measured electric field amplitude with the theoretical prediction of eq. (1). The electric field strength decreases with distance to the shower axis. A lateral distribution function is fitted to the corrected electric field strength measured in at least three radio stations. The electric field strength interpolated to a distance $d_0 = 110\,\mathrm{m}$ is used as a radio energy estimator of the primary cosmic ray. This radio energy estimator is calibrated with the energy of the primary cosmic ray measured with the two baseline detectors of the Pierre Auger Observatory. A publication about the radio energy reconstruction of the primary cosmic ray is in preparation.

7 Conclusion

The Pierre Auger Observatory is a well calibrated environment for the development of future cosmic ray detector technologies, e.g. the radio detection technique. Radio detection of cosmic-ray induced air showers is expected to

combine a good sensitivity to the longitudinal shower development and thereby a measurement of the cosmic-ray particle type with a duty cycle close to 100 %. Currently, the Auger Engineering Radio Array is the largest experiment to measure radio emission of extensive air showers. Well calibrated radio stations allow a precise reconstruction of the cosmic ray arrival direction and the electric field vector as well as an estimate of the energy of the primary cosmic ray. The geomagnetic emission process is determined as the dominant radio emission process. The relative strength of the second order charge excess emission process has been measured to be on average (14 ± 2) %. With AERA measurements of the longitudinal shower profile are being investigated to obtain information on the composition of UHECRs.

References

1. J. Abraham *et al.*, Nucl. Instrum. Meth. A **523**, 50–95, (2004)
2. G. Askaryan, Soviet Phys. JETP Lett. (USSR) **14**, 441, (1962)
3. F. Sanchez *for the Auger Collaboration*, 32nd ICRC, Beijing, China, (2011)
4. H. J. Mathes *for the Auger Collaboration*, 32nd ICRC, Beijing, China, (2011)
5. D. Charrier *for the Codalema Collaboration*, Nucl. Instrum. Meth. A **662**, 142–145, (2012)
6. P. Abreu *et al.*, JINST **7**, P10011, (2012)
7. P. Abreu *et al.*, Nucl. Instrum. Meth. A **635**, 92, (2011)
8. NEC2++, `http://elec.otago.ac.nz/w/index.php/Necpp.`
9. K. Weidenhaupt, PHD Thesis, Aachen, Germany, (2014)
10. K. Weidenhaupt *for the Auger Collaboration*, Acta Polytechnica **53** (Supplement), 825–828, (2013)
11. A. Aab *et al.*, Phys. Rev. D **89**, 052002, (2014)

Frascati Physics Series Vol. 58 (2014)
Frontier Objects in Astrophysics and Particle Physics
May 18-24, 2014

THE HOT AND ENERGETIC UNIVERSE WITH ATHENA

Giorgio Matt (on behalf of the Athena team)
Dipartimento di Matematica e Fisica, Università degli Studi Roma Tre

Abstract

Athena is an X-ray observatory, selected as a large mission for the ESA science program for a launch in 2028. It is conceived to answer some of the most pressing questions in Astrophysics for the late 2020s that can uniquely be addressed with X-ray observations.

In particular, Athena will transform our understanding of two major components of the Cosmos, the *Hot* and the *Energetic* ones.

1 Introduction

In March 2013, the European Space Agency (ESA) issued a call for scientific themes and related mission concepts for the Cosmic Vision Large Class Missions, to fill in the L2 (2028) and L3 (2035) slots. An ad hoc Senior Survey Committee (SSC) was appointed to review the themes. In response to this call,

The Hot and Energetic Universe theme and the Athena mission concept were submitted in May 2013. The theme was based on two pillars:

The Hot Universe: the bulk of visible matter in the Universe comprises hot gas which can only be accessed via space-based facilities operating in the X-ray band. Revealing this gas and relating its physical properties and evolution to the cosmological large-scale structure, and the cool components in galaxies and stars, is essential if we are to have a complete picture of our Universe.

The Energetic Universe: accretion onto black holes is one of the major astrophysical energy generation processes, and its influence via cosmic feedback is profound and widespread. X-ray observations provide unique information about the physics of black hole growth and the causes and effects of the subsequent energy output, as well as revealing where in the Universe black hole accretion is occurring and how it evolves to the highest redshifts.

In October 2013, the *Hot and Energetic Universe* and *The Gravitational Universe* themes were recommended by the Senior Committed for L2 and L3, respectively. In November, this recommendation was approved by ESA's Science Programme Committee (SPC). Following this decision, in February 2014 ESA issued a call for missions addressing *The Hot and Energetic Universe* theme, in April the Athena mission proposal was submitted, and in June it was approved by the SPC.

2 The Hot and Energetic Universe theme

The Hot and Energetic Universe theme advocates the need for a transformational leap in our understanding of two key questions in astrophysics:

- How does ordinary matter assemble into the large scale structures that we see today?
- How do black holes grow and shape the Universe?

To understand the first of these questions, we must determine the physical evolution of clusters and groups of galaxies from their formation epoch at z$\sim$2-3 to the present day. These structures grow over cosmic time by accretion of gas from the intergalactic medium, with the endpoint of their evolution being today's massive clusters of galaxies, the largest bound structures in the Universe. Hot gas in clusters, groups and the intergalactic medium dominates the

baryonic content of the local Universe, so understanding how this component forms and evolves is a crucial goal.

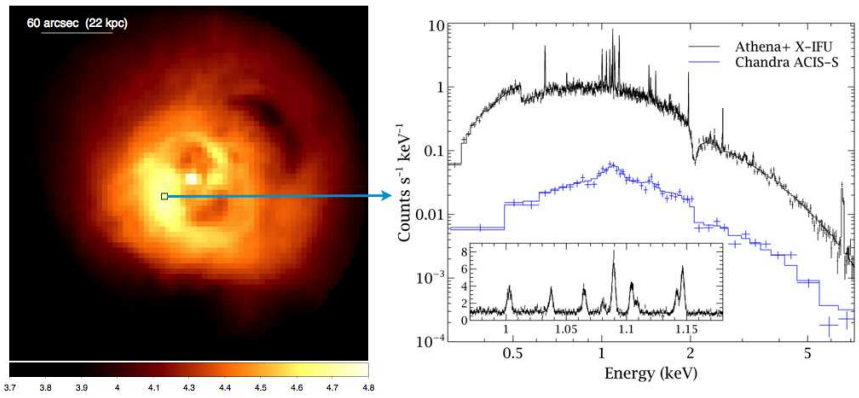

Figure 1: *Simulated Athena observations of the Perseus cluster, highlighting the advanced capabilities for revealing the intricacies of the physical mechanisms at play. The left panel shows a simulated 50 ks X-IFU observation (0.5-7 keV), displayed on a log scale. The spectrum on the right is from the single* $5'' \times 5''$ *region marked by the box, with the existing Chandra ACIS spectrum for comparison. The inset shows the region around the iron L complex. With such observations velocity broadening is measured to 10–20 km* s^{-1}*, the temperature to 1.5% and the metallicity to 3% on scales* < 10 *kpc in 20–30 nearby systems, and on* < 50 *kpc scales in hundreds of clusters and groups. Such measurements will allow us to pinpoint the locations of jet energy dissipation, determine the total energy stored in bulk motions and weak shocks, and test models of AGN fueling so as to determine how feedback regulates hot gas cooling*

While the framework for the growth of structure is set by the large scale dark matter distribution, processes of an astrophysical origin also have a major effect. To understand them, it is necessary to measure the velocities, thermodynamics and chemical composition of the gas to quantify the importance of non-gravitational heating and turbulence in the structure assembly process. The temperature of the hot gas is such that it emits copiously in the X-ray band, but current and planned facilities do not provide sufficient collecting area and spectral resolution to settle the issue of how ordinary matter forms the large scale structures that we see today. The key breakthrough is to enable

spectroscopic observations of clusters beyond the local Universe, out to z=1 and beyond, and spatially resolved spectroscopy to map the physical parameters of bound baryonic structures. Technological advances in X-ray optics and instrumentation can deliver simultaneously a factor 10 increase in both telescope throughput and spatial resolving power for high resolution spectroscopy, allowing the necessary physical diagnostics to be determined at cosmologically relevant distances for the first time.

One of the critical processes shaping hot baryon evolution is energy input commonly known as feedback from supermassive black holes. Remarkably, processes originating at the scale of the black hole event horizon seem able to influence structures on scales 10 orders of magnitude larger. This feedback is an essential ingredient of galaxy evolution models, but it is not well understood. X-ray observations are again the key to further progress, revealing the mechanisms which launch winds close to black holes and determining the coupling of the energy and matter flows on larger galactic and galaxy cluster scales. The widespread importance of black hole feedback means that we cannot have a complete understanding of galaxies without tracking the growth of their central supermassive black holes through cosmic time. A key goal is to push the frontiers of black hole evolution to the redshifts where the first galaxies are forming, at z=6-10. X-ray emission is the most reliable and complete way of revealing accreting black holes in galaxies, but survey capabilities need to be improved by a factor $\sim$100 over current facilities to reach these early epochs and perform a census of black hole growth. This requires a combination of high sensitivity, which in turn depends on large throughput and good angular resolution, and wide field of view. Again, the required technologies to provide this leap in wide field X-ray spectral imaging are now within our grasp. The same high throughput needed to detect these early black holes will also yield the first detailed X-ray spectra of accreting black holes at the peak of galaxy growth at z=1-4, measurements which are impossible with current instrumentation. These spectra will show, for example, if the heavily obscured phase of black hole evolution is associated with the termination of star formation in galaxies via feedback.

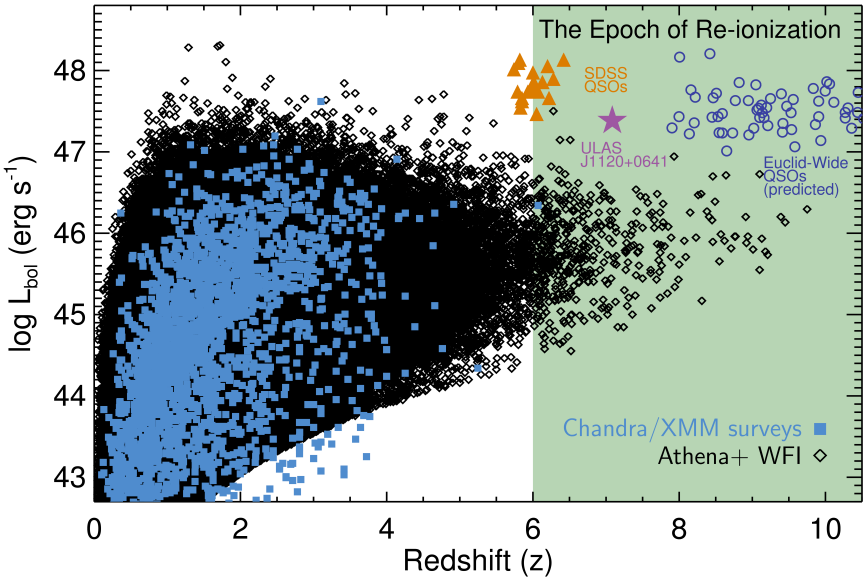

Figure 2: *Predictions for the redshifts and luminosities of 600,000 AGN that will be identified with a multilayered 1-year Athena WFI survey, compared to current Chandra and XMM-Newtton surveys. Athena will discover hundreds of X-ray selected AGN in the epoch of reionization at z>6, sources which are around 2 orders of magnitude fainter than current optical and near-IR surveys (e.g. SDSS, UKIDSS), thus providing an essential complement to the luminous QSOs that Euclid will identify in the next decade, including in particular the most obscured ones missed by those surveys.*

3 The Athena mission

The scientific theme described in the previous section calls for spatially-resolved X-ray spectroscopy and deep wide-field X-ray spectral imaging with performance greatly exceeding that offered by current X-ray observatories like XMM-Newton and Chandra, or by missions soon to be launched such as Astro-H and SRG/eROSITA. This capability requires an X-ray telescope combining unprecedented collecting area (2 m^2 at 1 keV) with an excellent angular resolution (5") and a wide field of view (40'x40'). New instrumentation providing spatially-resolved high resolution spectroscopy will yield the physical parame-

Parameter	Requirements
Effective Area	2 m^2 @ 1 keV (goal 2.5 m^2) 0.25 m^2 @ 6 keV (goal 0.3 m^2)
Angular Resolution	5″ (goal 3") on-axis 10" at 25' radius
Energy Range	0.3-12 keV
Instrument Field of View	Wide-Field Imager: (WFI): 40' (goal 50') X-ray Integral Field Unit: (X-IFU): 5' (goal 7')
Spectral Resolution	WFI: < 150 eV @ 6 keV X-IFU: 2.5 eV @ 6 keV (goal 1.5 eV @ 1 keV)
Count Rate Capability	> 1 Crab (WFI) 10 mCrab, point source (X-IFU) 1 Crab (30% throughput)
TOO Response	4 hours (goal 2 hours) for 50% of time

Table 1: Key parameters of the Athena mission.

ters of hot gas structures out to high redshift and map the intergalactic medium in the nearby Universe. A wide field instrument performing spectrally-resolved imaging over a broad energy band is required to determine the evolution of supermassive black holes into the early Universe, and shed new light on black hole accretion and ejection processes, over a wide range of masses from Galactic compact objects to the largest supermassive black holes.

A detailed analysis of the scientific questions underlying *The Hot and Energetic Universe* theme sets the key performance parameters for the mission. Mapping the dynamics and chemical composition of hot gas in diffuse sources requires high spectral resolution (2.5 eV) imaging with large area and low background; the same capabilities also optimize the sensitivity to weak absorption and emission features needed to uncover the hot components of the intergalactic medium. High resolution X-ray spectroscopy of distant gamma-ray bursts (GRBs) may reveal the signature of the first generation of stars, provided that the observatory can be repointed within 4 hours of an external trigger. An angular resolution of about 5" is needed to disentangle point-source and subclump contaminants from the extended thermal emission in clusters, groups

and galaxies. The same angular resolution is needed to resolve the dominant core emission and smaller accreting structures in galaxy clusters and groups up to redshift z$\sim$2. This resolution, when combined with the mirror effective area, also provides the necessary flux sensitivity ($\sim 10^{-17}$ erg cm^{-2} s^{-1} in the 0.5-2 keV band) to uncover typical accreting SMBH at z>6. The areal coverage needed to detect significant samples of these objects within a reasonable survey time demands a large field of view instrument, combined with excellent off-axis response for the X-ray optics. The spectral resolution of the same instrument will reveal the most obscured black holes at the peak of the Universe's activity at z=1-4. High timing resolution and high count rate capability will shed new light on nearby accreting black hole systems.

All these capabilities combine in the Athena concept (see Table 1). Athena consists of a single X-ray telescope with a fixed 12 m focal length, based on ESAs Silicon Pore Optics (SPO) technology. SPO provides an exceptionally high ratio of collecting area to mass, while still offering the necessary angular resolution. It also benefits from a high technology readiness level and a modular design highly amenable to mass production, necessary to achieve the unprecedented telescope collecting area. The telescope focuses X-ray photons onto one of two instruments, which can be moved in and out of the focal plane using a movable instrument platform. In combination with the telescope, these two instruments provide the capabilities required to meet *The Hot and Energetic Universe* science goals.

The first instrument, the X-ray Integral Field Unit (X-IFU), provides spatially-resolved high resolution spectroscopy. The instrument is based on cooled Transition Edge Sensors (TES). These can deliver the necessary energy resolution, while providing exceptional efficiency compared to the dispersive spectrometers flown on the current generation of X-ray observatories. The TES technology has already demonstrated the required spectral resolution (2.5 eV) but needs to be developed further to provide this over a large field of view (5' diameter). Background in the X-IFU is mitigated using an active anti-coincidence layer, which is important to achieve the science goals for spectroscopy of faint extended sources.

The second instrument, the Wide Field Imager (WFI), is a Silicon-based detector using DEPFET Active Pixel Sensor (APS) technology. As X-ray spectroscopic imaging devices, the DEPFETs provide almost Fano-noise-limited

energy resolution and minimal sensitivity to radiation damage. Because each pixel is addressed individually, readout modes can be highly flexible and extremely fast. With the development of appropriate readout ASICs, a time resolution of around 10μs is achievable as well as a count rate capability sufficient to deal with the brightest X-ray sources in the sky. The large field of view is achieved via a focal plane composed of several chips, where one of them will be enable fast readout to accommodate measurements of very bright targets.

It is expected that Athena will be launched via an Ariane V-class launch vehicle into a halo orbit around the Sun-Earth second Lagrangian point (L2), with a nominal mission lifetime of 5 years. L2 provides a stable environment and high observing efficiency. The Athena spacecraft design is relatively conventional, and benefits from much heritage from XMM-Newton, and prior studies for the International X-ray Observatory (IXO) and the Athena concept proposed for the L1 slot.

Athena will be operated as an observatory. Besides the two main scientific themes discussed above, it is expected to provide a signficant and often dramatic improvement in our knowledge and understanding of basically any class of astrophysical sources, from planets to Supernova Remnants to the interstellar medium.

To summarize, the implementation of Athena for a launch in 2028 will guarantee a transformation in our understanding of *The Hot and Energetic Universe*, providing an essential complement to contemporary facilities working in other wavebands in that timeframe. Athena will exploit the strong European heritage in hardware development and scientific discovery in X-ray astronomy, maintaining leadership in high-energy astrophysics from XMM-Newton into the foreseeable future.

4 Further reading

Informations and documents on Athena, including the *The Hot and Energetic Universe* white paper (together with supporting papers) and the Athena mission proposal to ESA can be found at:

http://www.the-athena-x-ray-observatory.eu/

The list of people involved in the project can also be found there.

Frascati Physics Series Vol. 58 (2014)
Frontier Objects in Astrophysics and Particle Physics
May 18-24, 2014

LHAASO: Science and Status

Zhen Cao
(for LHAASO Collaboration)
Institute of high energy physics, 19B Yunquan St. Beijing, 100049, China

Abstract

A major instrument for very high energy gamma ray astronomy and researches on cosmic rays around knees will be built at 4400 m above sea level in Sichuan province, China. With a sensitivity of 10 mili-Crab, LHAASO will survey the entire northern sky for gamma ray sources with a 100% duty cycle. The spectra of all the sources will be measured simultaneously over a wide energy range from 300 GeV to 1 PeV. This will offer a great opportunity for identifying cosmic ray origins among the sources. With its wide field of view, LHAASO is particularly sensitive to the spatially extended sources and temporally transient phenomena. Equipped also with Cherenkov/fluorescence telescopes and infilled burst detector array, LHAASO will serve as the most effective detector for energy spectra of different mass groups of cosmic rays. Features of cosmic rays associated with the transition from the galactic to extra galactic originated will be the main topics of the LHAASO cosmic ray researches, including the accelerating mechanisms and the maximum energy of galactic cosmic rays, components of nearby celestial objects and so forth. The LHAASO site is

decided at Mt. Haizi in Daocheng county. The construction will be started next year.

1 Introduction

The Large High Altitude Air Shower Observatory (LHAASO) project is planned to be built a complex array of particle detectors in an area of 1 km^2 at 4410 m above sea level in Sichuan province, China. A water Cherenkov detector with an area of 90,000 m^2 will be built at the center of the array to detect gamma ray showers above 300 GeV from all directions. It works as a survey telescope for all gamma ray sources in the northern sky. A larger detector array is necessary for the much smaller gamma ray fluxes at higher energies. It is an array of 5600 scintillator detectors of 1 m^2 in a triangle grid with a spacing of 15 m. It covers an area of 1 km^2 which is sufficient to observe the gamma rays above 10 TeV up to 1 PeV for many sources. In order to suppress the cosmic ray back ground, muons in the showers must be detected. They can be recognized in the water Cherenkov telescope because they generate huge signals in the pool particularly at large distances from shower cores. About 1200 muon detectors of 36 m^2 each are built evenly in the array of 1 km^2, also using the water Cherenkov technique. Among the total active area of 40,000 m^2, the muon-less criterion guarantees a background-free detection of gamma ray fluxes above 50 TeV. The features of the combination of the arrays enable measurements of energy spectra of most galactic sources over a very wide energy range from 300 GeV to 1 PeV. It will be the most powerful tool in search for cosmic ray pevatrons in our galaxy. The all sky survey using the combination will reach to a depth of 10 mili-Crab. The detailed comparison of the sensitivity of the instrument with other experiments and future projects is displayed in Figure 1.

90,000 m^2 full coverage of the water Cherenkov detector with the cell size of 5×5 m^2, is also a very good detector for cosmic rays at energies below 10 PeV where the knees are. Shower geometry and muon content can be measured very well. On top of those, 24 wide field of view (FoV) imaging Cherenkov telescopes and about 200 m^2 "burst" detectors will be deployed close by. The combination of all the techniques offers great opportunity of multi-parameter analysis for shower composition before knowing the shower energy. For identified primary nuclei, the shower energy can be measured by

using the total numbers of Cherenkov photons in the images. The telescopes will be re-configured to make the other combination with the scintillator array and muon detector array in 1 km^2 for detection of showers at higher energies up to 100 PeV. The telescopes can be further modified as fluorescence detectors to cover higher energies up to 1 EeV for detecting the "second knee" of the cosmic ray spectrum.

It is clear that the LHAASO instrument offers great opportunities for both gamma ray astronomy and cosmic ray physics. In following sections, the science cases in both fields are discussed. The status of the project is reported as well in the last section of this paper.

2 Gamma Astronomy

In last two decodes, gamma ray astronomic observations over a wide energy range from 1 GeV to tens of TeV have had great progresses. FERMI has finished the full sky survey and found more than 1800 gamma ray sources [1)] below tens of GeV. Mainly Cherenkov telescopes have found nearly 150 gamma ray sources [2)] in the energy range above 100 GeV. Many sources have been identified by combining all observational data in bands of radio, optical, X-ray and gamma ray together. The spectral energy distribution (SED) of the sources over the very wide range greatly enhanced one's knowledge about the high energy non-thermal radiation mechanism of those sources. There are still many phenomena that are totally beyond our understanding. The radiation mechanism of shell-type supernova remnants (SNRs, e.g. RXJ-1713.7-3946 [3)]), electron or hadron originated, is the most important issue among others, such as the fast transient active galactic nuclei (AGN, e.g. PKS 2155-304 [4)]), very clear SED evolution during flares (e.g. a flare on Mrk501 in Figure 1), the very remote quasars (e.g. 3C279 [5)] with z=0.5362), the very hard SED of very extended sources (e.g. MGRO J2019+37 [6)]) and the very big gamma ray super-bubble FERMI-Cocoon [7)], also referred to ARGO J3031+4157 [9)]. The main topics are clear for the further experiments, 1) surveying for more sources, such as those in the FERMI catalog, and 2) deep investigations on the interesting sources in both spectroscopy and morphology. Before getting in more details about the all sky surveying, it is interesting to note that only 2/3 of the TeV sources are found in the FERMI catalog. This is not expected. One thought that there would be a boost of the discovery of the TeV gamma ray

sources because the telescopes know where to point with the FERMI catalog.

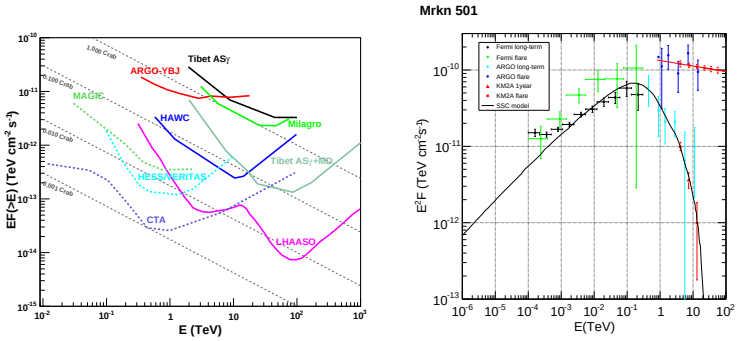

Figure 1: *The left panel is the sensitivities of current VHE gamma ray astronomic instruments and projects in near future. The solid curve in purple represents LHAASO. It is clearly divided in two parts. The one below 10 TeV is due to the water Cherenkov array of 90000 m^2, and the other in high energy range is due to the array of the scintillator and muon detectors covering 1 km^2. In the right panel, the SED of a flare of Mrk501 and its steady gamma ray emission measured by ARGO-YBJ and FERMI* [12]*. The expectations of the observation of the similar flare and the steady emission by LHAASO are also plotted here. The detailed evolution of the SED from the steady state to the flare state and return back to the steady state will be able to be observed in details*

LHAASO is designed to carry out a full sky survey to the depth of 10 mili-Crab in the northern sky. The energy coverage will be extended to 1 PeV. This feature is very useful in search for very extended sources with very hard SED that were expected to be likely hadronic accelerators, or Pevatrons in other name. In Cygnus region, MGRO J2019+37 is a mystery source not being seen by any detector for long time except the high threshold MILAGRO [6] above 20 TeV, even not by the ARGO-YBJ experiment [6], until recent deep-scanning of this region by VERITAS [8] at a depth of 10 mili-Crab at energies above 1 TeV. The reason for such hard SED from such a spatially extended region is totally unknown. The discovery of many this type of sources and detailed multi-wavelength spectroscopic investigations in particular seems to be an efficient way to clarify the radiation mechanism of them. In the same region, FERMI found an even larger object called Cygnus Cocoon which may be asso-

ciated with a super-bubble. Recent observation of ARGO-YBJ on this source identified it as the counterpart of the Cocoon at TeV range [9]. In Figure 2, the coincidence of the spatial location and extension between FERMI, ARGO-YBJ and MILAGRO is displayed, together with the consistent connection of SED by FERMI and ARGO-YBJ. Combining the MILAGRO measurement at higher energies, one may recognize an interesting cut-off feature. LHAASO will well cover the range in which the spectrum may be cut off depending on the acceleration model in the cocoon. As shown in the figure, one year operation of LHAASO will be sufficient to make a clear choice between the cut-off models. This might be useful in identification whether or not it is a hadronic cosmic ray source. In the TeV catalog, there are many SNRs and pulsar-wind-nebulae. Recent observation of the interaction between the shock front and molecule clouds [10] opens a window for searches for the cosmic ray origins. In [11], authors detailed the multi-wavelength investigation on NSRs with future instruments such as LHAASO. LHAASO is suitable not only to measure their SEDs over a wide range but also carry out morphologic investigations on those sources at high energies. The angular resolution of 0.2° of LHAASO above 10 TeV enables the study and may locate spatial regions where the gamma rays are emitted.

LHAASO is also useful in monitoring flares of AGNs. The advantage is that there is no need for organizing any champaign of multi-wavelength observation of those flares by using the wide FoV instruments LHAASO, FERMI and X-ray telescopes in the sky. Any flare of any AGN in the common FoV will be observed continuously. Very importantly, the evolution of the flares will be recorded over a wide energy range by the full duty cycle detectors. In Figure 1, an evolution of the flare on Mrk501 for 35 days measured by SWIFT, FERMI and ARGO-YBJ [12] is demonstrated by its SED. It is clearly differ from the stable emission which is fitted well with the Synchrotron Self-Compton (SSC) model. Assuming the similar flare occurs again, the prediction for LHAASO's observation is also plotted in the figure taking into account the sensitivity of LHAASO. It is expected that many AGNs flares, not only Mrk421 and Mrk501, will be measured at different flux levels everywhere in the sky. LHAASO not only serves as a global alarm system for the high energy flares, but also opens a great opportunity to identify the emitting mechanism during the flares. The potential of LHAASO in these researches, including exploring on new physics

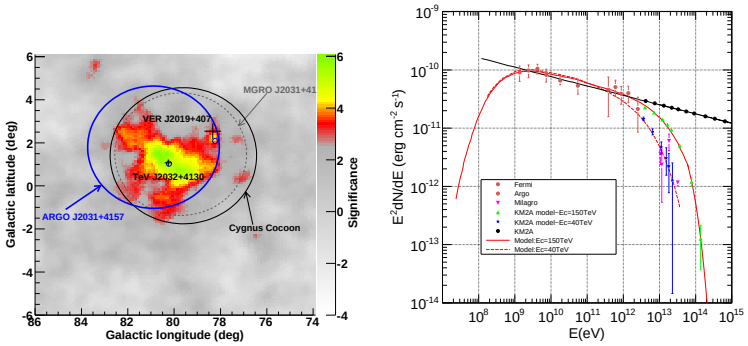

Figure 2: *In left panel, the sky map of the Cygnus Cocoon is plotted using ARGO-YBJ data. The location and the extension of the super bubble according to FERMI, MILAGRO and ARGO-YBJ are also plotted. In the right panel, the SED of the extended source measured by FERMI, ARGO-YBJ and MILAGRO shows a smooth power law with a possible cut-off which implies a hadronic origin. More details can be found elsewhere* [9]*. Here the expectation of LHAASO observation to the cocoon will extend at least by one order of magnitude in energy depending on the acceleration models. It shows that LHAASO will clearly make choice between the models with 1 year operation.*

such as intergalactic magnetic field detection and Lorentz invariance tests, has been discussed in depth elsewhere [13]. Statistic observation with many sources may help to improve our knowledge about the fascinating flaring phenomena, including the fast variation in the light curves.

AGNs are possibly sources of high energy cosmic rays above 10 PeV. Neutrinos observed by IceCube above 1 PeV reveal important clues of tracing back to the origins. The observation of the SED at high states demonstrates evidences of large deviation from the electron originated SSC model. A multi-messenger investigation combining X-rays, gamma rays, neutrinos and other observations focus on the flares of the AGNs may find useful clues. At distances of few hundred Mega-pc, radio relics and radio halos, such as CIZA J2242.8+5301, A667, A2163 and A2744, produced in the cluster merges, are pointed out by Brunetti et al. [14] in his paper in the same proceeding to be potentially the high energy cosmic ray acceleration regions. Only high sensi-

tive detectors such as LHAASO and CTA may possibly detect the spectrum of those very remote giant cosmos accelerators at scales of 1 Mpc.

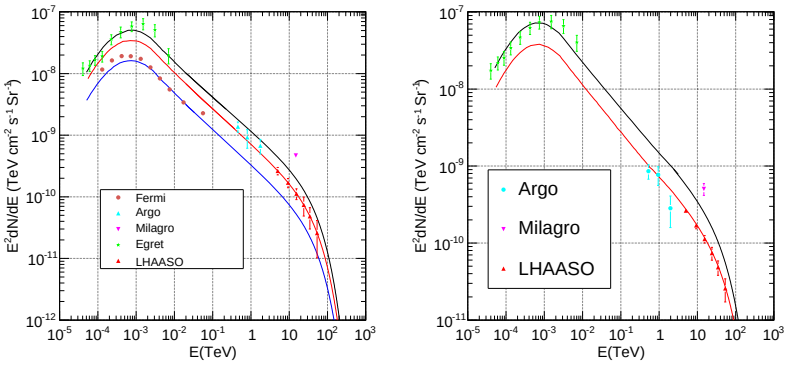

Figure 3: *The diffusive gamma ray on the galactic plane. The left is for the fluxes measured by FERMI, EGREAT and ARGO-YBJ, MILAGRO from the Cygnus region, i.e.* $65^\circ < l < 85^\circ$*, where* l *is the galactic latitude. The right is for the fluxes measured by ARGO-YBJ, MILAGRO and EGRET in the region* $25^\circ < l < 100^\circ$ *excluding the Cygnus region. A detailed analysis of this topic can be found elsewhere* [15]*. The expectations in both longitude windows of LHAASO are plotted with a cut-off of 50TeV. With 1 year operation, the observation will cover the cut-off which will strongly coupled with the knee of cosmic ray proton spectrum.*

3 Cosmic Ray Observation

The propagation through our galaxy of baryon cosmic rays can be traced by diffusive gamma rays from π^0 decay. This can be done only by the survey detectors such as FERMI at GeVs and ARGO-YBJ/HAWC at TeVs. LHAASO will extend the measurement to higher energies. The newest results by ARGO-YBJ experiment show good agreement with FERMI which measures fluxes at lower energies both from the Cygnus region and outside this region, as shown in Figure 3. It is going to be interesting to observe a cut-off at slightly higher energy of this spectrum. It can be done by a much more sensitive detector, e.g. LHAASO, as shown in Figure 3 at high energies. It would play a key role in

understanding of the knee of the proton spectrum.

LHAASO is also equipped with wide FoV Cherenkov telescopes to measure shower images which is useful in shower energy measurements and identification of the primary cosmic ray species using the shape of the images. The telescopes will cover the sky up to 30° from the zenith. In the central part of the array, an infilled scintillator array with a spacing of about 4 m is deployed to catch the high energy gamma rays in showers. Each detector, referred to burst detector, is covered with a lead layer of 7 radiation length which is useful for those high energy gamma rays to initiate showers inside and develop the showers to their maxima before reach to the scintillator. The high energy gamma rays mainly from the decay of π^0s usually distributed near the shower cores. The effective area of the infilled array is about 5000 m^2 to guarantee sufficient exposure for cosmic rays up to 30 PeV for a coverage of the knees of the spectra of all species. Above 10 PeV, the shower detection is mainly rely on the 1 km^2 array with its measurements of the shower electrons and muons. The Cherenkov telescope array will be re-configured to optimize declined showers in the high energy range. For showers at even higher energies, above 100 PeV, the telescopes needs to be converted into fluorescence light detectors to make a hybrid measurement only with the muon detectors in the 1 km^2 array and the surface water Cherenkov detectors. The cosmic ray composition variation with energy and the second knee of the spectrum are the focus in this energy region. A transition from the galactic origin to the extra-galactic is the main topic. Both spectrum and composition could have many fine structures which may reveal important information about the transition. It is important to note that the whole interesting energy range is covered by the latest accelerator based experiments such as LHCf. The latest interaction models tuned with the LHC data is quite convergent at energies well below 100 PeV. Models are consistent with data in 20% for most of distributions of measurable parameters. See papers in the same proceedings [16) 17)] for more details. It enables us focusing the cosmic ray own topics, such as composition and energy spectrum, with minimized uncertainties associated with interaction models.

At the altitude of 4400 m a.s.l., a fully covered charged particle detector like water Cherenkov detector array in LHAASO can be triggered by 1 TeV showers that are well measured by space borne detectors such as AMS02 and CREAM for their charges and energies separately. They are also calibrated at

test beams before launched. Therefore the overlap of the LHAASO detector with them is very important in both fixing the energy scale and obtaining the absolute fluxes for all species as references. Using the prototype of the LHAASO Cherenkov telescopes, we demonstrated that the hybrid measurement with the full coverage ARGO-YBJ detector array measured a spectrum of cosmic $H\&He$ nuclei without any knee structure up to 600 TeV. Our spectrum is quite consistent with ARGO-YBJ [18] and CREAM [19] up to an uncertainty in energy scale of $\pm 3.5\%$. It is also discovered that the knee of the proton spectrum is around 630 TeV with an uncertainty of 78 TeV [20], see Figure 4. This just gives us a taste of the LHAASO experiment which, at its full scale, there will be 24 Cherenkov telescopes and 90,000 m^2 water Cherenkov detector which will measure the muon contents in showers as well. The huge statistics and multi-parameter analysis will enable separation between species and precise measurement of shower energies below 20 PeV. Above the energy, composition will be measured statistically, instead of event by event basis. The detector will be sufficiently sensitive to measure the change of composition with energy and energy spectrum. The transition of the origins of the cosmic rays is the topic, from galactic to extra-galactic.

4 Status of the LHAASO Project

In Feb. 2013, the Chinese government released the "mid- to long-term perspectives for the development of major national infrastructures in science and technology". 16 mega projects, including LHAASO, are suggested to be supported in the first five year cycle. Since 2009, the prototypes of LHAASO detector array at a scale of 1%, including a 9-unit water Cherenkov detector, 42-unit scintillator array, two water Cherenkov muon detectors, two wide FoV Cherenkov telescopes and 100-unit burst detector array, are developed and continuously deployed to the Tibet site that hosts AS_γ and ARGO-YBJ experiments. They are tested with the coincidence with the existing experiments. All of them are successfully operated over years and collected sufficient technical or even scientific data that are very essential in finalizing the detector designs. The collaboration is working on finalizing the technical design report. The first piece of important physics results has been reported and sent for publishing as described above.

Simultaneously, the LHAASO site selection has been carried out over the

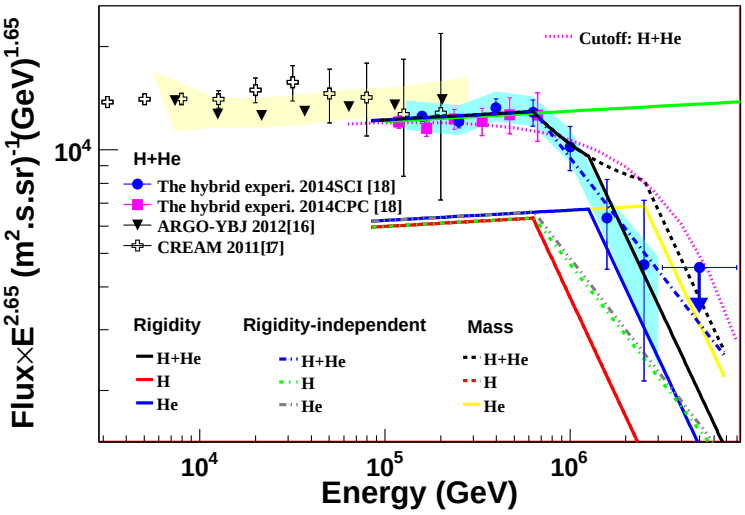

Figure 4: *The spectrum of proton and helium nuclei measured by the hybrid experiment with the LHAASO prototype Cherenkov telescopes and the ARGO-YBJ fully covered surface detector array. The bending at 630 TeV is due to the knee of the proton spectrum at the same place. LHAASO will measure even more parameters including muon content in showers and therefore will be able to separate pure samples out for several species. The knees and the spectra of the nuclei will be directly measured.*

Qing-Zang plateau of China. Among four candidates, the site at Mt. Haizi in Daocheng county, Sichuan province is finally selected. The site is in the middle of a plateau of thousands of square kilometers at about 4400 a.s.l. A brand new airport started to operate at the same altitude since last summer. It is 15 km from the site. The major highway from Chengdu, the capital city of Sichuan province, to Daocheng is just passing-by within 1 km. Nearby streams from the snow caps surrounding the plateau provide clear water to the site which is needed by the water Cherenkov detectors. It is very sunny on the plateau with a total 2700 hours of sunshine per year. The precipitation is about 700 mm and more than 80% of it is rains in three summer months. There is nearly no snow accumulation in winter. The site is 50 km from the town of Daocheng

county at 3750 m a.s.l. The LHAASO base is going to be built in the town with the living base and monitoring facility. The field preparation will be done by Sichuan province after the evaluation on environment impact. The detector deployment will start next year. The construction of the whole array will last for four years since it starts. The scientific operation may start from the end of 2016 with the first quarter of the array.

5 Acknowledgements

This work is supported in China by NSFC (Contract No. 10975145 and No. 11075170), the Knowledge Innovation Fund (H85451D0U2) of IHEP, the Chinese Ministry of Science and Technology, the Chinese Academy of Science, and the Key Laboratory of Particle Astrophysics, CAS. We also acknowledge the essential support of W.Y. Chen, G. Yang, X.F. Yuan, in the installation, debugging, and maintenance of the detector.

References

1. on-line data center of FERMI LAT: http://fermi.gsfc.nasa.gov/ssc/data/access/lat/2yr_catalog/.
2. on-line catalog of the VHE gamma ray sources: http://tevcat.uchicago.edu/.
3. Aharonian, F.A. et al., Nature 432, p75-77 (2004).
4. Aharonian, F. et al., ApJ 664, pL71-L74 (2007).
5. MAGIC Collaboration, Albert, J. et al., Science 320, p1752 (2008).
6. Abdo, A.A. et al., ApJ 658, pL33-L36 (2007); B. Bartoli et al. (ARGO-YBJ Coll.), Astrophys.J. 745, pL22 (2012).
7. Ackermann, M., et al. (FERMI-LAT Coll.), Science, 334, p1103 (2011).
8. Ong, Rene A.; for the VERITAS Collaboration, arXiv1307.5003O (2013).
9. B. Bartoli et al. (ARGO-YBJ Coll.), Astrophys.J. 790, p152 (2014).
10. Ackermann, M., et al. (FERMI-LAT Coll.), Science, 339, p807 (2013).

11. W.Tian & J. Zhang, Science China, Physics, Mechanics & Astronomy, 56, p1443 (2012).

12. B. Bartoli et al. (ARGO-YBJ Coll.), Astrophys.J. 758, p2 (2012).

13. S. Chen, Science China, Physics, Mechanics & Astronomy, 56, p1455 (2012).

14. Brunetti et al., "Diffuse radio emission in galaxy clusters: crossroad between astrophysics and cosmology", This proceeding, p?? (2014).

15. B. Bartoli et al. (ARGO-YBJ Coll.), arXiv??, submitted to ApJ (2014).

16. R. Engel, T. Pierog, and R. Ulrich, "LHC Results and the Interpretation of Cosmic-Ray Data", This proceeding, p?? (2014).

17. A. Tricomi, "Astroparticle Physics with the LHCf Detector at LHC", This proceeding, p?? (2014).

18. B. Bartoli et al. (ARGO-YBJ Coll.), Phys.Rev. D85, p092005 (2012).

19. Y. S. Yoon et al. (CREAM Coll.), Astrophys. J. 728, p122 (2011).

20. B. Bartoli et al. (ARGO-YBJ Coll. and LHAASO Coll.), Chin.Phys. C38, p045001 (2014); B. Bartoli et al. (ARGO-YBJ Coll. and LHAASO Coll.), arXiv??, submitted to Science (2014).